Estimating fracture probability of Antarctic Peninsula ice shelves using Bayesian non-parametric statistical modelling

By

Marko Closs

A thesis submitted to
the University of Birmingham
for the degree of
DOCTOR OF PHILOSOPHY

School of Geography, Earth and Environmental Sciences
College of Life and Environmental Sciences
University of Birmingham
October 2021

UNIVERSITY OF
BIRMINGHAM

University of Birmingham Research Archive

e-theses repository

This unpublished thesis/dissertation is copyright of the author and/or third parties. The intellectual property rights of the author or third parties in respect of this work are as defined by The Copyright Designs and Patents Act 1988 or as modified by any successor legislation.

Any use made of information contained in this thesis/dissertation must be in accordance with that legislation and must be properly acknowledged. Further distribution or reproduction in any format is prohibited without the permission of the copyright holder.

ABSTRACT

Drainage of the Antarctica Peninsula is mainly through its floating ice shelves, which play a vital role in limiting the flow of grounded ice into the ocean via buttressing. The magnitude of the AP contribution to sea-level rise is dependent on the health of its ice shelves. Fractures are a key part of the calving process; however, observing or predicting fractures has proven difficult.

The annual extent of four AP ice shelves is delineated from 1990-2019. Quantile regression analysis draws inferences between retreat and contributing processes. The analysis suggests a statistically significant association between increasing mean annual 2 m air temperature and ice shelves that have retreated the most. Additionally, a reduction in summer and autumn sea ice concentration correlates with retreat.

Fracture probability is estimated for the Larsen C, Wilkins and George VI Ice Shelves using flow parameters as the predictors in a Bayesian Gaussian process mixed effect model. A hybrid Monte Carlo inference scheme enables Markov Chain Monte Carlo application while remaining computationally inexpensive. The fracture probability estimations matched observed fractures in some key regions. The fracture probability of 100-year transient flow simulations under possible climate scenarios is estimated. Under the higher emissions scenario, fracture probability is significantly higher on floating ice.

DEDICATION

Dedicated to the loving memory of my Mom

Ivana Closs

ACKNOWLEDGMENTS

First and foremost, I would like to thank my supervisors Dr Nicholas Barrand and Dr Sergio Bacallado, for their advice, continuous support, enthusiasm, and patience throughout this research. I am grateful to NERC and the DREAM CDT for funding this research and the opportunities offered to me and my fellow PGRs. I would like to thank Mathieu Morlighem for his guidance in understanding the ISSM model and helping me fix my many errors. I would also like to thank everyone at the Geophysical Institute University of Fairbanks, Alaska, for inviting me to the 2018 International Summer School in Glaciology. Spending ten days living and working at the Wrangell Mountain Centre was a highlight of the last four years. I was lucky to learn from some of the worlds best glaciologists and meet some fantastic people.

I want to express how grateful I am to everyone in the School of Geography, Earth and Environmental Sciences (GEES) at the University of Birmingham; it has been amazing being part of the GEES community. I want to thank all of my officemates in room 425 who have been supportive, ready to help and go for second lunch during late nights in the office.

Finally, I would like to thank my friends Joe and Tom for their constant encouragement, and most of all, Bryony. The last four years have been both amazing and difficult, and without your unconditional support over the past four years, this would not have been possible.

Contents

Page

List of Figures **ix**

List of Tables **xvii**

1 Introduction **1**

1.1 Background and Rationale 1

1.2 Research Gaps 5

1.2.1 Research gap 1 - Twenty-first century AP ice shelf extent and contributors to retreat 6

1.2.2 Research gap 2 - A statistical framework to estimate ice shelf probability of multiple AP ice shelves that is computationally inexpensive and scalable 7

1.2.3 Research gap 3 - Evolution of ice shelf fracture over the next 100 years 8

1.3 Research Objectives 8

1.4 Thesis Structure 9

2 Literature review **10**

2.1 Introduction 10

2.1.1 Ice sheet formation and mass balance 11

2.1.2 The Antarctic Ice Sheet 12

2.2 Ice Shelves 15

2.2.1 Effect on inland ice 17
2.3 Structural Glaciology of Ice Shelves 21
2.4 Ice Shelves of the Antarctic Peninsula 24
2.4.1 Prince Gustav Ice Shelf 25
2.4.2 Larsen Ice Shelves 26
2.4.3 George VI Ice Shelf 29
2.4.4 Wordie Ice Shelf 31
2.4.5 Wilkins Ice Shelf 32
2.4.6 Stange Ice Shelf 32
2.4.7 Muller Ice Shelf 33
2.4.8 Jones Ice Shelf 33
2.4.9 Bach Ice Shelf 34
2.5 Mechanisms of Collapse and Stability 34
2.6 The Effect of Climate Forcing on Ice Shelf Viability 37
2.7 Representative Climate Pathways 39
2.8 Modelling of Calving 40

3 Study Site **42**
3.1 Antarctica Peninsula 42
3.2 Larsen B Ice Shelf 44
3.3 Larsen C Ice Shelf 46
3.4 George VI Ice Shelf 49
3.5 Wilkins Ice Shelf 52

4 Updated assessment of ice shelf extent on the Antarctic Peninsula and links to potential glaciological and environmental drivers **56**
4.1 Aims and Objectives 56
4.2 Data and Methods 57

4.3 Previous ice front studies . . . 57
4.3.1 Initial data and image selection for ice shelf extent mapping . . . 58
4.3.2 Environmental and glaciological predictor data . . . 60
4.3.3 Quantile regression . . . 64
4.4 Ice shelf extent . . . 67
4.4.1 Results . . . 67
4.4.2 Discussion . . . 73
4.5 Quantile regression analysis . . . 79
4.5.1 Results . . . 80
4.5.2 Discussion . . . 91
4.6 Conclusions . . . 95

5 Modelling Antarctic Peninsula ice shelf fracture probability using a Gaussian process mixed effects model. 97

5.1 Aims and Objectives . . . 97
5.2 Background . . . 99
5.3 Data and ISSM Model Predictors . . . 100
5.3.1 Fracture locations and fracture zones . . . 101
5.3.2 ISSM setup . . . 102
5.3.3 Predictors . . . 103
5.4 Methods . . . 107
5.4.1 Mixed-effects Gaussian process model . . . 107
5.4.2 Variational Bayes . . . 111
5.4.3 Convergence criteria . . . 114
5.5 Results . . . 115
5.5.1 High resolution fracture data simulations . . . 115
5.5.2 Low resolution . . . 123

5.5.3 Lengthscale 127
5.6 Discussion 128
5.7 Conclusions 135

6 Damage evolution and future fracture probability for Antarctic Peninsula ice shelves. 136

6.1 Aims 136
6.2 Background 137
6.3 Data and Climate Scenarios 139
6.3.1 Basal melting and surface mass balance 139
6.3.2 Fracture index data from satellite images 141
6.3.3 ISSM setup 143
6.3.4 Predictors 144
6.3.5 Transient simulation setup 148
6.3.6 Forcing selection 149
6.3.7 Transient simulations 150
6.4 Methods 154
6.4.1 Variational Bayes 157
6.4.2 Convergence criteria 160
6.4.3 Model training 160
6.5 Results 166
6.5.1 Scenario 1 (No Forcing) 167
6.5.2 Scenario 2 (RCP2.6) and 3 (RCP4.5) 168
6.5.3 Scenario 4 (RCP8.5) 170
6.6 Discussion 171
6.7 Conclusions 175

7 Conclusions 177

7.1 Summary of Main Findings 177
7.1.1 Twenty-first century AP ice shelf extent and contributors to retreat . 178
7.1.2 A statistical framework to estimate fracture probability of multiple AP ice shelves that is computationally inexpensive and scalable 179
7.1.3 Evolution of ice shelf fracture over the next 100 years 182
7.2 Limitations and Future Work 183

A Appendix 1 **186**

References **218**

List of Figures

2.1 Schmatic of an ice shelf system inculding sources of accumulation/ablation, ocean systems and measuring instruments. Figure was taken from Padman et al. (2018) and created by Jennifer Matthews, IGPP, Scripps Institution of Oceanography. 15

2.2 Location map of the Antarctic Peninsula with ice shelf. Major ice shelves are highlighted with boxes. 24

2.3 Satellite image from 05 February 2009 with the Prince Gustav, Larsen A, and Larsen B basins and Larsen C Ice Shelf annotated in blue. Major geographical features are annotated in red. Large tributary glaciers are annotated in green. Imagery from the NASA MODIS instrument, courtesy NASA NSIDC DAAC. 26

2.4 Satellite image from 15 February 2018 with the LCIS annotated in blue. Major geographical features are annotated in red. Imagery from the NASA MODIS instrument, courtesy NASA NSIDC DAAC. 28

2.5 Satellite image from 23 February 2020 with the Wordie, Wilkins, GVIIS, Bach and SIS annotated in blue. Major geographical features are annotated in red. Imagery from the NASA MODIS instrument, courtesy NASA NSIDC DAAC. 30

3.1 This satellite image from NASA's MODIS sensor aboard the Terra spacecraft shows the Larsen B Ice Shelf region on November 1, 2003. Important features are annotated, including the 1998, 1999, 2000/1, and 2002 ice front position. Credit: NSIDC, derived from Scambos et al. (2004) 44

3.2 Map of the Larsen C Ice Shelf taken from Jansen et al. (2010). The locations of major features are annotated. Data: MODIS Mosaic of Antarctica (MOA) image of the Larsen C ice shelf (http://nsidc.org/data/nsidc-0280.html). . . 46

3.3 Structural Map of the George VI Ice Shelf (2010) taken from (Holt et al., 2013a). The dominance of longitudinal structures from Palmer Land can be seen. Another notable feature is the retreat of the northern ice front between 1974 - 2010. The insert shows the southern ice front, showing that the retreat between 1973 - 2010 mostly occurred in the centre. 49

3.4 Map of the Wilkins Ice Shelf taken from Rankl et al. (2017). The ice front positions of the years 1993, 2006, 2008 and 2010 are shown, the background image from 2015. The ice bridge between Charcot and Latady Island was visible in 2008 prior to its collapse. (b) Fracture formation at the southwestern ice front in 2011 and 2015 from Envisat ASAR, Sentinel1A and TanDEM-X imagery. P is the Petrie Ice Rises and V is the Vere Ice Rise. Images are taken from: (a) Sentinel-1A 21 May 2015 and (b) Sentinel-1A 6 April 2015. 52

4.1 Ice shelf front extent: Larsen C (TL), George VI North (TC), Wilkins (TR), Larsen B (BL), George VI South (BC) 60

4.2 Annual ice shelf area time-series from 1990-2019. Each vertical grey line represents an image used for the extent delineation. 68

4.3 Annual area (km^2) gain/loss of the Larsen B Ice Shelf between 1993-2009. Each bar represents the retreat (red) or advance (blue) since the previous year. 69

4.4 Annual area (km^2) gain/loss of the Larsen C Ice Shelf between 1993-2019. Each bar represents the retreat (red) or advance (blue) since the previous year. 70

4.5 Annual area (km^2) gain/loss of the northern front (left), the southern front (middle) and the whole George VI Ice Shelf (right) between 2002-2019. Each bar represents the retreat (red) or advance (blue) since the previous year. . . 71

4.6 Annual area (km^2) gain/loss of the Wilkins Ice Shelf between 1991-2019. Each bar represents the retreat (red) or advance (blue) since the previous year. . . 72

4.7 Quantile regressions of ice shelf area (% of maximum area) with annual maximum temperature (° C) (Left) and annual mean temperature (° C) (Right). The blue line is the median (50th quantile) and the grey lines are the 20th and 80th quantiles. 81

4.8 Slope estimate (coefficient) of area regressed with annual mean 2 m air temperature (top) and annual max 2 m air temperature (bottom). Slopes estimated from the 15th to the 85th quantile with a 5% interval. Grey shading is the 95% confidence interval. Solid red line is the simple linear regression slope estimate with confidence intervals (red dashed line). 82

4.9 Slope estimate (coefficient) of ice shelf area regressed with annual mean 2 m air temperature highlighting the influence of each ice shelf for annual mean 2 m air temperature. Grey shading is the 95% confidence interval. Solid red line is the simple linear regression slope estimate with confidence intervals (red dashed line). 84

4.10 Quantile regressions of ice shelf area (% of maximum area) regressed with annual Minimum SMB (Left) and annual mean SMB (Right). The blue line is the median (50th quantile) and the grey lines are the 20th and 80th quantiles. 85

4.11 Slope estimate (coefficient) of ice shelf area regressed with annual mean SMB (top) and annual minimum SMB (bottom). Slopes estimated from the 15th to the 85th quantile with a 5% interval. Grey shading is the 95% confidence interval. Solid red line is the simple linear regression slope estimate with confidence intervals (red dashed line). 87

4.12 Slope estimate (coefficient) of ice shelf area regressed with annual mean SMB highlighting the influence of individual ice shelves. Grey shading is the 95% confidence interval. Solid red line is the simple linear regression slope estimate with confidence intervals (red dashed line). 88

4.13 Quantile regressions of ice shelf area change regressed with summer mean SIC (Left) and autumn mean SIC (Right). The blue line is the median (50th quantile) and the grey lines are the 20th and 80th quantiles. 90

4.14 Slope estimate (coefficient) of ice shelf area regressed with Summer Sea ice Concentrations (SIC) (top) and Autumn SIC (bottom). Slopes estimated from the 15th to the 85th quantile with a 5% interval. Grey shading is the 95% confidence interval. Solid red line is the simple linear regression slope estimate with confidence intervals (red dashed line). 91

5.1 Fracture index locations for the Wilkins, George VIII, Larsen C Ice shelves. The high-resolution fracture index locations (left) are delineated using images available in Google Maps Pro with a 10 m horizontal resolution or less. Only points locations that are fractured or blue ice zone (non-fractured points) are included. The low-resolution fracture index (right) use all available images (up to 30 m horizontal resolution) to delineate fracture point; all other points are set to non-fractured. 108

5.2 Evolution of the HRM hyperparameter ($\theta = (\sigma^2_{fixed} I, \sigma^2_{random} k_\lambda)$) values as a function of the Hamiltonian Monte Carlo (HMC) iterations - 10000 samples with 5000 burn-in steps 116

5.3 HRM Posterior distributions of the predictor coefficients after 10000 samples - y-axis is the number of samples, x-axis is the coefficient. All of the distributions are set away from 0 suggesting that the correlation to fractures are statistically significant. 117

5.4 The fracture prediction of the high-resolution fracture index model $p(y = 1|x)$ as a function of the predictors x for the grid locations in the ISSM datasets. On the left is the predicted fracture probability (posterior mean) of the fixed and random effects. On the right is the posterior variance (Right) of the fixed and variance effects. 119

5.5 Comparison of fractures in the southeast section of the Larsen C between images acquired on August 22, 2016, with the Multi-angle Imaging Spectro-Radiometer (MISR) taken from the NASA Earth Observatory images by Jesse Allen (Left) and HRM estimated fracture probability (Right). Rifts from the Gipps ice-rise and Hollick-Kenyon peninsula are visible in both. 120

5.6 Landsat 8 image of the northern George VI ice shelf from January 19, 2020. Lateral fracture from Palmer Land are visible. 121

5.7 On the left is the posterior mean of the random effects for the high-resolution fracture index model $p(y = 1|x)$. The posterior variance of the random effects for the high-resolution fracture index model $p(y = 1|x)$ is on the right. The sections where random effects are non-zero influence the fixed effects, hence influencing the fracture probability. 123

5.8 WIS ice bridge before collapse in 2007 (left) and after collapse in 2009 (right), both images are from ESA ENVISAT. 124

5.9 Evolution of the LRM hyperparameter ($\theta = (\sigma^2_{fixed} I, \sigma^2_{random} k_\lambda)$) values as a function of the Hamiltonian Monte Carlo (HMC) iterations. 125

5.10 LRM Posterior distributions of the predictor coefficients after 10000 samples - y-axis is the number of samples, x-axis is the coefficient. All of the distributions are set away from 0 suggesting that the correlation to fractures are statistically significant. 126

5.11 The predictions of the high-resolution fracture index model $p(y = 1|x)$ as a function of the predictors x for the grid locations in the ISSM datasets. On the left is the predicted fracture probability (posterior mean) of the fixed and random effects. On the right is the posterior variance (Right) of the fixed and variance effects. 131

5.12 On the left is the posterior mean of the random effects for the low-resolution fracture index model $p(y = 1|x)$. The posterior variance of the random effects for the high-resolution fracture index model $p(y = 1|x)$ is on the right. The sections where random effects are non-zero influence the fixed effects, hence influencing the fracture probability. 132

5.13 Estimate of the random effects of 4 models with different lengthscales (λ) $\lambda = 1$ (top left), $\lambda = 0.5$ (top right), $\lambda = 0.25$ (bottom left), $\lambda = 0.1$ (bottom right). As the lengthscale increases the random effects have more influence. . 133

5.14 Estimated fracture probability (posterior mean) of 4 models with different lengthscales. All models use the high-resolution dataset. λ - $\lambda = 1$ (top left), $\lambda = 0.5$ (top right),$\lambda = 0.25$ (bottom left),$\lambda = 0.1$ (bottom right). As the lengthscale increase the estimated probability becomes smoother. 134

6.1 AP map with observed fracture locations (red points), observed non-fracture locations, and inducing point locations on the LCIS, GVIIS, and WIS ice shelves. Inducing points reduce the effective size of the data to reduce the computational expense of sampling the posterior. The inducing point locations are calculated using a K-means cluster algorithm with 200 centroids, giving 200 inducing points. 142

6.2 ISSM 100-year transient simulation of mean velocity (m/yr), mean damage, thickness (m), and ice volume (m^3/yr) for a) Larsen C Ice Shelf (LCIS) b) George VI Ice Shelf (GVIIS) c) Wilkins Ice Shelf (WIS) under the no forcing scenario. 151

6.3 ISSM 100-year transient simulation of mean velocity (m/yr), mean damage, thickness (m), and ice volume (m^3/yr) for a) Larsen C Ice Shelf (LCIS) b) George VI Ice Shelf (GVIIS) c) Wilkins Ice Shelf (WIS) under the RCP2.6 scenario. 152

6.4 ISSM 100-year transient simulation of mean velocity (m/yr), mean damage, thickness (m), and ice volume (m^3/yr) for a) Larsen C Ice Shelf (LCIS) b) George VI Ice Shelf (GVIIS) c) Wilkins Ice Shelf (WIS) under the RCP4.5 scenario. 153

6.5 ISSM 100-year transient simulation of mean velocity (m/yr), mean damage, thickness (m), and ice volume (m^3/yr) for a) Larsen C Ice Shelf (LCIS) b) George VI Ice Shelf (GVIIS) c) Wilkins Ice Shelf (WIS) under the RCP8.5 scenario. 154

6.6 Posterior distributions of the predictor coefficients after 10000 samples - y-axis is the number of samples, x-axis is the coefficient. All but one of the distributions are set away from 0 suggesting that the correlation to fractures are statistically significant. 162

6.7 Evolution on the hyperparameter ($\theta = (\sigma^2_{fixed} I, \sigma^2_{random} k_\lambda), \lambda$) values as a function of the Hamiltonian Monte Carlo (HMC) iterations. 163

6.8 Model prediction of training data as a function of the predictors x for the grid locations in the ISSM datasets. The plot contains the estimated fracture probability (posterior mean) (left) and posterior variance (right) of the function $p(y = 1|x)$. 165

6.9 Prediction of the model $p(y = 1|x)$ s a function of the predictors x for the grid locations in the ISSM datasets. Posterior mean of the random effects (Left) and posterior variance of the random effects (Right) of the function. 166

6.10 Model prediction of scenario 1 (no forcing) as a function of the predictors x for the grid locations in the ISSM datasets. The plot contains the posterior mean (Left) and posterior variance (Right) of the function $p(y = 1|x)$. 168

6.11 Model prediction of scenario 2 (RCP2.6) as a function of the predictors x for the grid locations in the ISSM datasets. The plot contains the estimated fracture probability (posterior mean) (left) and posterior variance (right) of the function $p(y = 1|x)$.. 169

6.12 Model prediction of scenario 3 (RCP4.5) as a function of the predictors x for the grid locations in the ISSM datasets. The plot contains the estimated fracture probability (posterior mean) (left) and posterior variance (right) of the function $p(y = 1|x)$. 170

6.13 Model prediction of scenario 4 (RCP8.5) as a function of the predictors x for the grid locations in the ISSM datasets. The plot contains the estimated fracture probability (posterior mean) (left) and posterior variance (right) of the function $p(y = 1|x)$. 171

List of Tables

4.1 Previous ice shelf extent studies, ice shelves included in the study, and measurement frequency 59

4.2 List of predictor data used in our analysis, the associated publication, temporal and spatial resolution of each predictor variable. 63

4.5 Slope estimates (coefficient - *statistically significant) of area regressed with annual, mean and maximum 2m air temperature for the 20th, 50th and 80th regression lines. 83

4.6 Slope estimates (coefficient - *statistically significant) of area regressed with annual, mean and minimum SMB for the 20th, 50th and 80th regression lines. 86

4.7 Slope estimates (coefficient - *statistically significant) of area change regressed with the summer and autumn, mean SIC. 90

4.3 Predictors, the ice shelves that the data covered, and the statistical descriptors used. Prev refers to the values of the previous year. For example, the prev mean of the 2001 extent would have the 2000 mean. This aims to infer the role of preconditioning on ice shelf retreat. The 1st Quartile (Q) is the 25% quantile and the 3rd Quartile (Q) is the 75% quantile. 93

4.4 Overview of the ice shelf area of the first and last observation, total area loss during this period, and the per cent of the area remaining. 94

5.1 Predictor parameters and the method use to calculate them 107

6.1 Predictor parameters and the method use to calculate them or data source. . 147

6.2 The forcing applied to the 4 transient simulations of the Larsen C Ice Shelf (LCIS), George VI Ice Shelf (GVIIS) and Wilkins Ice Shelf (WIS), representing varying RCP scenarios. Surface Mass Balance (SMB) projections are from Kittel et al. (2021) and consistently changed for all ice shelves. Basal Melt Rate (BMR) projections are from Naughtena et al. (2018) and vary independently. All forcing is applied linearly from the beginning of the simulation for 100 years. 147

Acronyms

AIS Antarctic Ice Sheet.

AP Antarctic Peninsula.

$AVHRR$ Advanced Very High-Resolution Radiometer.

BMR Basal Melt Rate.

$CISM$ Community Ice Sheet Model.

$EAIS$ East Antarctic Ice Sheet.

GP Gaussian Process.

$GRACE$ Gravity Recovery and Climate Experiment.

$GVIIS$ George VI Ice-Shelf.

HMC Hamiltonian Monte Carlo.

HMR High-Resolution Model.

$IPCC$ International Panel on Climate Change.

$ISSM$ Ice Sheet System Model.

JIS Jones Ice-Shelf.

LAIS Larsen A Ice-Shelf.

LBIS Larsen B Ice-Shelf.

LCIS Larsen C Ice-Shelf.

LDIS Larsen D Ice-Shelf.

LRM Low-Resolution Model.

MAP Maximum A Posteriori.

MCMC Markov Chain Monte Carlo.

MISR Multi-angle Imaging SpectroRadiometer.

MODIS Moderate Resolution Imaging Spectroradiometer.

NSIDC National Snow and Ice Data Center.

PGIS Prince Gustav Ice-Shelf.

PISM Potsdam Parallel Ice Sheet Model.

QR Quantile Regression.

RCP Representative Climate Pathway.

SIC Sea-Ice Concentration.

SIS Stange Ice-Shelf.

SLE Sea Level Equivalent.

SLR Sea Level Rise.

SMB Surface Mass Balance.

SSA Shallow-Shelf Approximation.

$T2M$ 2 m Air Temperature.

$WAIS$ West Antarctic Ice Sheet.

WIS Wilkins Ice-Shelf.

Chapter One

Introduction

1.1 Background and Rationale

Since the industrial revolution, the mean global atmospheric temperature has risen by around 1° C, leading to 2 m of sea-level rise (SLR) (IPCC, 2021), most of that taking place in the last 30 years. Coastal ecosystems and communities are already feeling the effects of SLR. Globally, 40% of people on Earth live within 100 km^2 of the coast (United Nations, 2007). In the USA, 132 million people live in densely populated coastal cities that are at risk from further SLR and extreme weather (Wu et al., 2002). As water levels increase, cities lose natural protection from storms and are at greater risk of floods that can destroy the infrastructure needed to maintain the local economy (Jacob, 2015). Hurricane Katrina devastated New Orleans and the surrounding area in 2005. More than 900 people lost their lives and causing over $125 billion of damage. Still, 15 years on, the city has not fully recovered (Burton and Hicks, 2005; Brunkard et al., 2008). In the UK, extreme weather, plus the rising coastline, has seen flood defences breached, causing widespread flooding that has destroyed many peoples homes (Crooks, 2004).

All over the world, major cities are currently battling with keeping flooding at bay,

with the number of people exposed projected to increase by threefold by 2070 (Nicholls et al., 2007). In south Asia, megacities Mumbai and Dhaka are the most populous cities in their respective counties, home to 50 million people. Given a conservative estimate of 1 ± 4 m of global SLR by the end of the century, projections show a potential land loss due to coastal inundation of 4% in Mumbai (Pramanik, 2017; Pavri, 2009). Dhaka, located in Bangladesh off the Bay of Bengals, experiences extreme weather and is particularly susceptible to storm surges, leading to widespread flooding. The infrastructure is unable to deal with current flooding levels. Unless significant steps are taken, the region is at considerable risk from SLR related disaster (Ali, 1996; Castro Ortiz, 1994). SLR of less than 1 m over the next century could see an increase in inundation area of 81% in Bangkok, the worlds most-visited city and economic hub of Thailand (Dutta, 2011). Shanghai is China's most populated city, with a population of over 20 million people. It has more flood mitigation in place than other less developed megacities such as Dhaka; regardless, it is arguably the most concerning city globally. A combination of subsidence and SLR could see half of the city flooded by 2100 and 46% of sea wall breached (Wang et al., 2012; Balica et al., 2012). In North America, Florida has allocated $4 billion over the next 40 years to keep Miami above water. Between $2006 - 2013$ local sea level rise has been around 9 ± 4 mm per year (Wdowinski et al., 2016). Increased flooding and extreme weather would have substantial social and economic harm as the state's financial centre. The property market has seen the most at-risk property lose almost $500 million in total value (McAlpine and Porter, 2018). These are a handful of the major cities at risk of SLR and natural hazards that accompany it. While there risk is of great concern, a proper flood mitigation strategy could help to contain at least some of the risk. However, those living in rural coastal regions tend to be more disadvantaged and do not poses the same social or economic power to mitigate the risk (Bhattachan et al., 2018).

The IPCC report found that not only has the sea-level has risen for the last century, but that the yearly rate has more than doubled over the last 30 years compared to the

previous 90 years (IPCC, 2021). The mechanisms for SLR are multifaceted, with thermal expansion due to ocean warming being the primary cause of SLR for 75 - 100 years after the industrial revolution. However, the most significant contributor to present SLR is the melting of glacial ice. Ice caps such as the Vatnajökull ice cap in Iceland, and Alpine glaciers found worldwide, have been the dominating source of SLR, with over 60% of total ice loss coming from these regions rather than the ice sheets (Meier et al., 2007). However, the risk that the Greenland Ice Sheet and Antarctic Ice Sheet (AIS) face due to future projected warming suggest that if anthropological climate forcing is left unchecked, the contributions of the ice sheets could rapidly increase. Ice loss from the ice sheets has increased by around 29% over the last decade compared to the previous decade (IPCC, 2021).

Given the effect warming is projected to have on ice loss from the ice sheets, it has become crucial to understand its impact on global SLR. Antarctica stores 98% of the Earth's freshwater and is 98% ice-covered, equivalent to 58 m SLE (Fretwell et al., 2013). While the whole ice sheet is not at risk of collapse in the next century, if the climate continues to warm at its current rate as projected by the RCP8.5, it could lead to 0.63-1.32 m of global sea-level rise SLR (Horton et al., 2020). The Arctic is the fastest-warming region on Earth, with temperature increasing by 2.3° C (IPCC, 2021). In recent years, between 1995 - 2015, Greenland had an average annual mass loss of 0.47 ± 0.23 mm sea-level equivalent (SLE), peaking in 2012 with 1.2 mm SLE (Broeke et al., 2016). Depending on the method used and climate scenario studied, projections for sea-level contribution from Greenland by 2100 are between $3 - 33$ cm (Aschwanden et al., 2019; Goelzer et al., 2020).

A priority for the scientific community and policymakers is to develop strategies to reduce global SLR and mitigate its impacts. Crucial to this objective is predicting changes in the ice-sheet melt, stability, and sea-level contribution. This process helps to build on our understanding of the physical processes and forecast potential possibilities. Over the past two decades, the development of sophisticated mathematical models that use the phys-

ical equations of ice flow to model ice-sheet dynamics has proven to be highly effective, particularly on a large scale.

The AIS has three ice sheets, the East Antarctic Ice Sheet (EAIS), the West Antarctic Ice Sheet (WAIS), and the Antarctic Peninsula (AP). The majority of Antarctic ice loss is from the WAIS and the AP due to the acceleration and thinning of its major glaciers, lead by the retreat of their supporting ice shelves (Shepherd et al., 2018). The AP makes up only 4% of the area of Antarctica, however, is the most dynamic and climate-sensitive (Rignot et al., 2004). It is the most northern region of Antarctica, extending up to 63°. Extensive research has taken place to understand its response to historical and future climate change (Morris and Vaughan, 2013; Etourneau et al., 2019; Barrand et al., 2013; Davies et al., 2014; King, 1994; Schannwell et al., 2016; Kittel et al., 2021). It is one of the most rapidly warming areas on Earth (Vaughan et al., 2003). The majority of AP glaciers drain into floating ice shelves (Doake, 2001). Due to its thin mountainous topology, it has a high concentration of ice shelves under different pressures depending on the coast they are situated (Rignot et al., 2013).

The ice shelves result from glacier ice flowing into the ocean water cold enough that it does not melt, forming large floating ice masses. Once established, ice shelves can survive millions of years. Ice shelves play a crucial role in stabilising the AP via the process of buttressing (Gudmundsson, 2013). Buttressing is a mechanical effect of direct contact between the floating ice shelf and the grounded glacier ice at the grounding line (Dupont and Alley, 2005). Hence, removing an ice shelf would increase grounded ice flow, leading to sea-level rise (Scambos et al., 2004). Future SLR contributions of Antarctica rely heavily upon the stability of its ice shelves. Over the last 20 years, the AP has seen the collapse of 4 ice shelves, with the largest being the Larsen B ice shelf in 2002, followed by thinning and acceleration of many of its tributary glaciers (Berthier et al., 2012; Rignot et al., 2004). More recently, in 2017, a significant calving event occurred at the front of the Larsen C ice

shelf, raising questions about its stability (Han et al., 2019).

The study of AP ice shelves has been a priority for the scientific community over the past two decades. Through advancements in remote sensing and computational modelling, there have been giant leaps in our ability to observe the behaviour of glaciers and ice sheets. Several physical ice-sheet models are available that model flow regimes of both the GIS and the AIS for both grounded and floating ice (Lipscomb et al., 2019; Martin et al., 2011; Larour et al., 2012). However, there is a gap in the ability to predict ice shelf retreat and advance accurately. Calving is a highly dynamic process that has many potential triggers. Unobserved fractures pose a particular difficultly. To be able to predict retreat better, a framework for fracture modelling needs to be developed.

This thesis seeks to draw inferences based on a statistical sample between climate and glaciological stresses, and interannual ice shelf variability, by introducing new remote sensing data of ice shelf area and applying statistical regression analysis. Further, a statistical fracture model that can combine modern physical flow model outputs with modern statistical analysis on the AP ice shelves is presented. Finally, the statistical model is applied to transient physical simulations over the next century to determine potential fracture changes under varying climate scenarios.

1.2 Research Gaps

In this thesis, three research gaps are identified and addressed to better understand the risk of AP ice shelf destabilisation. By introducing statistical methods and updated data sets that will allow for advancement in understanding potential ice shelf collapse and the contributing mechanisms.

1.2.1 Research gap 1 - Twenty-first century AP ice shelf extent and contributors to retreat

A key challenge to understanding AP ice shelf retreat and advance is the highly dynamic non-linear relationships between the physical, mechanical and environmental processes. Significant surface and ocean warming occurred in the region throughout the 20th century (Meredith and King, 2005; Vaughan et al., 2003); while surface warming has been absent throughout the 21st century, ocean warming has continued adjacent to the West Antarctic Peninsula (Schmidtko et al., 2014; Turner et al., 2016). Long term warming has negatively impacted the physical state of most AP ice shelves. Numerous mechanisms have been identified to have triggered significant collapse events, linking them to changes in environmental conditions (Massom et al., 2018; Scambos et al., 2009; MacAyeal et al., 2003; Braun and Humbert, 2009; Scambos et al., 2000). However, the interannual impact of warming and the glaciological conditions that arise have not been largely explored. This is due primarily to a lack of annual area data for the majority of AP ice shelves. Decadal ice shelf area data is available, showing that the overall ice shelf area surrounding the AP has decreased over the last 50 years (Cook and Vaughan, 2010). More recent studies presented more frequent ice front data for the Larsen C, Stange, Bach and George VI ice shelves (Rankl et al., 2017; Holt et al., 2014; Holt et al., 2013a; Holt, 2013). The importance of understanding the impact of short term variation in environmental conditions was identified during the collapse of the Larsen B Ice Shelf (Broeke, 2005), where significant surface temperature anomalies led to excessive melt, leading to its collapse. *There is a need for improved annual ice shelf extent data for the major AP ice shelves to enable the investigation of the implications of interannual changes in glaciological and environmental processes on AP ice shelf area.*

1.2.2 Research gap 2 - A statistical framework to estimate ice shelf probability of multiple AP ice shelves that is computationally inexpensive and scalable

Calving and basal melt are the primary sources of ice loss for AP ice shelves, with calving varying from 10% to 90% dependent on the ice shelf (Depoorter et al., 2013). Stable ice shelves have a natural process of retreat and advance that does not impact their stability. When an ice shelf becomes unstable, the nature of its calving can range from small, steady retreats to catastrophic collapses, such as with the Larsen B Ice Shelf (Shepherd et al., 2003). Several sophisticated physical ice flow models offer various calving laws or criteria. While the process that leads to calving varies, all major calving events occur along surface and basal fractures. A major challenge in studying fractures is observing them in satellite imagery; snow cover often obscures their visibility. There are two modelling approaches to estimate ice shelf fractures. The first utilises physical flow dynamics by introducing a damage calculation that can represent fracture that impacts strain rate. Damage cannot be used as a proxy for fracture modelling as it is not intended to calculate any fracture that has not impacted the strain rate (Borstad et al., 2013). The second introduces statistical regression methods that can calculate a fracture probability by using many flow parameters (including damage). Emetc et al. (2018) introduced this idea successfully by introducing Bayesian logistic regression analysis. When modelling multiple ice shelves, a critical consideration is how to deal with the issue of non-independence of fractures on each ice shelf. Their method modelled each ice shelf region individually to find the best fitting predictors, focusing on small sections of the ice shelf, then organised them into four groups using a classification criteria based on resemblance to the best fitting model. This is an intuitive but fairly ad hoc solution to the problem and does not allow multiple ice shelves to be studied in the same model. An analysis using a sophisticated, mathematically rigorous technique that can

estimate the fracture probability of multiple ice shelves while accounting for the correlating fractures while remaining computationally inexpensive has not occurred. *There is a need to introduce a modelling framework that can utilise physical flow model output to model the fracture probability of multiple AP ice shelves simultaneously.*

1.2.3 Research gap 3 - Evolution of ice shelf fracture over the next 100 years

The international community's decisions regarding greenhouse gas emissions over the next 100 years will be critical in limiting SLR (IPCC, 2021). The destabilisation of major glaciated regions is ongoing; if emissions are not lowered significantly, ice shelf collapse could lead to a significant discharge from the AP (DeConto and Pollard, 2016). Surface Mass Balance (SMB) and Basal Melt Rate (BMR) projections suggest that mass loss from melt is going to increase under all RCP greenhouse pathways, even the best case scenario (Kittel et al., 2021; Naughtena et al., 2018). However, transient simulations have not taken place to understand how AP ice shelf dynamics could change in response to changes in SMB and BMR. Further to this, there have not been any studies to understand the potential evolution of ice shelf fractures under different future climate scenarios. *There is a need to apply a framework for ice shelf fracture study that can model fractures using transient simulations for a variety of potential climate scenarios, which would inform our understanding of the behaviour of fractures as the flow regime develops.*

1.3 Research Objectives

To address the three research gaps, the following objectives have been set:

1. Investigate the correlation between AP ice shelf area change and potential contributing environmental and glaciological predictors by applying a Quantile Regression analysis.

2. Quantify future fracture probability on major AP ice shelves by introducing a Gaussian process (GP) mixed-effects model framework.

3. Apply the model framework from Objective 2 to a forced transient simulation to project fracture changes under the RCP2.6, 4.5 and 8.5 emissions scenarios over the 21st century.

1.4 Thesis Structure

In chapter 2, Antarctic Peninsula ice shelves, mechanisms for stability, and retreat history are discussed over the century in detail. In Chapter 3, the study site is introduced. Chapters 4, 5 and 6 are the main research sections of this thesis, each tackling one of the leading research gaps outlined in this chapter. In chapter 4, new annual ice shelf extent data are presented for the Larsen B, Larsen C, Wilkins and George VI ice shelves and a Quantile Regression analysis is implemented to investigate the correlation between changes in annual ice shelf area and potential retreat triggers. In Chapter 5, a novel approach is introduced to predict ice shelf fracture probability for the Larsen C, Wilkins and George VI ice shelves within the same simulation. In Chapter 6, the fracture probability model is used to make predictions for future ice shelf fracture probability for the same ice shelves. In Chapter 7, the thesis is concluded by discussing the main findings and suggesting future work.

Chapter Two

Literature review

2.1 Introduction

Ice sheets are large ice complex that overrides the underlying topography. There are two ice sheets left, Antarctica and Greenland; they contain 70% of the freshwater on Earth. The Antarctic Ice Sheet contains 58 m SLE of ice (Fretwell et al., 2013), while Greenland holds 7 m SLE of ice (Morlighem et al., 2017). The rest of the Earth's glaciers and ice caps account for around one per cent of the total ice on Earth and could contribute 0.5 m to sea level rise (Farinotti et al., 2019). Glacial melt from Alpine glaciers and ice caps have been the most significant contributor to SLR over the last century; however, as the climate continues to warm, the potential SLR from the ice sheets increase (Meier et al., 2007). Ice streams and glaciers within the ice sheets are the main transportation methods of ice. As they thin and retreat, the freshwater they hold is discharged into the ocean. Calving and basal melt are the primary contributors to mass loss from Antarctica, and melt run off, make up just over 50% of the mass loss from Greenland (Depoorter et al., 2013; Shepherd et al., 2020); however, unlike much of Greenland, the conditions around Antarctica allow for the formation of ice shelves, floating extensions connected to grounded glaciers. As we will discuss later, they

play an essential role in stabilising the region.

2.1.1 Ice sheet formation and mass balance

The accumulation of snowfall over millennia forms ice sheets. Snow accumulates on the surface, compacting to become firn. Defined by the Glossary, firn is snow that has survived at least one summer (IACS, 2011). Layers of firn accumulate; once the layers are thick enough, the pressure acting on the lower layers causes the air passages between the grains within the firn to close and become solid ice. This transition takes place at a density of around 830 kg m^{-3}. Once there is enough mass, the ice will move under its weight and become a glacier. This process on a continental scale is defined as an ice sheet (Paterson, 1994). Ice-sheet flow is determined by a combination of the gradient and ice volume. They form dome-like centres with no gradient that is the slowest moving and thickest areas (Rémy and Parouty, 2009).

Mass balance plays a vital role in the study of glaciers and ice sheets. It is the difference between the accumulation (mass gained) and ablation (mass loss) over time. Accumulation includes precipitation, including snow, hail and rainwater that can refreeze, hoar frost, and avalanching, on the surface. Basal accumulation occurs through the refreezing of liquid water at the base of the glacier. Debris accumulation can take place when the surface of basal debris becomes entrapped within the ice. Surface debris accumulation occurs more frequently in valley glaciers and is largely absent from the ice-sheets. However, basal debris accumulation takes place as debris at the bed becomes entrained (Shaw, 1977). Ablation includes surface melt, calving, basal melt of ice shelves, snow-drift. An ice sheet is in balance if the total loss in ice equals the mass gained through accumulation. The primary source of accumulation and ablation depends significantly on the type of glacier. For both the Antarctic and Greenland Ice Sheets, precipitation is the primary source of accumulation.

On Antarctica, calving and basal melt of its ice shelves are the primary ablation sources, with surface melt runoff playing a much smaller role. On the other hand, Greenland has warmer surface temperatures resulting in melt runoff, also playing a key role in its ablation (Shepherd et al., 2020). Over the past three decades, advances in remote sensing through improved satellite altimetry and gravimetry have vastly improved the ability of the scientific community to measure ice sheet mass balance. In 1992 the European remote sensing satellite (ERS-1) was deployed (Wingham et al., 2006; Wingham et al., 2009). Measurements revealed rapid thinning at the western margins of Antarctica (Shepherd et al., 2002) and increased thickness toward the centre due to changes in accumulation (Helsen et al., 2008). A limitation of altimetry is the uncertainties that arise when converting the measurements to mass due to density estimations. In 2002, the Gravity Recovery and Climate Experiment (GRACE) satellites launched (Tapley et al., 2004). The twin satellite measures the gravitational anomalies by measuring the distance between each other. While GRACE has its limitation as the measurements require complex analysis, it can make accurate mass balance measurements. Mass balance measurement calculated by GRACE in the Gulf of Alaska supported its validity. The GRACE estimates were comparable to altimetry estimates; however, the uncertainties improved greatly. (Luthcke et al., 2008; Arendt et al., 2008). GRACE measurements from Greenland and Antarctica highlight a worrying acceleration of mass loss between 2002-2009, translating to a combined SLR acceleration of 0.17 ± 0.05 mm/yr (Velicogna and Wahr, 2005; Velicogna, 2009).

2.1.2 The Antarctic Ice Sheet

The West Antarctic ice sheet (WAIS) and the Antarctic Peninsula (AP) are situated on the west of the Transantarctic Mountains in the western hemisphere, while the larger East Antarctic ice sheet (EAIS) is in the eastern hemisphere, east of the Transantarctic Mountains.

With multiple 4000 m peaks, the Transantarctic Mountains are one of the largest ranges on Earth, with an apprioximate length of 3500 km and peak elevation of 4528 m. They traverse the whole width of Antarctica, starting in the Weddell Sea and finishing in the Ross Sea. The EAIS holds the majority of the ice volume for the continent. From BEDMAP2, a data product describing surface elevation, ice-thickness and the sea floor and subglacial bed elevation of Antarctica, the total volume of ice is 26 x 10 km^3, which is 58.3 m SLE from the whole of Antarctica. With the EAIS contributing 53.3 m, WAIS 4.3 m and the AP contributing 0.2 m (Fretwell et al., 2013).

The WAIS and EAIS experience hugely different geographical and environmental conditions. Bed topography is the most significant difference affecting future stability. The EAIS has a bed that is largely above sea level, and some sections that are below sea level would rebound above sea level if it were absent, limiting the effect of ocean induced melting that the region could experience (Joughin and Alley, 2011). For much of the history of the glaciological study, the EAIS was thought to be stable. Additionally, there is evidence that the EAIS climate was homogenous over the last three glacial cycles (Watanabe et al., 2003). While some studies argued that the EAIS experienced large scale deglaciation during the warming of the Pliocene period (3 million years ago), Sugden (1996) challenged the idea concluding that it has been stable for at least 14 million years. However, more recent studies have expressed concern that the EAIS may not be as stable as previously thought, particularly in the event of deglaciation of the WAIS (Pingree et al., 2011).

The WAIS is a marine-based ice sheet as most of its bed lies below sea level. In some cases, as deep as 2500 m (Morlighem et al., 2020). Between 1979-2017 the WAIS had a cumulative mass loss of 2700 GT. Around 65% of the drainage occurred through the Thwaites ice stream and the Pine Island Glacier (Rignot et al., 2019). Both glaciers are grounded far below sea level and have thinned due to warming from circumpolar deep water. The marine ice sheet instability hypothesis is that a marine ice sheet with its grounding lines

located on a retrograde bed is unconditionally unstable (Gudmundsson et al., 2012). As it retreats, the grounding line becomes deeper and the ice thicker, leading to further instability. The first publication to raise concern for the stability of the WAIS was Mercer (1978). To see this, first, consider an ice column passing the grounding line. The column must weigh the same as the water it displaces. Mathematically $\rho gH = \rho_w gD$ where D is bedrock depth and H is the thickness of the ice, ρ and ρ_w are the ice and water densities (Goldberg, 2017). For an ice sheet such as the WAIS to be stable, it needs flux of ice leaving the ice sheet and accumulation to be balanced. However, it can also be shown that flux across the grounding line increases with depth (Goldberg, 2017). A retreat in the grounding line would decrease surface area, decreasing accumulation simultaneously; as the grounding line retreats, the flux increases as the bed gets deeper, further exacerbating the imbalance (Goldberg, 2017). Thus this type of ice sheet is unstable (Goldberg, 2017); however, a confined ice shelf is able to stabilise the grounding line (Pegler, 2018).

The Antarctic Peninsula is one of the most climate-sensitive sections of the Antarctic ice sheet (King, 1994). As it features many ice shelves at risk of collapse, it is the focus of this thesis. It is situated in the northwest of the AIS and is the north-most part of the ice sheet made up of a narrow mountain range extending up to $63°S$. Its area is over $500,000$ km^2 and accounts for 4% of the total area of Antarctica. While its proportion of the area is small, the AP experiences 25% of the total snowfall (Drewry, 1991). Its climate sensitivity can be seen through the retreat and disintegration of many of its ice shelves. The AP features a large proportion of coastline for its size separated east to west by its mountain range. On the east coast is the Weddell Sea, and on the east is the Bellingshausen sea (Figure 2.1). The two coasts experience vastly different climates and environmental pressures, with a $3-5°$ C difference between the east and west coast of the AP (Vaughan et al., 2003).

2.2 Ice Shelves

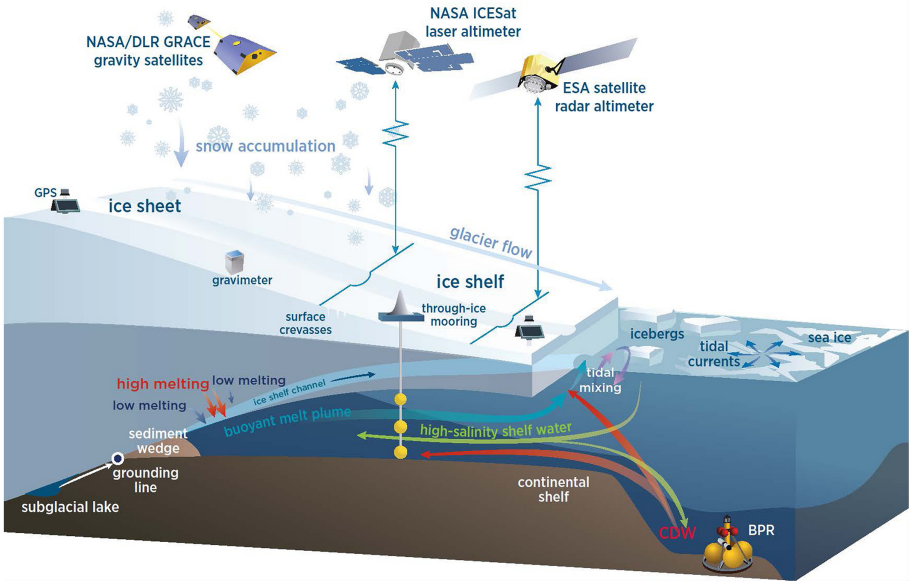


Figure 2.1: Schmatic of an ice shelf system inculding sources of accumulation/ablation, ocean systems and measuring instruments. Figure was taken from Padman et al. (2018) and created by Jennifer Matthews, IGPP, Scripps Institution of Oceanography.

An ice shelf is a sheet of ice that is floating on the sea, and that is still attached to grounded in-land ice, or land (Paterson, 1994) (Figure 2.1). An ice shelf can be differentiated from sea ice as it is much thicker, meteoric in origin, and has a stronger connection to the inland ice at the grounding line (IACS, 2011). Surface melting is a negligible component of AIS mass balance (Bentley, 1993). Ice mostly leaves the continent via the calving of tidewater glaciers and ice shelves. Greenland has a few small ice shelves; however, most are found in Antarctica. Ice shelves are formed by the seaward extension of meteoric ice from ice streams and tributary glaciers (Robin, 1979).

The area where an ice shelf connects to the ice sheet or land is called the grounding line or grounding zone. Ice shelves gain mass from the flow of inland glacier ice, snowfall

and basal accumulation (IACS, 2011). The flow of inland ice towards the ocean is not uniform. Ice streams are major outlets of the ice sheets that have increased flow, and they are the primary source of ice transport from inland ice to the ice shelf. Snowfall and basal accumulation are generally minor contributors to mass gain and vary significantly between ice shelves. Ablation takes the form of surface melt, basal melt and calving (Singh and Haritashya, 2011). Ice shelves are often confined in a bay or by ice rises, grounded ice that is surrounded by floating ice (Pegler, 2016). The hypothesised role of ice shelves is to buttress the inland ice by producing a drag against its margins or pinning points (Goldberg, 2017), decreasing the velocity at which the inland ice can flow into the ocean reduces the sea-level rise (Dupont and Alley, 2005). The velocity of an ice shelf can be hundreds of meters per year at the grounding line and a few kilometres per year at the ice front. At the shear margins, the velocity slows, sometimes being close to zero (Pegler, 2016). Unlike glaciers, where velocity increases at the surface due to bed friction (Weis et al., 1999), ice shelves have the same horizontal velocity at depths, and the fastest ice is usually found toward the shelf front where backward stresses are minimal (Doake, 2001).

For an ice shelf to have a major buttressing effect on the flow of inland ice, it must be confined in some way, either at its margins or by ice rumples/rises (Doake, 2001). The Ross and Ronne-Filchner ice shelves are both extremely wide, so the effect of the shear stress provided by the margins would be unlikely to provide much restraint. However, both have areas that they make contact with the bed, causing either ice-rises or ice-rumples to form, providing a buttressing effect (Goldberg, 2017). These are referred to as pinning points. As well as restraining an ice shelf, ice becomes thicker around pinning points, adding to stability. However, during retreat via the growth of crevasses and rifts, ice-rises can act as a wedge helping to destabilise an ice shelf (Doake, 2001). Historically non-confined ice shelves are thought to provide no buttressing effect. Gudmundsson (2013) constructs a model that allows variation in the stresses in both horizontal directions, showing that non-confined ice

shelves can have a small buttressing effect if a section of the grounding line flows over a more stable section than the rest. In this situation, the ice shelf can spread the effect of the more stable grounding line to weaker sections. Sea ice reinforces ice shelf buttressing during the winter months before the ice shelf accelerates during the spring (Greene et al., 2018).

Ice shelf calving does not directly affect sea-level rise as they are in hydrostatic balance; however, they play a crucial role in the mass balance of the AIS and the potential to contribute to SLR (Goldberg, 2017). Ice shelves fringe the entire of the AIS, including EAIS. Since the EAIS is the most stable region and has little risk of collapse, ice shelf research has focused on the large ice shelves found on the WAIS and those that drain the AP. The Ross and Ronne-Filchner ice shelves on the WAIS are the two largest ice shelves on Earth with an area of $472,000$ km^2 and $422,000$ km^2, respectively. These have been the centre of many studies; however, the research suggests they are stable (Larour et al., 2004; Paolo et al., 2015). The AP ice shelves have been the focus of most ice shelf research over the past few decades. The AP has experienced the most change over the past few decades, and the health of the fringing ice shelves is vital for the region's future stability.

2.2.1 Effect on inland ice

Unlike ice sheets, which react to climate change over more extended periods, ice shelves react rapidly (Morris and Vaughan, 2013). Once an ice shelf collapses, the effect on inland ice can be instant (Dupont and Alley, 2005). A key motivation for the study and modelling of ice shelf collapse is to determine how their absence will affect the outlet glaciers and ice streams that they buttress. There have been conflicting studies on how tributary glaciers behave after the collapse of an ice shelf. When comparing satellite imagery of the Wordie ice shelf collapse, which experienced retreat events from 1960 to the 1990s, Vaughan et al. (1993) observed that the tributary glaciers did not experience any change in grounding line

position and velocity. Wordie had three main inlet areas that are a combination of the tributary glaciers. Medial plumes were created at the confluence of two glaciers, similar to medial moraines (Macayeal and Sergienko, 2013). A change in velocity following the removal of buttressing would impact the position of these plumes. As the plumes did not move post-collapse, Vaughan et al. (1993) concluded that removing ice shelves may not affect the tributary glaciers, hence, not contribute to SLR. However, other data contradicts this claim, showing that the Fleming Glacier that previously fed the Wordie ice shelf experienced increases in velocity and thinning. Fleming glacier had sped up by $40 - 50\%$ from 1974 - 2004 (Rignot et al., 2004), and comparing data from 2004 to 2008 showed a thinning of 4.1 ± 0.2 ma^{-1} (Wendt et al., 2010). This disparity between velocity changes following significant ice shelf collapse suggests an extreme gradient insensitivity to ice shelf removal for the tributary glaciers or the time frames taken to respond.

Bed topography of the grounding line and confinement of the ice shelf potentially playing an important role in how the ice shelf buttresses the tributary glaciers. One of the first studies to quantify buttressing was Fürst et al. (2016), which calculated the amount of 'passive shelf ice' that each ice shelf contained. Passive ice refers to ice that does not provide buttressing. The findings of this study suggest that ice shelves in the Bellingshausen coast provide a high level of buttressing, so their tributary glaciers are more at risk. In contrast, the Larsen C ice shelf provides little buttressing to it tributary glaciers. Models suggest the removal of the Larsen C ice shelf will not result in significant SLR under a variety of experiments. However, George VI tributaries are much more reliant on the buttressing provided, with one experiment predicting that 95% of the sea-level contribution from LCIS and GVIIS coming from GVIIS (Schannwell et al., 2018).

Observations of tributary glaciers of the Larsen A Ice Shelf (LAIS) after its 1995 collapse showed significant dynamic response. Using synthetic aperture radar (SAR) images from 1995 to 1999 Robertson et al. (2002) showed that the velocity of the larger glaciers

(Drygalski, DBE, Sjgren and Boydell glaciers) that previously fed the LAIS and Prince Gustav Ice Shelf (PGIS). The Rohss Glacier that previously fed the PGIS from Ross Island retreated rapidly after its collapse in 1995, eventually becoming a tidewater glacier in 2002 following the complete removal of the remnants. Rohss Glacier retreated by 15 km^2 by 2009 and lost 70% of its total area. Its velocity and thickness were also affected over the same period, with the velocity increasing nine-fold and a reduction in thickness by approximately 150 m (Glasser et al., 2011).

De Angelis and Skvarca (2003) found that 6 of the glaciers that previously fed PGIS and LAIS had accelerated. The first evidence for this was ice terraces found on the Sjogren, Bogdell and Drygalski glaciers. Ice terraces are slices of stranded ice attached to a margin 20-40m above the glacier surface. The local topography rules out avalanche deposits, indicating a lowering of the glacier surface, suggesting thinning. Surface lowering can indicate surge-type behaviour as well as marginal crevassing, surge waves and looped moraines. Observations revealed that the Sjogren and Bogdell glaciers had surged between Feb 2000 and Sept 2001. They advanced 1.25 km and gaining 7.6 km^2 in area. Between September 2001 and March 2002, they had retreated, losing 12.1 km^2 in area. During the same period, the Bombardier and Edgeworth glaciers advanced 1.65 km, gaining 6.5 km^2 in area, followed by retreat seeing the Bombardier, Edgeworth and Dinsmoor glaciers losing 6.5 km^2 in area. Analysis of the velocities over the period (1999-2002) showed that the affected glaciers also experienced velocities increases. Notably, these are fast-flowing tributaries. The slower and smaller glaciers did not experience speed up or surging, suggesting that glaciers heavily buttressed by ice shelves can have a drastic response when they retreat.

The most significant collapse in the AP has been that of the Larsen B Ice Shelf. In 1995 the Larsen B Ice Shelf had an area of $11,512$ km^2, steadily decreasing to $6,664$ km^2 in February 2002 (Cook and Vaughan, 2010). In 2002 it experienced a collapse event decreasing to $3,463$ km^2 in the first three weeks of March following a warm summer (Rack and Rott,

2004; De Rydt et al., 2015). After the collapse, the tributary glaciers of the Larsen B Ice Shelf have accelerated and experienced a lowering in surface elevation. There was an increase in velocity of up to 80% from four glaciers (Hektoria, Green, Jorum and Crane) that fed the section of the Larsen B Ice Shelf that collapsed. The same study presented ICESat elevation profiles, indicating that the same four glaciers experienced a decrease in elevation. Particularly Hektoria glacier, which saw a surface elevation decrease of 38 ± 6 m. The Flask and Leppard glaciers that fed into the remnant of the Larsen B ice shelf saw little change in elevation or velocity. As the remnant is in a separate embayment, the ice shelf buttressing is still acting on these ice shelves (Scambos et al., 2004). Rignot et al. (2004) produced a similar study using data from the ERS-1 and Radarsat-1 satellites presenting similar results for velocity. Hektoria, Green and Evans glaciers accelerated by a factor of 8 between 2000 and 2003. While Jorum and Crane accelerated twofold in the same period, this translated into a mass loss of 27 km^3 per year.

Before its collapse, the tributary glaciers of the Larsen B Ice Shelf were in a balanced state. Post collapse, the glaciers experienced a mass deficit. The duration of this imbalance is an important consideration for how inland ice reacts to the removal of a buttressing ice shelf. Using Digital elevation models Berthier et al. (2012) evaluated mass loss of the Larsen B tributaries from 2006-2011. The rate of mass loss was 9 ± 2.1 GTa^{-1} between 2006 and 2011. Similar to that of 2001 to 2006, suggesting that the tributaries had continued to lose mass at a rapid rate. Rott et al. (2011) produced a similar study using TerraSAR-X images to map glacier motion for 2008/9. Frontal velocities are used to estimate calving fluxes, then pre and post collapse fluxes to estimate imbalance. Also, finding that the glaciers showed no signs of stabilizing. However, The two studies disagreed on the mass-loss rate with Rott et al. (2011) finding it to be much lower at 4.34 ± 1.6 GTa^{-1}. This discrepancy in mass loss calculation will not significantly impact sea-level estimates as this region is small. However, a more accurate assessment of the mass balance following ice shelf collapse will play an

essential role in the future as further retreats are likely.

2.3 Structural Glaciology of Ice Shelves

As a glacier deforms, structural features are left behind, leaving a record of its evolution. The mapping of these structures can offer an insight into the ice dynamics. This section describes the key surface features found on ice shelves, with a primary focus on ice shelf fracture.

Longitudinal structures (commonly referred to as flow stripes, flow bands, and streaklines) align parallel to the primary flow direction (Holt et al., 2013b). The length of the structures can vary from a few hundred meters on valley glaciers to hundreds of kilometres in Antarctica (Glasser and Gudmundsson, 2012). They are extensive at the grounding line, particularly at tributary glaciers, although they can also form on ice shelf surfaces. There has been extensive debate on the formation of longitudinal structures. The three primary hypotheses of how they form are: 1) They form from lateral compression when a glacier flows into a narrow tongue from a wide accumulation basin (Hambrey, 1977; Hooke and Hudleston, 1978). 2) They form through shear margins between the convergence of two tributary glaciers (Merry and Whillans, 1993). 3) They are surface expressions of subglacial bed topography (Gudmundsson et al., 1998).

Ice dolines are surface depressions unique to ice shelves from surface or englaciated meltwater drained through hydrofracture (Holt et al., 2013b). Dolines enable surface meltwater to drain into the ocean rapidly. The resulting local mass loss can lead to ice shelf flexural stress (Warner et al., 2021). Dolines form only in regions with a supply of excess meltwater, near flow unit boundaries, and previously crevassed areas (Bindschadler et al., 2002). During the austral summer, they tend to refill. The doline boundaries change depending on the flow

patterns on the surrounding ice.

Fracturing occurs when a temperature-dependent tensile stress threshold is exceeded (Vaughan, 1993; Rist et al., 2002). The following definitions are taken from Holt et al. (2013b). Fracture is a general term for any crack in the ice that forms within the ice shelf, regardless of direction, location, or formation. Crevasses are openings that form on grounded ice and flow over the grounding line. Rifts are large fractures that visibly penetrate the full thickness of the ice shelf. The opening of a rift is usually filled with water, sea ice, or ice melange from calving. As a shorthand, this thesis uses the term fracture to mean any fracture, crevasse or rift on the ice shelf surface, as the implemented model does not make predictions or assumptions on depth or origin.

The fractures described above are brittle failures, which feature little to no plastic deformation prior to the fracture. Fractures, crevasses, and rifts on a glacier or ice shelf surface are brittle structures. Benn et al. (2007) illustrated that there are 3 basic modes of fracture. In Mode 1 (tensile), tensile stress pulls the ice apart, and the fracture is perpendicular to the direction of maximum tensile stress. In Mode 2 (shearing), the faces of the fracture remain together, and the fracture propagates in line with a shear plane. In mode 3 (tearing), fracture occurs at a right angle to the shear plane. Mixed-mode fractures arise when two or more processes take place at the same time. How deep a crevasse propagates is determined by the point that the stress that initiated the fracture is equal to the ice overburden pressure.

Glaciers flow through ice creep and basal slippage. Glacial creep is a ductile process caused by the slippage within or between internal ice crystals due to stress from their weight. Ductile failure features significant plastic deformation before fracture; they propagate slowly compared to brittle fractures as much of the potential energy is absorbed through this deformation. Examples of visible ductile structures on glaciers include folds, foliation, and ogives (Kellerer-Pirklbauer and Kulmer, 2019).

Other important surface structures include fracture traces that are the remnants of fractures, crevasses and rifts that have closed up. Ice rises and ice rumples are both areas where the ice shelf has become grounded, visible as an elevated portion on the ice shelf surface. Ice rises are pinned to the bedrock below. Ice rumples are also grounded, but there is still flow over the bedrock. Pressure ridges are regions where deformation has taken place due to longitudinal or transverse compression.

2.4 Ice Shelves of the Antarctic Peninsula

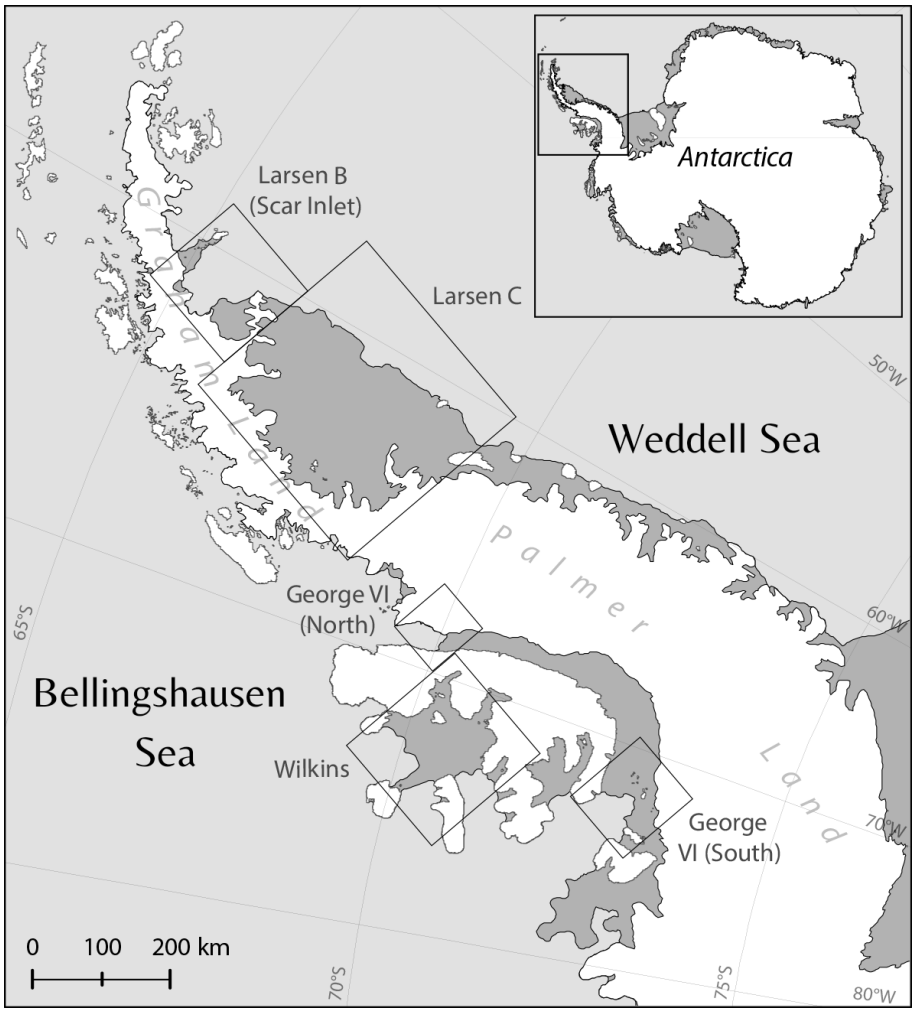


Figure 2.2: Location map of the Antarctic Peninsula with ice shelf. Major ice shelves are highlighted with boxes.

In the section, we will discuss the ice shelves of the Antarctic Peninsula and understand how they have changed over the last century. The first distinction is the coast that the ice shelves are situated. On the Weddell Sea coast (east coast) are PGIS, LAIS, LBIS, LCIS and Larsen D Ice Shelf (LDIS). On the Bellingshausen coast (west coast) are the GVIIS, WIS, Muller, Jones, Bach, Wordie and SIS (Figure 2.2). Cook and Vaughan (2010) gives the most comprehensive overview of area change of the AP ice shelves from the mid 19th century to

the present. The George VI, Wilkins, Larsen B and Larsen C ice shelves are discuss in more detail in Chapter 3.

Using radar Altimeter data from ERS-1, ERS-2, Envisat, and Cryosat-2 Adusumilli et al. (2018) produced a 23-year time series (1994-2016) of ice shelf height change for some of the ice shelves on AP, partitioning the height change into the contributing factors of surface mass balance (SMB), ice dynamics, firn air content and basal mass balance (BMB). This work is the most comprehensive study in AP ice shelf height change.

2.4.1 Prince Gustav Ice Shelf

Situated on the east coast of the Antarctic Peninsula, PGIS was the most northerly ice shelf in Antarctica, covering the Prince Gustav Channel, which separates the Trinity Peninsula and James Ross Island (Ferrigno et al., 2004) (Figure 2.3). Its main tributary glaciers were the Sjogren and Boydell glaciers that flowed from Trinity Peninsula northwards into Rohss Glacier that flowed south from James Ross Island. Until the 1980's, Tait Glacier was also a tributary until the ice shelf retreated past it. The PGIS is also one of the small number of ice shelves within the AP that has two fronts. The northern, more stable front sat within convergent margins. The southern front was situated in a wider divergent margin (Cooper, 1997). Using satellite images Cook and Vaughan (2010) observed the total area to be 1600 km^2 in 1957, which retreated over the next 50 years before the total collapse in 1995. Ice-core samples from the PGIS surface suggest that the PGIS had retreated previously in the Holocene period corresponding to local climate warming (Pudsey and Evans, 2002; Nývlt et al., 2014; Johnson et al., 2011).

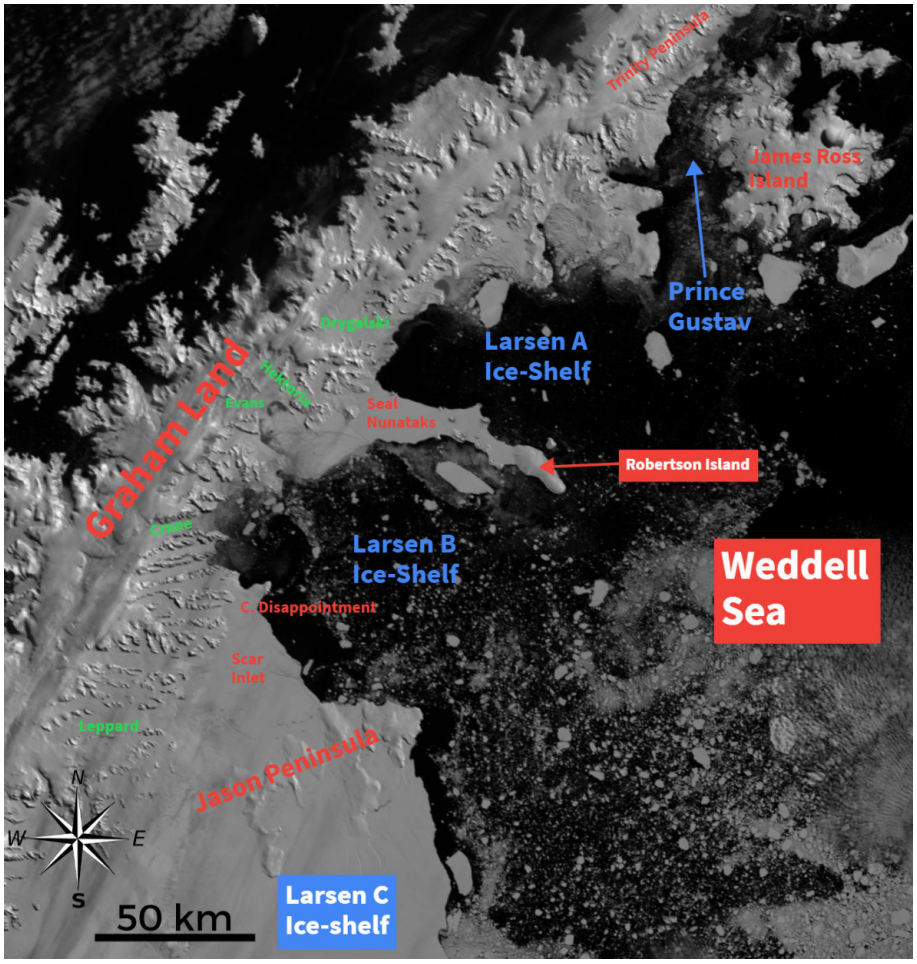


Figure 2.3: Satellite image from 05 February 2009 with the Prince Gustav, Larsen A, and Larsen B basins and Larsen C Ice Shelf annotated in blue. Major geographical features are annotated in red. Large tributary glaciers are annotated in green. Imagery from the NASA MODIS instrument, courtesy NASA NSIDC DAAC.

2.4.2 Larsen Ice Shelves

The Larsen ice shelves most northerly point starts south of the remnants of the Prince Gustav ice shelf at the Sobral Inlet, down the whole east coast of the AP, ending at New Bedford Inlet. It has become common to discuss this ice shelf as four distinct sections: Larsen A, Larsen B, Larsen C, and Larsen D (Vaughen and Doake, 1996). Comparisons between recent

AP warming and temperatures during the Holocene suggest that the northeastern AP is not a viable region for ice shelves. Continued atmospheric warming could lead to the southward migration of ice shelf instability as temperatures pass the stable conditions that were present during 9,200 – 2,500 years before present (Mulvaney et al., 2012).

The Larsen A Ice Shelf (LAIS) was the most northern section of the Larsen Ice Shelf (Figure 2.3). It remained stable until the 1980s when it had an area of 4000 km^2 before it began to retreat steadily; this was the first ice shelf collapse event observed (Doake et al., 1998). Like Prince Gustav, Larsen A had a major collapse in 1995, losing 2000 km^2 in a matter of a couple of weeks in January/February of that year. In 2008/9, there was only 397 km^2, and what was left may not be afloat (Cook and Vaughan, 2010). The main tributaries of the LAIS are the Drygalski, Dinsmoor, Edgeworth and Albone, Fyke, Polaris and Eliason glaciers (Ferrigno et al., 2004). The collapse of the LAIS resulted in the removal of the back stress on inland ice, leading to an instantaneous twofold increase in surface velocity of the Drygalski Glacier (Royston and Gudmundsson, 2016).

Larsen B is situated south of Larsen A, and in 2002 suffered a similar fate (Figure 2.3). It had an area of 12000 km^2 in 1963 and advanced until the 1990s. Its retreat began in 1995, which continued until 2002 when it collapsed, losing 3250 km^2 in less than a week (Rack and Rott, 2004). It had entirely collapsed between Cape Disappointment and Cape Fairweather by 2005. The main tributaries of this section had been Crane, Jorum, Evans, Green and Hektoria glaciers, with some smaller glaciers also feeding them (Figure 2.3). A section remains in the Scar Inlet between Jason Peninsula and Cape Disappointment (Cook and Vaughan, 2010).

Larsen C is the largest ice shelf on the Antarctic Peninsula, extending south of Jason Peninsula down to Ewing Island (Figure 2.4). Its area was recorded to be 51,000 km^2 in 2010. In 2017, a 58,000 km^2 iceberg (A68) calved from the front of Larsen C, which was

approximately 10% of the total area of the ice shelf (Hogg and Gudmundsson, 2017).

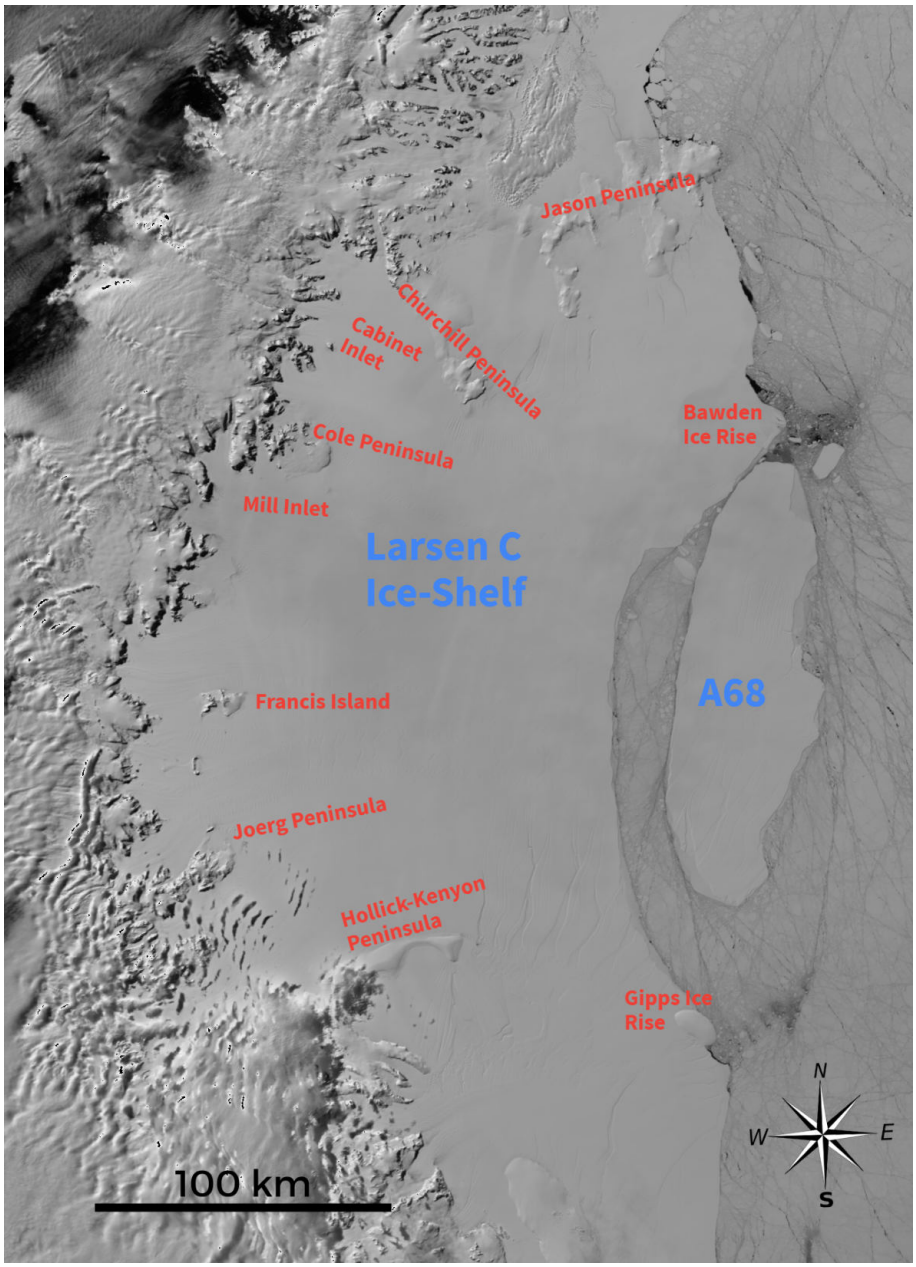


Figure 2.4: Satellite image from 15 February 2018 with the LCIS annotated in blue. Major geographical features are annotated in red. Imagery from the NASA MODIS instrument, courtesy NASA NSIDC DAAC.

Larsen D in the southernmost section of the Larsen Ice Shelf. It is often overlooked

in studies as it appears to be stable and has advanced slightly over the 50 years. It had a area of $21,700$ km^2 in 1963 and an area of $22,600$ km^2 in 2008/9. Poor signal to noise ratio for the radar altimeter data as a result of steep topography makes it impossible to make a deduction (Adusumilli et al., 2018).

2.4.3 George VI Ice Shelf

George VI is the largest ice shelf on the west coast of the AP and has some unique characteristics. It has two fronts that are over 500 km^2 apart. The northern front terminates in Marquerite Bay, and a south front terminates in the Ronne Entrance with two ice-rise (Figure 2.5). The two fronts both have distinct conditions and geometry. Cook and Vaughan (2010) observed that the northern front advanced until the 1960s before a steady retreat until the last observation in 2008. This retreat totalled a loss of 610 km^2 between 1947 and 2008.

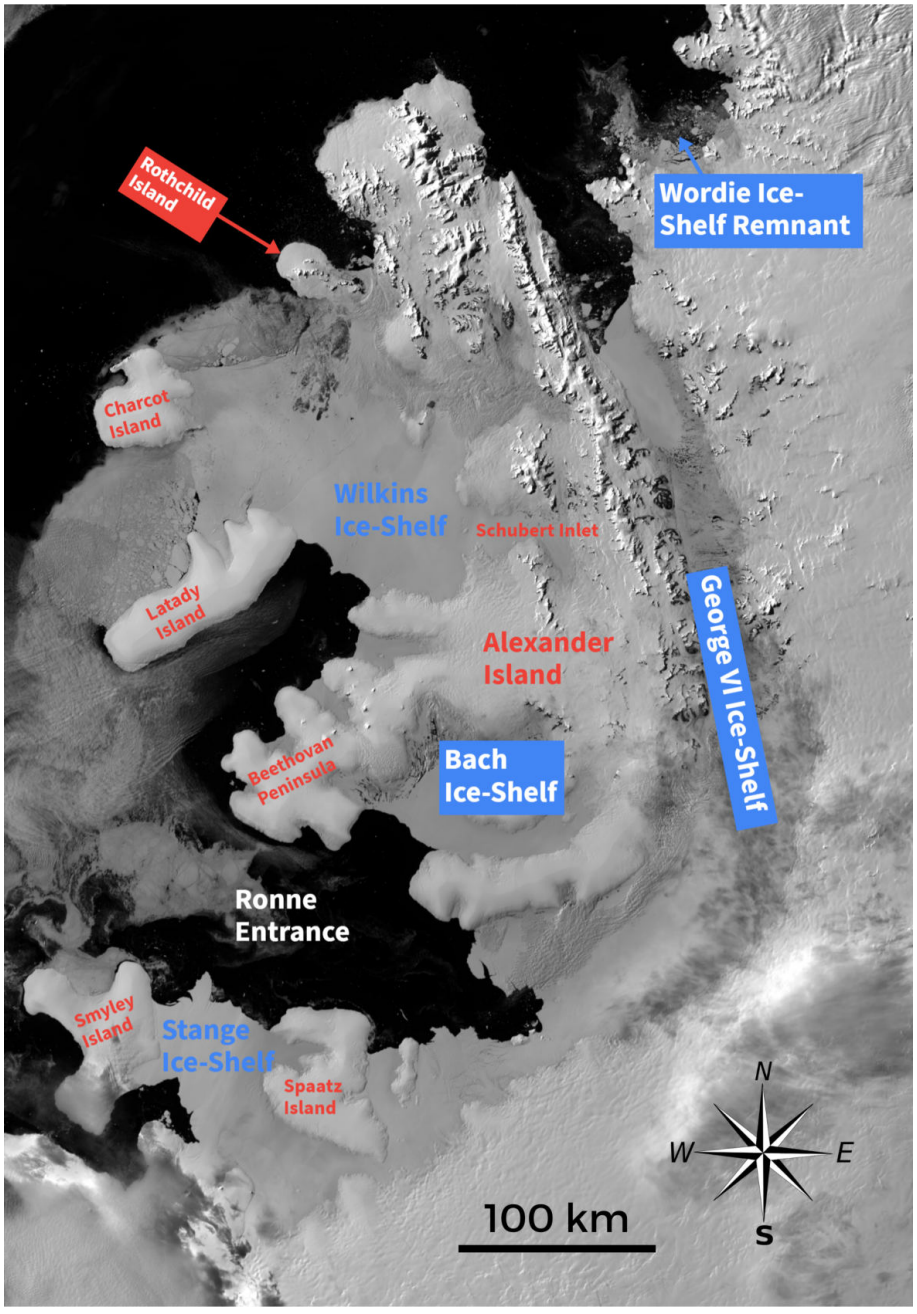


Figure 2.5: Satellite image from 23 February 2020 with the Wordie, Wilkins, GVIIS, Bach and SIS annotated in blue. Major geographical features are annotated in red. Imagery from the NASA MODIS instrument, courtesy NASA NSIDC DAAC.

In contrast, the southern front was observed to steadily retreat from 1947 until the

last observation in 2008, totalling a loss of 1320 km^2. George VI is located in a narrow channel that is 25 km wide at the northern front and 75 km at the southern front. A possible cause for the southern front experiencing more significant retreat is that it is situated in a large divergent section of the channel. Conversely, the northern front is a much narrower convergent section, more prone to restricted flow and stabilizing features such as a compressive arch. The ice shelf fills the space between the mainland of the AP at Palmer Land and Alexander island (Ferrigno et al., 2004). Adusumilli et al. (2018) found that GVIIS south had the highest melt rates at 7 ± 2 ma^{-1}. Basal melt is the primary ablation source of the GVIIS (Rignot et al., 2013). This coincides with the increased velocities of the tributary glaciers. Consistent with the reduced buttressing from ice mass removal.

2.4.4 Wordie Ice Shelf

The Wordie Ice Shelf had largely collapsed by 1992. During the first phase of collapse, approximately 10 ice-rises/rumples were discovered. The numerous ice-rises would have acted as wedges during the retreat, aiding in collapse rather than acting as pinning points (Vaughan et al., 1993). Increased ablation and fracture due to meltwater were likely contributors to the retreat of the Wordie ice shelf. It previously drained a catchment area of over $15,000$ km^2 (Vaughan et al., 1993). From the aerial image from 1947, the area was 1420 km^2. After a series of collapse events in the 1970s and 1980s, the area was 139 km^2 in 2008. The only ice left of the Wordie ice shelf being a few ice tongues of the glaciers that had previously fed it (Cook and Vaughan, 2010). It is was fed by 7 glaciers, with the main tributaries being the Fleming, Seller, Airy, Hariot and Carlson Glaciers (Ferrigno et al., 2004).

2.4.5 Wilkins Ice Shelf

Wilkins extends from the Mozart ice piedmont to the Eroica peninsula on the mainland AP to Latady and Rothschild islands (Figure 2.5). Up until 2008, the Wilkins also connected to Charcot Island. WIS experienced a break-up event in May 2008 in which the ice "bridge" connecting it to Charcot Island collapsed. No meltwater was present this time, suggesting bending stress caused the break-up event in austral winter due to an extreme thickness gradient (Braun and Humbert, 2009). WIS experienced a surface lowering of 1.1 $\pm$ 0.1 m from 1994 to 1998. Lowering reduced to 0.4 ± 0.1 m until 2013 when it gained 1.2 $\pm$ 0.1 m. This increase is likely due to changes in firn air content Adusumilli et al. (2018). Since 1995 the Wilkins ice shelf (WIS) has had a series of collapse events. WIS experienced two retreats in 1995, totalling an area loss of 1360 km^2 of ice and another event in 1998 lost 1098 km^2. These were rapid break-up events rather than a series of smaller calving events (Scambos et al., 2000).

2.4.6 Stange Ice Shelf

Often left out of discussions and analysis of the ice shelves of the Antarctic Peninsula, the Stange ice shelf (SIS) is has been stable over the past 50 years. The mean annual air temperature of $-11°C$ to $-15°C$ is comfortably within viable limits (Vaughan et al., 1993). It has maintained 96% of its original area since the 1950s (Cook and Vaughan, 2010). Stange Ice Shelf connects the mainland AP at Ellsworth Land to Smyley Island, Case island, Spaatz Island and Detley Island (Cook and Vaughan, 2010) (Figure 2.5). It is fed from 3 distinct areas and has 3 fronts. The most comprehensive and robust study of the SIS is Holt et al. (2014), which presents the extent and surface structure of SIS from 1973 to 2001. SIS experienced a net loss of 338 km^2 between 1973 and 2011. All the loss came from the northern front as the central and southern fronts gained 45.2 km^2 and 0.8 km^2 respectively.

Velocity did not change drastically on much of SIS. There was a deceleration in the southern part of the south front. Between the English Coast and the Case Island, there was an acceleration of up to 400 ma^{-1}. The southern section of the ice shelf also experienced some shear fracturing between 2001 and 2011. SIS experienced widespread lowering, with average rates of -0.17 ± 0.01 ma^{-1}. The melt days of the ice shelf were low, with 60-80 days in the north section, 35 days in the centre and less than 10 days in the south. The shear fracturing is likely caused by thinning, suggesting that ocean forcing will be the primary driver of any future instability (Holt et al., 2014).

2.4.7 Muller Ice Shelf

At only 40 km^2 in 2008, Muller is one of the small ice shelves on the AP. It is situated on the west coast of the AP and is fed by the Bruckner and Antevs glaciers. It is pinned by Humphreys Ice Rise, which separates the two fronts of the ice shelf (Ferrigno et al., 2004). Aerial photography from 1957 shows the ice shelf extended far beyond the island, where the two fronts joined, reaching Hooke point, with a maximum area of 78 km^2 before its steady retreat (Cook and Vaughan, 2010). A study by Ward (1995) shows that the regression is not linear. The 1947 area was 51 km^2 when it advanced to its maximum observed area by 1956.

2.4.8 Jones Ice Shelf

Situated in the Jones Channel between Bigourdan Fjord and Bourgeois Fjord, the Jones Ice Shelf (JIS) is a small ice shelf with an area of 29 km^2 in 1947. It was observed to advance until the 1970s when it steadily retreated from its maximum area of 36 km^2. It had completely collapsed by 2008. Its main tributary was the Heim Glacier (Ferrigno et al., 2004). A study by Fox and Vaughan (2005) examined how the two fronts of the Jones

Ice Shelf reacted differently to the same climate conditions. The eastern front of the JIS advanced from 1947 to 1969, followed by a steady retreat. The western front showed no retreat until 1991, retreating rapidly from there until its collapse. The two fronts would experience the same climate conditions; however, the embayment of each front is hugely different. The eastern front sat in a divergent channel where it was 2.6 km wide in 1947 and 1 km wide in 1996. Conversely, the western front sat in a convergent channel, retreating from its narrowest point of 1.75 km to 4.6 km in 1998. The retreat patterns of the western front are consistent with the idea of restricted flow from a compressing arch stabilizing the ice shelf. Once the compressive arch is broken, collapse can follow rapidly. Climate forcing can precondition an ice shelf for collapse; the geometry of the ice shelf will guide the pattern of collapse.

2.4.9 Bach Ice Shelf

The Bach Ice Shelf is between the Beethoven Peninsula and Monteverdi Peninsula at the southern end of Alexander Island (Figure 2.5). Like the SIS, it is often not discussed. It has remained relatively stable over the past 50 years, likely due to its small front. Observations show it had an area of 4800 km^2 in 1947, and it only lost 300 km^2 of its area by 2008 (Cook and Vaughan, 2010). It has four inlets, the Weber, Boccherini, Williams and Stravinsky inlets. The main tributaries are the Arenskyu, Alyabiev and DarGomyzhsky glaciers (Ferrigno et al., 2004).

2.5 Mechanisms of Collapse and Stability

The mechanism of ice shelf retreat has been studied in great detail; however, multiple mechanisms occur simultaneously, and there is often disagreement as to which mechanisms played

the most significant role in a retreat event.

Fractures play a critical role in ice shelf stability and calving (Hughes, 1983). Hydro-fracture is the primary mechanic for ice shelf fracture propagation. In the presence of excess meltwater, the water level rises within the fracture until the water pressure at the crack tip exceeds the fracture toughness of the ice and any compressive stresses transverse to the fracture orientation. The fracture will continue to propagate if the water pressure at the crack tip exceeds overburden pressure from the surrounding ice (Alley et al., 2018). Not all ice shelves are equally as susceptible to hydro-fracture. High firn air content can act as absorbing buffer for excess meltwater, prior to collapse the Larsen A and B Ice Shelves both had low firn air content (Munneke et al., 2014). The resulting hydrostatic pressure causes the fracture to propagate, on a large scale, destabilising the ice shelf (Lai et al., 2020; Robel and Banwell, 2019). A fracture with a depth of $16-30$ m would be deep enough to propagate through the entire thickness of the ice shelf when filled with water (Scambos et al., 2000; Veen, 1998). It played an essential role in the collapse of the Larsen A and Larsen B ice shelves (Scambos et al., 2000). Excess surface water due to surface warming was the primary preconditioning factor that led to the collapse of Larsen B (Rebesco et al., 2014). During the austral summer of 2001/2002, the surface melt was three times greater than the previous five years (Broeke, 2005). The excess water collected on the surface before over 2750 supraglacial lakes drained a few weeks before the collapse, leading to propagation through hydrofracture (Banwell et al., 2013; Leeson et al., 2020; Banwell et al., 2014). Flexure also takes place in conjunction with hydrofracture following the drainage of meltwater ponds once the water drains. A 2 m deep lake can rebound by up to 1 m in the centre and not reaching zero until 500 m (Banwell et al., 2019). The loading and unloading on the ice shelf surface can produce fracture in and around the melt pond basin (Banwell et al., 2013; Macayeal and Sergienko, 2013). Basal crevasses can also experience hydrostatic pressure that results in propagation; however, more damaging is their role in exacerbating surface fracture propagation. Reduce

thickness, surface depression, and shape changes due to bending stresses all occur in the presence of a basal crevasse, producing surface fractures and minimising the distance for full-thickness propagation (McGrath et al., 2012a; Luckman et al., 2012).

Heterogeneity of the ice shelf surface is a protective mechanism from fracture propagation. Suture zones are regions of material heterogeneity between meteoric inflow made up of marine ice, meteoric ice with modified rheological properties, and fractures; they are longitudinal bands that form downstream of peninsulas (Borstad et al., 2017). A 25 m rift terminated at the Churchill suture zone, located on the LCIS, contains around 60% of marine ice (McGrath et al., 2014; Jansen et al., 2013; Glasser and Scambos, 2008).

Through the study of stress patterns, Doake (2001) hypothesised the concept of a compressive arch for ice shelves and its role in the collapse of the LAIS and LBIS. A compressive arch is a curve that extends across the entire width of the ice shelf. The compressive arch is the curve across the ice shelf such that the 2nd principal strain is always negative upstream of it (the 1st principal strain is always positive). The location of the compressive arch cannot be easily determined. The hypothesis is that all downstream of the compressive arch can calve without impacting the compressive arch; however, if calving breaches the arch, retreat occurs quickly and continues until a new compressive arch is formed (Doake, 2001). Simulations of the LCIS suggest that the compressive arch position changes as the ice shelf dynamics change. The presence of soft marine ice within suture zones and rift push the compressive arch position upstream. This could act as a protective mechanism as warming occurs (Kulessa et al., 2014).

Downstream of the compressive arch is ice that is labelled 'passive ice' (Fürst et al., 2016). Passive ice refers to ice that can be removed with loss of buttressing or impacting stability. The LCIS contains a significant amount of passive is so it is not at risk of rapid dynamic change; however, the ice shelves of the Amundsen and Bellingshausen seas have

little to no passive ice, making them more susceptible to dynamic change triggered by calving (Fürst et al., 2016).

The retreat events of the WIS highlight the complexity of ice shelf collapse. Braun and Humbert (2009) show the collapse of the ice bridge that connects the WIS to its confining islands occurred in the austral winter when no meltwater was present. Due to thickness gradients in the region, bending stresses induced by buoyancy forces are responsible for fracture formation. While the situation will likely not occur in most ice shelves, it highlights that glaciological stresses can also impact retreat. Interestingly, before the collapse, both sides of the bridge experienced calving in the presence of meltwater. Another situation where glaciological stresses caused retreat was on the Ross ice shelf. A gravitational force led to significant rifts that eventually led to the formation of large tabular iceberg calving (Joughin and MacAyeal, 2005).

2.6 The Effect of Climate Forcing on Ice Shelf Viability

The mechanisms discussed above are closely tied to climate forcing. A significant climate factor in ice shelf collapse is the warming that leads to excess surface melt. Weather station data along the west of the AP has shown that the region has been warming consistently; measurements from Faraday station showed an increase of approximately 2.5° C (Vaughen and Doake, 1996). Morris and Vaughan (2013) mapped mean annual air temperature over the AP for the 20th century, finding that the whole region warmed by around 3.5° C. They found significant temperature contrast between the east (3° C) and west AP (5° C). Both suggest that there is an isothermal limit of −9° C for ice shelf viability. Above that, a progressive retreat will take place.

Surface meltwater can begin to accumulate rapidly, causing ponding. Eventually, the

excess water will drain, leading to hydrofracture (Scambos et al., 2000). Further highlighting the impact the warming has on the ice shelf surface are the strongly positive trends in the duration of melting conditions; positive degree days have almost doubled since 1948 at Faraday/Vernadsky (Barrand et al., 2013). As discussed, the surface melt was a significant driver for the LBIS collapse (Broeke, 2005). Over the past 20 years, AP mean annual temperature has been decreasing at a statistically significant rate (Turner et al., 2016). However, some ice shelves are still experiencing significant melt. The LCIS melt duration and intensity have decreased for the last 20 years; however, the 2019/2020 melt is the most intense for the last 40 years (Bevan et al., 2020). Melt duration has increased such that winter melt has been a significant contribution to total melt flux. Between 2015-2017, 23% of the total melt flux occurred during the austral winter.

Over the past 50 years, ocean warming has induced significant basal melt, a primary driver of ice shelf ablation in some regions. Ocean temperatures around the western AP have risen by more than 1° C since 1951 (Meredith and King, 2005). On the northeastern AP, temperatures have increased by around 0.3° C since 1979 (Etourneau et al., 2019). Ice shelf that terminate in the Bellingshausen and the Amundsen Sea are far more susceptible to melt than those on the Weddell coast. Warm Circumpolar Deep Water (CDW) ($> 1°$ C) floods the continental shelf leading to the high melt rates under the Bellingshausen Ice shelves (Schmidtko et al., 2014; Meredith and King, 2005). Strong winds increase the mixing of CDW and water on the continental shelf (Dinniman et al., 2012). Due to its unique geometry and warm cavity water, the GVIIS has the highest basal melt rate of the whole AP (Rignot et al., 2013). GVIIS lost 89 ± 17 GT/year to melt while only losing 5.7 ± 1.2 GT/year to calving between 2003 and 2008. During this period, the AP lost a total mass of -9 ± 74 GT/year (Rignot et al., 2013). Ocean temperature prediction under RCP8.5 predicts warming of 0.3° C by 2100 using 24 CMIP5 models (Heuzé et al., 2015). Warming of this magnitude will undoubtedly significantly increase basal melt, reducing buttressing

and potential destabilising ice shelves.

2.7 Representative Climate Pathways

A Representative Climate Pathway (RCP) is a greenhouse gas trajectory used by the IPCC in the fifth assessment report. The pathways describe project future climate scenarios depending on the severity of greenhouse emissions (IPCC, 2021). The RCPs are numbered by the radiative forcing increase from pre-industrial conditions; for example, RCP2.6 (the lowest original pathway) is 2.6 W/m^2 (watts per meter squared) (Moss et al., 2010). The Paris Agreement set out targets to limit global temperature rise to 1.5° C by 2100 or RCP1.9; this is an aggressive target that will require substantial international cooperation (Geiges et al., 2020). The RCP8.5 has long been the "business as usual" climate trajectory (Vuuren et al., 2011; Riahi et al., 2011); however, recent estimates have challenged this idea. RCP8.5 would lead to a global temperature increase of 5° C by 2100. A five-fold increase in coal use would be needed; modern estimates suggest that an increase of 4° C by 2100 is more accurate, closer to the RCP6.0 (Hausfather and Peters, 2020). As we will discuss, the AP ice shelves have been retreating for at least the last 60 years; their future viability depends significantly on limiting further climate change. Schannwell et al. (2016) modelled sea-level contribution of the AP glaciers under high (RCP8.5) and low (RCP4.5) emissions scenarios by 2100 and 2300. They predict that under high emissions, sea-level contributions from the AP would be 28 ± 16 mm to 32 ± 16 mm by 2300 with an even split from tidewater glaciers and ice shelf tributaries. Under low emission, the contributions from ice shelves fall to 2.4 ± 1 mm in the same period. Out of the 10 AP ice shelves, 5 are projected to collapse under the low emissions and 10 under the higher emissions.

2.8 Modelling of Calving

The development of numerical ice-sheet models has led to considerable advancements in understanding ice-sheet flow and future SLR projections; however, the coupling of ice shelf calving modelling is still limited. In this section, ice flow models are discussed and how they deal with the ice shelf calving. Glacier flow is described by the full momentum balance equations (full-Stokes). On a large scale, such as an ice sheet, full stoke models are too computationally expensive. Approximations to the full Stokes equations maintain key physical processes while being far easier to calculate (Van Der Veen and Payne, 2009). The approximation for ice shelf modelling is the shallow shelf approximation (SSA) which, makes the assumptions neglects vertical resistive and the vertical shear stress (Blatter et al., 2011; Pattyn, 2003). Since there is no basal resistance, this approximation can be applied.

Calving parameterisations are often calibrated for a specific glacier/ice shelf or geometric configuration (Pralong and Funk, 2005; Krug et al., 2014). An accurate ice shelf calving model would need to incorporate all contributing forcings, material properties, and glaciological stresses. Since this is not feasible, calving models use simplified physics, focusing on the most critical contributors to calving, such as stress criteria or criteria based on crevasse depth (Alley et al., 2008). The Parallel Ice Sheet Model (PISM) has incorporated two calving laws; for marine-terminating glaciers, a critical thickness threshold is implemented. A calving law that assumes the first-order kinematic contribution of calving depends kinematically on first-order horizontal strain rates is used for floating ice (Levermann et al., 2012; Martin et al., 2011). The horizontal spreading rate criteria produce realistic fronts in some ice shelves, particularly the Ronne-Filchner and Ross ice shelf (Martin et al., 2011). The Community Ice Sheet Model (CISM) uses a flotation criteria to initiate calving when ice is no longer grounded (Lipscomb et al., 2019). While this approach successfully models the terminating marine glaciers of Greenland, it cannot be applied to ice shelves (Nick et al.,

2010).

While these methods have been successful in some study areas, a general calving model needs to incorporate fractures. One approach to this is the introduction of continuum damage mechanics. Under creep at low deformation rates, a material will fail due to the accumulation of microcracks (Kachanov, 1999). Damage is a common idea in the study of viscous materials; for ice shelves, damage is a scalar that describes the changes in ice rheological properties due to fractures. An important note is that damage does not directly calculate fracture; it calculates the areas that have had an increase in strain rate due to degradation (fracture) (Borstad et al., 2013). Damage has been successfully calculated for multiple glaciers and ice shelves (Borstad et al., 2012; Borstad et al., 2013; Pralong and Funk, 2005). However, it is limited in its ability to calculate all fracture zones.

Emetc et al. (2018) introduces statistical methods to estimate fracture probability on Antarctic ice shelf regions. Statistical methods allow for any potential contributors to fracture to be incorporated into the model. A difficulty with modelling multiple ice shelves is that each ice shelf has unique flow regimes and geometries. Thus, it cannot be assumed that all points are independent. Emetc et al. (2018) use logistic regression to models each ice shelf individually and groups them together by the common characteristic using a classification criteria based on resemblance to the best fitting model. While this is effective and intuitive, it would not be scalable to be integrated into large ice-sheet models. We discuss this work in more detail in chapter 4. This thesis aims to build on Emetc et al. (2018) by creating a statistical framework that can incorporate multiple ice shelves in the same model while accounting for the correlation of each ice shelf.

Chapter Three

Study Site

3.1 Antarctica Peninsula

The Antarctic Peninsula (AP) is the northernmost region of the AIS. Its latitude and mountainous topography contribute to it being the most sensitive region of the AIS to climate change (King, 1994). Warming has resulted in many changes to the dynamics of glaciers in the region, including flow acceleration, the retreat of ocean terminating glaciers, an increase in melt season length and intensity, and retreat or collapse of floating ice shelves (Rignot et al., 2004; Scambos et al., 2004; De Angelis and Skvarca, 2003; Wendt et al., 2010; Cook et al., 2005). Retreat and extension are natural ice shelf processes; however, the past century has seen an ice shelf loss far out of natural fluctuations (Cook and Vaughan, 2010). Much research has focused on understanding the environmental and glaciological drivers contributing to AP ice shelf retreat and predicting future ice shelf stability using structural analyses of retreats and physical models (Massom et al., 2018; Vaughan et al., 1993; Macayeal and Sergienko, 2013; Depoorter et al., 2013). This study combines observations and physical flow models with statistical methods to predict future fracture probability.

In this study, the focus is on the larger AP ice shelves. In chapters 5 and 6, we focus

on the Larsen C, Wilkins and George VI Ice Shelves. Chapter 4 includes the Larsen B Ice Shelf. This choice of ice shelves was partly practical. These are well-researched ice shelves with sufficient available data. Also, their size is conducive to a high volume of remote sensing data. Additionally, these ice shelves buttress the flow of most of the major outlet glaciers of the AP, their stability will impact future SLR from the region.

3.2 Larsen B Ice Shelf

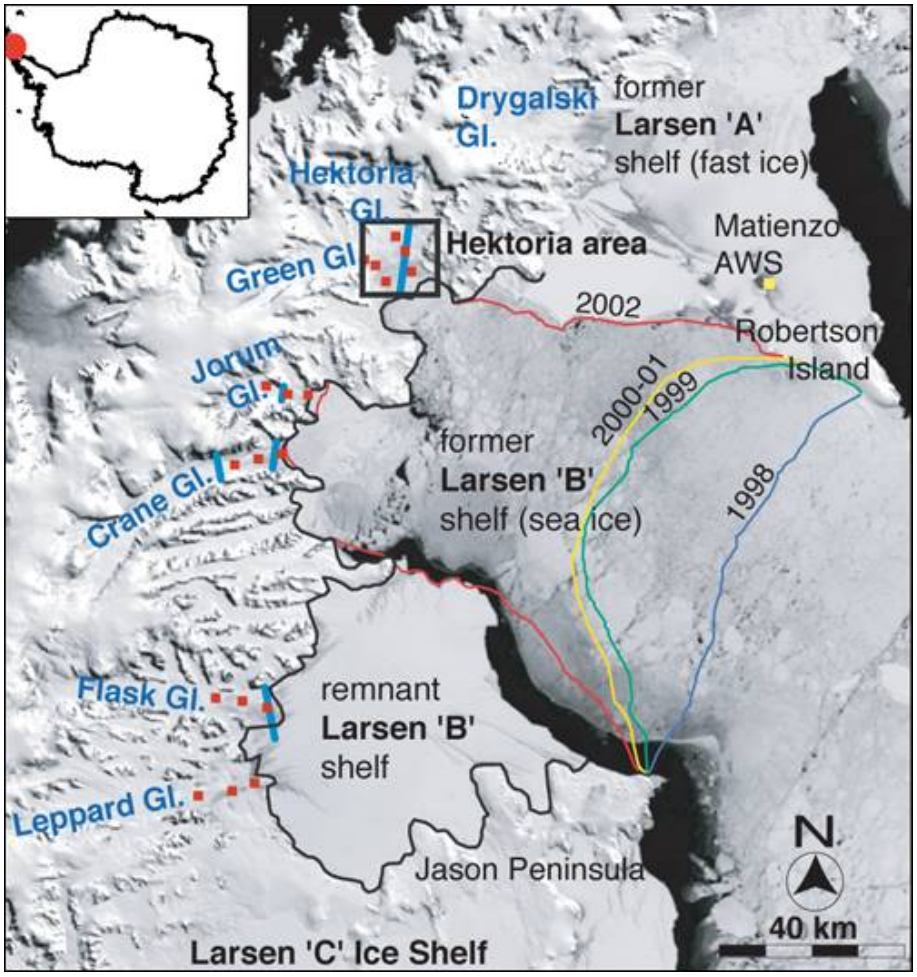


Figure 3.1: This satellite image from NASA's MODIS sensor aboard the Terra spacecraft shows the Larsen B Ice Shelf region on November 1, 2003. Important features are annotated, including the 1998, 1999, 2000/1, and 2002 ice front position. Credit: NSIDC, derived from Scambos et al. (2004)

The LBIS is one of four ice shelves that make up the Larsen Ice Shelf. The Larsen A ice shelf collapsed in 1995, and only the scar inlet of the LBIS and the Larsen C and D remain. The LBIS is located between Seal Nunatuks and Jason Peninsula in the northeast AP (Figure 3.1). It is one of the most studied ice shelves due to its near complete collapse in 2002.

Glasser and Scambos (2008) identified 14 ice domains within the ice shelf system. Four ice domains have been identified as primary sources of inflow: Hektoria/Green/Evans glacier system, Punchbowl Glacier, Jorum Glacier and Crane Glacier (Figure 3.1).

It had an area of 12,000 km^2 in 1963 and advanced until the 1990s. Its retreat began in 1995 and continued until 2002, when it collapsed, losing 3,250 km^2 in less than a week (Rack and Rott, 2004). It had entirely collapsed between Cape Disappointment and Cape Fairweather by 2005. A section remains in the Scar Inlet between Jason Peninsula and Cape Disappointment, often called the Scar Inlet Ice Shelf (Figure 3.1). This section continued to retreat, and two large calving events occurred in 2006 and 2008, where an area of 650 km^2 and 140 km^2 was lost (Qiao et al., 2019). In 2009 the remaining area was 2,407 km^2, since the ice front had steadily advanced by a total of 7 km by 2018 (Cook and Vaughan, 2010; Qiao et al., 2019). Growing instability is a major concern for the Scar Inlet Ice Shelf as significant dynamic changes and thinning have taken place at the Flask and Leppard glaciers, two of the primary tributaries (Khazendar et al., 2015).

Major changes occurred prior to the disintegration in 2002. Surface velocity measurements show that velocity increased from 1.12 $md^{\check{}}1$ in 1997–99 to 1.42 $md^{\check{}}1$ in 1999–2001 (Rignot et al., 2004; Vieli et al., 2006; De Angelis and Skvarca, 2003). Previous velocity increases of 10-20 % were measured after the 1995 retreat, attributed to the rift formation after frontal retreat past the compressive arch (Doake et al., 1998). Speed up of the tributary glaciers was thought to be the primary cause of the dynamic change; however, Vieli et al. (2007) showed that speed up of the tributaries was not enough to increase ice shelf flow to observed speeds. The LBIS featured areas of narrow weak zones around the margins and shear zones, these already soft areas are sensitive to changes in ice rheology (Vieli et al., 2007). The weakening at these key shear margins and the frontal retreat led to the dynamic changes observed prior to collapse (Borstad et al., 2012; Vieli et al., 2007). Between 1997 and 2001, the longitudinal strain rate increased by 50 % in the same location. Additionally,

the average thinning rate over this period was 0.3 ma^{-1}, with a sharp increase prior to the collapse. Glasser and Scambos (2008) mapped the structural features of the ice shelf surface, noting the formation of new rifts that were not present in the 20 years prior to collapse, with more forming after the removal of the strongest section of the ice front in the 1995 retreat event.

3.3 Larsen C Ice Shelf

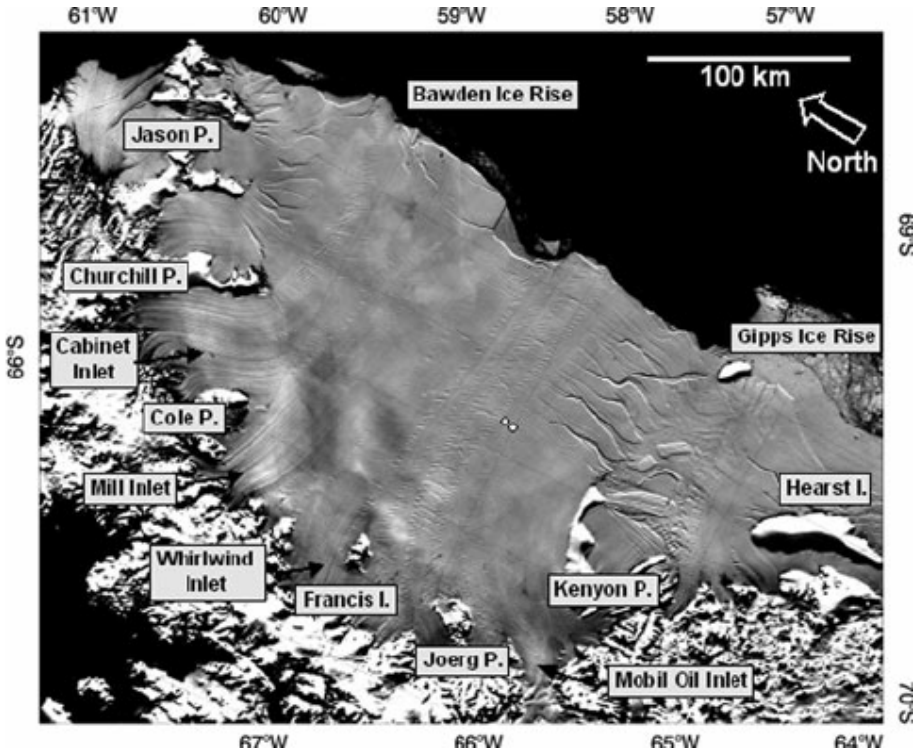


Figure 3.2: Map of the Larsen C Ice Shelf taken from Jansen et al. (2010). The locations of major features are annotated. Data: MODIS Mosaic of Antarctica (MOA) image of the Larsen C ice shelf (http://nsidc.org/data/nsidc-0280.html).

Larsen C is the largest ice shelf on the Antarctic Peninsula, extending south of Jason Peninsula down to Kenyon Peninsula and Gipps Ice Rise (Figure 3.2). There are over 10 inlets

that feed the LCIS, some with up to 10 glaciers. The primary flow units originate from: the Cabinet Inlet, Mill Inlet and Whirlwind Inlet, and the Mobil Oil Inlet (Riedl et al., 2005). The catchment area for the LCIS is 27,000 km^2, a ratio of 0.5. Much of the catchment is located on high plateaus that drain through steep and narrow glaciers, where the ice shelf is thickest. Ice shelf thickness can be up to 500 m at the grounding line, it thins toward the centre of the ice front to 250 m thick. The southeast region between the Gipps Ice Rise and Kenyon Peninsula has ice less than 100 m thick. Velocity over the grounding line is between 100 - 200 $ma^{-}1$, and as the ice spreads, it reaches a velocity of 700 $ma^{-}1$ at the centre of the ice front ((Jansen et al., 2010)).

Its area was 51,000 km^2 in 2010. Currently, it appears stable but has had a few significant retreat events. In 1976 a section broke off after being hit by an iceberg from the Ronne-Filchner Ice Shelf; in 1986, two large icebergs calved (6,520 km^2 and 1,260 km^2) (Cook and Vaughan, 2010). In 2017, a large iceberg with an area of 5,800 km^2 (A68) calved from the ice front, which was approximately 10 % of the total area of the ice shelf (Hogg and Gudmundsson, 2017).

Adusumilli et al. (2018) showed that the LCIS had a mean basal melt rate was 0.5 $\pm$ 1.4 ma^1 between 1994 - 2016, this low basal melt rate coincides with Nicholls et al. (2004), where the water in the LCIS cavity was determined to be cold and have high salinity. Basal melt was most pronounced at the Bawden Ice Rise and the southern grounding line. The Bawden Ice Rise is a major pinning point for the LCIS as it slows flow upstream, creating compressive stress (Favier and Pattyn, 2015). The compressive arch of the LCIS is pinned between the Bawden Ice Rise and the Jason Peninsula. The weakening of the ice shelf in contact with either of these points will destabilise the ice front. Following a surface lowering of 1 $\pm$ 0.3 m between 1994 - 2009, there was a rise of 0.5 $\pm$ 0.3 m between 2009 - 2017, suggesting an increase in firn air content (Adusumilli et al., 2018).

The LCIS is considered to be stable, in large part due to its ice heterogeneity that acts as a protective mechanism against the propagation of rifts (Jansen et al., 2010). Due to its large number of inlets, the LCIS consists of multiple flow units visible through the longitudinal surface structures (Glasser et al., 2009). Binding these flow units are soft ice regions called suture zones that form downstream of peninsulas. Suture zones consist of heavily fractured ice with a variable amount of accreted marine ice. Rift-tip analysis has shown that a significant number of the rifts on the LCIS terminate at the boundary of suture zones. McGrath et al. (2014) found that 60 m of marine ice (only 40 % of total ice thickness) in the Churchill Peninsula Suture Zone was sufficient to halt the propagation of 25 km rift.

3.4 George VI Ice Shelf

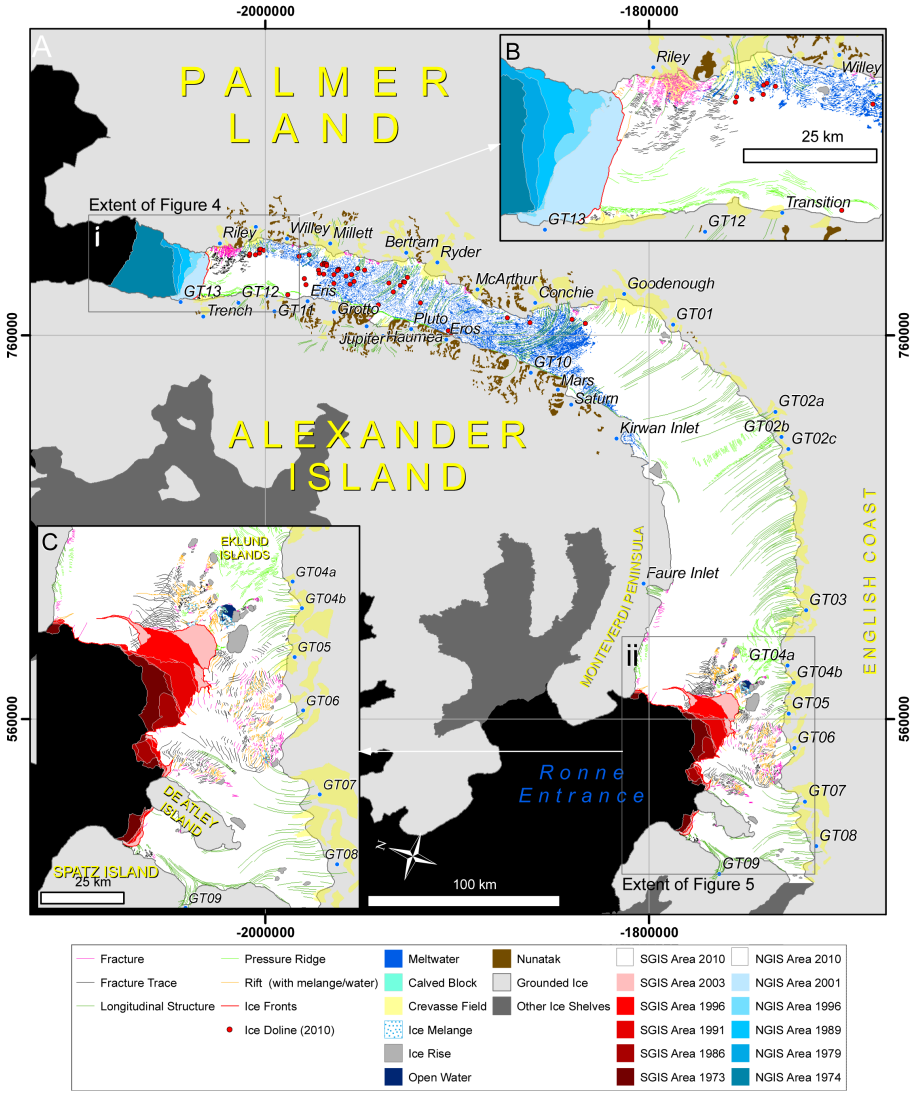


Figure 3.3: Structural Map of the George VI Ice Shelf (2010) taken from (Holt et al., 2013a). The dominance of longitudinal structures from Palmer Land can be seen. Another notable feature is the retreat of the northern ice front between 1974 - 2010. The insert shows the southern ice front, showing that the retreat between 1973 - 2010 mostly occurred in the centre.

The George VI Ice Shelf is the largest ice shelf on the western AP (24,000 km^2 in 2009), and the second largest on the whole AP behind the Larsen C Ice Shelf. It is located in George VI Sound with boundaries along Palmer Land and Alexander Island (Figure 3.3). It has a unique configuration as it has two ice fronts located approximately 450 km^2 apart along the centreline. The northern front is approximately 20 km wide and terminates in Marguerite Bay. The Southern front is approximately 75 km wide and terminates in Ronne Entrance, where a series of ice rises split it. The ice shelf thickness varies considerably; at the northern front is as little as 100 m. The ice shelf thickness is greatest in the central shelf, reaching 600 m before thinning again toward the southern front (Lucchitta and Rosanova, 1998; Smith et al., 2007; Talbot, 1988).

The ice shelf catchment covers much of both Palmer Land and Alexander Island; however, the glaciers from Alexander Island are much smaller (9 – 16 km long and 6 – 9 km wide) (Lucchitta and Rosanova, 1998; Humbert, 2007). Flow from Alexander Island does not extend far into the ice shelf. Around 95 % of flow onto the ice shelf is from Palmer Land, led by the Goodenough Glacier, the main contributor to inflow. Surface accumulation makes up a further 20 % of the total mass budget (Potter et al., 1984). The flow of the larger glaciers from Palmer Land extends laterally across the ice shelf until a few kilometres from the Alexander Island grounding line, where the direction of flow changes. This leads to stagnant points where flow direction changes (Humbert, 2007).

Observations show that the northern front advanced from 1947 - 1960 (Smith et al., 2007; Cook and Vaughan, 2010). (Holt et al., 2013a) showed that the northern front lost 1255 km^2 between 1974 and 2010. The most significant retreat occurred between 1974 and 1979 when it lost 820 km^2; this corresponds to a 40.6 km retreat of the centre of the northern front. Much rifting took place between 1979 and 2010 at the northern front, with the largest propagated along the Alexander island margin and facilitated calving in January of 2010. As for velocity, the northern front experienced velocity increases that propagated upstream

of its main tributary, the Riley glacier. In 2009 velocity at the centre of the front was 390 ± 15 ma^1 , a significant increase from 214 ± 38 ma^1 in 1989.

From the same study, the southern front lost 743 km^2 between 1973 and 2010. The retreat was limited mainly to the centre, with little calving around the pinning points; this led to the creation of 3 distinct fronts on the southern section. The De Atley and Spatz Islands partition it. Velocity was varied in the south, with the front between Ekland and De Atley island accelerating by 340 ± 38 ma^1, reaching a max of 796 ma^1. The other front did not experience any significant change in velocity during this period. The grounding line was observed to retreat all over the ice shelf.

The GVIIS experiences high basal melt rates. Various studies have estimated the basal melt rate ranging from an ice shelf average of 2.1 ma^1 up to 6 ma^1 (Jenkins and Jacobs, 2008; Dinniman et al., 2012; Potter et al., 1984). Oceanographic forcing strongly impacts the GVIIS; it is only 1.5 % of the total Antarctic ice shelf area but could contribute up to 10 % to the total mass if in equilibrium (Jacobs, 1992). The high basal melt rate is attributed to the intrusion of warm CDW from the southeast pacific basin that flows across the continental shelf (Dinniman et al., 2012). Warm water is present under the entire ice shelf, with the warmest recorded temperature being 1.1 ^oC (Talbot, 1988).

Surface melt is prevalent on GVIIS, particularly in the north. Holt et al. (2013a) mapped the presence of an abundance of melt ponds throughout the summer. Winter snowfall rarely makes it past the summer melt season. Evidence suggests that much of the surface melt refreezes during the winter months, limiting the mass loss due to melt. Frontal calving and basal melt are the primary ablation sources for the GVIIS.

3.5 Wilkins Ice Shelf

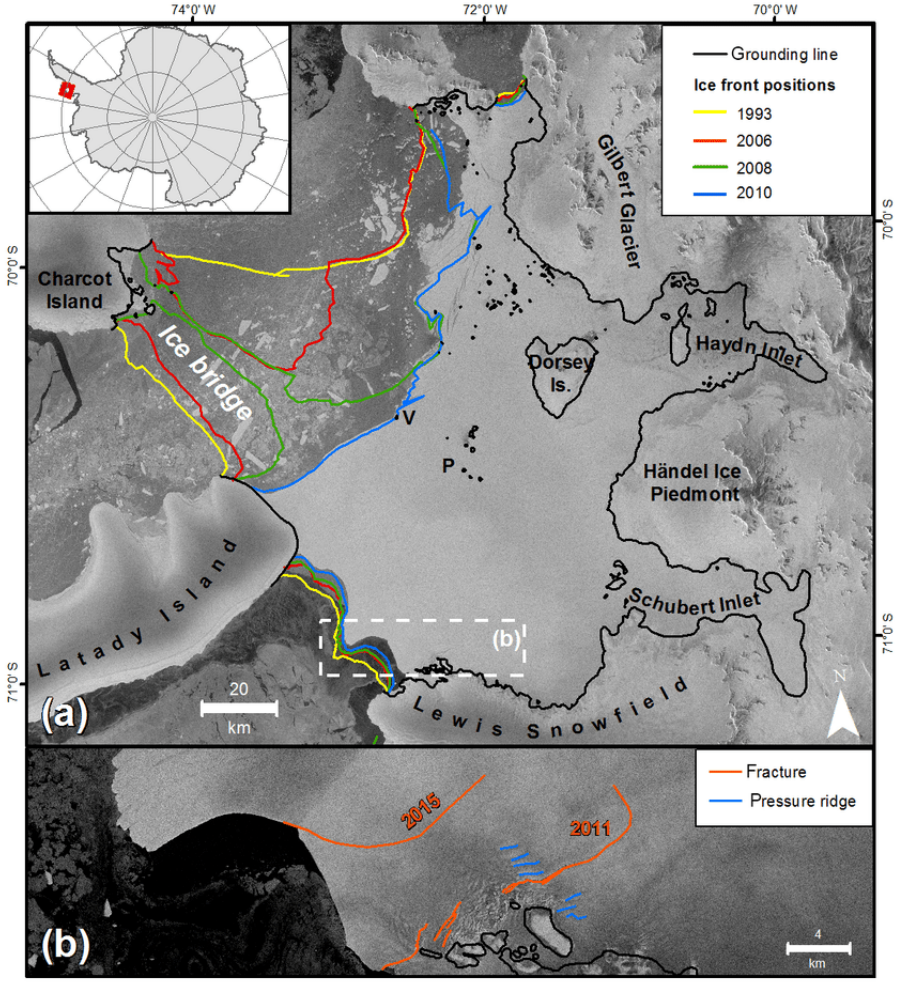


Figure 3.4: Map of the Wilkins Ice Shelf taken from Rankl et al. (2017). The ice front positions of the years 1993, 2006, 2008 and 2010 are shown, the background image from 2015. The ice bridge between Charcot and Latady Island was visible in 2008 prior to its collapse. (b) Fracture formation at the southwestern ice front in 2011 and 2015 from Envisat ASAR, Sentinel1A and TanDEM-X imagery. P is the Petrie Ice Rises and V is the Vere Ice Rise. Images are taken from: (a) Sentinel-1A 21 May 2015 and (b) Sentinel-1A 6 April 2015.

The Wilkins ice shelf is one of two ice shelves in this study located on the west Antarctic Peninsula (Figure 3.4). The Wilkins Ice Shelf occupies the Wilkins Sound in southwestern

AP, embayed between Alexander, Rothchild, Latady, and until 2008, Charcot Island. The WIS has four primary areas of inflow, the Hayden inlet, Chubert Inlet, Gilber Glacier and the Lewis Snowfield. Inflow to the centre of the ice shelf is mainly from the Lewis Snowfield, Gilbert Glacier and the Hayden ice Pediment. Ice rises adjacent to the Schubert and Hayden Inlets restrict inflow to the ice shelf, diverting it from the centre (Braun and Humbert, 2009).

Vaughan et al. (1993) found that the mass balance of the WIS is dominated by surface accumulation and basal melt, with inflow playing a minor role in overall mass balance. Velocity measurements have determined that the WIS is relatively slow compared to other AP ice shelves. The floating portion of the ice shelf has a velocity range of 50 - 100 $ma^{-}1$. Ice shelves whose accumulation is predominantly insitu are more susceptible to surface and ocean temperature changes. Braun and Humbert (2009) found that the WIS is also thin, with much of the centre being less than 200 m thick. Thickness was greatest at the Lewis Snowfield and the Hayden Inlet, where inflow is greatest. Measurements from the north showed that the shelf was less than 50 m thick, compounding its vulnerability to basal melt.

Advection of warm Circumpolar Deep Water across the continental shelf has been linked to the increasing temperature of the Bellingshausen Sea, leading to an increase in basal melt under the west AP ice shelves (Dinniman et al., 2012). Since the WIS is thin, CDW upwelling is less influential than other ice shelves, and short-term changes in coast ocean temperature play a significant role (Padman et al., 2012).

Since the 1990s, the WIS has experienced significant mass loss in a series of catastrophic retreat events. Prior to 2008, the WIS had three distinct ice fronts. The first was between Rothchilds and Charcot Islands. The second was between Charcot and Latady Island, and the third was between Latady Island and the Lewis Snowfield. Limited satellite data is available before 1990; the first recorded area for the WIS is from 1947, when it had an area of 16,577 km^2. By the next recorded area in 1990, it had lost 591 km^2. Between

1990 - 1993 two major retreats place 544 and 655 km^2 from the north and northwest fronts (Lucchitta and Rosanova, 1998; Braun and Humbert, 2009). In March 1998, a rapid retreat event occurred, which led to an area loss of 1100 km^2. This retreat formed a prominent ice "bridge" that connected the shelf to Charcot Island (Braun and Humbert, 2009). Margins of the ice bridge calved steadily over the next decade until it collapsed in April of 2009.

In 2008, the WIS experienced significant mass loss in three large collapse events. The first two occurred in February and May of that year, where an area of 425 km^2 and 160 km^2 was lost. Finally, in July, 1,220 km^2 was lost in a two-phase retreat event. Firstly, ice melange in the western margin of the northern front moved east, fracturing and displacing the northmost region of the northern front, which led to a loss of 540 $\pm$ 75 km^2. This region was particularly damaged by the breakup event that occurred in 1998. The second phase was caused by the formation and capsizing of an iceberg inward of the ice front, leading to a loss of 680 km^2 (Humbert and Braun, 2008). The capsize mechanic is discussed in Chapter 2. Until these events, the northwestern front had not significantly contributed to the overall mass loss.

After the 2008 retreats, the collapse of the ice bridge was imminently expected as the widest point was on 900 m. However, the collapse did not occur for another 9 months, in April 2009. The collapse began with a series of fractures forming parallel to the long axis of the bridge. Previous damage on the bridge surface preconditioned the formation of new fractures. Westerly winds acting on the ice bridge frontal surface and the rough textured ice melange exerted pressure at the centre of the bridge, causing the bridge to bend at the narrowest part. This collapse detached the WIS from Charcot Island, connecting the northwestern and northern fronts. During the ice bridge collapse, the total area lost was 330 km^2 (Humbert et al., 2010).

Braun and Humbert (2009) conducted a structural analysis of the WIS, showing that

the remaining ice was damaged after each breakup event. Fractures and rifts had formed at both the northern front and on the ice bridge, aided in retreat. The WIS is unique as it experienced major breakup events outside of the Austral summer. However, surface melt and hydro-fracture could have played a preconditioning role in these events Scambos et al. (2009). Before its collapse, dynamic changes occurred at the ice bridge, where velocity increased by over 0.3 m per day (Rankl et al., 2017).

Chapter Four

Updated assessment of ice shelf extent on the Antarctic Peninsula and links to potential glaciological and environmental drivers

4.1 Aims and Objectives

This chapter is the first experimental chapter of this thesis. The primary aim of this chapter is to understand the triggers of significant AP ice shelf calving events. The first step to achieve this is to index annual ice shelf front position and area for the Larsen B, Larsen C, Wilkins and George VI Ice Shelves from 1990 - 2020. Furthermore, using these observations and previously available data to infer a linear relationship between these new observations and these data sets. The triggers that are investigated are: 2m air temperature, sea ice concentration, surface mass balance, and surface height change. To achieve these aims, the following objectives are set out:

- Use satellite imagery and GIS software to map annual ice front position and calculate ice shelf area.
- Use a quantile regression analysis to infer a statistical relationship between ice shelf area observations and the hypothesised calving triggers. If a relationship exists, quantify the impact that the corresponding trigger has on calving.

By completing these objectives, the first research gap outlined in chapter 1 will be addressed. The first objective is relevant to ice front position change for both collapsed and present ice shelves. The second objective offers addition knowledge to the triggers for ice shelf calving and introduces a unique method that has further glaciological utility. This chapter presents new annual ice shelf extent for the Larsen B (LBIS), Larsen C (LCIS), George VI (GVIIS), and Wilkins Ice Shelves (WIS) between 1990-2019. GVIIS is split in two because of its geometry; some analysis includes George VI North (GN) and George VI South (GS). We aim to draw inferences between climate and glaciological stresses, and interannual ice shelf variability with quantile regression. We discuss the details of the predictors in section 2.2. Trends of 3 quantiles (20%, 50%, and 80%) are estimated and compared to the slope of the mean.

4.2 Data and Methods

4.3 Previous ice front studies

Cook and Vaughan (2010) was the first study to map all AP ice shelves on a regular time series (1950-2010) before this Cook et al. (2005) delineated the extent of the tidewater glaciers of the AP. Previous studies focused on mapping individual ice shelves. The ice shelves on

the Weddell coast are mapped as follows: Cooper (1997) mapped the Prince Gustav ice shelf between 1945-1995. The LAIS and LBIS are mapped from 1986 to 1995 and 2002 respectively (Rott et al., 1996; Rott et al., 2002). The LCIS is mapped between 1976-1986 (Skvarca, 1994; Vaughen and Doake, 1996). The ice shelves on the Bellingshausen coast are mapped as follows: Muller between 1947-1993 (Ward, 1995), Jones between 1947-2003 (Fox and Vaughan, 2005), Wordie between 1966-1989 (Doake and Vaughan, 1991), George VI between 1974-1995 (Lucchitta and Rosanova, 1998), and Wilkins between 1990-1995 (Lucchitta and Rosanova, 1998; Scambos et al., 2000; Braun and Humbert, 2009). Until now, no study has mapped multiple ice shelves annually. The motivation for an annual time series is to observe annual ice shelf extent variability and produce an ice shelf extent data set that we can incorporate into a statistical model.

4.3.1 Initial data and image selection for ice shelf extent mapping

A combination of data collating and mapping from satellite images was applied to produce an annual ice shelf extent time series for the large AP ice shelves. Table 4.1 is an overview of the ice shelf extent/front data that was initially available. Cook and Vaughan (2010) is the most comprehensive study; it presents the decadal front position for each AP ice shelf from over the last 50 years. Braun and Humbert (2009) present near-annual time-series from 1991-2009 of the WIS with only a few missing entries.

Data from the National Snow and Ice Data Center (NSIDC) were used to complete the annual time series. Images are available from two sensors. Firstly, the Advanced Very High-Resolution Radiometer (AVHRR) sensor has images from October 1992 – 2009 and a resolution of 1 km. Secondly, the Moderate Resolution Imaging Spectroradiometer (MODIS) sensor has images available from January 2002 – present with a resolution of 500 m. The AVHRR images are provided without georeferencing, while the MODIS images are georef-

Table 4.1: Previous ice shelf extent studies, ice shelves included in the study, and measurement frequency

Data Source	**Ice shelf**	**Frequency (years)**
Cook and Vaughan (2010)	PGIS LAIS LBIS LCIS LDIS WIS GVIIS Bach SIS Wordie Muller Jones	~ 10
Holt (2013)	George VI,Bach,SIS	~ 5
Braun and Humbert (2009)	Wilkins	1

erenced. AVHRR images were georeferenced using tie points referenced against appropriate MODIS images with an accuracy of the resolution of AVHRR image, which is 1 km. A limiting factor in this study is that images are only available for the Larsen B, Larsen C, George VI and Wilkins Ice Shelves. For the most accurate view of the ice shelf front, images were selected from the austral summer, with minimal cloud cover, when sea ice was not present. In some cases, we used multiple images.

Ice shelf delineation involved using the GIS software ArcMap to update the extent using the corresponding images manually (Figure 4.1). As a starting point, we used the ice shelf extents from Cook and Vaughan (2010). Allowing us to ensure the grounding lines and boundaries are essentially the same with an exception at the boundary between Larsen A and Larsen B. To obtain uncertainties, we performed the same manual extent delineation 10 times. Each delineation was within 5% of the mean.

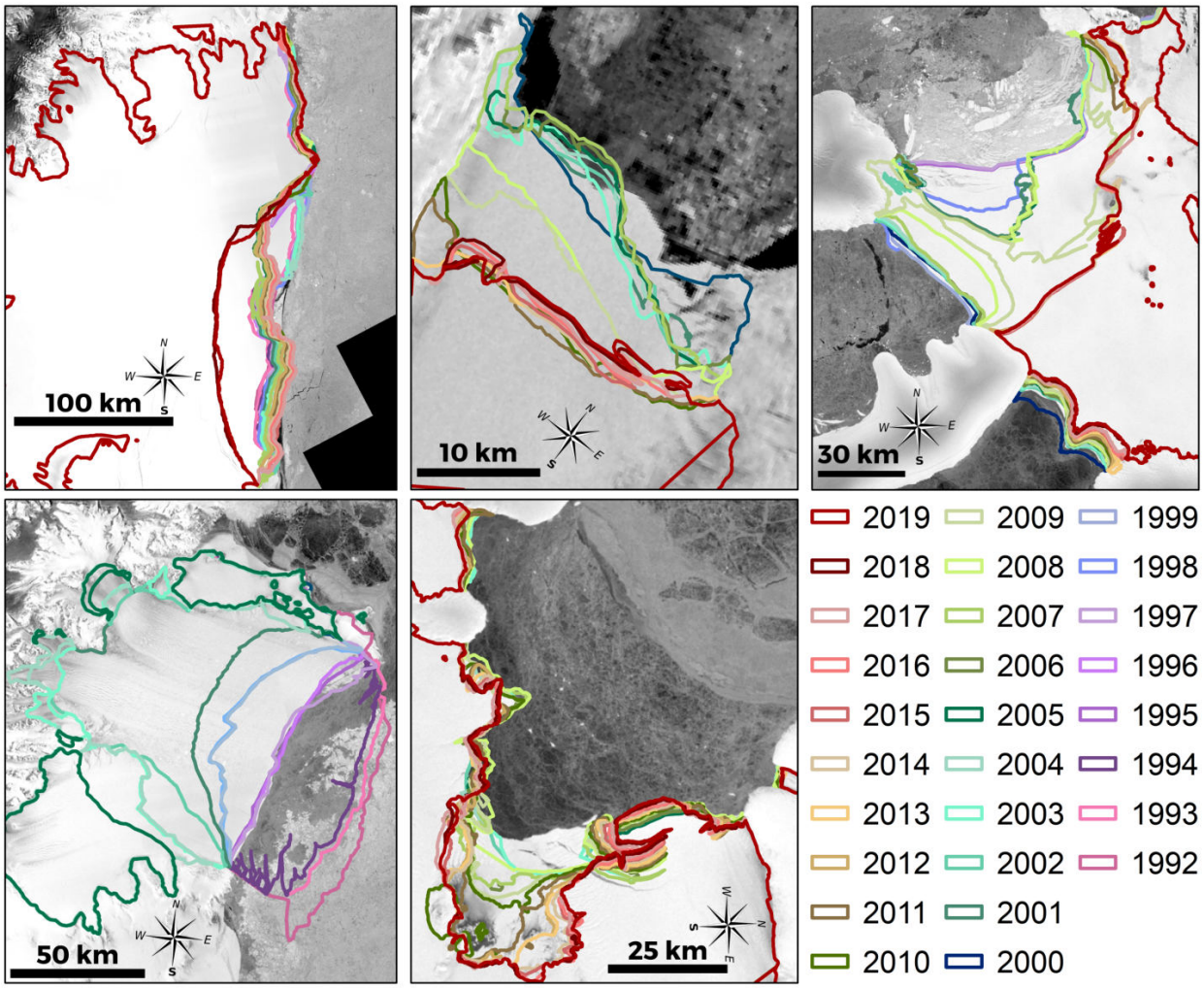


Figure 4.1: Ice shelf front extent: Larsen C (TL), George VI North (TC), Wilkins (TR), Larsen B (BL), George VI South (BC)

4.3.2 Environmental and glaciological predictor data

Ice shelf stability is affected by multiple physical mechanisms and environmental processes. A difficulty of this area of study is that there are multiple processes at play at once in most cases of retreat. The exact mechanisms at play for a calving event depend on ice shelf geometry and the climate conditions, both current and previous. The presence of fractures and crevasses near the front will drive calving, and once fractures have propagated throughout

the entire ice shelf, this can lead to a significant collapse event (Albrecht and Levermann, 2014). Hydrofracture is fracture propagation due to increased hydrostatic pressure from excess meltwater within the pre-existing fractures (Rack and Rott, 2004). During the collapse of the LAIS and LBIS, excess meltwater was present before the retreat (Scambos et al., 2000; Vieli et al., 2007). The firn layer is able to hold additional water, acting as a buffer layer. Once it has become entirely saturated, excess water forms supraglacial lakes (also called melt ponds). Before its 2002 collapse, the > 2750 supraglacial lakes on the surface of the LBIS drained, likely causing significant hydrofracture (Banwell et al., 2014; Leeson et al., 2020).

If peninsulas are present in flow confluence ice shelves can form flow bands known as suture zones. These regions contain elevated levels of marine ice (up to 60%) (Kulessa et al., 2014), leading to softening. The heterogeneity that suture zones provide is able to limit fracture propagation, acting as a protective mechanism (Kulessa et al., 2014). The curve where the principle strain rate transitions from compressive to tensile is known as the compressive arch; it traverses the entire ice shelf and represents a stable calving limit before a significant retreat is triggered. Downstream from the compressive arch is passive ice that does not affect buttressing (Fürst et al., 2016). The recent calving of the A-68A iceberg from the Larsen C Ice Shelf did not threaten its stability as it calved a passive ice section (Han et al., 2019).

A hypothesised mechanism suggested by MacAyeal et al. (2003) is that a group of ice shelf fragments that have detached from the rest of the ice shelf release gravitational potential energy via capsizing, as by the nature of their formation, they are gravitationally unstable. Another trigger for calving is flexure due to ocean swell. During the ice bridge collapse connecting the WIS to its confining islands, plate bending stresses exacerbated by a strong thickness gradient were the primary trigger (Braun and Humbert, 2009). This is a unique configuration to the WIS, but most ice shelves are susceptible to ocean swell when insufficient buffering sea ice is present (Massom et al., 2018).

Atmospheric and ocean warming are the main destabilising forcing across the AP, preconditioning the ice shelf for the calving mechanisms discussed to occur (Rott et al., 1996; Etourneau et al., 2019). Warming air temperatures have increased melt duration and intensity, with warming occurring during the austral winter on the LCIS (Barrand et al., 2013; Kuipers Munneke et al., 2018). Surface melt due to warming increases excess surface water, potentially leading to hydrofracture. If the excess melt does not refreeze, this decreases overall Surface Mass Balance (SMB). SMB is the difference between all mass gain and loss from the glacier/ice shelf surface. Defined by,

$$\int_{year} (PR - SU_s - SU_{ds} - ER_{ds} - RU)dt,$$

where PR is total precipitation, SU_s is surface snow, SU_{ds} is snow drifting, ER_{ds} is erosion/deposition from snow drifting, RU meltwater runoff (not refrozen) (Wessem et al., 2016). High surface melt rate combined with increased basal melt due to ocean warming has caused rapid thinning in all major AP ice shelves, excluding the LDIS (Adusumilli et al., 2018).

Motivated by the mechanisms of calving, this study investigates data from multiple drivers (Table 4.2). Two-meter air temperature (T2M) and Surface Mass Balance (SMB) are from the regional atmospheric climate model (RACMO2.3), which combines a high-resolution limited-area numerical weather model with the integrated forecast system physics from the European Centre for Medium-range weather. Both have mean monthly temporal coverage with reanalysis over the ERA-interim period (1979-2017) and 5.5 km spatial resolution. Their domain is limited to the Antarctic Peninsula (Wessem et al., 2016).

The height change data set is a 23-year time series (1994-2017) that combines outputs from four radar altimeters over AP ice shelves. It has a spatial resolution of 30 km and a 3-month temporal resolution (sampled, not averaged) (Adusumilli et al., 2018). Finally, monthly sea ice concentrations are computed using daily estimates of satellite-derived sea ice

concentrations at a resolution of 25 km x 25 km. Sea ice concentrations anomalies were then calculated relative to a long term mean for 1979-2010 (Massom et al., 2018). Basal melt is a critical contributor to ice shelf ablation, particularly those that drain into the Bellingshausen Sea (Rignot et al., 2013); however, due to a lack of suitable data, we are not able to include it in this study.

The digitised annual ice shelf extent data we produced was the boundary for extracting the relevant SMB, T2M, and height change data. The extent was dynamically changed for each year, such that all temporal intervals within that year used the same extent. Since we ensured to digitise the ice shelf during the austral summer, the extent would be close to the yearly minimum. However, the extraction of the winter months may be short of the ice shelf calving front, although the data resolution would likely not be sensitive enough for this to be a concern. We chose to find the mean value of the predictors across the entire ice shelf rather than selecting data exclusively from the grounding line, centre or the calving front.

Table 4.2: List of predictor data used in our analysis, the associated publication, temporal and spatial resolution of each predictor variable.

Predictor	**References**	**Temporal resolution**	**Spatial resolution**
2 m air Temp	Wessem et al. (2016)	Monthly	5.5km
Surface Mass Balance	Wessem et al. (2016)	Monthly	5.5km
Sea ice Concentration	Massom et al. (2018)	Seasonal	
Height Change	Adusumilli et al. (2018)	Quarterly	0.25 (Lat) x 0.75 (lon)

We incorporated various temporal statistical descriptors to thoroughly investigate the relationship between ice shelf retreat and the predictors. Table 4.3 shows the temporal statistical descriptors considered for each predictor; there are variations due to different temporal resolutions. Mean and median are both used to allow for the inclusion and exclusion

of outlier points. The first and third quantiles allow the measure of spread to be taken into consideration. The maximum and minimum values investigate the extreme outliers. For example, the maximum value of the T2M corresponds to the hottest average month for each, investigating whether a particularly warm melt season correlated with retreating, as was the case with during the LBIS collapse where surface melt was 3 times great then the proceeding 5 years (Broeke, 2005). The minimum T2M investigates the coldest average month for each year; warmer than usual minimum average monthly temperatures could suggest an extended melt season. To investigate if preconditioning has a significant relationship to retreat, we used a subset of the statistical descriptors with a one year delay. Seasonal means investigate if the correlation is more significant during specific seasons. Note, SIC data are only available for the LBIS and WIS.

4.3.3 Quantile regression

Statistical methods offer easy-to-implement techniques when studying time-series or relationships between dependant and independent variables. Standard linear regression estimates the slope of the mean of the conditional distribution; for this to be effective, the regression coefficients must be constant throughout the entire population. If the conditional distribution is not normal, the slope of the mean will not provide much helpful information (Cook and Manning, 2013). Using quantile regression, a method that calculates the slope of any quantile, we can investigate the relationship between ice shelf retreat and the predictors across the entire distribution (Cook and Manning, 2013). Quantile regression is used in multiple areas of study; however, we do not know of any other work that applied it to the ice shelf extent. Tareghian and Rasmussen (2013) applied it to investigate the Arctic and Antarctic sea ice trends successfully.

The least-squares regression assumes that regression coefficients are constant over the

entire population; however, this is often not the case. Quantile regression offers an alternative to least squares regression that better describes the relationship between dependant and independent variables when there are group differences across the distribution. Loosening the assumptions of least-squares regression QR allows for data that is not normally distributed and may have a non-linear relationship with the predictor variables. From figures, 4.3-4.5, annual retreat as a percentage of maximum area is not normally distributed for the ice shelves in this study since small calving and advance is common in a stable ice shelf with sporadic significant retreat events.

To understand quantile regression, it is best explained in the context of simple linear regression, a standard but limited statistical tool. Simple linear regression estimates the conditional mean of the distribution by solving the least-squares problem of minimising the sum of the squares of the residuals. The first limitation is that it cannot be extended to non-central locations, giving a one-dimensional view of the distribution. The following major limitation is that the model assumptions, homoscedasticity and normality, are rarely met in the real world. Homoscedasticity, meaning that the conditional variance $var(y|x)$ is a constant. Modifications can be made when this is not the case; however, these are often difficult and unavailable within software packages. The other critical important assumption is that the conditional distribution is normal. Simple linear regression can be used when normality is violated for descriptive purposes; however, if used for hypothesis testing where p-values give significance, violation of normality will lead to unreliable results. The final limitation is the handling of outliers. Outliers drastically skew the results, and it is common practice to find and eliminate them. Outliers are often the points that contain the essential information. For example, an outlier could signify a significant ice shelf collapse event during low temperatures, such as in the WIS retreat. Using quantile regression in place of simple linear regression solves these limitations (Hao and Naiman, 2007).

The simple linear regression model is expressed by:

$$y_i = \beta_0 + \beta_1 x_i + \epsilon_i \tag{4.1}$$

where ϵ_i is identically, independently and normally distributed with a mean of zero and variance σ^2 that is unknown. The assumption of a mean of zero leads to the function in equation 4.1 corresponding to the conditional mean of y given x ($E[y|x]$).

Koenker and Bassett (1978) developed quantile regression. It estimates the effect that the predictor variable has on various quantiles in the conditional distribution which, offers a method of estimating conditional quantiles. A quantile is a point that splits a given population. For example, the median or 50th quantile is where half the populations are above, and half is below. Quantile regression model for τth quantile the can be expressed analogously as equation 4.1 as follows:

$$y_i = \beta_0^{(\tau)} + \beta_1^{(\tau)} x_i + \epsilon_i^{(\tau)}, \tag{4.2}$$

where $0 < \tau < 1$ is the proportion of the population below that quantile τ. The unconditional median is calculated by minimising the sum of absolute residuals (difference between the observed value and sample mean). The function required has the property of being symmetric, so it must have an equal number of positive and negative residuals, which by definition is the median. This can be generalised to other quantiles by minimising a sum of asymmetrically weighted absolute residuals. Given by solving:

$$\min_{\xi \in \mathbb{R}} \sum \rho_\tau(y_i - \xi), \tag{4.3}$$

where $\rho_\tau()$ is the tilted absolute value function that yields the τ th sample quantile as its solution. The conditional quantile function follows from this by replacing the scalar ξ with the parametric function $\xi()$. To obtain estimates of the other conditional solve the following:

$$\min_{\xi \in \mathbb{R}} \sum \rho_\tau(y_i - \xi(x_i, \beta)), \tag{4.4}$$

The minimisation problem that arises when $\xi(x_i, \beta)$ is a linear function of parameters can be solved using linear programming (Koenker and Hallock, 2001). This study used the quantreg R package (Koenker, 2010). All p-values reported are calculated via its bootstrapping protocol.

4.4 Ice shelf extent

4.4.1 Results

The ice shelves in this study lost an average 21.5% ±0.2% of their total area between the first and last observation (Table 4.4). Ice shelf fronts have a natural process of retreat and advance; however, a loss of this magnitude strongly suggests a declining trend in ice shelf extent around the AP. Figure 4.1 shows the degree of the retreat that has taken place over the past couple of decades (GVIIS has two fronts which separated into North and South). Two of the ice shelves, LBIS and WIS, have significantly reduced in area, with LBIS almost entirely collapsing. GVIIS and LCIS have had noticeable calving but remain stable for now.

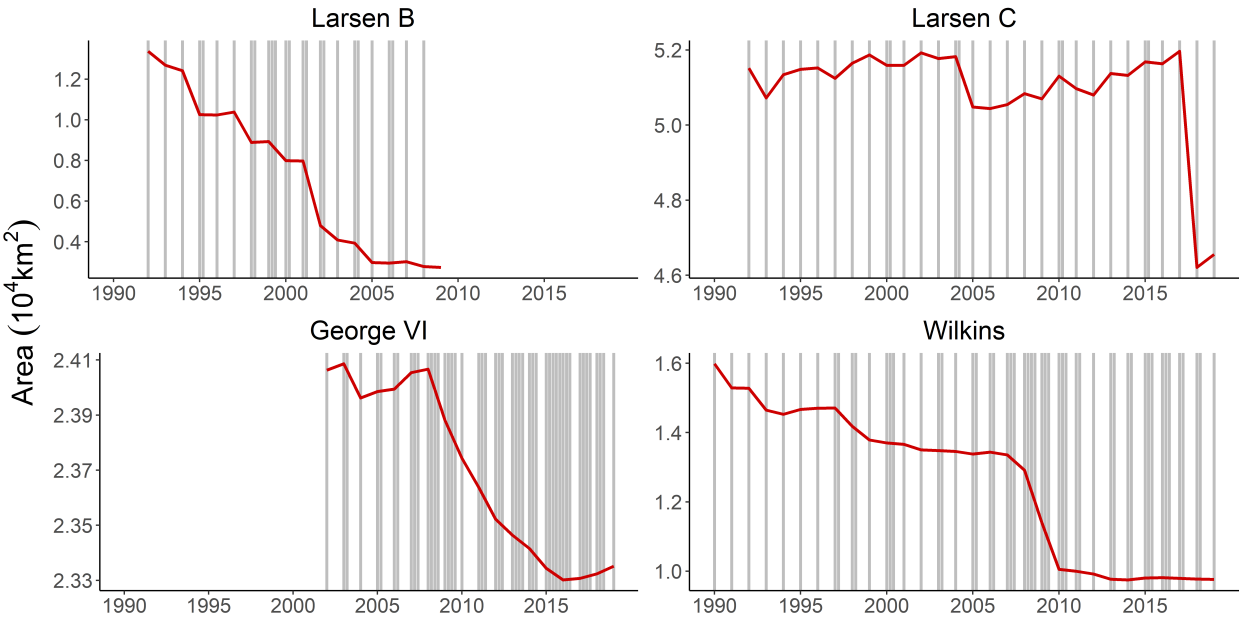


Figure 4.2: Annual ice shelf area time-series from 1990-2019. Each vertical grey line represents an image used for the extent delineation.

Larsen B Ice Shelf

The LBIS is located in the northeast AP on the Weddell coast between Robertson Island and the Jason Peninsula. This study includes an annual extent from 1992-2009 for the LBIS. Over this period, it almost entirely collapsed, consistently retreating with only a few years that had any advance (Figure 4.2). The two largest events took place in 1995 and 2002 with losses of $2,162$ km^2 and $3,184$ km^2 respectively (Figure 4.3).

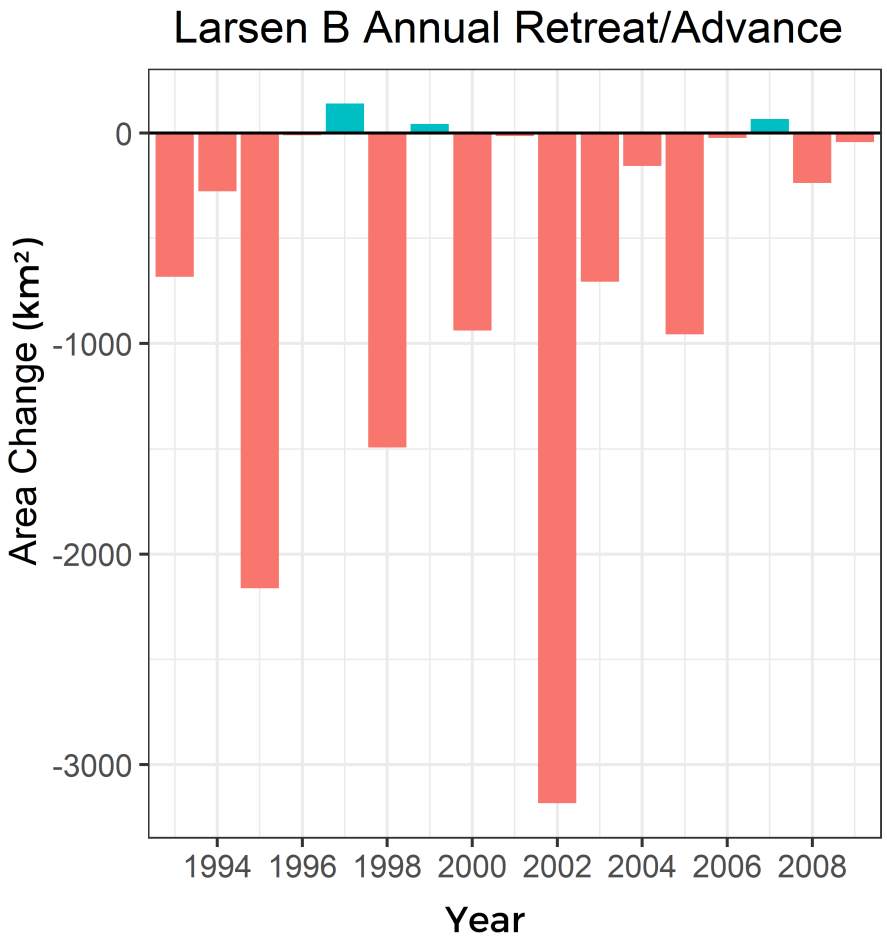


Figure 4.3: Annual area (km^2) gain/loss of the Larsen B Ice Shelf between 1993-2009. Each bar represents the retreat (red) or advance (blue) since the previous year.

Larsen C Ice Shelf

LCIS is the largest ice shelf on the AP located south of LBIS between the Jason Peninsula and the Gipps Ice-rise. This study produced an annual time series from 1992-2019. Over this period, it experienced episodic advance and retreat cycles until a significant calving event in 2017 (Figure 4.2), contributing to a total loss of 5347 km^2 since 1991. There were small retreats and advances between 1992 and 2004 with a net growth of 500 km^2. In 2005 it lost 1452 km^2 from a calving event, mainly due to the loss of a giant iceberg in the Northern

part of LCIS. In the event, it lost 2.6% of its total area. The pattern of retreat and advance continued between 2005 to 2017 with a net advance of 1601 km^2, where it reached a new maximum area of 56,145 km^2. Following the propagation of a large crevasse over several years, in 2017, an iceberg with an area of 6202 km^2 detached from the front (Figure 4.4). Around 11% of the total area at the time, the largest calving event since the 1980s.

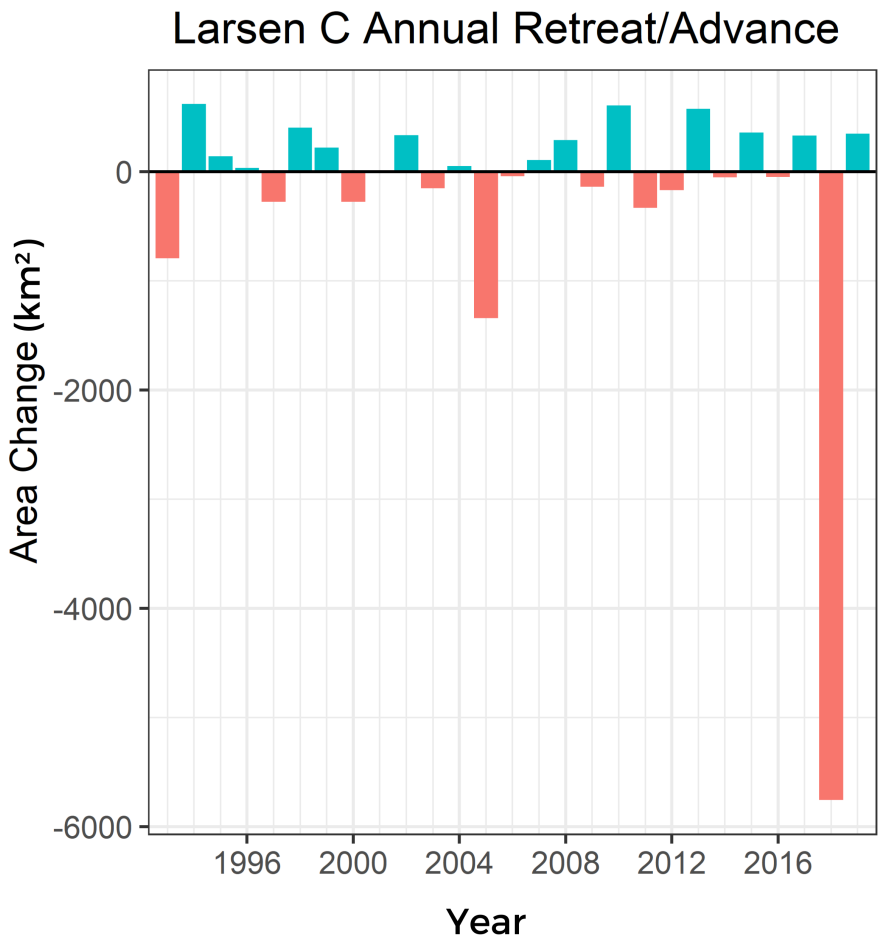


Figure 4.4: Annual area (km^2) gain/loss of the Larsen C Ice Shelf between 1993-2019. Each bar represents the retreat (red) or advance (blue) since the previous year.

George VI Ice Shelf

GVIIS is unique amongst the AP ice shelves as it sits within a narrow channel with two different fronts, 500 km apart. It is located in the George VI Sound that separates the west coast of Palmer land from the eastern coast of Alexander Island. The northern front is 25 km wide and located in Marguerites Bay. The southern front has a width of 75 km and is located in the Ronne Entrance. This unique geometry means that the driver of mass loss from GVIIS is melt rather than calving (Rignot et al., 2019). This study presents an annual time series from 2002-2019 for the southern front and whole ice shelf, and 2000-2019 for the northern front. Overall, GVIIS did not retreat significantly over this period, maintaining 97% of its 2002 area. Given its geometry, this is not surprising, although both fronts have retreated into George VI Sound. Figure 4.5 shows that the northern front had a period of retreat between 2008 to 2011 with no notable advance following. The southern front has substantial retreated in the middle, as can be seen in Figure 4.1, consistently retreating between 2009-2016, losing 664 km^2.

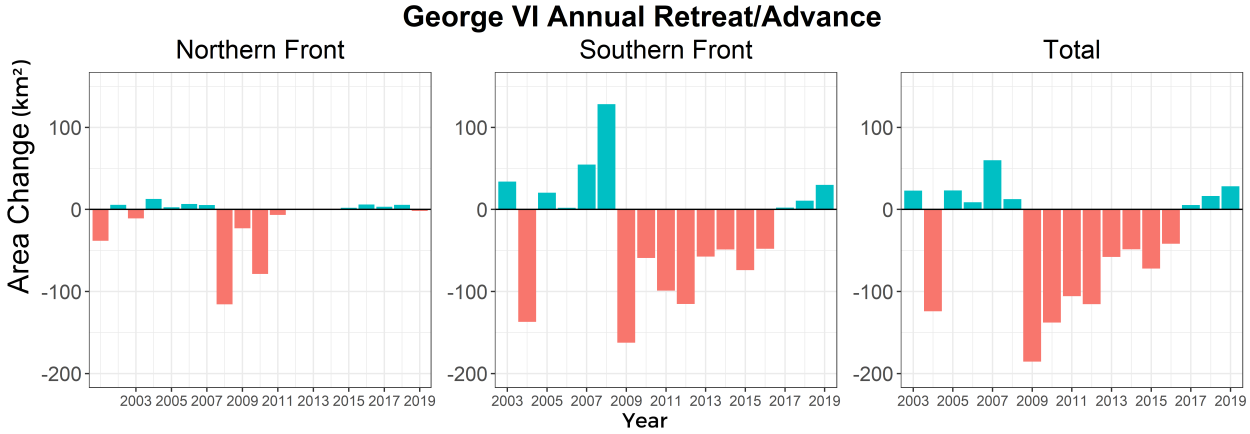


Figure 4.5: Annual area (km^2) gain/loss of the northern front (left), the southern front (middle) and the whole George VI Ice Shelf (right) between 2002-2019. Each bar represents the retreat (red) or advance (blue) since the previous year.

Wilkins Ice Shelf

This study includes annual extent from 1990 to 2019 for WIS. Before 2008, WIS had three different fronts as it previously connected three islands off the west coast of Alexander island: Latady island, Charcot Island, and Rothschild island. In 2009 the ice "bridge" that attached Charcot Island collapsed, removing Charcot Island as a pinning point and connecting two separated fronts. In 1991 WIS had an area of $15,985$ km^2. Since then, it has lost over a third of its area. There have been three periods of retreat since 1990, separated by small advances.

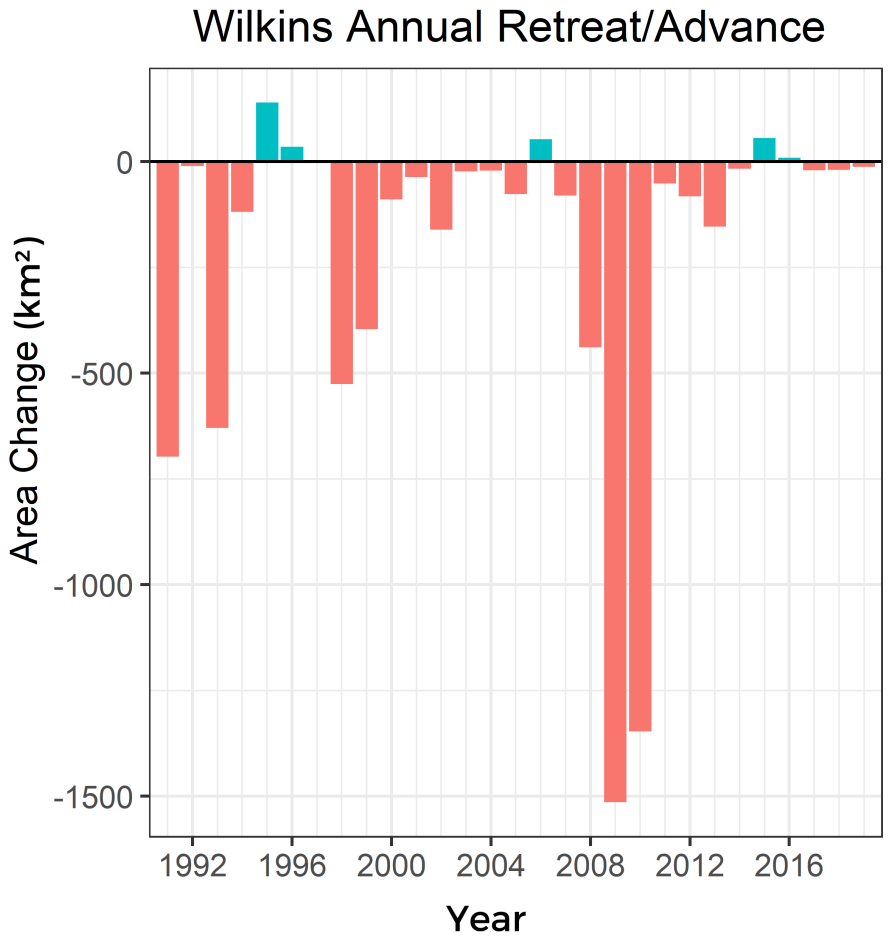


Figure 4.6: Annual area (km^2) gain/loss of the Wilkins Ice Shelf between 1991-2019. Each bar represents the retreat (red) or advance (blue) since the previous year.

4.4.2 Discussion

The rate of frontal retreat found in this study is consistent with Cook and Vaughan (2010), which found that the same ice shelves lost a total area of 20% between the 1950s/60s and the late 2000s. Since 1979 the AP has been losing mass every decade, with the rate of mass loss increasing (Rignot et al., 2019). If this trend continues as is predicted, the stability of the remaining ice shelves is at risk.

Larsen B Ice Shelf

In 1995 the AP experienced high temperature and strong winds that contributed to the retreat that we see in the LBIS as well as the collapse of Larsen A and Prince Gustav ice shelves (Rott et al., 1996). In only a few days in march 2002, over a third of the ice shelf broke up. Much of what was left of the LBIS rapidly retreated in the following years, leaving floating ice only in the scar inlet and a few ice tongues attached to some of the tributary glaciers (Rott et al., 2011; Rignot et al., 2004; Rott et al., 2011).

Earlier observations by Skvarca et al. (1999) and Cook and Vaughan (2010) show that Larsen B had three decades of advance between the 1950s and 1990s. During the early 1990s, there were minor calving events, but the front shape hardly changed. While it was slowly retreating, it appeared stable until the 1995 calving event; after this, comparisons could be made with the Larsen A before its collapse. Velocity increased, and rifting parallel to the front started. The ice shelf front had retreated to within a few kilometres of the compressive arch, where a small retreat would have resulted in an unstable front geometry (Doake et al., 1998).

Larsen B was sensitive to environmental changes. Particularly increased atmospheric temperatures that cause extended periods of summer melt, leading to hydro-fracture due

to additional meltwater entering crevasses (Scambos et al., 2000). In addition to hydro-fracture, the drainage of meltwater lakes from the ice shelf surface exposes its tensile flexure stress both at the surface and base, causing further fractures (Macayeal and Sergienko, 2013). Föhn winds, warm-dry winds down a mountains lee side, further contributed to surface meltwater on the LBIS (Cape et al., 2015; Ashmore et al., 2017). Ice rheology is also affected by increased atmospheric temperatures limiting the load-bearing capacity of the ice and weakening vulnerable shear margins, contributing to the observed acceleration in the years before the collapse (Borstad et al., 2012; Vieli et al., 2006; Vieli et al., 2007).

Warming of the ocean reduces the stability of the whole Larsen Ice Shelf. Warmer water circulates under the ice shelf resulting in basal metal, thinning the ice shelf (Shepherd et al., 2003). These reactions to environmental change and frontal geometry are likely to lead to collapse by pre-conditioning the ice shelf. Ice shelves can tolerate short term negative mass balance, not the prolonged negative mass balance LBIS experienced leading to its collapse. However, negative mass balance does not explain why it rapidly disintegrate in a series of small fragments rather than gradual retreat, as seen prior. Glasser and Scambos (2008) showed that the intersection of flow domains from tributary glaciers form suture zones made up of thin, heavily rifted ice. An additional mechanism that played a role in the destabilising of the LBIS is the rupturing of suture zones caused by the change in flow velocity from a flow domain (Glasser and Scambos, 2008).

The effect of removing the ice shelf has been significant. The removal of buttressing provided by the ice shelf led tributary glaciers accelerating, some by a factor of eight (Rignot et al., 2004). Slower glaciers whose bed and thermal conditions stabilise them are not affected as their stability does not rely on buttressing (De Angelis and Skvarca, 2003; Scambos et al., 2004). Six years after the collapse, some of the tributary glaciers had still not reached an equilibrium and continued to accelerate (Rott et al., 2011). The sediment sample shows that LBIS had not been absent during the entire Holocene, implying the collapse is a result of

climate conditions that have not been present before (Domack et al., 2005). For the Larsen B Ice Shelf to return to its 1980s extent, it would take hundreds of years of positive mass balance (Rott et al., 1996; Rack and Rott, 2004).

Larsen C Ice Shelf

Cook and Vaughan (2010) observed that this is not unusual behaviour for LCIS. It had been stable between the 1950s and 2008, with two significant calving events in that period. In the 1970s, an impact with a giant iceberg caused an iceberg with an area of 1200 km^2 to detach. Secondly, in 1986 an iceberg detached that had an area of 6502 km^2. Both of these are likely natural patterns of retreat and advance. Whether environmental factors played a role is unknown. There is evidence that cycles of calving and advance have been a feature of LCIS for 560 years (Glasser et al., 2009).

The effect that the 2017 calving event will have on the stability of the LCIS is not known; however, it cannot be assumed that the result will be the same as the 1986 event. If the iceberg consists of passive ice, ice that does not contribute to the stability of the front, LCIS should remain stable. However, if this is not the case, the front geometry may have disturbed the compressive arch, resulting in an unstable front likely to retreat further. Future observations will find how quickly LCIS was able to adapt to its new boundary conditions. The surface of LCIS has many suture zones where flow units meet. The ice in these zones is heterogeneous. The combination of accumulated marine ice, soft meteoric ice, and fractured ice help stabilise it by dissipating shear stress without causing crevasses and limiting crevasse propagation (McGrath et al., 2014; Jansen et al., 2013; Glasser et al., 2009).

How environmental factors have contributed to the stability of LCIS is less clear than with the LBIS. Adusumilli et al. (2018) found that the surface of LCIS has lowered by 1.0 ± 0.3 m during 1994-2009 before rising by 0.5 ± 0.3 m by 2017. Nicholls et al. (2004)

hypothesised that basal melt is unlikely to have played a role in this behaviour since the modified Weddell deep water is filling the LCIS cavity providing saline, cold water that is too cold to melt ice. Without warm water, this suggests that on the LCIS, surface factors mainly drive height change, such as firn air densification and surface melting; however, there is evidence that basal melt plays at least a small role in LCIS surface lowering (Rignot et al., 2013; Holland et al., 2015). Western inlets of Larsen C have many melt ponds, some 10 km in length, which could drain into crevasses. Fohn winds play a crucial role in this by transporting warm air over the lee side of the AP, contributing to melt ponding near the grounding line (Luckman et al., 2014; Elvidge et al., 2015). Observations have found basal crevasses due to fracture propagation from meltwater hydro-fracture and stress downstream of the grounding line. Luckman et al. (2012) found that many surface fractures and crevasses may be a trough of basal crevasses, and LCIS has some basal crevasses that penetrate half the ice shelf thickness. These can affect stability as they allow potential heat exchange between ocean and ice. These are not currently a threat to the stability as they have been present for 400 years, and Larsen C does not have sufficient meltwater ponding. However, if the atmospheric temperature were to continue to increase, surface melt would rapidly increase, driving an increase in meltwater ponding, as was observed on both the Larsen A and Larsen B ice shelves before their collapse (McGrath et al., 2012b; Khazendar et al., 2011).

George VI Ice Shelf

Cook and Vaughan (2010) found that the whole ice shelf maintained 92% of its area between 1947 and 2008. The north front had advanced until the 1960s, followed by a consistent retreat with a total loss of 610 km^2. The southern front regularly retreated, losing a total area of $1,,330$ km^2 between 1947 and 2008. This study shows that this historical retreat has continued until the present. The total ice shelf area loss over the past 70 years is low; however, this consistent retreat could signify instability and the beginning of a collapse.

Conditions at either front vary greatly. The north front is in a much narrower part of the channel with a high sea ice concentration that plays a crucial role in controlling calving. Sea ice concentration is less in the Ronne Entrance, but the southern front has pinning points that will help stabilise it (Holt et al., 2013a). Ice flow toward Alexander Island from Palmer Land in the east dominates GVIIS mass gain. Alexander Island only has small glaciers (Reynolds and Hambrey, 1988), creating strong uniaxial compression. Its surface is heavily ponded, with most of it covered in the summer melt period. Melt ponding is not a new phenomenon resulting from recent atmospheric warming; it was first observed in the 1960s (Smith et al., 2007). Uniaxial compression likely plays a vital role in keeping GVIIS stable despite the abundance of meltwater as crevasses cannot form. The mechanisms that influence the retreat of GVIIS are not understood. Atmospheric warming led melt has been shown to have driven collapse in other ice shelves; however, migration of the thermal limit does not appear to have influenced calving of GVIIS. The northern front has not retreated faster than the south, like would be expected with the migration of the thermal limit. Ocean induced basal melt likely plays a more significant role in the stability of GVIIS. Warm modified Circumpolar Deep Water (CDW) that is above 3° C floods the continental shelf and fills the cavity underneath GVIIS (Jenkins and Jacobs, 2008; Zhang et al., 2016).

GVIIS was absent during the early Holocene, collapsing after a period of simultaneous atmospheric and ocean warming. It coincides with the deglaciation of the many AP coastal regions and the influx of the circumpolar deep water onto the AP continental shelf (Bentley et al., 2005). Removal of the GVIIS would cause acceleration of tributary glaciers leading to sea-level rise (Schannwell et al., 2018).

Wilkins Ice Shelf

As first observed by Lucchitta and Rosanova (1998) between 1990 - 1995, retreat had taken place at the northern edge of the ice shelf near Rothschild Island. The calved icebergs had a long tabular shape, reminiscent of those seen during the retreat of the Wordie ice shelf (Doake and Vaughan, 1991). The other periods of retreat 1998-2005 and 2006-2014 were dominated by the retreat of the two fronts that joined Charcot island, creating the narrow bridge (Figure 4.6).

No data are available between 1947 and the 1980s. Its exact behaviour in this time is unknown; however, its total area only reduced a fraction (Cook and Vaughan, 2010).

Unlike its neighbours GVIIS and the Wordie ice shelf that are fed by glacier flow, WIS mass balance is dominated by in situ accumulation (Vaughan et al., 1993). It has an interior velocity as low as $30 - 90$ ma^{-1} compared to around 200 ma^{-1} for Wordie. Slow velocity implies that it would have different triggers for collapse than ice shelves such as the Wordie, which after retreating past a critical limit, could no longer restrain its tributaries, and they began to aid in its collapse (Vaughan et al., 1993). WIS has the same ocean features as GVIIS. The warm water from the modified CDW causes high rates of basal melting at the front, creating a thickness gradient that has a significant influence on the tensile stress at the front because of the altered buoyancy force (Braun et al., 2009). Hence, in May 2008, the austral winter, a significant calving event took place in the absence of meltwater. Hydro-fracture from meltwater certainly played a role in the fracturing and rifting that took place at the ice shelf front; however, unlike with the LBIS was not the calving trigger (Scambos et al., 2009). As with LBIS, low Sea ice concentrations coincided with collapse events (Massom et al., 2018).

Since 2014 and there have been no more retreat events. However, with rising temper-

atures over the AP and the collapse events of the last couple of decades, the stability and future viability of the WIS is unclear.

4.5 Quantile regression analysis

The slopes of the 20th, 50th and 80th quantiles are estimated for the ice shelf area (given as a percentage of max extent) against various statistical descriptors for each predictor. The 80th quantile represents the small changes in area and advancement, the 20th quantile represents the largest changes in area, and the median represents the average area change. The predictors used are 2 m air temperature, SMB, height-change, and sea ice concentrations anomalies. The output tables and coefficient plots inform whether the model outputs are statistically significant. Coefficient plots include slope estimations at more quantiles across the conditional distribution (0.15 to 0.85 in this study) with associated confidence intervals. There are many methods to calculate the standard errors in confidence intervals calculation. In this study, we use the bootstrapping method as it best avoids over-optimistic confidence intervals (Koenker and Hallock, 2000). The estimate is statistically significant if the zero lines are not included in the confidence interval. For completeness, Table 4.3 contains every statistical predictor that we used in a model. Refer to the appendix for the coefficient plots for the statistical predictors that are not presented below.

The best performing descriptor for each predictor was used in an expanded model that included an ice shelf factor variable. This indicates the influence of each ice shelf in the model.

4.5.1 Results

2 meter air temperature

As discussed in the previous section, surface temperature plays an important role in ice shelf stability. In this study, 2 meter air temperature (Celsius) from the RACMO3.2p global climate model was used (table 4.2 for more details). The statistical descriptors presented are annual mean and maximum temperature and their slopes are estimated. Note that as the temporal resolution is monthly, the annual max temperature represents the hottest average month.

There is a negative correlation in the 20th and 50th quantile between ice shelf extent and the annual mean and maximum. The 20th quantile slope is much greater than the 50th and 80th for both mean and maximum temperature. This indicates that the variability of the ice shelf extent increases as temperature increases (Figure 4.7).

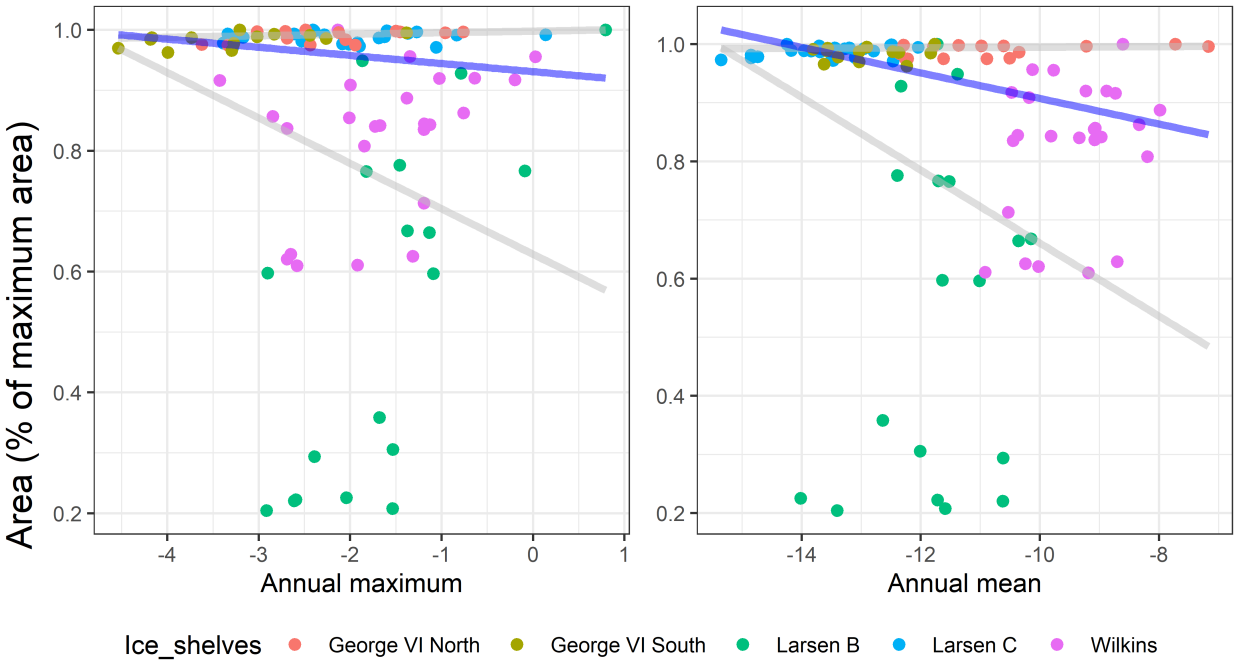


Figure 4.7: Quantile regressions of ice shelf area (% of maximum area) with annual maximum temperature (° C) (Left) and annual mean temperature (° C) (Right). The blue line is the median (50th quantile) and the grey lines are the 20th and 80th quantiles.

Figure 4.8 estimates the slope of other quantiles. The annual mean is statistically significant at the 20th quantile and between the 30th to 65th quantiles. The most significant slope is at the 20th quantile with a value of -0.06, which means for every 1° increase in 2m air temperature, there is a 6% decrease in ice shelf area during retreat events. Annual maximum is only significant at the 35th quantile, and there is little variance in the estimated slope values. Annual mean is a better predictor than annual maximum, suggesting that warming in other parts of the seasonal cycle plays a key role, not just the hottest average month. Figure 4.9 shows that LBIS and WIS are most influenced by T2M. It was thought that all melt-water that remained from the melt season refroze during the winter; however, Kuipers Munneke et al. (2018) recorded temperatures warm enough for melting to take place during the winter.

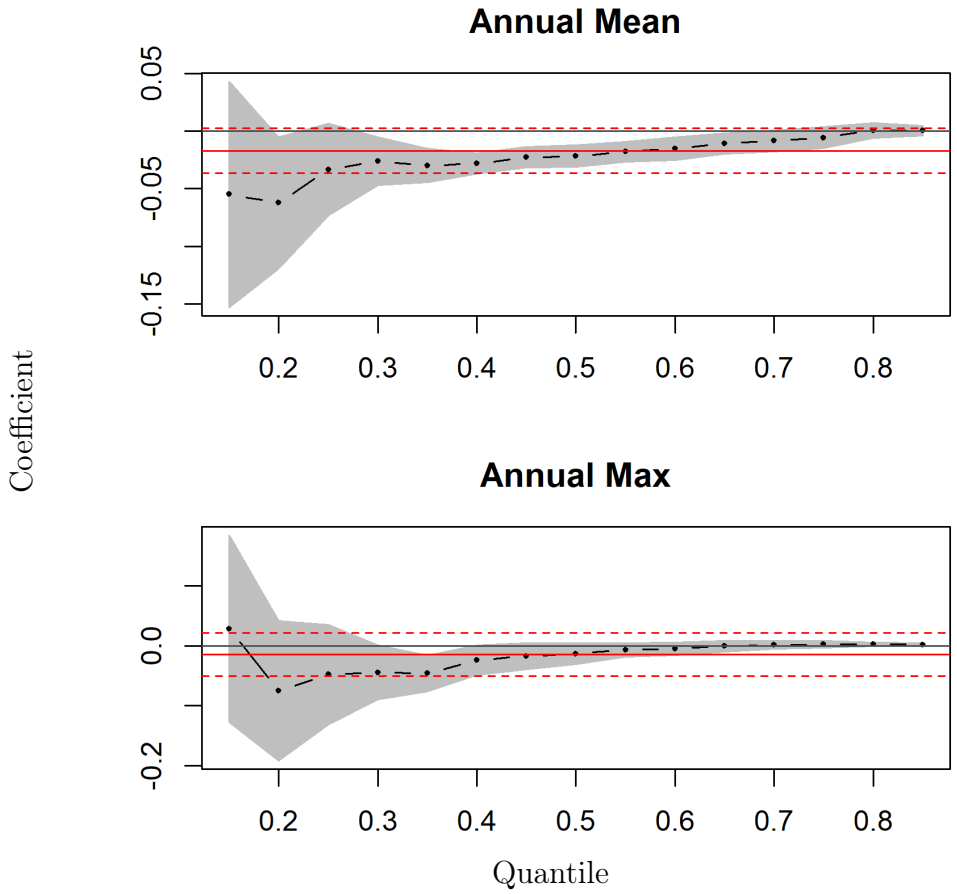


Figure 4.8: Slope estimate (coefficient) of area regressed with annual mean 2 m air temperature (top) and annual max 2 m air temperature (bottom). Slopes estimated from the 15th to the 85th quantile with a 5% interval. Grey shading is the 95% confidence interval. Solid red line is the simple linear regression slope estimate with confidence intervals (red dashed line).

Slope (%)			
Variable	20th quantile	50th quantile	80th quantile
Annual Mean	-0.06227^{*}	-0.02182^{*}	0.00049
Anuual Max	-0.07515	-0.01347	0.00253

Table 4.5: Slope estimates (coefficient - *statistically significant) of area regressed with annual, mean and maximum 2m air temperature for the 20th, 50th and 80th regression lines.

Figure 4.9 is the coefficient plot when the model includes annual mean temperature and an ice shelf indicator as regressors. LBIS and WIS act as strong predictors for decreased ice shelf extent, as would be expected. For each of them, the slope value significantly increases as the quantile increases (0.45 for LBIS and 0.25 for WIS). These correspond to significant collapse events. Variability changes for LBIS and WIS considerably over the quantiles, crossing the least-squares line (red).

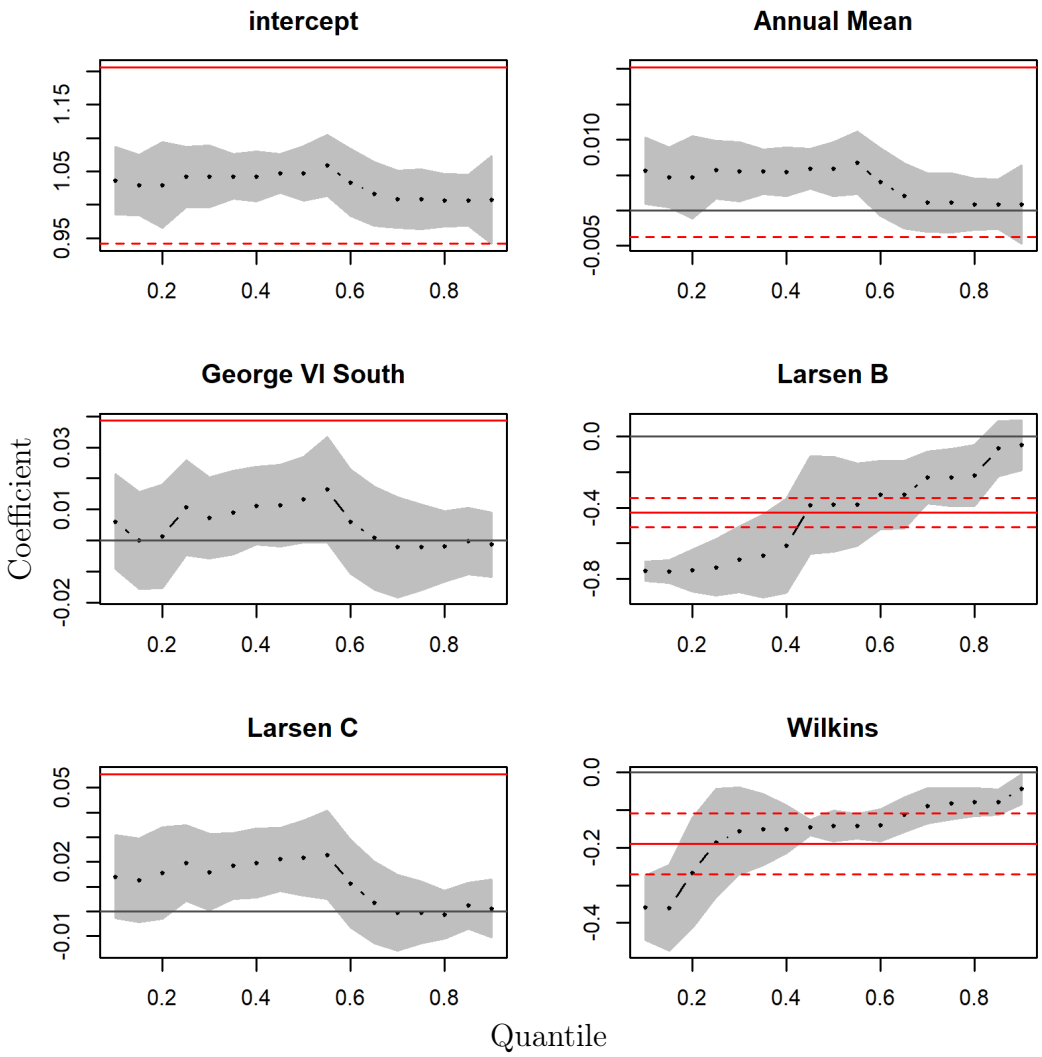


Figure 4.9: Slope estimate (coefficient) of ice shelf area regressed with annual mean 2 m air temperature highlighting the influence of each ice shelf for annual mean 2 m air temperature. Grey shading is the 95% confidence interval. Solid red line is the simple linear regression slope estimate with confidence intervals (red dashed line).

Surface mass balance

SMB is important when considering the total mass balance of the ice shelf. However, in the absence of basal mass balance and ice dynamics, it offers a chance to investigate the

role surface behaviour plays in ice shelf retreat. The SMB data used in this study is from RACMO2.3 and a firn densification model. More details can be found in table 4.2. Below we present the annual mean and annual minimum SMB.

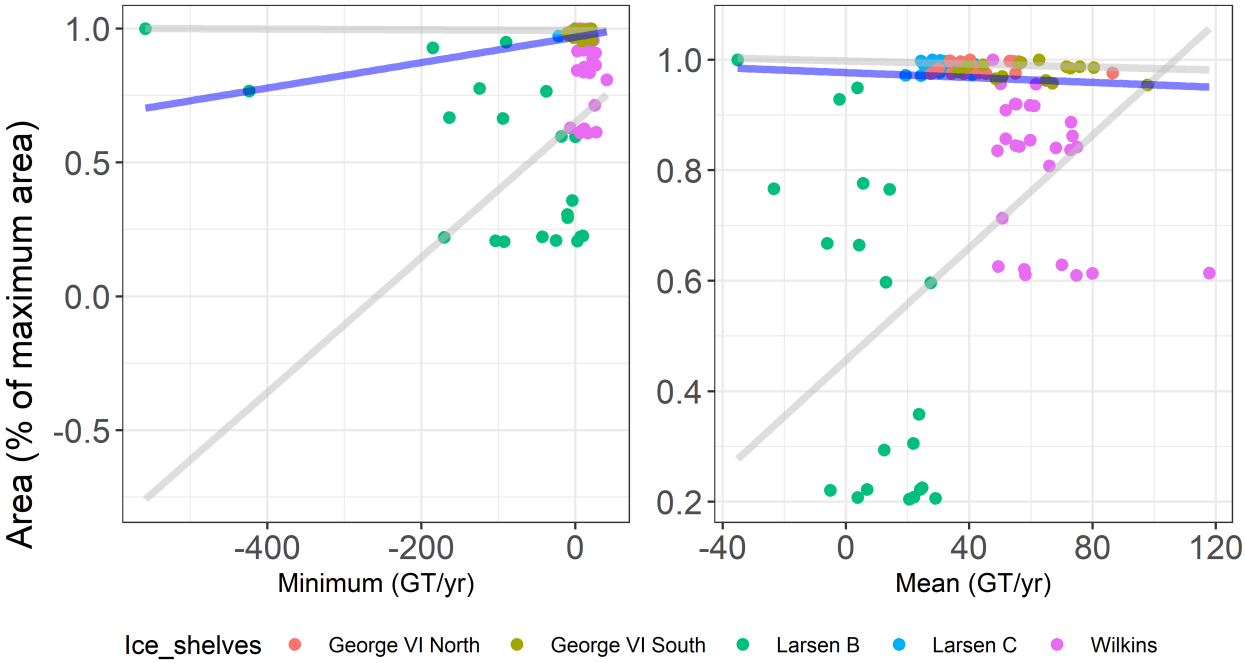


Figure 4.10: Quantile regressions of ice shelf area (% of maximum area) regressed with annual Minimum SMB (Left) and annual mean SMB (Right). The blue line is the median (50th quantile) and the grey lines are the 20th and 80th quantiles.

There is a positive correlation with ice shelf area extent at the 20th quantile for both minimum and mean. A large amount of change in the variability can be as the slope of the 20th quantile is so much greater than that of the 50th and 80th. In the case of the mean SMB, the slope even changes direction between the 20th and 50th quantiles (Figure 4.10). Table 4.6 gives the corresponding regression coefficient.

Slope (%)			
Variable	20th quantile	50th quantile	80th quantile
Annual Mean	0.00509	−0.00022	−0.00014
Anuual Min	0.00252	0.00047	−0.00001

Table 4.6: Slope estimates (coefficient - *statistically significant) of area regressed with annual, mean and minimum SMB for the 20th, 50th and 80th regression lines.

Figure 4.11 shows that the slope value decreases to almost 0 after the 50th quantile for both mean and min. Variability changes significantly from the 15th quantile until the median. In both models, only the 15th quantile is statistically significant. Figure 4.12 has a similar form the Figure 4.9. LBIS and WIS are again, strong predictors of change in extent.

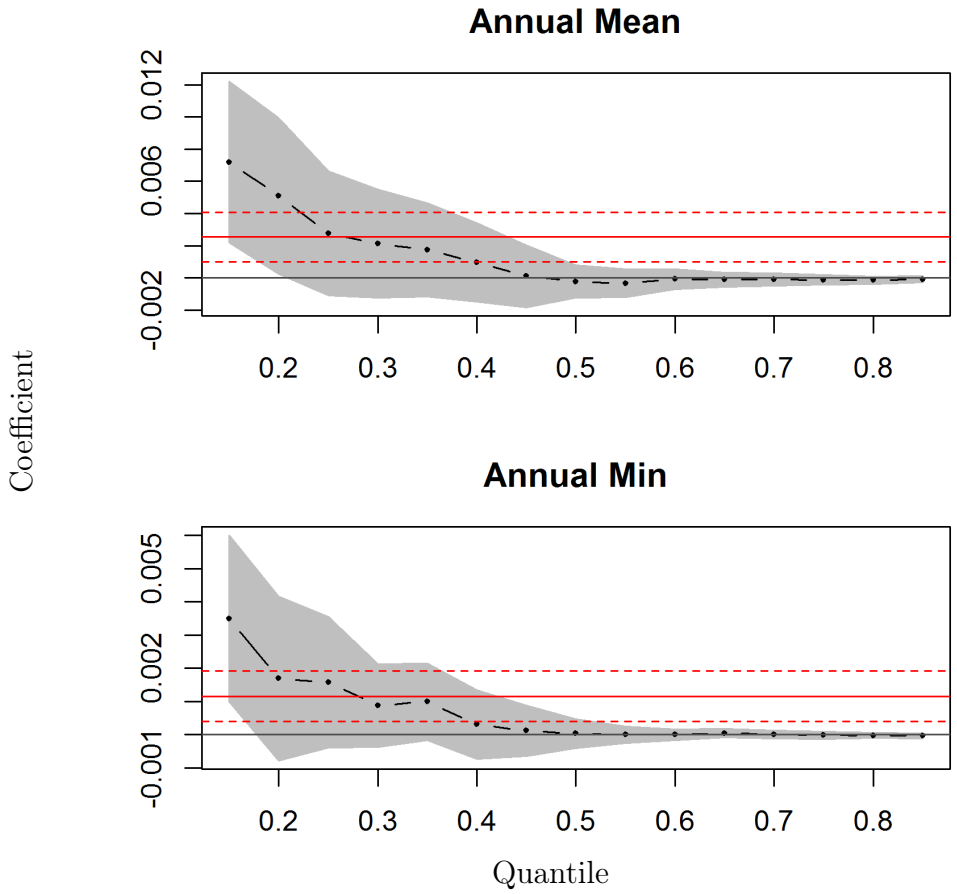


Figure 4.11: Slope estimate (coefficient) of ice shelf area regressed with annual mean SMB (top) and annual minimum SMB (bottom). Slopes estimated from the 15th to the 85th quantile with a 5% interval. Grey shading is the 95% confidence interval. Solid red line is the simple linear regression slope estimate with confidence intervals (red dashed line).

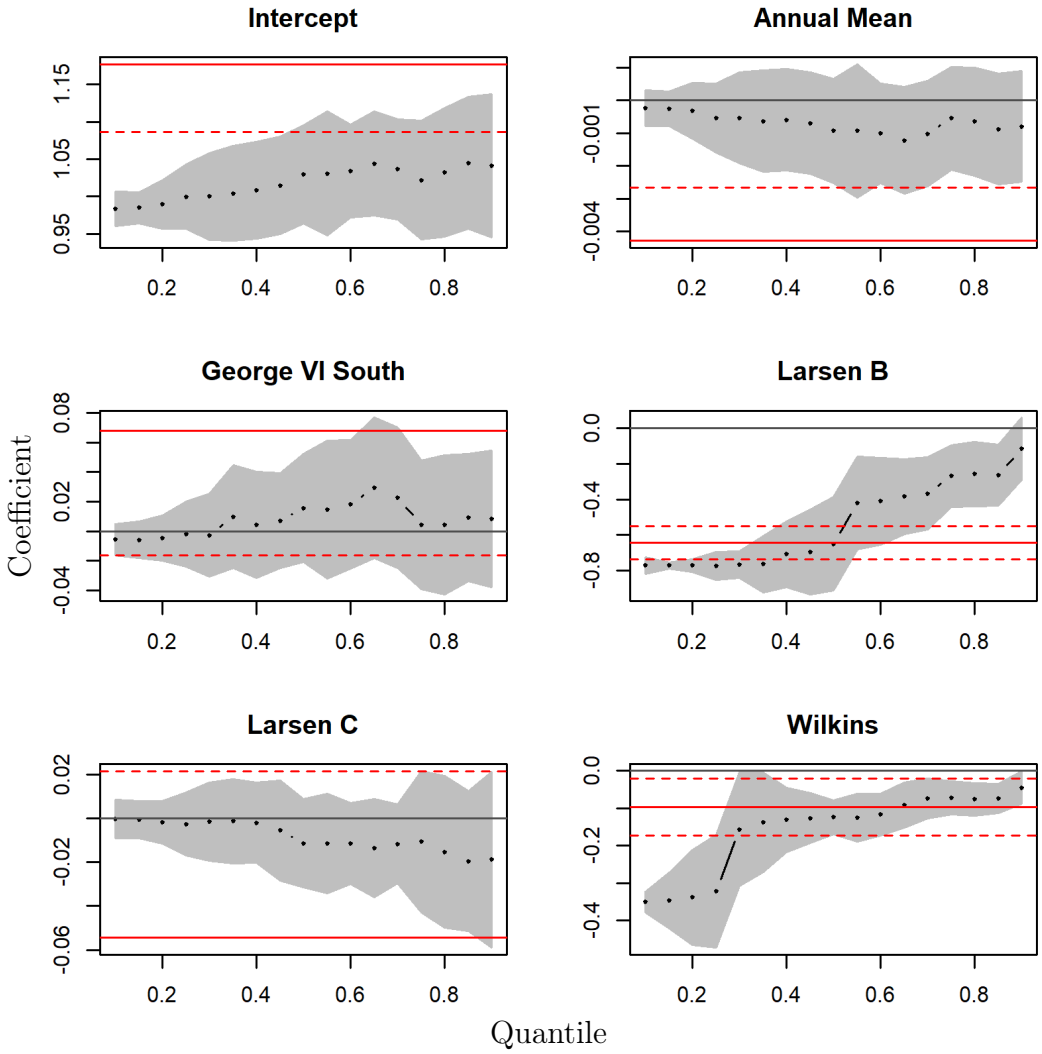


Figure 4.12: Slope estimate (coefficient) of ice shelf area regressed with annual mean SMB highlighting the influence of individual ice shelves. Grey shading is the 95% confidence interval. Solid red line is the simple linear regression slope estimate with confidence intervals (red dashed line).

Ice shelf surface elevation change

The height change data used in the study was constructed from four satellites to produce a 23-year time series for 1994-2016. For more detail refer to table 4.2.

No results for these analyses are presented as none are statistically significant. This suggest that height change does not have a strong association with ice shelf retreat. This is likely due to the complexity of ice shelf height change. Many factors contribute to the ice shelf surface height change, such as SMB, firn air content, and ocean surface height due to changing atmospheric pressure and basal melting. When pooling all available ice shelves as in this study, it is thus likely that this level of complexity means meaningful inference cannot be obtained as the height change of each ice shelf is driven by a different variable.

Sea ice concentration

Sea ice plays a crucial role in buffering storm-induced long-period ocean swell. The absence of sea ice swells causes flexural oscillations in the outer ice shelf margins, leading to calving, particularly in already weakened ice shelves. Exposure of the ice shelf front to ocean swell triggers retreat, so the model design needed to change. It is more appropriate to consider it regressed with annual area change rather than area as this will better reflect short-term effects.

Data are only available for LBIS and WIS. For more detail refer to table 4.2. Since the data are seasonal, each season is included in the QR model along with others listed in table 4.3. The only results presented are that of the summer (December, January, and February) and autumn (March, April, and May) as it is these periods that the ice shelves are most vulnerable.

Both summer and autumn SIC anomalies have similar slopes for the 20th, 50th and 80th quantiles; for both, the variability increases as the anomalies become more negative (Figure 4.13). At the 20th quantile, 10% lower SIC in both summer and autumn corresponds to around a 1.6% per cent annual ice loss (Table 4.7).

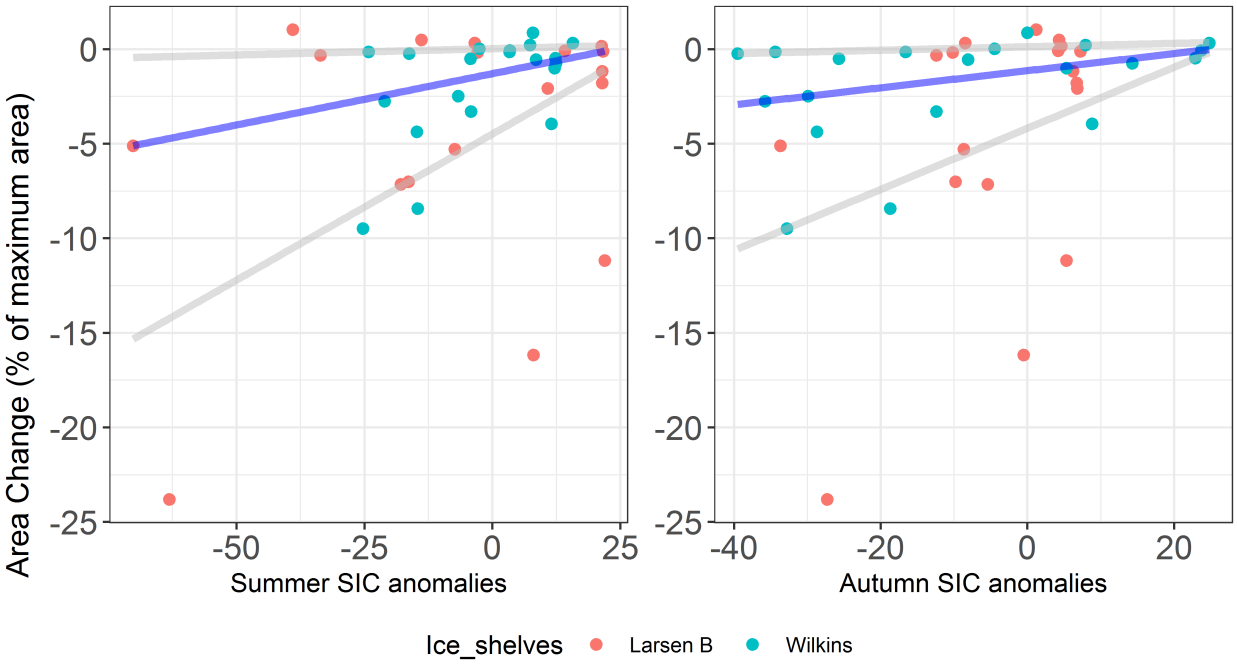


Figure 4.13: Quantile regressions of ice shelf area change regressed with summer mean SIC (Left) and autumn mean SIC (Right). The blue line is the median (50th quantile) and the grey lines are the 20th and 80th quantiles.

Slope (%)			
Variable	20th quantile	50th quantile	80th quantile
Summer	0.00155*	0.00054	0.00007
Autumn	0.00162*	0.00045	0.00009

Table 4.7: Slope estimates (coefficient - *statistically significant) of area change regressed with the summer and autumn, mean SIC.

When we include all quantiles at an interval 5% from the 15th to the 85th, we find the 20th, 25th and 30th to be statistically significant for summer and 20th, 25th and 40th to be statistically significant for autumn (Figure 4.14).

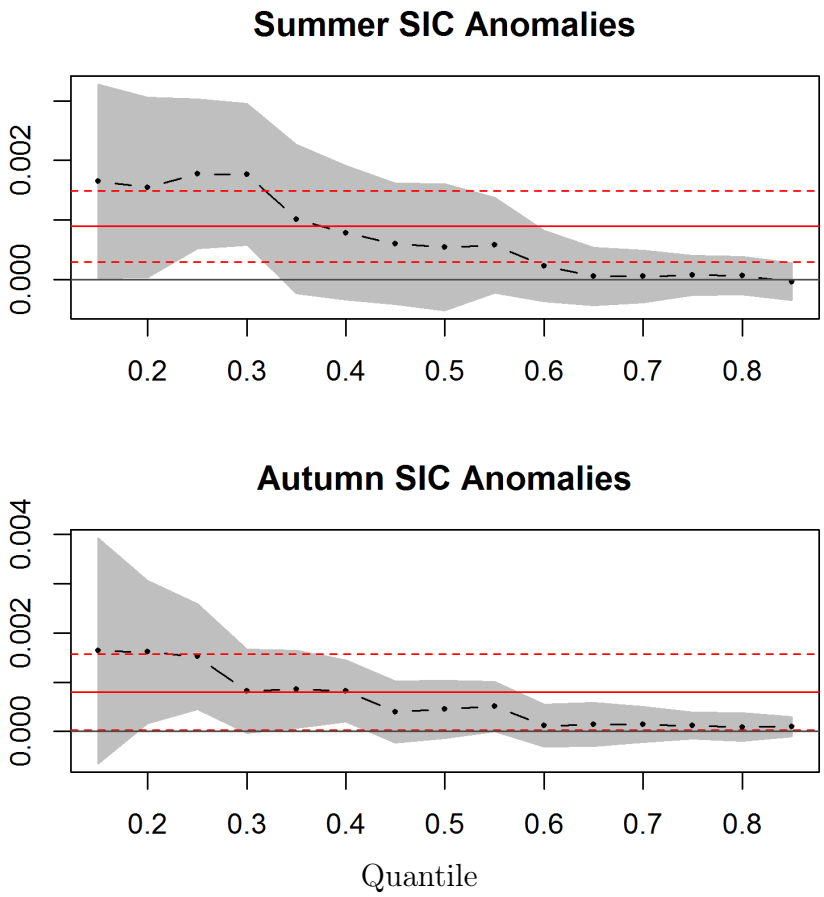


Figure 4.14: Slope estimate (coefficient) of ice shelf area regressed with Summer Sea ice Concentrations (SIC) (top) and Autumn SIC (bottom). Slopes estimated from the 15th to the 85th quantile with a 5% interval. Grey shading is the 95% confidence interval. Solid red line is the simple linear regression slope estimate with confidence intervals (red dashed line).

4.5.2 Discussion

Our results indicate that 2m air temperature and sea ice concentration correlate with the changes in ice shelf area. As mean annual 2m air temperature had the strongest results, it suggests that not only warm summers play an important role in ice shelf stability but also temperature throughout the year. While most melt occurs in the summer, melt is

not limited to this time of year as previously thought. Kuipers Munneke et al. (2018) recorded temperatures warm enough for melting to take place during the winter. Since, Maximum temperature was also a significant descriptor, it suggests that the hottest month is an important indicator of stability. Clearly, a period of high temperature is going to increase surface melt, exposing the ice shelves to more risk of calving. Prior to the break up of the LBIS, there was an increase in the magnitude and duration of the melt (Broeke, 2005), eventually leading to hydrofracture through the drainage of the excess meltwater (Banwell et al., 2013; Banwell et al., 2014; Rack and Rott, 2004).

The SIC findings suggest an unusually low SIC during the summer and autumn corresponds with retreat events. This is consistent with the findings of Massom et al. (2018), in the absence of sea ice plate bending induced by ocean swell can trigger significant calving, as was the case for both the LBIS and WIS. Modelling by Sergienko (2010) showed that waves could induce stresses of significant magnitude to not only trigger calving but also control the size of the icebergs. If low SIC becomes more frequent, ocean swell induced calving will become more frequent. However, it is important to note that some ice shelves do not rely on sea ice for buffering as the LBIS and WIS have been shown to. A large break up following plate bending requires excess melt water and a lack of internal compression (Massom et al., 2018). An ice shelf like the GVIIS is less reliant on sea ice since it has a significant internal compression due to its geometry.

Table 4.3: Predictors, the ice shelves that the data covered, and the statistical descriptors used. Prev refers to the values of the previous year. For example, the prev mean of the 2001 extent would have the 2000 mean. This aims to infer the role of preconditioning on ice shelf retreat. The 1st Quartile (Q) is the 25% quantile and the 3rd Quartile (Q) is the 75% quantile.

Driver	**Ice shelf**	**Statistical descriptors**
2 m air Temperature	LBIS, LCIS GN, GS, WIS	mean, median, 1st Q and 3rd Q, min, max, prev mean, prev median prev max, seasonal means
Surface Mass Balance	LBIS, LCIS GN, GS, WIS	mean, median, 1st Q and 3rd Q, min, max, prev mean, prev median prev max, seasonal means
Sea ice Concentration	LBIS, WIS	mean and minimum, prev mean, prev minimum. Seasonal means
Height Change	LBIS, LCIS GN, GS, WIS	mean, median, min, max max, 1st Q and 3rd Q prev mean, prev median, prev and max

Ice shelf	**First obs.**	**Area** (km^2)	**Last obs.**	**Area** (km^2)	**Loss** (km^2)	**Remaining**
Larsen B	1992	13,373	2009	2737	-10,636	20.5%
Larsen C	1992	51,517	2019	46,558	-4959	90.4%
George VI	2002	24,063	2019	23,351	-711	97%
Wilkins	1990	15,985	2019	9763	-6223	61%
Total		104,939		82,410	-22,529	78.5%

Table 4.4: Overview of the ice shelf area of the first and last observation, total area loss during this period, and the per cent of the area remaining.

4.6 Conclusions

This chapter presents new satellite-derived annual ice shelf extent time series that reveals a lot about the evolution of the Larsen B, Larsen C, Wilkins and Geoge VI Ice Shelves over the last 25 years. Long term time-series had been available previously; however, this is the first with the annual extent for multiple ice shelves. All of the ice shelves had retreated; however, the magnitude and patterns of retreat were varied. Unique environmental conditions and geometry cause different threats to stability and potential failure points. Changes in climate that have taken place over the past 25 years have contributed to retreat; however, the relationship is not linear.

Annual extent gives insight into the nature of the changes in ice shelf extent; however, we can only speculate on what glaciological processes are taking place. Each ice shelf will likely be experiencing a subset of these forces to various degrees. The exact processes that take place for each ice shelf are not yet understood. By applying QR, it has been possible to explore further the role of some of these variables. While statistical modelling has its limitation and care needs to be taken when interpreting the results, they offer guidance on which areas to focus further study.

Results showed a 2% decrease in median ice shelf extent per $1°C$ increase in mean annual air temperature and a 6% decrease in the 20th quantile of ice shelf extent per $1°C$ of mean annual air temperature for the four ice shelves. These findings suggest that continued warming of the AP will lead to further ice shelf retreat. This agrees with the hypothesis that there is a thermal limit of viability for ice shelves, although it does not explicitly support the -9^o C suggested by Vaughan et al. (1993). Further, the results for SIC anomalies gave further evidence that exposure of the ice shelf front to the open ocean can trigger calving. At the 20th quantile, 10% lower SIC in both summer and autumn corresponds to around a 1.6% per cent annual ice loss, supporting the finding of Massom et al. (2018).

A key benefit to QR is that estimating slopes at all quantiles across the conditional distribution provides a more detailed understanding of the interactions. Not making assumptions about the distribution is more appropriate in most cases than standard linear regression. Focusing on the mean with a standard linear regression would have caused many undiscovered results. An additional advantage that QR is that it is easy-to-implement, and its transparency when compared to other techniques such as neural networks (Baur et al., 2004).

Chapter Five

Modelling Antarctic Peninsula ice shelf fracture probability using a Gaussian process mixed effects model.

5.1 Aims and Objectives

This chapter is the second experimental chapter of this thesis. The primary aim of this chapter is to introduce a novel framework for predicting ice shelf fracture probability. The framework that is introduced solves a primary issue that other fracture models do not address, the ability to model multiple ice shelves (regardless of geometry or location) within the same simulation, this is key to making a model that is scalable to larger systems. Secondly, accounts for dependence between adjacent fractures. To achieve this aim, the following objective is set out:

- Implement a Gaussian process (GP) mixed-effects model framework to predict the fracture probability on major AP ice shelves.

- Determine whether the high or low resolution fracture index dataset produces better results.

By completing this objective, the second research gap highlighted in Chapter 1 is addresses. This chapter presents a new method for modelling surface fracture probability account for the non-independence of adjacent fractures. Bayesian nonparametric models are a class of models that have an infinite-dimensional parameter space, such that the parameter space is a set of all possible solutions that can be learned (Orbanz, 2010). The model we utilise is a Gaussian Process (GP) mixed-effects model. GPs are probability distributions over functions that can be updated in a Bayesian way using observational data (Mackay, 2004). Mixed-effects models include both fixed and random effects. Fixed effects infer relationships between the independent variable and the predictors, while random effects account for any other variability. An example of a fixed effect in this study is the ice rheology, an example of a random effect is that measurements are taken from different ice shelves. Including both fixed and random effects, we can model multiple ice shelves with the same model while accounting for correlation between nearby data points. These models were first developed in the 1980s. However, the tools that enable us to apply them to large datasets is a relatively recent development. Matthews et al. (2017) developed an inference scheme that drastically reduces the computational time of MCMC sampling, making it viable for large dataset. Various parameterisations of the model are investigated to investigate the model changes depending on the data available. We produced two fracture datasets to investigate model performance under different satellite image availability; this is discussed further in Section 4.2. In Section 4.3, we discuss in detail the model that we used; in Section 4.4, we present the model's results, and in Section 4.5, we discuss how the model performed.

5.2 Background

While a universal calving law does not yet exist, fractures must be present for calving to occur. Hence, to model calving the location of fractures are vital. Fractures can be determined through satellite imagery. However, high enough resolution images are available in only a limited number of regions for each ice shelf. Additionally, indexing fractured and non-fractured locations manually have limitations as snow cover restricts surface visibility. Two methodologies have been applied to this area of research. A damage calculation was made using inverse methods, while useful, this is not a substitute for fracture as damage on only detects fractures formed such that they reduce the ice viscosity causing changes in the velocity (Borstad et al., 2012). More recently, work by Emetc et al. (2018) introduced statistical methods to model fracture probability. They used logistic regression to model fracture probability of the multiple ice shelf regions individually and then sorted them into 4 groups. The groups represent roughly similar geometries, and an ice shelf is put into the group whose predictors closest match the best fitting model. The motivation for this grouping is to estimate the fracture probability of similar ice shelves. This method could predict probability fractures accurately; however, it is not scalable as it cannot model multiple ice shelves together. This highlights a challenge in modelling the ice shelves of an entire ice sheet. The model needs to be able to distinguish between different ice shelves, particularly as ice shelf geometry and dynamics varies drastically.

Despite there importance, existing models do not take into account fractures. There have been multiple studies that implement a calving criterion into a flow model. Most of these leave out any attempt to model fractures implicitly. Two models that have calving criteria are the Community ice sheet model (CISM), which has two methods for implementing calving. Firstly, to calve all floating ice (so it cannot be used to model ice shelves). Secondly, to calve when the bedrock is below a prescribed elevation (Lipscomb et al., 2019). The Potsdam

Parallel ice sheet model (PISM) also has two implementations for calving. The first is based on horizontal spreading rates; the second is a criterion based on ice thickness (Martin et al., 2011; Levermann et al., 2012). The second does not apply to marine-terminating glaciers because of the different physics between floating and grounded ice.

We apply a spatial mixed-effects model to the Larsen C Ice Shelf (LCIS), George VI Ice Shelf (GVIIS) and WIS. These are the three largest ice shelves remaining on the AP. All have had some retreat, with the most significant being the bridge's collapse that connects the WIS to Charcot Island (although we model pre bridge collapse). LCIS had a significant calving event in 2017 in which an iceberg that was approximately 10% of its total area calved from its front following the propagation of a large crevasse (Han et al., 2019). While this calving event has not compromised the compressive arch or buttressing capabilities of the ice shelf; thinning, and increased surface melt may indicate that it is not as stable as it once was (Bevan et al., 2020). The geometry of GVIIS is stable overall; however, heavy fracturing and thinning have led to retreat at both calving fronts (Holt et al., 2013a). These three ice shelves have disparate geometries, flow parameter profiles and data availability. This disparity will test the model's ability to predict fracture probability over a range of ice shelf types within the same simulation.

5.3 Data and ISSM Model Predictors

To build the statistical model, we need two datasets. Firstly, the locations on the ice shelf and nearby grounded ice surface can be indexed as either fractured or non-fractured. Secondly, we need to have a group of predictor variables. In this section, we discuss the sources and methods used to produce these datasets.

5.3.1 Fracture locations and fracture zones

Indexing ice shelf surface fractures accurately is difficult as high-resolution satellite images are not available for the entire surface via the method that is used in this study. This study compares two methods for categorising surface fracture observations. The first is similar to that used in Emetc et al. (2018), which identified fractured and non-fractured locations on the ice shelves and their tributary glaciers using high resolution (10 m horizontal resolution) images that are available in Google Earth Pro between 2011-2015. This criterion ensuring accurate indexing but is limited to particular regions. The second method that we used is to use the highest resolution satellite images available in Google Earth Pro to categorise each point on the ice shelf as either fractured or not fractured. The low-resolution images have a horizontal resolution of 30 m.

Emetc et al. (2018) made the surface fracture data available. We updated this dataset with new observations where possible and produced our own non-fractured dataset as this was not publicly available. Their original dataset included "ice shelf zones", including glaciers 100 m upstream of the grounding line. We also included these in our simulations as observations are too limited when considering floating ice only. High-resolution satellite images focus on the grounding line, with almost none in the centre of the ice shelves. The process for producing the dataset involved manually selecting the fracture locations and non-fractured zones. Smooth blue ice determines non-fractured zones as ice is visible without snow cover. There is no sure method for distinguishing between surface and basal fractures and rifts. However, surface expressions of basal crevasses will be hundreds of meters wide and perpendicular to the direction of flow (Luckman et al., 2012).

The second method for categorising surface fracture used both high-resolution and coarser images to categorise each point on the ice shelf as either fractured or non-fractured, including coarser images allowed for better categorisation of the centre and front, rather than

just the grounding line. The process was similar to the above. Each fracture observation was manually recorded and interpolated to an evenly spaced grid using all available images in Google Earth. All other points were categorised as non-fractured, resulting in a complete fracture index of the ice shelves. However, incorrect categorisation is inevitable with this method. It is impossible to distinguish between basal crevasses and surface fractures on the lower resolution images based on width, so would not be suitable for modelling basal fracture alone. Snow cover is likely to have hidden fractures. Additionally, there may be other noise and artefacts within these images that would also cause miss categorisation.

5.3.2 ISSM setup

The predictors used in the statistical model are flow parameters calculated with the Ice Sheet System Model (ISSM), an open-source model developed by the University of California at Irvine and the Jet Propulsion Laboratory to model the evolution of the polar ice caps. It is capable of solving stress balance equations in both 2D and 3D (full stokes), utilises finite element modelling, and anisotropic mesh refinement that can use unstructured meshes to more accurately model areas with more complex dynamics while saving computational resources on other areas, and inverse methods to infer unknown parameters (Larour et al., 2012). SSA was more appropriate than full stokes for floating ice and allowed the damage calculation, which is incompatible with the full stokes model. We ran simulations that solved stress balance equations for each of the ice shelves to obtain the predictors needed for our statistical model. Cost functions for inversion were tuned manually such that modelled velocity was a good match with observed velocity.

The setup used for our simulations are as follows: Basal melt is set to 0. BedMachine was used to generate thickness (Morlighem et al., 2020). SeaRISE is used for climate forcing, including air temperature, surface mass balance, upward geothermal, and heat flux (Bind-

schadler et al., 2013). Surface temperature is used as the steady-state depth-averaged ice temperature over each of the ice shelves. Ice front boundary is assigned a Neumann boundary condition. The rest of the lateral boundary is assigned a Dirichlet boundary (observed velocity). The upper surface is stress-free. The grounding line position is determined using flotation criteria. Friction is applied between the ice and bedrock, and floating ice has no friction. Velocity observations are taken from (Rignot et al., 2011a).

5.3.3 Predictors

Below, we give details on how they are calculated and why they may be relevant predictors for fracture creation. For a brief overview, see Table 5.1.

Rheology

Glacier movement involves the ice-crystal slippage as a result of stress applied to it in a process called creep (Weertman, 1983). Increased ice stiffness can lead to the creep being too slow for the amount of stress resulting in the formations of fractures.

The inverse control method is used to calculate a depth-averaged spatial distribution of ice rigidity, B, such that it minimises the difference between observed and modelled velocities (Larour et al., 2005; Khazendar et al., 2007).

Damage and backstress

Damage is a variable that quantifies the loss in load-bearing potential due to fractures. Backstress quantifies the buttressing effect on the ice. Damage and backstress are both calculated as in Borstad et al. (2013) in which a partition of inverse method solution is

implemented to calculate separate and independent solutions for damage and backstress. These calculations rely on the inverse solution to ice rigidity and an initial ice rigid estimation.

The damage calculation can be made as follows:

$$D = 1 - B_1/B_T \tag{5.1}$$

where B_1 is the inversion of rigidity, B_T is initial rigidity, $D \in [0, 1]$. The main uncertainty of the calculation is from the estimation of B_T, due to the often unknown ice temperature that is difficult to measure accurately.

It is important to note that damage is not intended to capture all surface fractures. Instead, the fractures formed such that they reduce the ice viscosity causing changes in the velocity. It captures areas of increased flow rather than every fracture location. Damage is a valuable predictor for our statistical model; however, it can be a tool to help understand how well the other prediction factors perform; this is done by running simulations excluding damage and simulation with damage as the only predictor.

Decreased backstress results in increased longitudinal tensile stress making it more susceptible to fractures. The reduction in backstress can be from the weakening of the ice from thinning (Shepherd et al., 2003). The inversion calculation for backstress leads to the simplified damage equation 5.1 but is left out for brevity.

Principal and effective stress

Since this study opts for a shallow shelf approximation model, transverse and longitudinal stress are neglected. Velocity observations are used to calculate the principal and effective stresses. Stress is a significant predictor in the ice shelf fracture, as increased stress is the

direct course of fracture formation. As ice is subjected to increased stress, it becomes brittle as it moves from an elastic state to a ductile one (Paterson, 1994).

Principal stresses are the maximum and minimum values of the normal stresses when the plane is orientated so that the shear stresses are 0. The sign of the principal stresses determines whether the stress being applied is compressive or tensile.

Given that the deviatoric stress $\sigma^{'}$ is given by:

$$\sigma^{'} = \begin{bmatrix} \sigma^{'}_{xx} & \sigma^{'}_{xy} & 0 \\ \sigma^{'}_{xy} & \sigma^{'}_{yy} & 0 \\ 0 & 0 & -\sigma^{'}_{xx} - \sigma^{'}_{xy} \end{bmatrix} \tag{5.2}$$

The effective stress $\sigma^{'}_{e}$ can be calculated as follows:

$$\sigma^{'}_{e} = \sqrt{\sigma'^{2}_{xx} + \sigma'^{2}_{yy} + \sigma'^{2}_{xy} + \sigma^{'}_{xx}\sigma^{'}_{yy}} \tag{5.3}$$

Principal and effective strain rate

Strain rate plays a crucial role in new fracture formation. Glacier ice has a critical strain rate threshold that, once reached, will result in crevasse formation (Vaughan, 1993). The value of the threshold varies depending on the conditions of the ice, such as rheology properties, firn density, and water and debris inclusions (Campbell et al., 2013).

Given that u and v are horizontal components of observed surface velocity, the principal strain rates can be calculated from the matrix.

$$\dot{\varepsilon} = \begin{bmatrix} \frac{\partial u}{\partial x} & \frac{1}{2}(\frac{\partial u}{\partial y} + \frac{\partial v}{\partial x}) & 0 \\ \frac{1}{2}(\frac{\partial u}{\partial y} + \frac{\partial v}{\partial x}) & \frac{\partial v}{\partial y} & 0 \\ 0 & 0 & -\frac{\partial u}{\partial x} - \frac{\partial v}{\partial y} \end{bmatrix} \tag{5.4}$$

Effective strain can then be approximated by:

$$\dot{\varepsilon}_e = \sqrt{\dot{\varepsilon}_{xx}^2 + \dot{\varepsilon}_{yy}^2 + \dot{\varepsilon}_{xy}^2 + \dot{\varepsilon}_{xx}\dot{\varepsilon}_{yy}} \tag{5.5}$$

Thickness

Ice shelf thickness likely plays a role in the length and depth of fracture propagation as basal channels cause thinning that result in fractures perpendicular to flow (Dow et al., 2018; Alley et al., 2016). Thickness data is taken directly from BedMachine (Morlighem et al., 2020).

Velocity

Ice velocity is included as a predictor as an increase in velocity could play a role in the formation of new fractures. Velocity observations are taken directly from InSAR data between 2007 - 2009 (Rignot et al., 2011b).

Table 5.1: Predictor parameters and the method use to calculate them

Predictor	Calculation/Description
Observed Velocity	Taken directly from inSAR (Rignot et al., 2011a)
Modelled Velocity	Calculated from stress balance equations
Damage	Calculated via inversion in ISSM (Borstad et al., 2012)
Backstress	Similar to that of damage
Principal stress components	Calculated using equation 5.2
Effective stress	Calculated using equation 5.3
Principal strain components	Calculated using equation 5.4
Effective strain	Calculated using equation 5.5
Rheology factor B	Calculated via an inversion of the observed velocity.
Thickness	Taken directly from BedMachine (Morlighem et al., 2017)

5.4 Methods

5.4.1 Mixed-effects Gaussian process model

Models that utilise Gaussian processes are advantageous as they are non-parametric. Therefore, these models can be applied to a vast range of machine learning problems. When using GP models, the critical consideration is to approximate the posterior distribution when the data is large. This study applies a mixed-effects GP model that uses a hybrid variational and Markov Chain Monte Carlo (MCMC) sampling scheme developed by Hensman et al. (2015). MCMC methods are a class of algorithms for sampling from a distribution. Briefly, a Markov chain is the concept that random samples are generated from only considering the

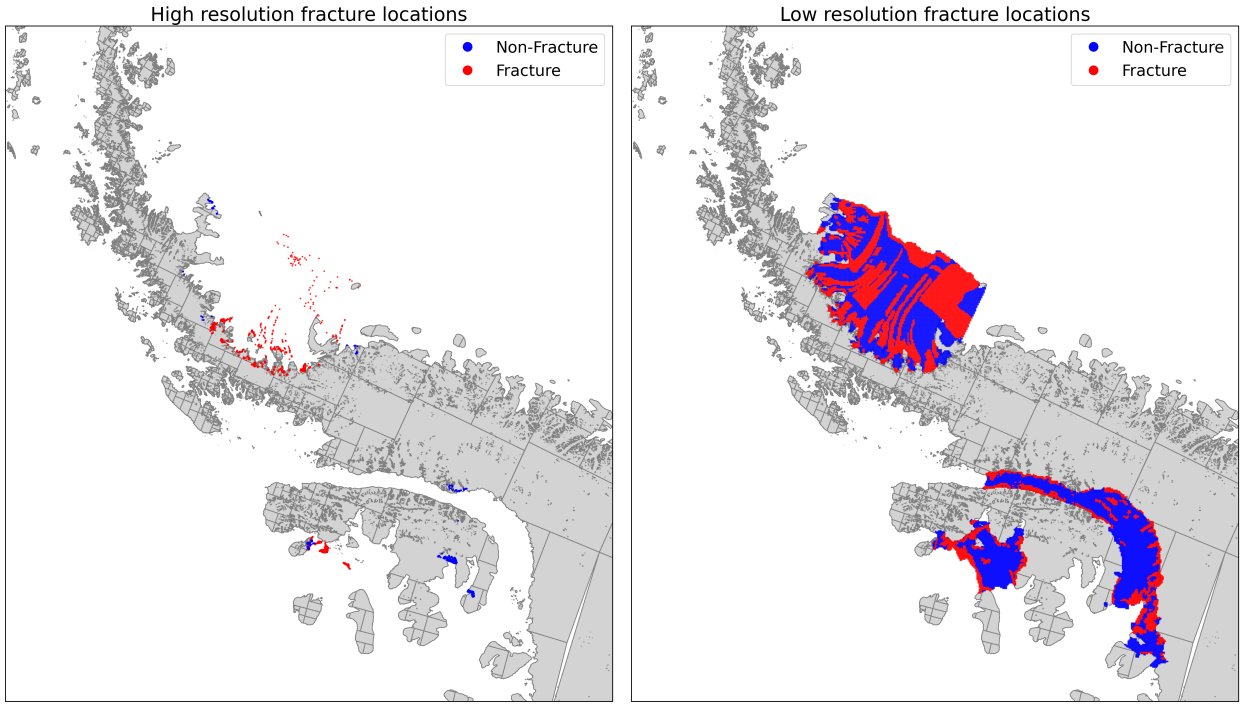


Figure 5.1: Fracture index locations for the Wilkins, George VIII, Larsen C Ice shelves. The high-resolution fracture index locations (left) are delineated using images available in Google Maps Pro with a 10 m horizontal resolution or less. Only points locations that are fractured or blue ice zone (non-fractured points) are included. The low-resolution fracture index (right) use all available images (up to 30 m horizontal resolution) to delineate fracture point; all other points are set to non-fractured.

sample before it; this is known as a Markov process. Monte Carlo is a method of estimating the parameters of a distribution from a random sample of points from the distribution (Ravenzwaaij et al., 2018). The hybrid inference scheme that we use offers a computationally inexpensive way to sampling the posterior distribution using MCMC without making any specific requirements of the covariance function or the data. Other methods to sample the posterior using MCMC involve iteratively sampling the function values and covariance parameters. This type of scheme requires the inversion of the covariance matrix for each step. Such inversions are computationally expensive, making them unsuitable when the data is

large.

In both high and low-resolution datasets, the fractures and non-fractured locations are not well mixed. Focusing on the high-resolution data, since the data is poorly distributed, there are clear clusters of fractured points at Larsen C and non-fractured points at George VI. Fitting a simple logistic regression to this type of data is problematic because the points within the clusters will not be independent. These regions undoubtedly have differing flow parameter values, so the model would be learning to differentiate between the two locations rather than finding the underlying correlation between the predictors and fractures. Emetc et al. (2018) get around this issue by grouping similar regions by the number of matching predictors. It can then be assumed that the data in each group are independent.

This non-independence between data points arises from a hierarchical structure within the data. There are two standard methods of modelling this type of data. Firstly, by aggregating the data between groups (ice shelf in this case). While this does get around the non-independence, it removes most of the data points when there are only a few groups and lots of data within them. Secondly, is to model group-wise as in Emetc et al. (2018). The result is multiple models where no one model uses the whole dataset. The alternative method that we implement is the use of a mixed-effects model. A spatial mixed-effects model contains both fixed and random effects. It is a beneficial method for modelling when there is a spatial correlation. The fixed effects assumption is that the variance is correlated with the model predictors. The random-effects model the spatial correlation between the data.

Given that Y_i is the binary fracture indicator at location i, x_i is the predictors and z_i is the coordinates of ith location. The model can be defined as follows:

$$\ell(p(Y_i = 1)) = x_i^T \beta + g(z_i) \qquad\qquad i = 1, 2, ..., n. \tag{5.6}$$

where ℓ is a link function, a probit link function is implemented because of its ease of implementation, but a logit is also an option. The regression coefficients β are the fixed effects and the function g are the random effects. We assume g varies slowly in space. So g captures any other features of z_i. If two-point within close proximity are highly correlated, it can be because of the random effect g rather than being independent of one another.

To perform Bayesian inference on the model, we assign a prior on the parameters. Priors represent our belief about the parameters.

$$\beta \sim N(0, \sigma^2_{fixed} I) \qquad\qquad g \sim N(0, \sigma^2_{random} k_\lambda) \tag{5.7}$$

where k_λ is the kernel on $\mathbb{R}^2$. We have defined g as a Gaussian process. A Gaussian process generalises the Gaussian probability distributions, which are defined over scalars or vectors. Gaussian processes are defined over functions. Since functions have an infinite domain, a Gaussian process is a Gaussian random variable with infinite dimensions. Any subset of its random variables has a multivariate normal distribution. A Gaussian process is specified by its mean function and covariance function, also known as the kernel. The kernel inputs 2 points $z, z^{'} \in \mathbb{R}^n$ and outputs the similarity measure between them as a scalar, $k : \mathbb{R}^n \times \mathbb{R}^n, \Sigma = Cov(X, X^{'}) = k(z, z^{'})$. By evaluating all the points pairwise, the kernel function calculates the covariance matrix. The choice of the kernel determines the shape that the fitted functions can take. The kernel used here is the Radial Basis Function (RBF) kernel.

$$k_\lambda(z, z^{'}) = exp(-||z - z^{'}||^2 / 2\lambda^2) \tag{5.8}$$

where λ is the lengthscale parameter. As $k_\lambda(z, z^{'}) \in (0, 1)$ the closer 2 points are

the closer the similarity is to 1, and the further away 2 points are the closer the similarity is 0. The lengthscale can be interpreted as the kernel's influence between points (so how correlated those two points are). The hyperparameters (parameters of the prior distribution) are $\theta = (\sigma^2_{fixed} I, \sigma^2_{random} k_\lambda, \lambda)$. By assigning priors onto θ, we will learn them in a fully Bayesian way. Lengthscale can be set before training the model, or it assigned a prior becoming a trainable parameter. We train the lengthscale in our initial simulations that train the model on the whole fracture dataset to obtain an appropriate value. When withholding part of the data, we set the lengthscale to that value.

5.4.2 Variational Bayes

To perform inference in a Bayesian way we need to sample the posterior distribution which is the conditional distribution of the parameters β, g, θ given the data $\{Y_i, x_i, z_i\}_{i=1,\dots,n}$. The posterior is proportional to the likelihood times the prior:

$$p(\beta, g, \theta | \{Y_i, x_i, z_i\}_{i=1,\dots,n}) \propto \prod_{i=1}^{n} p(Y_i | x_i, z_i, \beta, g, \theta) p(\beta, g | \theta) p(\theta). \tag{5.9}$$

by finding the marginal distribution, we can isolate the fixed effects β. The most studied method for sampling the posterior is to use an MCMC. The benefit of using MCMC is that it offers asymptotically exact samples from the posterior distributions. However, it is computationally expensive. For example, sampling the posterior of a general linear model has $O(n^3)$ computations. Variational methods offer a far cheaper alternative by turning it into an optimisation problem. The main aim is to find a distribution that minimises the Kullback-Leibler (KL) divergence between it and the exact posterior. Since it does not find the exact solution, it is not as accurate as the MCMC approach.

The inference scheme developed by Hensman et al. (2015) combines variational meth-

ods with MCMC by making an inducing point approximation. Inducing points methods (also known as sparse GPs) reduce effective data by selecting a small subset of a total number of samples (fracture index locations), thus reducing the size of the covariance matrix. The locations of the inducing points are defined with a K-mean clustering algorithm. The inducing points are defined by the K centroid locations. For 200 inducing points, we set $K = 200$.

We can rewrite the model as follows:

$$\Phi(p(Y_i = 1)) = x_i^T \beta + g(z_i) := f(x_i, z_i). \tag{5.10}$$

Since $x_i^T \beta + g(z_i)$ and $g(z_i)$ is Gaussian then $f(x_i, z_i)$ is a Gaussian process, $f \sim N(0, \widetilde{k})$ where the kernel is defined by

$$\widetilde{k}((x, z), (x', z')) = \sigma^2_{\text{fixed}} x^T x' + \sigma^2_{\text{random}} k_\lambda(z, z') \tag{5.11}$$

We will write $\mathbf{f} = ((f(x_1, z_1), ..., f(x_n, z_n))$, and the target of out algorithm will be to sample the posterior, which can be written as $p(\mathbf{f}, \theta | Y)$.

Variational methods introduce additional variables, known as variational parameters, to transform the problem into an equivalent minimisation problem. Define q^* as an approximation of the posterior that minimises the KL divergence to the true posterior in some family $\mathcal{Q}$:

$$q^*(\mathbf{f}, \theta) = \underset{q \in \mathcal{Q}}{\text{argmin}} KL(q(\mathbf{f}|\theta)||p(\mathbf{f}, \theta|Y)), \tag{5.12}$$

where the KL divergence is a similarity measure between distributions. To do this $\mathcal{Q}$ needs to be defined. This is done with the inducing point approximation (Titsias, 2009).

Let $\mathbf{u} = L\mathbf{f}$ for some linear operator $L \in \mathbb{R}^{m \times n}$ with $m \ll n$. We aim to approximate the joint posterior $p(\mathbf{f}, \mathbf{u}, \theta | Y)$. Since $\mathbf{u}$ is a function of $\mathbf{f}$ the joint posterior is the same as our target posterior. We also know a priori that $p(\mathbf{f}|\mathbf{u}, \theta)$ is normal. We define $\mathcal{Q}$ to be the family of distributions of the form $q(\mathbf{f}, \mathbf{u}, \theta) = q(\mathbf{u}, \theta)p(\mathbf{f}|\mathbf{u}, \theta)$. In the variational approximation, the marginal $q(\mathbf{u}, \theta)$ is unconstrained, but we restrict $\mathbf{f}|\mathbf{u}, \theta$ to have the prior conditional distribution.

It can be shown that solution the Variational Bayes problem is:

$$\log q^*(\mathbf{u}, \theta) = \mathbb{E}_{p(\mathbf{f}|\mathbf{u},\theta)}(\log p(\mathbf{Y}|\mathbf{f})) + \log p(\mathbf{u}|\theta) + \log p(\theta) - \log C \tag{5.13}$$

where C is an intractable constant that normalises the distribution and is independent of q. This variational approximation is sampled with MCMC. MCMC can be applied if we can calculate the log of the target distribution up to a constant. Therefore, if the right-hand side of equation 5.13 can be calculated, MCMC can be applied. The authors make a few observations to sample effectively. The first term in equation 5.13 is not known in closed form; however, it can be approximated effectively by Gaussian-Hermite quadrature. The distribution can be whitened, which is a transformation of a vector of random variables with a known covariance matrix to a new set of variables with the identity matrix as the covariance. The whitening transformation uses the reparameterisation $\mathbf{u} = \mathbf{R}\mathbf{v}$ such that $\mathbf{R}\mathbf{R}^T = \mathbf{K}_{uu}$,$v$ $N(0, \mathbf{I})$. Resulting in the optimal variational solution:

$$\log q^*(\mathbf{V}, \theta) = \mathbb{E}_{p(\mathbf{f}|\mathbf{u}=\mathbf{R}\mathbf{v})}(\log p(\mathbf{Y}|\mathbf{f})) + \log p(\mathbf{V}) + \log p(\theta) - \log C \tag{5.14}$$

this transformation changes the shape of the distribution to be more spherical. So far, we have not specified the MCMC algorithm that is used. The most common is a random walk

Metropolis algorithm that uses a two-step process: a proposal and a correction. The proposal is a stochastic perturbation from the initial value (MAP estimate in our case). A Maximum A Posteriori (MAP) estimation is closely linked to maximum likelihood estimation found in frequentist methods. It estimates the mode of the posterior distribution. The correction is the acceptance or rejection of the new sample based on its distance from the typical set (parameter values for which the log density is close to its expected value) of target distributions (Betancourt, 2017). This is an intuitive to understand and easy implement method; however, it is a "guess and check" approach that in high-dimensional spaces is not appropriate. The MCMC algorithm used is the Hamiltonian Monte Carlo (HMC) which is far more efficient than a standard random walk-Metropolis. HMC incorporates Hamiltonian dynamics in which the system is described by its total energy (combination of kinetic and potential energy), to make larger jumps to unseen regions of the typical set such that the adjacent samples are less correlated while maintaining a high probability of acceptance due to the energy conservation of the Hamiltonian dynamics. The Hamiltonian equation needs to be solved, and this is done using the leapfrog integrator (Betancourt, 2017). The only dependence on the number of samples n is a one time $O(n)$ computation. The reduction in computational cost allows models with large data to be solved in a fully Bayesian way. The implementation of this method is available via the GPFlow python package that utilises the Tensorflow Architecture (Matthews et al., 2017).

5.4.3 Convergence criteria

To test the convergence of the HMC chain, we implemented a potential scale reduction $\hat{R}$ to calculate the similarity between two independent chains. This is a ratio between the average variance of each chain to the average variance of the chains together. If the chain converges to a common distribution, then the ratio will be close to one. We follow standard practice by

concluding an approximate convergence if $\hat{R} \leq 1.2$. Comparing each of the inducing point coefficients would be too strict of a test. We limited it to the coefficients of the predictors and ten randomly selected inducing point coefficients. This leads to the number of burn-in steps and total samples being 5000 and 10,000 respectively for the high-resolution data and 7500 and 15000 for the low-resolution data.

5.5 Results

5.5.1 High resolution fracture data simulations

We trained the model with the high-resolution fracture index data, we will refer to this as the High-Resolution Model (HRM). We ran multiple simulations that sampled the hyperparameters, including lengthscale, from the posterior. From this, 0.1 is an appropriate value for the lengthscale. This value was used for the subsequent simulations that split the data into training and test sets described in section 3. A Maximum A Posteriori (MAP) estimation is used to estimates the initial values for the coefficients, which had a classification accuracy of 0.959 on the training set. The HMC is well mixed, and the hyperparameter values at the last HMC iteration for the fixed and random variance are 5.6, 16.4, respectively. The HMC was ran for sufficient iterations to ensure the sampler met the convergence criteria (Figure 5.2).

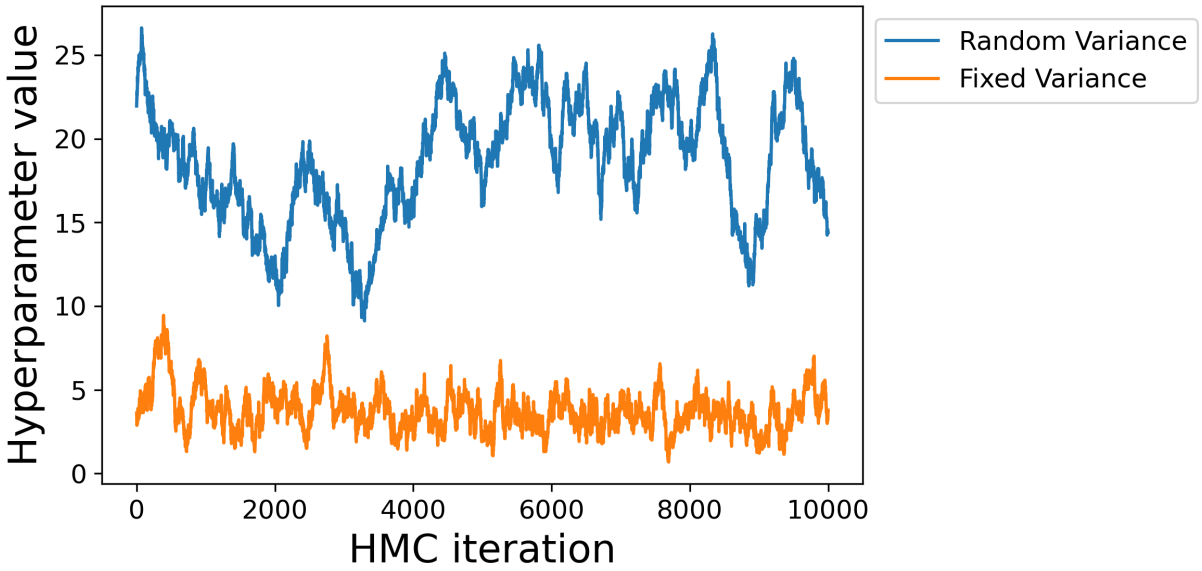


Figure 5.2: Evolution of the HRM hyperparameter ($\theta = (\sigma^2_{fixed} I, \sigma^2_{random} k_\lambda)$) values as a function of the Hamiltonian Monte Carlo (HMC) iterations - 10000 samples with 5000 burn-in steps

The posterior distributions for each of the predictor variables are set away from 0, suggesting that the correlation with an ice shelf fracture is statistically significant (Figure 5.3). The inclusion of random effects makes this a surprising result as the random effects assume that correlation could result from unknown latent variables. By noting which are set furthest from 0, the most robust predictors are modelled velocity, damage, principal and effective stress, and principal strain. Investigating posterior coefficients correlation shows there is little correlation between the posteriors, which affects the prior regularisation, unlike a non-penalised logistic regression where a strong negative correlation would be present.

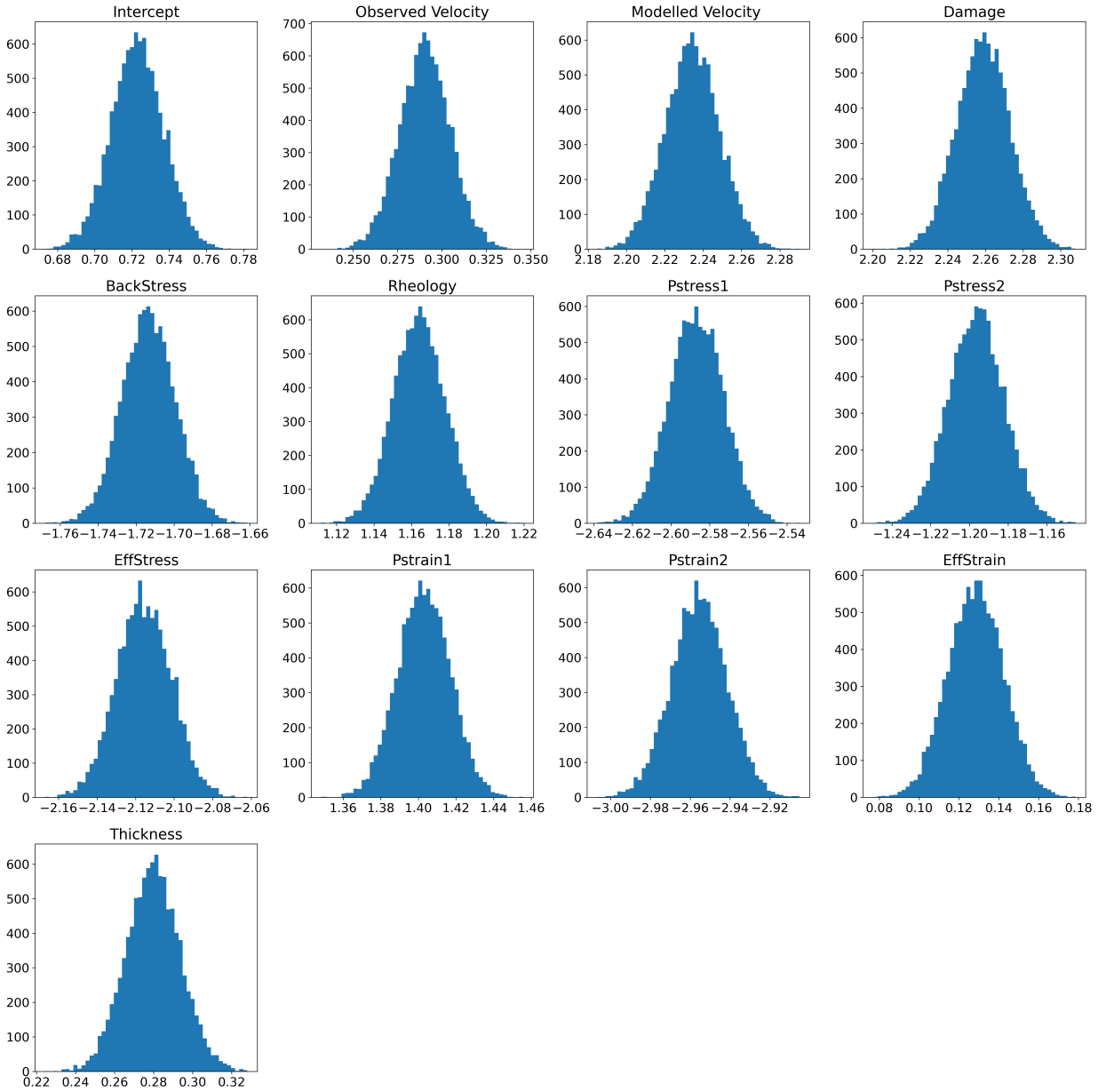


Figure 5.3: HRM Posterior distributions of the predictor coefficients after 10000 samples - y-axis is the number of samples, x-axis is the coefficient. All of the distributions are set away from 0 suggesting that the correlation to fractures are statistically significant.

The misclassification rate on the test set $20\% \pm 5\%$ on the ice shelf surface (grounded ice was not included). We can compare the modelled fracture probability for the three ice

shelf with what fractures have been observed.

The model predicts a high probability of fractures in the centre and at the calving front of the Larsen C ice shelf (Figure 5.4). Due to snow cover and lack of high-resolution imagery, the full degree to which the centre of the LCIS is fractured is not known. However, uniform high probability, while an indication of heavy fracturing is likely an overestimation. Observation agrees with our model that the calving front of the LCIS has experienced heavy fracturing. Including during the calving of iceberg A68. The input data has no non-fractured locations in these regions, which likely contributes to the lack of detailed predictions. Modelled fracture probabilities are the most detailed around the grounding line and surrounding inlet glaciers because most of the indexed points are in these regions. In the southeast of the ice shelf around the Hollick-Kenyon peninsula, large rifts can be seen in modelled fracture probability as lines of low probability where the ice has separated (Figure 5.5).

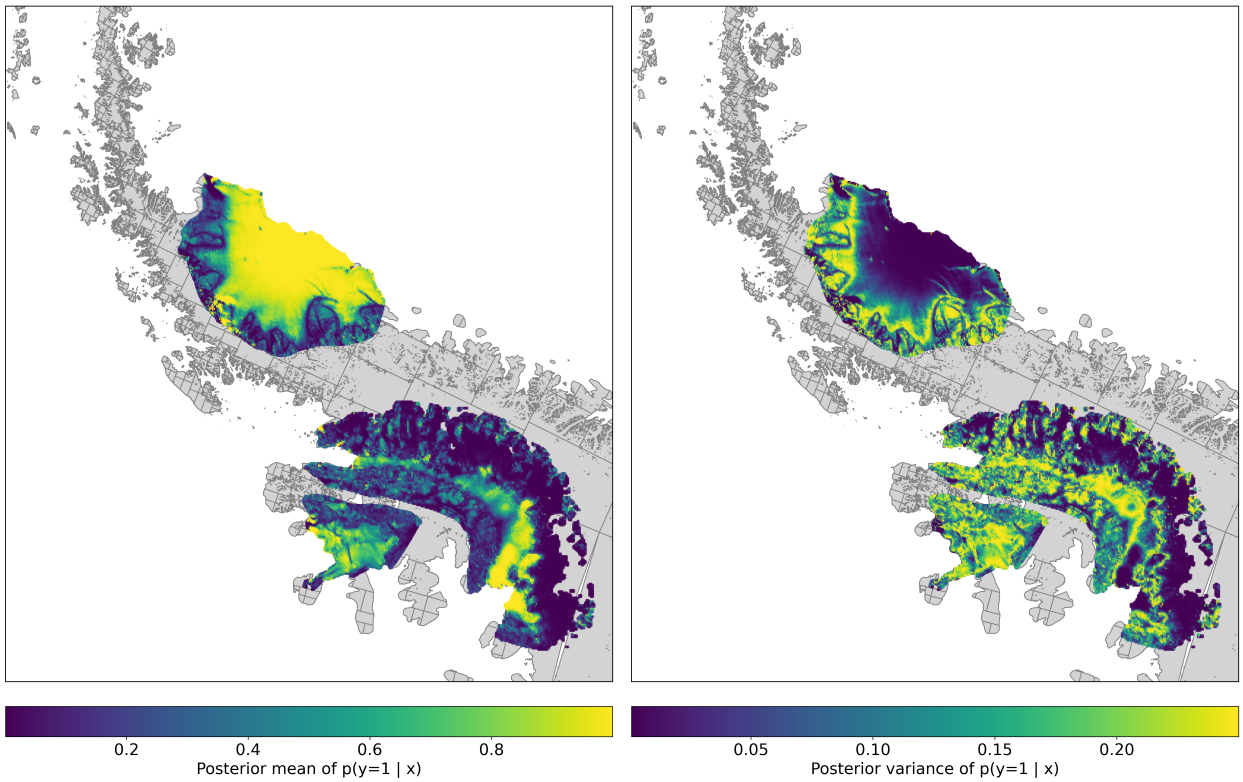


Figure 5.4: The fracture prediction of the high-resolution fracture index model $p(y = 1|x)$ as a function of the predictors x for the grid locations in the ISSM datasets. On the left is the predicted fracture probability (posterior mean) of the fixed and random effects. On the right is the posterior variance (Right) of the fixed and variance effects.

GVIIS is poorly indexed when using a strict condition for image resolution (Figure 5.1). At the centre of GVIIS (categorised as the entire region not directly near either ice front), the model predicts high fracture probability along the Palmer Land grounding line (Figure 5.4). Moving toward the Alexander Island grounding line, the probability decreases. At the northern front, we see it continue to predict fracturing at the Palmer Land grounding line, the high probability at the calving front, and this increased probability continues upstream of the front, agreeing with observations (Figure 5.6). The southern fronts and the surrounding region has a high fracture probability. However, the model predicts fractures on the left and right sections of the southern front and lower probability on the middle section

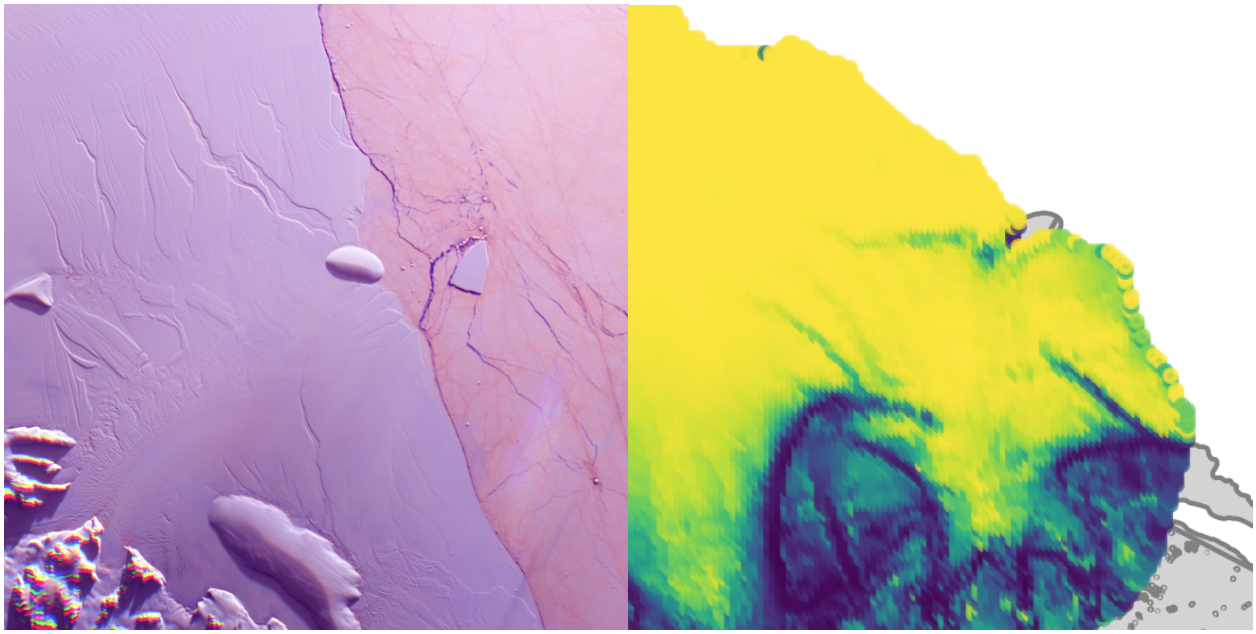


Figure 5.5: Comparison of fractures in the southeast section of the Larsen C between images acquired on August 22, 2016, with the Multi-angle Imaging SpectroRadiometer (MISR) taken from the NASA Earth Observatory images by Jesse Allen (Left) and HRM estimated fracture probability (Right). Rifts from the Gipps ice-rise and Hollick-Kenyon peninsula are visible in both.

of the front. Observations show that the middle section is highly fractured and has retreat the most. The Eklund Islands are a series of small islands the is in the centre of the southern front. Low probability predictions could be these islands.

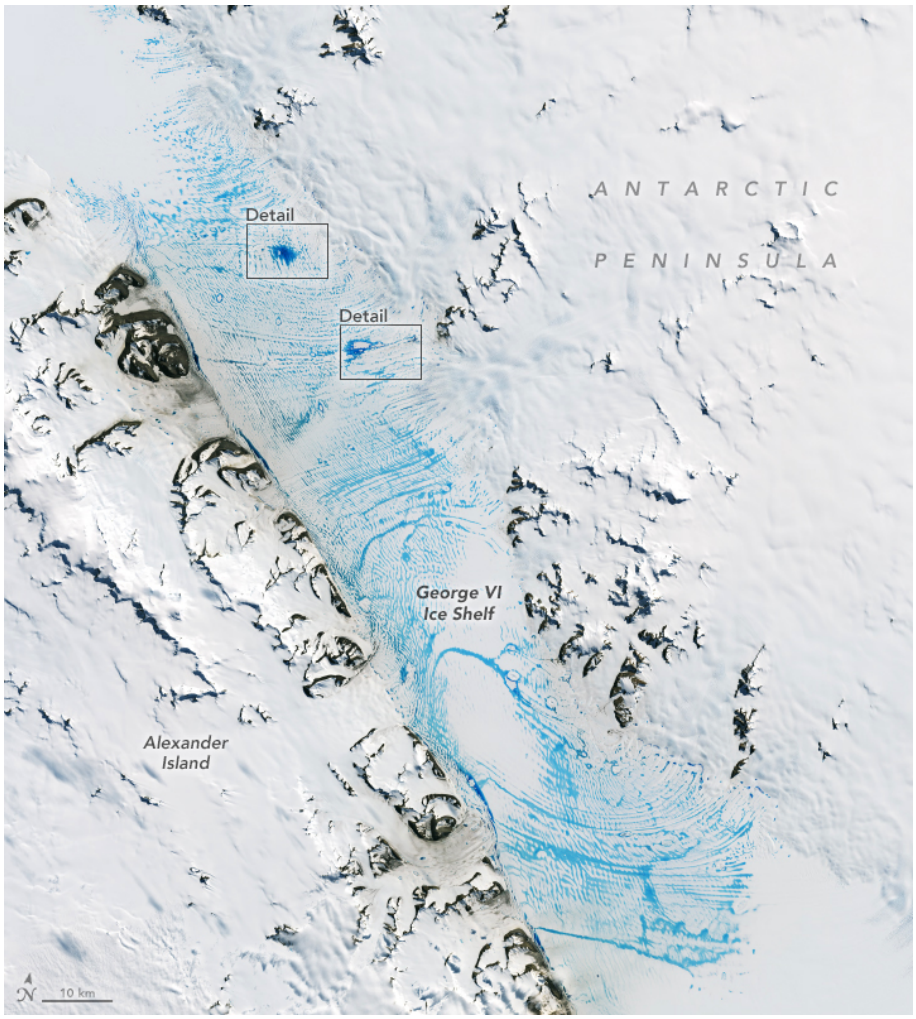


Figure 5.6: Landsat 8 image of the northern George VI ice shelf from January 19, 2020. Lateral fracture from Palmer Land are visible.

We applied the model to a pre-collapse map of the WIS to test its performance on the "bridge" attached at Charcot Island (Figure 5.4). The model predicted high fracture probability on either side of the bridge with a lower probability in the centre of the bridge, agreeing with observed fracture patterns at the time of collapse (Scambos et al., 2009)

(Figure 5.8). The section of the front north of the bridge was also predicted to have a high fracture probability; the centre was predicted to be somewhat fractured. The model predicts a rift parallel to the northern front (thin line of zero probability). From satellite images, it has been observed that the northern front retreated approximately to this rift following the bridge collapse.

Random effects allow variation between ice shelves to be incorporated rather than being ignored. If the random effect is non-zero, that indicates that the fixed effects do not fully describe the data, and some ice shelf specific variation occurs. Away from the inducing points and the kernel, influence the posterior variance of the random effects increases (Figure 5.7). As mentioned, lengthscale is a similarity measurement between adjacent points. As the lengthscale of 0.1 is small, the influence is limited to close fractures (Figure 5.7).

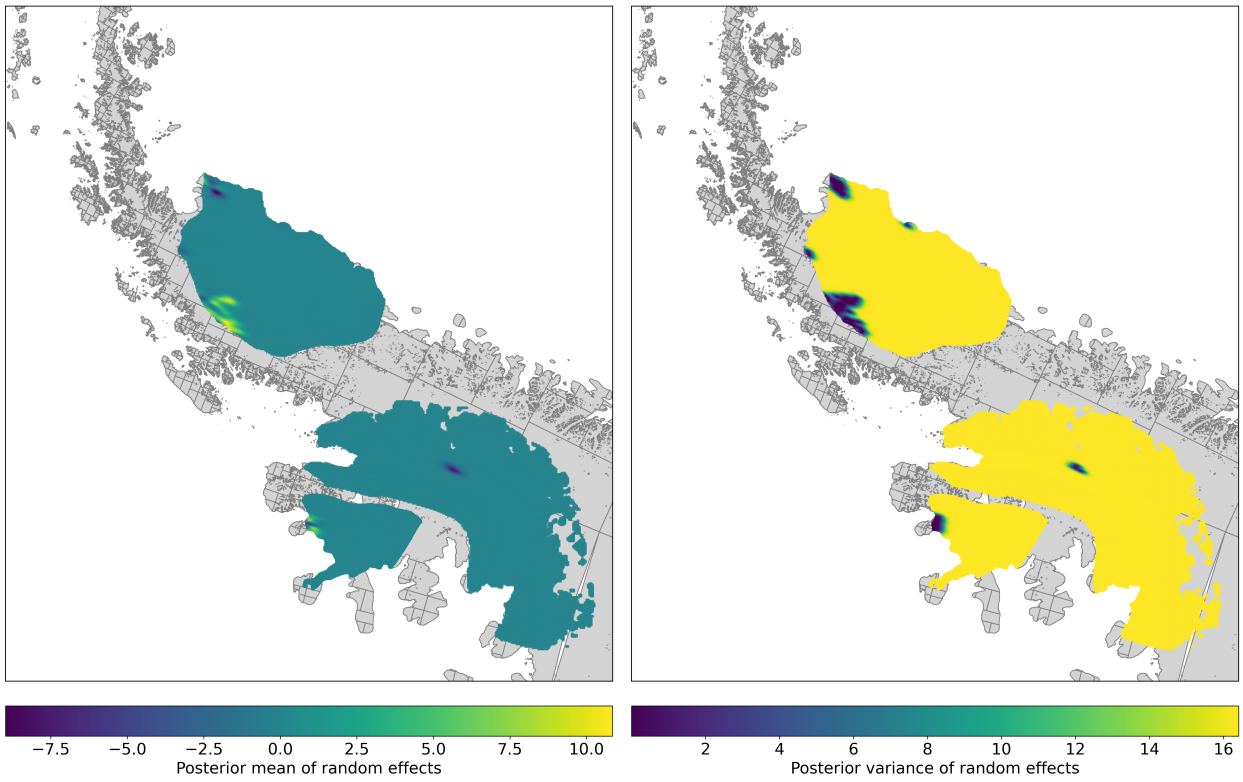


Figure 5.7: On the left is the posterior mean of the random effects for the high-resolution fracture index model $p(y = 1|x)$. The posterior variance of the random effects for the high-resolution fracture index model $p(y = 1|x)$ is on the right. The sections where random effects are non-zero influence the fixed effects, hence influencing the fracture probability.

5.5.2 Low resolution

We trained the model with the low-resolution fracture index data, we will refer to this as the Low-Resolution Model (LRM). After multiple simulations in which we trained the model on the whole low-resolution fracture dataset, an appropriate value for the lengthscale was determined to be 0.5. For the remainder of the simulations, we withheld 50% of the fracture dataset split randomly. Due to limitations of the GPflow framework, the number of inducing points used was limited to only 100 when training the model on the complete fracture dataset.

H

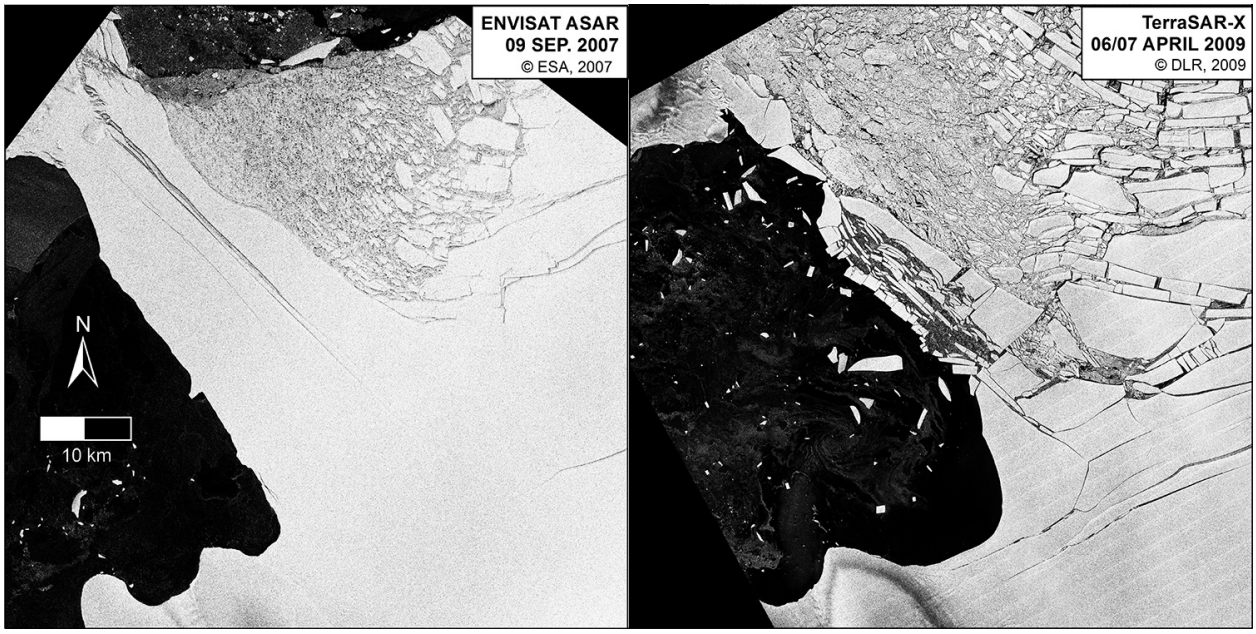


Figure 5.8: WIS ice bridge before collapse in 2007 (left) and after collapse in 2009 (right), both images are from ESA ENVISAT.

We were able to increase this to 150 when training the model on the training set only. We predict that the model would better fit the data if the number of inducing points were increased.

A MAP model estimates the initial values for the hyperparameters. For the LRM the classification rate on the training set was 0.8226. After running the HMC the hyperparameter values are 0.614 and 8.1 for the fixed and random variance, respectively (Figure 5.9). To satisfy the convergence criteria, HMC ran for 15000 iterations with a burn-in of 5000. The distributions indicate that all predictors excluding ice thickness are statistically significant as they are all set away from 0. The most important predictors are effective and principal, stress and strain (Figure 5.10). However, while many of the predictors are statistically significant, few are set that far from 0; after running multiple simulations, the test data miss-classification rate is $20\% \pm 8\%$.

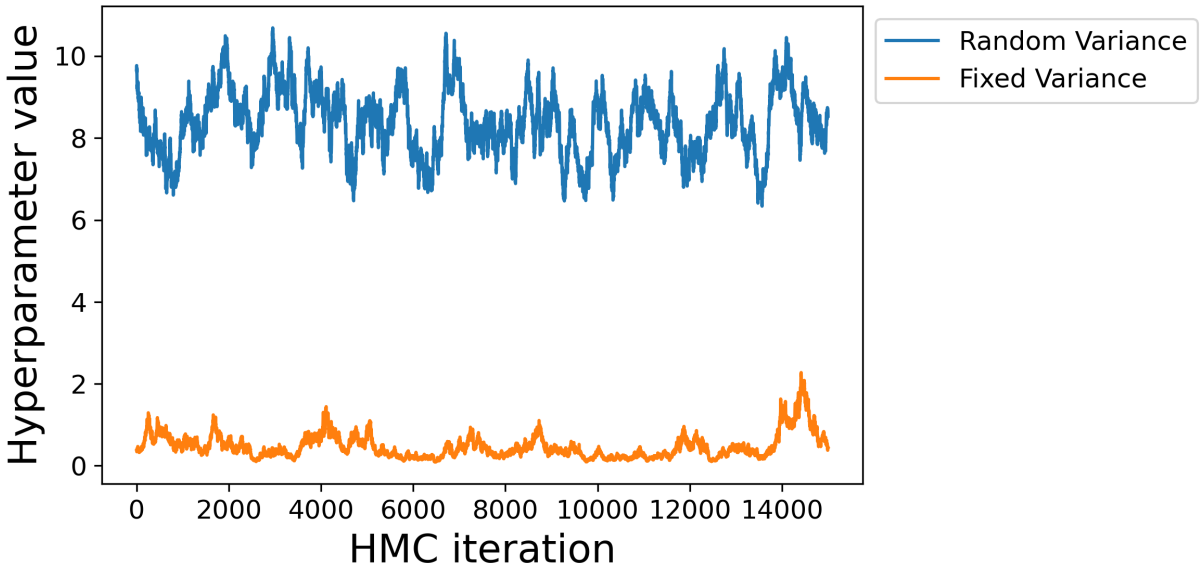


Figure 5.9: Evolution of the LRM hyperparameter ($\theta = (\sigma^2_{fixed} I, \sigma^2_{random} k_\lambda)$) values as a function of the Hamiltonian Monte Carlo (HMC) iterations.

Predictions for the fracture probability for the northern calving front of the LCIS are high, agreeing with observations about that region. Fracture probability is high along the grounding line as expected (Figure 5.11). The centre and southern regions have large areas of overestimation and underestimation, likely due to errors in the fracture indexing.

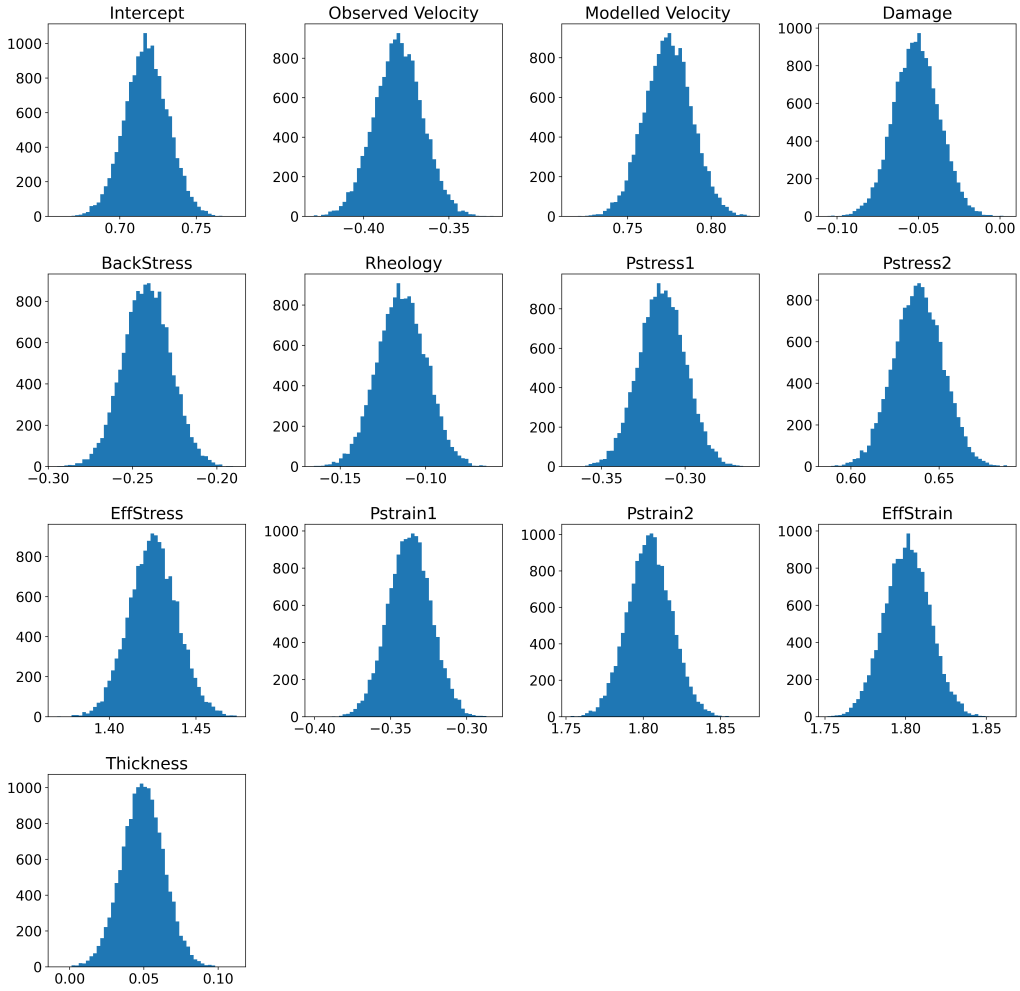


Figure 5.10: LRM Posterior distributions of the predictor coefficients after 10000 samples - y-axis is the number of samples, x-axis is the coefficient. All of the distributions are set away from 0 suggesting that the correlation to fractures are statistically significant.

The prediction for the northern half of the GVIIS did capture the fracturing around the grounding line at Palmer Land. However, it did not perform well at the northern calving

front (Figure 5.11). Fracture probability was near zero at the front, continuing away from the grounding line across the entire northern half of the ice shelf. The model continued to perform well at the Palmer Land grounding line; however, it underestimated fracture elsewhere. The southern front does have a higher probability in the middle section, which agrees with observations.

5.5.3 Lengthscale

The lengthscale λ, impacts the influence of the kernel function. The RBF kernel, defined in equation 5.8, is a similarity measurement of the coordinates z_i that determines the correlation between points. To show this, consider points z and $z^{'}$ that are λ apart. From equation 5.8 this gives $exp(\frac{-\lambda^2}{2\lambda^2}) = exp(-\frac{1}{2}) \approx 0.61$, highly correlated. If z and $z^{'}$ are 2λ apart, $exp(-2) \approx 0.14$, slightly correlated. If z and $z^{'}$ are 4λ apart, $exp(-8) \approx 0.0003$, basically independent. Hence, the lengthscale determines the distance that points are correlated. If λ is large, points within a large area will be correlated. As we assign the prior of the random effect to be a Gaussian process (Equation 5.7), λ determines the influence of the random effects. To highlight this, we train four models on the high-resolution fracture index data with the lengthscales 0.1, 0.25, 0.5 and 1. The estimated fracture probability and random effects give insight into the impact of the lengthscale.

Figure 5.13 has the random effects from the four models. As we increase the lengthscale, the distance the influence of the random effects increase. In Figure 5.13 (bottom right) $\lambda = 0.1$ (as in the HRM) the random effects only have a small influence. As λ increases, we see that radius of the random effect increase also, In Figure 5.13 (top left), where $\lambda = 1$, the random effects have a strong influence. This greatly impacts fracture probability (Figure 5.14). If we compare with the $\lambda = 0.1$ model, when $\lambda = 1$ the estimated probability for each ice shelf is smoother, there are fewer transitions between high and low probability.

Smoothing is a characteristic of changing of increasing the lengthscale in the RBF kernel. If we make λ too large, the predictions will miss so much detail that the model is not useful (arguably as in the $\lambda = 1$ model); however, if λ is too small, noise will be introduced into the model hiding and important patterns in the data.

5.6 Discussion

While both models performed well, the high-resolution model (HRM) performed better than the low-resolution model (LRM) in the training sets MAP model estimation and had a lower misclassification rate uncertainty on the test set partly explained by the posterior distribution of the predictor variables. Most predictors are statistically significant in both models; however, none of the predictors was set far from zero for the LRM. Comparing the posterior means of the random effects, we can see that the HRM had less influence from random effects suggesting that the fixed effects did a better job predicting the data than the LRM unsurprisingly, as the high error level is present in the LR fracture dataset.

While there is evidence of surface fractures in the centre of the LCIS, suture zones play a vital role in the stability of the LCIS. Suture zones appear smooth due to the lack of heavy fracturing observed in other regions (McGrath et al., 2014). However, the heterogeneity that defines them likely takes the form of many more minor fractures. Easily covered by surface accumulation. Even though they have different fracture profiles, our models do not distinguish between suture zones and meteoric inflows. A lack of the correct predictors and detailed indexing plays a role; however, our model does not attempt to determine fracture depth or size; only the probability of a fracture is present.

Holt is the most comprehensive index of GVIIS surface structure. That study found that the grounding line of Palmer Land is littered with crevasse zones (in the context of

this study are heavily fractured regions). Inlet glaciers flow from both Alexander Island and Palmer Land; however, the glaciers from Alexander Island are much smaller. Compressive forces from Palmer Land glaciers act on Alexander Land limiting to fractures around the Alexander Island grounding line. The majority of the ice in the GVIIS comes from Palmer Land. Both our model results fit well with these observations. Higher fracture probability was predicted along the Palmer Island grounding line. The HRM better predicted the fracturing patterns of the northern front of GVIIS. The LRM predicted low fracture probability for this region even though it experienced significant fracture and calving. Observation by Holt and Glasser (2022) found a strong link between declining sea ice concentrations and calving at the northern front of GVIIS, warm water travels to the ice front through sub surface channels and melts sea ice and thins the front. Furthermore, this process may lead to fractures at the ice front, suggesting that the underestimation in this region is due to the absence of sea ice concentration and movement of warm water toward the ice front. However, the LRM better predicted the observed fracture pattern of the southern front. The south front of the GVIIS has three smaller fronts separated by ice rises. The observations have shown that the middle front is the most fractured and has seen the most retreat, which matches the prediction from the LRM. The HRM overestimates the fracturing of the left and right fronts and underestimates the middle front.

Manual fracture/non-fracture indexing has limitations. One practical issue is that it is impossible to keep space between points consistent, which could lead to errors in the model's training. The absence of high-resolution images in key ice shelves regions is the most significant limitation of fracture models based on historic fracture indexing. This study has investigated an alternative method by the inclusion of lower resolution data with mixed results. Future work could compromise and employ relaxed indexing criteria for image resolution while only indexing what is visible in the images.

This study intends not to replace the damage modelling approach but rather be used

in conjunction with it. In our HRM, the damage is a strong predictor (Figure 5.3). The motivation for calculating damage is not to predict all surface fractures. Damage is a measure of elevated strain rate due to a fracture or region of fractures. Not all fractures have this effect on strain rate. We believe a joint statistical-physical approach will be the most successful.

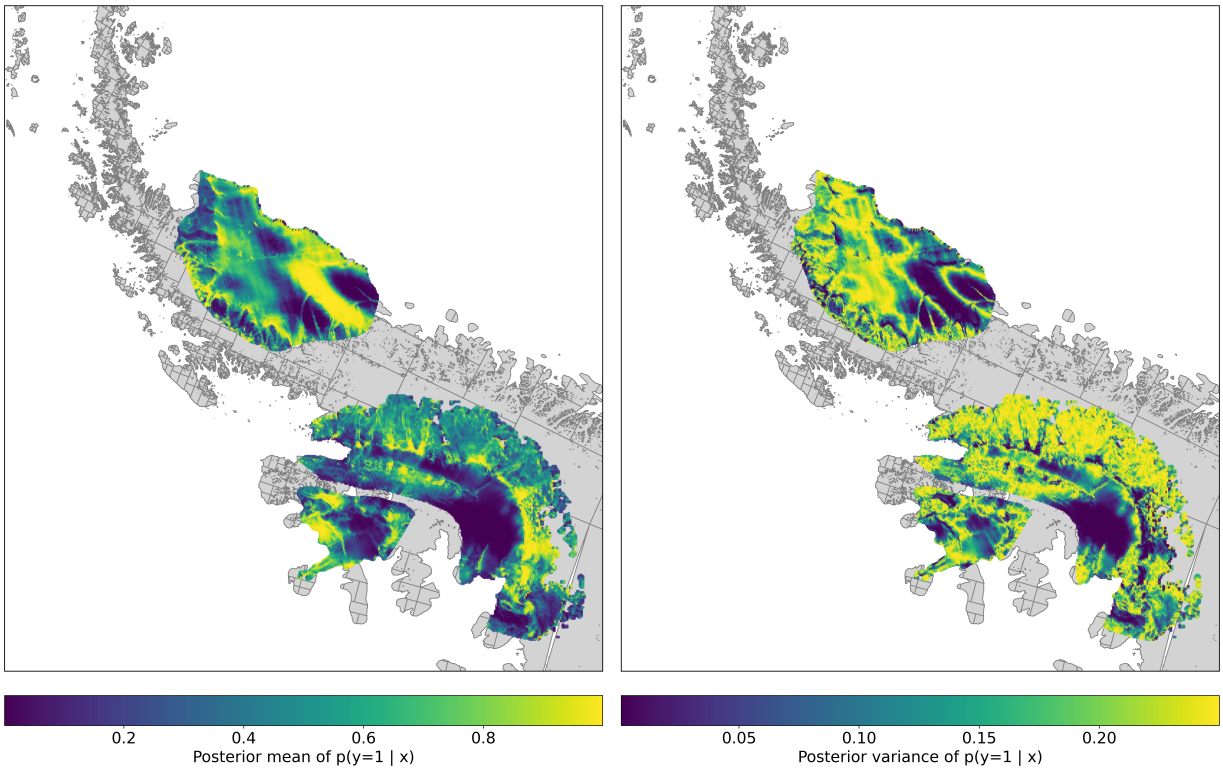


Figure 5.11: The predictions of the high-resolution fracture index model $p(y = 1|x)$ as a function of the predictors x for the grid locations in the ISSM datasets. On the left is the predicted fracture probability (posterior mean) of the fixed and random effects. On the right is the posterior variance (Right) of the fixed and variance effects.

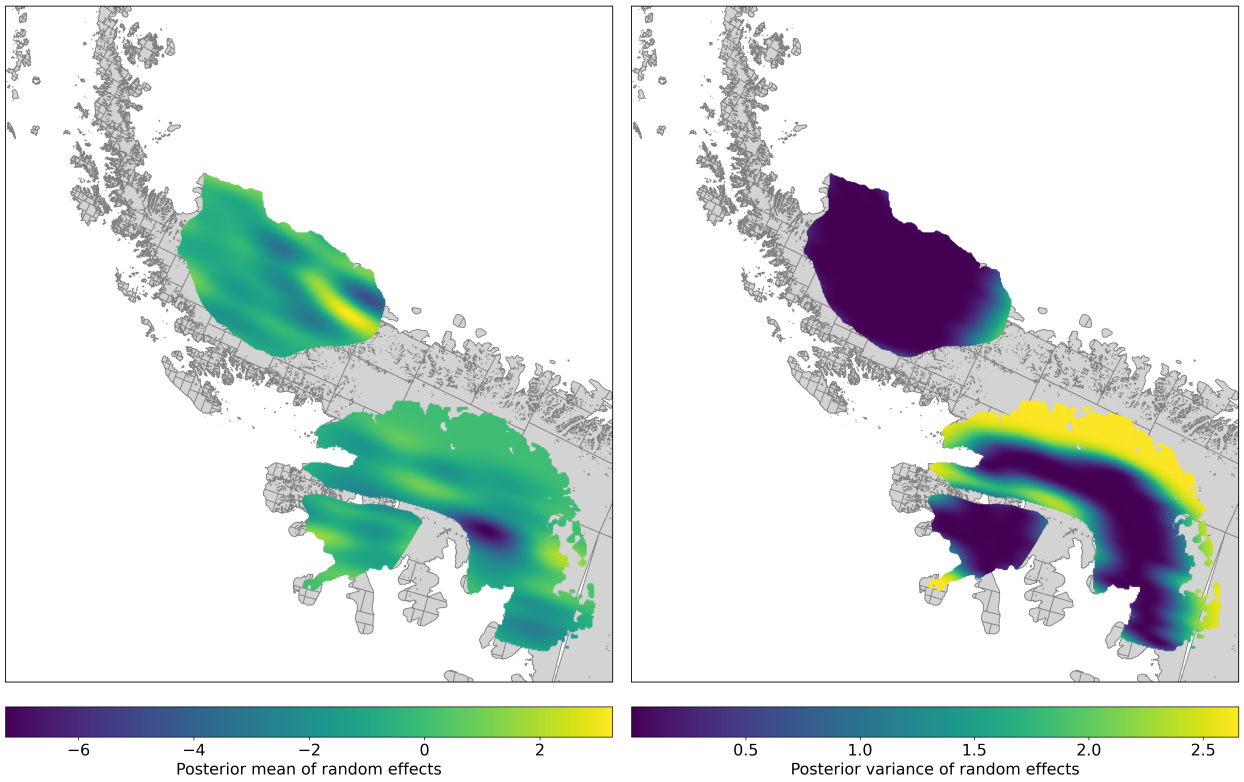


Figure 5.12: On the left is the posterior mean of the random effects for the low-resolution fracture index model $p(y = 1|x)$. The posterior variance of the random effects for the high-resolution fracture index model $p(y = 1|x)$ is on the right. The sections where random effects are non-zero influence the fixed effects, hence influencing the fracture probability.

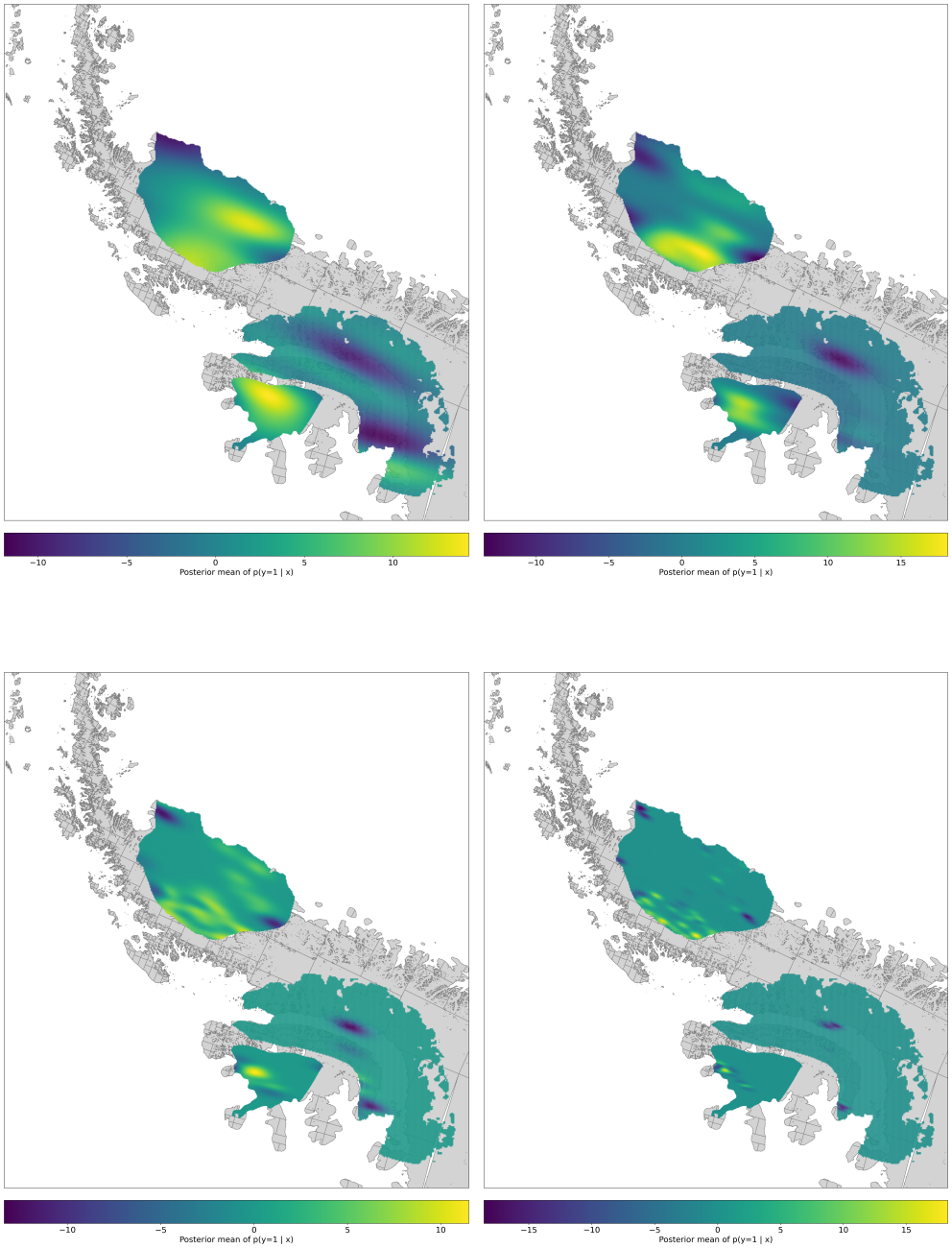


Figure 5.13: Estimate of the random effects of 4 models with different lengthscales (λ) $\lambda = 1$ (top left), $\lambda = 0.5$ (top right), $\lambda = 0.25$ (bottom left), $\lambda = 0.1$ (bottom right). As the lengthscale increases the random effects have more influence.

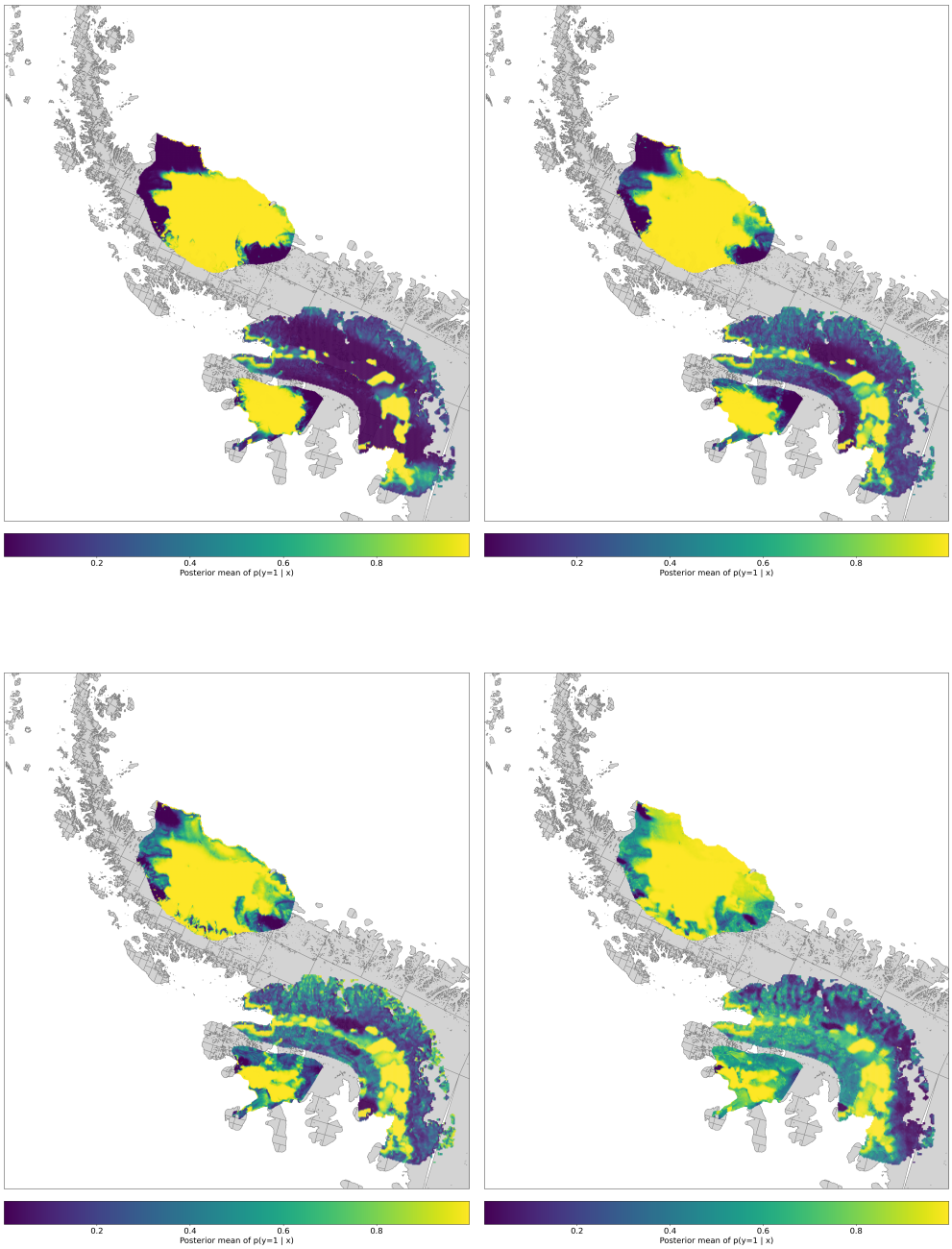


Figure 5.14: Estimated fracture probability (posterior mean) of 4 models with different lengthscales. All models use the high-resolution dataset. λ - λ = 1 (top left), λ = 0.5 (top right),λ = 0.25 (bottom left),λ = 0.1 (bottom right). As the lengthscale increase the estimated probability becomes smoother.

5.7 Conclusions

In this paper, we present a mixed effect Gaussian process fracture model sampled via modern statistical techniques that allow the application of MCMC to large data. This is a mathematically rigorous approach to using statistical methods to predict ice shelf surface fractures. The use of random effects enables us to run simulations with ice shelves with different geometries and flow mechanics. Crucial if a statistical-physical combined approach is to be implemented into full ice sheet models. In both the LRM and HRM, the model performed well on unseen data. Overall, HRM performed better on unseen data and matched observations closer in key areas. However, overestimation is high in some regions, particularly the centre of the LCIS and suture zones that are known to have different fracture patterns are not visible (Borstad et al., 2017). We believe there are two main contributors to poor results in some regions. Firstly, the high-resolution fracture index dataset is sparse and is poorly spatially distributed. This caused some regions to be poorly described by the data and limited the influence random effects can have. Secondly, the choice of predictors may not describe the data that well. (King et al., 2018) shows the potential for ground-penetrating radar-analysis to study the internal structure of the Brunt Ice shelf; this method would greatly improve the fracture indexing process. We chose to use flow parameters for our predictor variables that all play a role in fracture formation; however, other glaciological and climate variables could likely improve the model.

Future work will explore estimating future probability from transient physical models over the next 100-years under potential forcing scenarios. Fracture indexing remains the biggest hurdle for this type of classification model. We suggest that until a better indexing method is developed, high-resolution images are used as they better fit observed fractures in key areas.

Chapter Six

Damage evolution and future fracture probability for Antarctic Peninsula ice shelves.

6.1 Aims

The primary aim of this chapter is to predict AP ice shelf fracture probability under various future RCP scenarios. To do this the following aims are set:

- Using suitable SMB and BMR projection, force 100 year ISSM simulations that represent the RCP2.6, 4.5, 8.5 greenhouse gas pathways.
- Apply the model framework to the projections to predict AP ice shelf fracture probability.

These will address the final research gap set out in Chapter 1. This will be done by utilising the mixed-effects Gaussian Process model presented in Chapter 5. This model

utilises random effects to deal with dependant adjacent fractures, allowing the model to predict multiple ice shelves in one model. In order to sample the posterior distribution efficiently, we incorporate a Hybrid Monte-Carlo sampling scheme developed by (Hensman et al., 2015). To do this, we first use the Ice Sheet System Model (ISSM) to calculate flow parameters for a current and transient simulation, including a damage evolution module. The transient simulation is forced by varying the surface mass balance and basal melt rate to generate a set of predictors under four possible climate scenarios. Using SMB and BMR projections, we can force the model to represent the RCP2.6, 4.5, and 8.5 greenhouse gas pathways. We also run an unforced transient model such that SMB and BMR remain unchanged. These results act as predictors to model fracture probabilities and estimate potential ice shelf evolution over the next 100 years. We discuss this in detail in section 2. We train the statistical fracture model with a fracture datset as the response variable produced by manually selecting fractured and non-fractured locations from high-resolution images from Google Earth Pro and a non-transient ISSM simulation as the predictors, similar to the previous chapter. Section 3 will cover the statistical model and how we sample the posterior in detail. Using the trained model, we can estimate fracture probabilities for each RCP scenario.

6.2 Background

Over the last century, the AP has warmed by approximately 4° C, which exceeds the air temperature warming of both the global mean and the rest of AIS (Vaughan et al., 2003). Over the 21st century, warming has slowed to a level consistent with natural variability due to frequent cold winds and the advection of sea ice in the Weddell Sea (Turner et al., 2016). Warming of this magnitude has far-reaching implications that can be observed in reducing seasonal sea ice, an increase in melt days, and rising precipitation. The key to future AP ice

shelf stability is the global climate emissions over the next century. According to the IPCC Sixth Assessment Report, if emissions continue to rise as they have over the last century, the best estimate of global temperature increase by 2100 is 4.4° C past pre-industrial levels (IPCC, 2021). This warming would further exacerbate the adverse effects we have seen and cause southern migration for the thermal limit for ice shelf viability (Morris and Vaughan, 2013). AP ice shelves will be at risk of collapse and potentially destabilising the whole region. The signing of the 2015 Paris Agreement has laid out the goal of limiting temperature rise to 2° C over the next 100 years, the 2021 Glasgow Climate Pact has lowered the aim to 1.5° C. Meeting the target could avoid much of the potentially irreversible damage caused by ice shelf collapse (DeConto and Pollard, 2016; Rintoul et al., 2018). However, it is likely that even under the best scenario, further retreat is inevitable.

Changes in surface and basal conditions of the AP ice shelves play an essential role in the significant retreat events of the AP's largest ice shelves. The primary mechanism for instability is thought to be fracture propagation due to hydrofracture (Lai et al., 2020; Robel and Banwell, 2019). The firn layer which, acts as a buffer to surface meltwater, becomes saturated when excess meltwater is present. The excess water collects in preexisting crevasses. The resulting hydrostatic pressure causes the propagation of crevasses, potentially destabilising the ice shelf. Underneath the ice shelf, basal melt induced by the circulation of warm water within the ice shelf cavity is further destabilising the ice shelf through thinning and basal crevasses that are also able to propagate similarly from high water pressure (Veen, 1998). Increased volume of crevasses and rifts inevitably lead to increased calving (Albrecht and Levermann, 2014; Krug et al., 2014; Scambos et al., 2009). Calving and basal melt are the primary mechanisms of ice shelf mass loss (Depoorter et al., 2013). The area lost through calving leads to instability and a reduction in buttressing of tributary glaciers. Continued retreat of the calving front can lead to the collapse of the compressive arch, an essential protective mechanism that all ice shelves feature. The arch traverses the entire width of an

ice shelf. If calving breaks the compressive arch, a significant retreat will occur until the ice shelf reaches a new stable front (Holland et al., 2015). Couple the increase in fracture with the elevated risk of ocean swell as a result of decrease protection from sea-ice, ice shelves can transition from seemly stable to significant retreat with little warning (Massom et al., 2018).

6.3 Data and Climate Scenarios

6.3.1 Basal melting and surface mass balance

Basal melt is the largest ice shelf ablation source across Antarctica. The degree of melt under each ice shelf varies due to local ocean temperature and shelf thickness (Depoorter et al., 2013). Deep grounding lines are more at risk of basal melt, and grounding line melt has a more significant impact on ice shelf and glacier dynamics (Rignot et al., 2004). The ice shelves that calve into the Amundsen and Bellingshausen Sea on the West Antarctic ice sheet and AP have the highest melt rates of the whole AIS (Rignot et al., 2013). Oceanic heat transport from an enhanced inflow of circumpolar deep water that is above 0° C contributed to the increase in basal melt under the Bellingshausen sea ice shelves (Schmidtko et al., 2014; Meredith and King, 2005). Since the early 1990s, glaciers that drain from western AP sped up by 13% with the worst affected being those that grounded more than 300 m below sea level (Hogg et al., 2017). Increased wind strength contributes to the mixing of circumpolar deep water with water on the continental shelf normally colder (−1.8° C) (Dinniman et al., 2012). Conversely, the Ross and Ronne ice shelves contribute little to the overall melt considering their massive size due to the cold water circulating within their cavities (Pritchard et al., 2012).

The resulting thinning from high basal melt rates results in instability and is a precondition for retreat (Vieli et al., 2007). The thinning and acceleration of fast-flowing tributary glaciers coincides with thinning in the corresponding ice shelf via a reduction in buttressing (Reese et al., 2018). Basal melt rate plays a crucial role in surface lowering of the AP ice shelves, notably the George VI Ice Shelf (GVIIS) and Wilkins Ice Shelf (WIS) on the Bellingshausen coast (Adusumilli et al., 2018). Firn processes rather than basal melt were thought to be the primary driver of lowering on the LCIS (Pritchard et al., 2012); however, more recent studies have found that they could both play an important role (Holland et al., 2015). Adusumilli et al. (2018) found that under the LCIS, the basal melt is concentrated around the Bawden Ice Rise, a major pinning point that stabilises the LCIS.

Surface Mass Balance is the difference between the processes of accumulation and ablation on the surface of a glacier. It plays an essential role in the overall mass balance and ice dynamics. Long term trends show an increase in melt days across all ice shelves (Barrand et al., 2013). The mass-loss rate of the AIS increased each decade between 1979 and 2017 by 280%. Of the total ice loss, 17% came from the AP, a large proportion given its small size (Rignot et al., 2019). Ice dynamics is the most significant contributor to ice loss. SMB anomalies were positive between 1979 and the 1990s before becoming negative from then on (Rignot et al., 2019). As warming continues, the average precipitation rate for multiple CMIP5 models is projected to increase by approximately 7.4% per 1° C (Palerme et al., 2016). The increase in precipitation could help mitigate the mass loss from addition ablation due to melt in a scenario of moderate temperature increases, particularly on grounded ice where run-off is not expected to increase to compensate (Kittel et al., 2021). However, for floating ice, the run-off associated with higher temperatures would cause a decrease in SMB. Therefore, for ice shelves to reach a similar stable SMB as they have now, the trajectory of temperature increase under current anthropologic forcing would need to be decreased, as outlined in the Paris Agreement, to keep within this moderate range. If increased melting

can continue, the decrease in negative SMB will lead to irreversible ice shelf instability (Kittel et al., 2021). Warming of 4° C would lead to 67% on AP ice shelves becoming vulnerable to collapse (Gilbert and Kittel, 2021).

6.3.2 Fracture index data from satellite images

Our study area includes the LCIS, WIS, and GVIIS. These are the largest of the AP and most important for the stability of the region. Indexing fractured, and non-fractured location is an expensive and challenging task. There is no way of automating the process available; therefore, it must be done manually. Satellite images of a suitable resolution are sparse over the ice shelf surface. Non-fractured locations are particularly difficult as the only way to ensure that fractures are not covered by fresh snow is to locate blue ice areas. These are few and far between and limited near the grounding line. Further uncertainty arises through the process of manual classification. It is impossible to space out points consistently. The fracture index method is similar to the method used by Emetc et al. (2018). Google Earth Pro images are used to detect fractures from high-resolution images (10 m) manually. Emetc et al. (2018) made the fracture location data they produced available. We have updated this datset for this study by using new satellite imagery available through Google Earth Pro. The result is a sparse datset with a cluster of fractured and non-fractured points. GVIIS is very poorly indexed due to a lack of high-resolution images that are not snow-covered (Figure 6.1). In the previous chapter, we investigated using much looser criteria from image selection in which we used the best available image. This resulted in a far more extensive but less reliable datset. The high-resolution model performed slightly better on unseen data. When we compared the fracture probability from each model with satellite images, the higher resolution datset better matched known fracture locations. We concluded that using higher resolution sparse data is preferable.

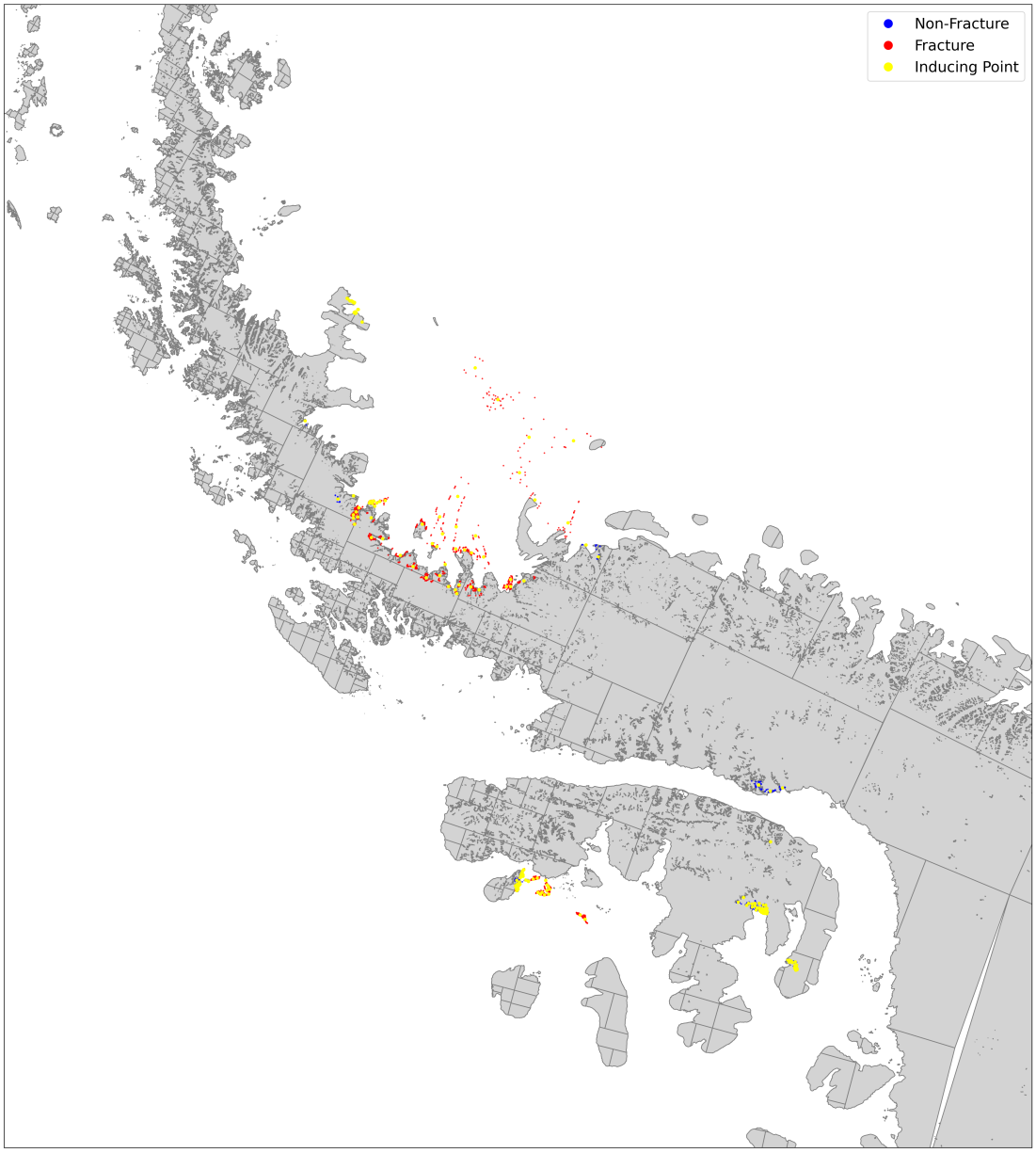


Figure 6.1: AP map with observed fracture locations (red points), observed non-fracture locations, and inducing point locations on the LCIS, GVIIS, and WIS ice shelves. Inducing points reduce the effective size of the data to reduce the computational expense of sampling the posterior. The inducing point locations are calculated using a K-means cluster algorithm with 200 centroids, giving 200 inducing points.

6.3.3 ISSM setup

ISSM is an open-source model developed by the University of California at Irvine and the Jet Propulsion Laboratory to model the evolution of the ice sheets (Larour et al., 2012). It is capable of solving stress balance equations in both 2D and 3D (full stokes), utilises finite element modelling, and anisotropic mesh refinement that can use unstructured meshes to more accurately model areas with more complex dynamics while saving computational resources on other areas, and inverse methods to infer unknown parameters. SSA was more appropriate than the full stokes model for floating ice and allowed the damage calculation, which is incompatible with the full stokes model. We ran simulations for the LCIS, GVIIS, and WIS that solved stress balance equations to calculate the flow parameters that acts as the predictors needed to train the statistical model. Cost functions for inversion were tuned manually such that modelled velocity was a good match with observed velocity.

The setup used for our simulations are as follows: Basal melt is taken from Adusumilli et al. (2018). Bed topography is taken from BedMachine (Morlighem et al., 2020). SeaRISE is used for climate forcing, including air temperature, surface mass balance, upward geothermal heat flux, and the calculation of ice thickness (Bindschadler et al., 2013). Surface temperature is used as the steady-state depth-averaged ice temperature over each of the ice shelves. Ice front boundary is assigned a Neumann boundary condition. The rest of the lateral boundary is assigned a Dirichlet boundary (observed velocity). The upper surface is stress-free. Grounding line position is determined using a flotation criteria. Friction is applied between the ice and bedrock. Floating ice has no friction. Velocity observations are taken from (Rignot et al., 2011a).

6.3.4 Predictors

We calculate the flow parameters that act as predictors for all ISSM simulations. For a brief overview, see Table 6.1. The predictors used are a subset of the predictors from chapter 5. For completeness, in this subsection, we give details on how the predictors for the statistical model are calculated and their relationship to fracture formation. These same predictors are calculated for future climate simulations.

Damage

Damage is a state variable that represents changes in materials rheological properties due to degradation. When modelling ice as a purely viscous material, this translates to increases in strain rate due to ice fracture. It does not predict fractures themselves or fractured regions that do not affect strain rate. Damage is calculated as in Borstad et al. (2013) in which a partition of inverse method solution is implemented to calculate separate and independent solutions for damage. These calculations rely on the inverse solution to ice rigidity (B) and an initial ice rigid estimation. These results become boundary conditions for the transient simulation.

The damage calculation can be made as follows:

$$D = 1 - B_1/B_T \tag{6.1}$$

where B_1 is the inversion of rigidity, B_T is initial rigidity $D \in [0, 1]$. The main uncertainty of the calculation is from the estimation of B_T, due to the often unknown ice temperature that is difficult to measure accurately. Backstress can also be calculated using inverse methods, as in chapter 5. However, as it cannot be calculated in the transient

simulations, we leave it out.

Principal and effective stress

This study opts for a shallow shelf approximation model; therefore, transverse and longitudinal stress is neglected. Velocity observations are used to calculate the principal and effective stresses. Stress is a significant predictor to include in the model as increased stress is the direct course of fracture formation. As ice is subjected to increased stress, it becomes brittle as it moves from an elastic state to a ductile one (Jaeger, 2009).

Principal stresses are the maximum and minimum values of the normal stresses when the plane is orientated so that the shear stresses are 0. The sign of the principal stresses determines whether the stress being applied is compressive or tensile.

Given that the deviatoric stress $\sigma^{'}$ is given by:

$$\sigma^{'} = \begin{bmatrix} \sigma^{'}_{xx} & \sigma^{'}_{xy} & 0 \\ \sigma^{'}_{xy} & \sigma^{'}_{yy} & 0 \\ 0 & 0 & -\sigma^{'}_{xx} - \sigma^{'}_{xy} \end{bmatrix} \tag{6.2}$$

The effective stress $\sigma^{'}_{e}$ can be calculated as follows:

$$\sigma^{'}_{e} = \sqrt{\sigma^{'2}_{xx} + \sigma^{'2}_{yy} + \sigma^{'2}_{xy} + \sigma^{'}_{xx}\sigma^{'}_{yy}} \tag{6.3}$$

Principal and effective strain rate

Strain rate plays a crucial role in new fracture formation. Glacier ice has a critical strain rate threshold that, once reached, will result in crevasse formation (Vaughan, 1993). The value

of the threshold varies depending on the conditions of the ice, such as rheology properties, firn density, and water and debris inclusions (Campbell et al., 2013).

Given that u and v are horizontal components of observed surface velocity, the principal strain rates can be calculated from the matrix.

$$\dot{\varepsilon} = \begin{bmatrix} \frac{\partial u}{\partial x} & \frac{1}{2}(\frac{\partial u}{\partial y} + \frac{\partial v}{\partial x}) & 0 \\ \frac{1}{2}(\frac{\partial u}{\partial y} + \frac{\partial v}{\partial x}) & \frac{\partial v}{\partial y} & 0 \\ 0 & 0 & -\frac{\partial u}{\partial x} - \frac{\partial v}{\partial y} \end{bmatrix} \tag{6.4}$$

Effective strain can then be approximated by:

$$\dot{\varepsilon}_e = \sqrt{\dot{\varepsilon}_{xx}^2 + \dot{\varepsilon}_{yy}^2 + \dot{\varepsilon}_{xy}^2 + \dot{\varepsilon}_{xx}\dot{\varepsilon}_{yy}} \tag{6.5}$$

Thickness and velocity

Ice shelf thickness affects an ice shelves resilience to fracture, length and depth of fracture propagation. Thickness data is taken directly from BedMachine Morlighem et al. (2020). Changes in ice shelf velocity can impact the stress dynamics leading to the formation of fractures. Velocity observations are taken directly from InSAR (Rignot et al., 2011a; Rignot et al., 2011b).

Predictor	**Calculation/Description**
Observed Velocity	Taken from inSAR (Rignot et al., 2011a)
Damage	Calculated as described in Borstad et al. (2013)
Principal stresses	Calculated using equation 6.2
Effective stress	Calculated using equation 6.3
Principal strain rates	Calculated using equation 6.4
Effective strain	Calculated using equation 6.5
Thickness	Taken directly from BedMachine (Morlighem et al., 2020)

Table 6.1: Predictor parameters and the method use to calculate them or data source.

		BMR (m/yr)		
Label	SMB (m.w.e.)	LCIS	GVIIS	WIS
Scenario 1 (No forcing)	0	0	0	0
Scenario 2 (RCP2.6)	-0.5	0.1	1.1	0.6
Scenario 3 (RCP4.5)	-1.0	0.2	2.2	1.3
Scenario 4 (RCP8.5)	-1.5	0.3	4.2	2.5

Table 6.2: The forcing applied to the 4 transient simulations of the Larsen C Ice Shelf (LCIS), George VI Ice Shelf (GVIIS) and Wilkins Ice Shelf (WIS), representing varying RCP scenarios. Surface Mass Balance (SMB) projections are from Kittel et al. (2021) and consistently changed for all ice shelves. Basal Melt Rate (BMR) projections are from Naughtena et al. (2018) and vary independently. All forcing is applied linearly from the beginning of the simulation for 100 years.

6.3.5 Transient simulation setup

A transient simulation computes the flow predictors as a function of time. These outputs will be used to estimate fracture probability with the trained statistical model. ISSM can calculate thermal solutions, stress balance, mass transport, and other modules in a transient run. The model calculates the solutions at each time step. Time step length can be the same interval each iteration or varying duration based on Courant–Friedrichs–Lewy condition. In this study, the time step is 0.2 years for all simulations. The simulations ran for 100 years (500-time steps). For the thermal model, heat transport equations are derived from the balance equation of internal energy (Aschwanden et al., 2012). The stress balance equations are the equations that describe the following physical principles. The conservation of linear momentum states that momentum is constant in a closed system, and momentum is conserved when objects interact. The law of conservation of angular momentum states that no change in angular momentum will occur when no external torque acts on an object. The constitutive equations for ice state that ice is a purely viscous incompressible material and a non-Newtonian fluid. Our simulations use a shallow shelf approximation (SSA) that assumes vertical shear is negligible. The mass transport equation is derived from the depth-integrated form of the conservation equation.

We include the damage evolution module in our simulations as we believe it will be a crucial predictor in our statistical model. This module is still under development by the model development team, so the fully analytical law for damage evolution described in (Borstad et al., 2012) is not yet available. A framework outlined in (Pralong and Funk, 2005) is available; however, the validity of this framework for larger-scale simulations is unknown. Results using this framework on Alpine glaciers have been highly accurate. Since the model focused on Alpine glaciers, ice temperatures are assumed to be close to the melting points. The AP is the warmest region of the AIS, suggesting that this model is appropriate. However,

other regions would need to use the analytical solution. Note that we do not update ice shelf geometry throughout the transient simulations, so retreat is not considered. However, under higher forcing scenarios, retreat would undoubtedly take place over the simulation period.

6.3.6 Forcing selection

In order to estimate fracture probability under future climate scenarios, we forced SMB and BMR in our transient simulations guided by projections under similar warming scenarios from Kittel et al. (2021) and Naughtena et al. (2018) respectively. We present 4 warming scenarios, 3 based on Representative Concentration Pathways (RCP), which represent greenhouse gas concentrations depending on emissions and 1 scenario with no forcing (SMB and BMR are consistent throughout the transient simulation). RCPs are calculated using the fifth phase Coupled Model Intercomparison Project (CMIP5) experiment; this has been updated to the sixth phase CMIP6, which has equivalent update concentration pathways called shared socioeconomic pathways (ssp). The pathways represented in this study are RCP2.6/ssp126, RCP 4.5/ssp245, and RCP 8.5/ssp585. If one of the desired scenarios is missing, we make the first-order estimation based on context.

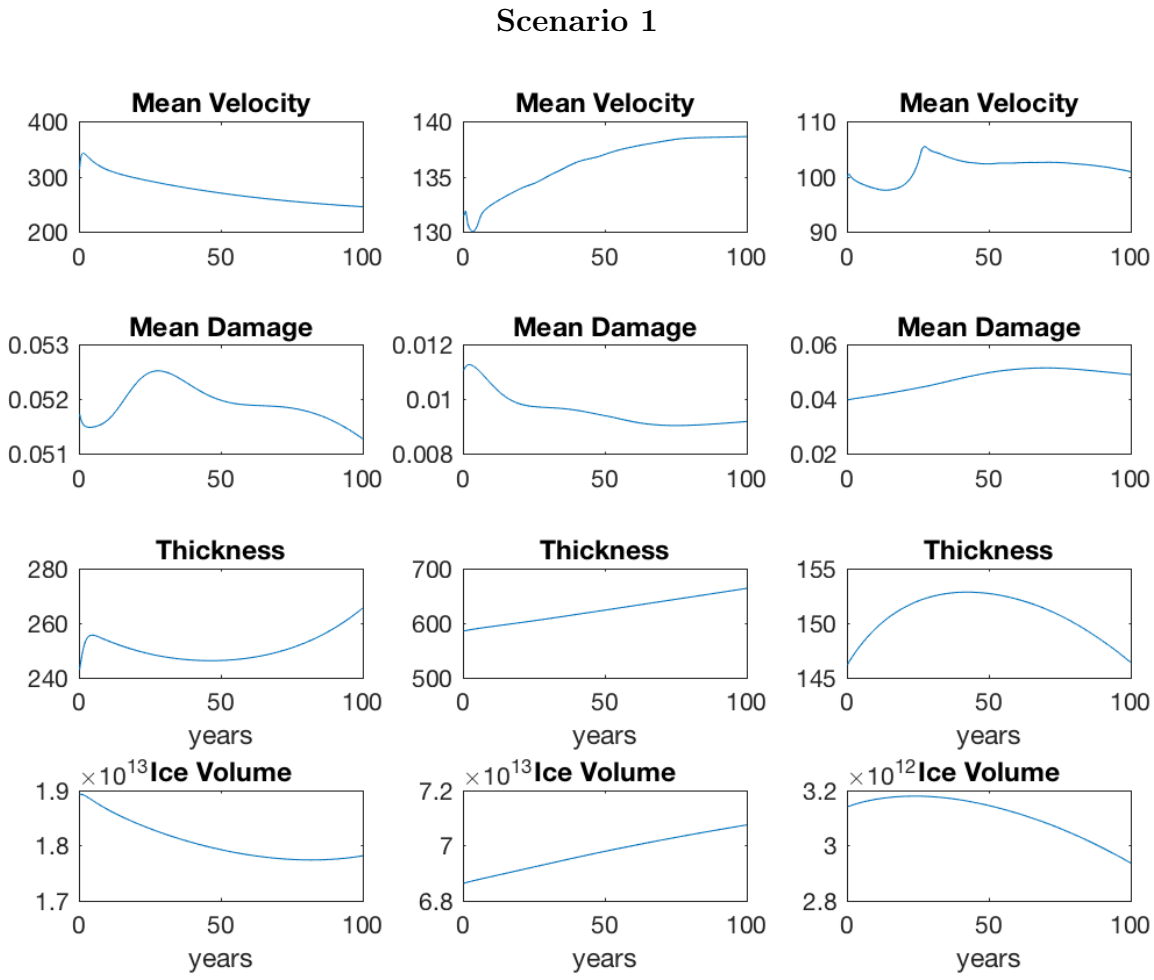
Kittel et al. (2021) projects SMB up to 2100 using the Modèle Atmosphérique Régional model forced by various climate scenarios including the updated CMIP6. They find SMB decrease over the projection period of up to 1.6 m.w.e. We use a conservative 1.5 m.w.e. for the RCP8.5/ssp585 forcing. Guided by this, assign intervals between this and the no forcing scenario (Table 6.2). Since SMB changes are largely uniform over the AP ice shelves, we apply equally to all ice shelf regions for each scenario.

Naughtena et al. (2018) projects basal mass loss using the Finite Element Sea Ice/Ice Shelf Ocean Model forced by the CMIP5 for the RCP4.5 and RCP8.5. The report projections

for proportional basal mass loss change from ten years between 1996-2005 and 2091-2100. These proportions guide the BMR forcing in this study. Due to high near-surface ocean temperature on the west coast of the AP, GVIIS and WIS have a more significant increase in BMR compared to LCIS (table 6.2).

6.3.7 Transient simulations

Scenario 1 has no forcing applied (Figure 6.2). The SMB and BMR stay constant throughout the 100 year model period. The final outputs from these simulations are consistent with finding from Adusumilli et al. (2018), positive SMB is not enough to balance out negative BMR for the LCIS and WIS resulting in a reduction in ice volume. For the LCIS and GVIIS, mean damage decreases and ice thickness increases. For the WIS, a slight increase in mean damage occurs and, after an initial period of increasing thickness to returns to a similar thickness by the end of the simulation.

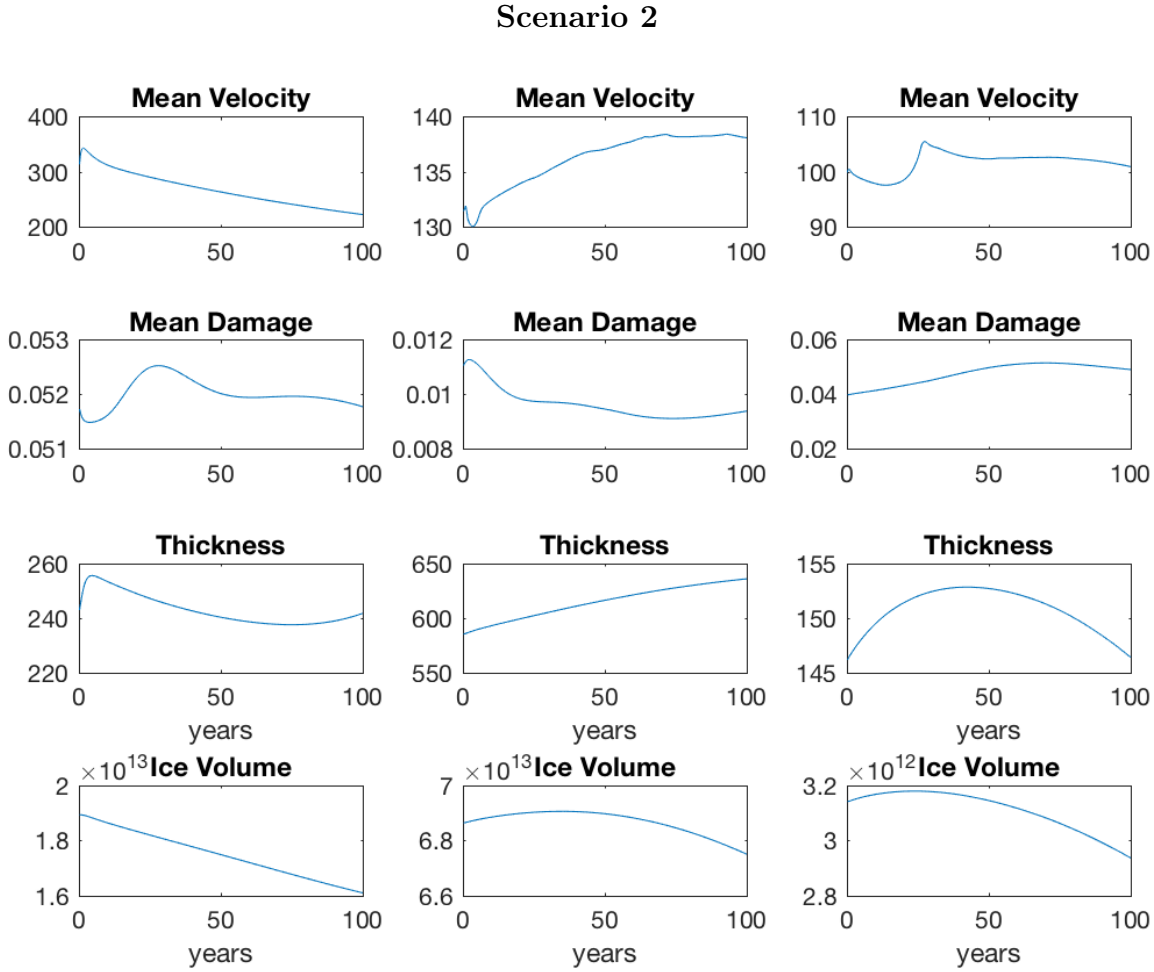


(a) Larsen C (b) George VI (c) Wilkins

Figure 6.2: ISSM 100-year transient simulation of mean velocity (m/yr), mean damage, thickness (m), and ice volume (m^3/yr) for a) Larsen C Ice Shelf (LCIS) b) George VI Ice Shelf (GVIIS) c) Wilkins Ice Shelf (WIS) under the no forcing scenario.

Under RCP 2.6 (Figure 6.3), we see a further decrease in ice volume for the LCIS and WIS and a decrease in ice volume for GVIIS by the end of the model period. Mean damage for the LCIS increases for around 30 years before decreasing close to its initial value. For the GVIIS and WIS, the damage remains similar to the no forcing simulations. Overall we see minor changes in flow parameters compared to the no forcing scenarios (except we see GVIIS ice volume become negative); the increased negative SMB and BMR from warming

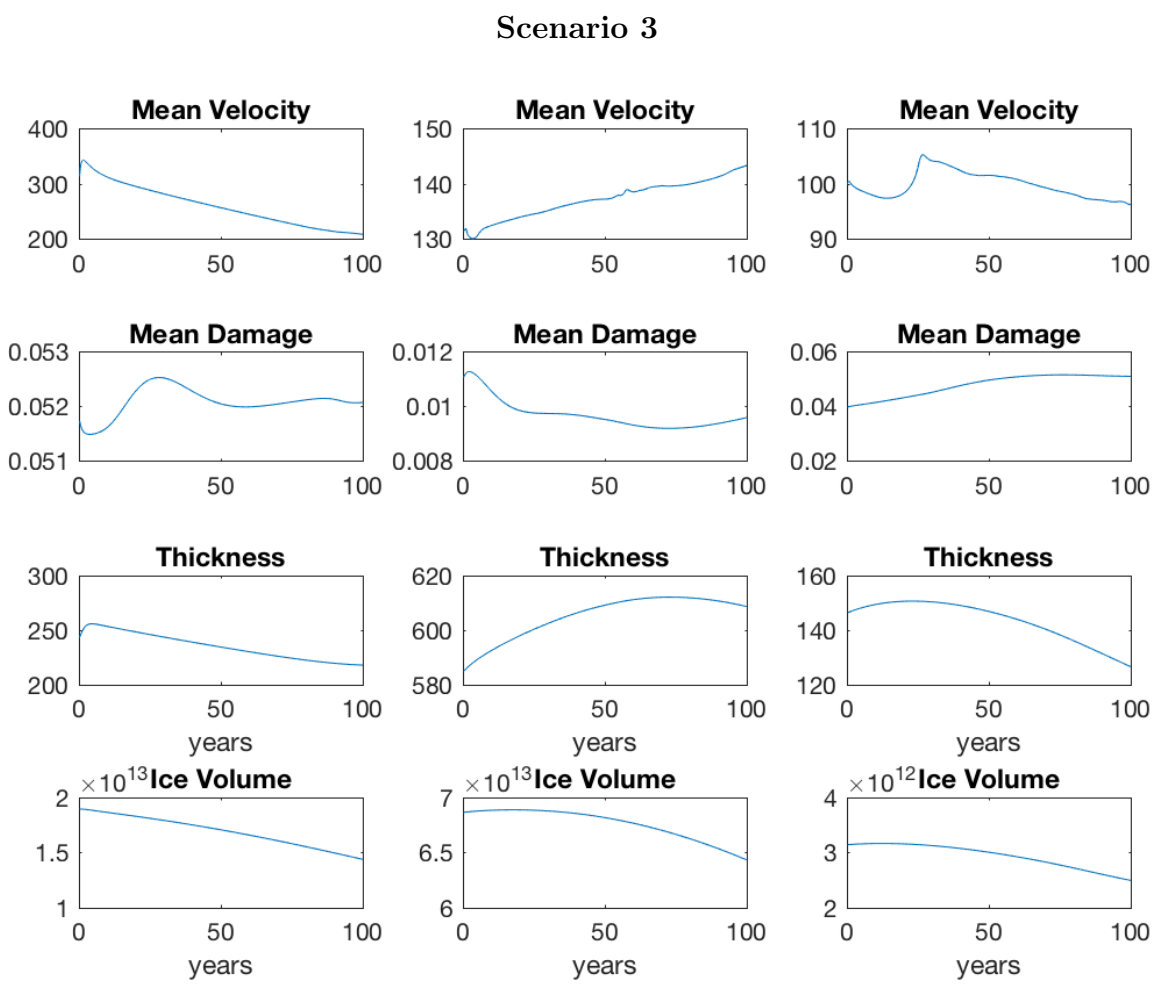
of the air and oceans have been simulated to make significant changes.



(a) Larsen C (b) George VI (c) Wilkins

Figure 6.3: ISSM 100-year transient simulation of mean velocity (m/yr), mean damage, thickness (m), and ice volume (m^3/yr) for a) Larsen C Ice Shelf (LCIS) b) George VI Ice Shelf (GVIIS) c) Wilkins Ice Shelf (WIS) under the RCP2.6 scenario.

Under the RCP 4.5 simulation (Figure 6.4), we start to see more significant changes when compared to the no forcing simulation. Ice volume dropped significantly for LCIS, dropping by around 25% compared to around 5% with no forcing. GVIIS ice volume has decreased by approximately 5% compared to an increase of a similar amount with no forcing. WIS also saw further decreases in ice volume.

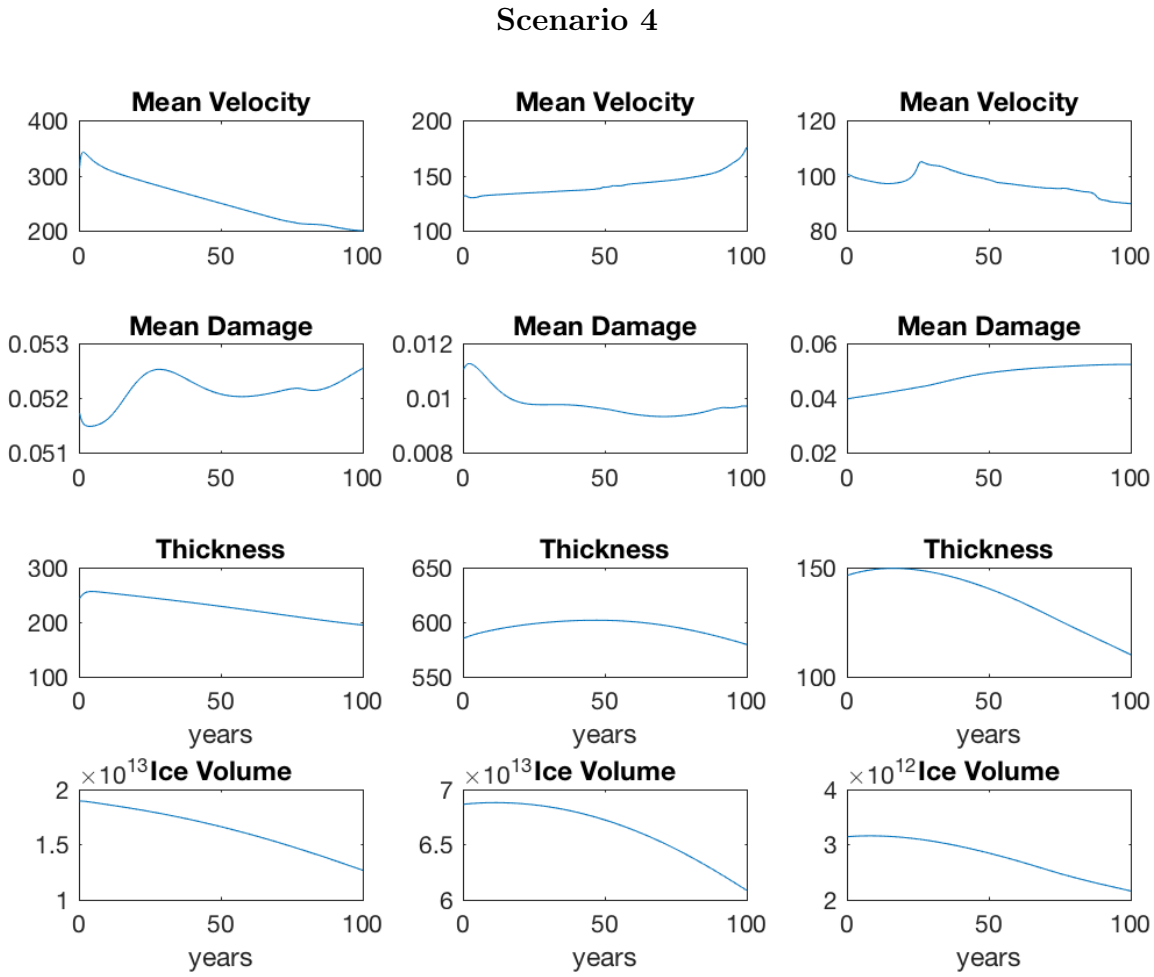


(a) Larsen C (b) George VI (c) Wilkins

Figure 6.4: ISSM 100-year transient simulation of mean velocity (m/yr), mean damage, thickness (m), and ice volume (m^3/yr) for a) Larsen C Ice Shelf (LCIS) b) George VI Ice Shelf (GVIIS) c) Wilkins Ice Shelf (WIS) under the RCP4.5 scenario.

Under the RCP 8.5 forcing scenario simulations (Figure 6.5), mean damage increased by the end of the simulation period for the LCIS, and the WIS increased further. The GVIIS damage remained lower at the end of the simulation period than the start but was higher than scenarios 1 and 2, finishing similar to scenario 3. Ice volume continued to decrease under strong forcing, with the most significant change being that of the LCIS, which decreased 35% over the simulation period. The ice volume of GVIIS and WIS decreased by around 13%

and 29% respectively.



(a) Larsen C (b) George VI (c) Wilkins

Figure 6.5: ISSM 100-year transient simulation of mean velocity (m/yr), mean damage, thickness (m), and ice volume (m^3/yr) for a) Larsen C Ice Shelf (LCIS) b) George VI Ice Shelf (GVIIS) c) Wilkins Ice Shelf (WIS) under the RCP8.5 scenario.

6.4 Methods

We utilise a spatial mixed-effects Gaussian process regression model first presented in Chapter 5. Gaussian processes have become a popular machine learning tool because they apply

to many problems and accurately estimate their uncertainty. The Bayesian analysis enables priors to be set on the hyperparameters. We must sample the posterior distribution to apply Bayesian inference, which has proven to be a computationally expensive task on large data. To combat this, we apply a hybrid variational and MCMC sampling scheme developed by Hensman et al. (2015). This inference scheme offers a computationally inexpensive way to sampling the posterior distribution using MCMC without making any specific requirements of the covariance function or the data. MCMC sampling involves iteratively sampling the function values and covariance parameters, requiring inversion of the covariance matrix for each step. This cannot be applied to large datsets as it is computationally expensive. Variational methods are a group of techniques that find an approximation to intractable integrals in machine learning problems (Jordan et al., 1999). The scheme we apply employs a variational inducing point approximation that reduces to a minimisation problem which, can then be sampled using an efficient MCMC algorithm.

An essential consideration in regression models is dealing with the variation in physical processes between ice shelves. Emetc et al. (2018) applied a logistic regression model to ice shelf fractures for many ice shelf regions though out the whole AIS. That study grouped each region by the set of predictors that closely matched its best-fitting model, and it can then be assumed that the data in each group are independent. Logistic regression is a fixed-effects model. Applying logistic regression to more than one ice shelf, as our approach aims, would be problematic. The model assumes no ice shelf to ice shelf variability. If we fit the model naively, a concern is it may train the model to differentiate between ice shelf regions rather than learn about underlying physical processes and their relationship to fractures. By introducing a mixed model with spatial random effect, we can model latent features to tackle this in a more mathematically rigorous way. Random effects enable us to incorporate the differences between ice shelves rather than ignore them.

Given that Y_i is the binary fracture indicator at location i, x_i is the predictors and z_i

is the coordinates of ith location. The model can be defined as follows:

$$\ell(p(Y_i = 1)) = x_i^T \beta + g(z_i) \qquad\qquad i = 1, 2, ..., n. \tag{6.6}$$

where ℓ is a link function, we use a probit link function because of its ease of implementation, but a logit is also appropriate. The regression coefficients β are the fixed effects and the function g are the random effects. We assume g varies slowly in space. This means that g captures any other features of z_i. If two points within close proximity are highly correlated, it can be because of the random effect g rather than being independent of one another.

To perform Bayesian inference on the model, we assign a prior on the parameters. Priors represent our belief about the parameters.

$$\beta \sim N(0, \sigma^2_{fixed} I) \qquad\qquad g \sim N(0, \sigma^2_{random} k_\lambda) \tag{6.7}$$

where k_λ is the kernel on $\mathbb{R}^2$. We have defined g as a Gaussian process. A Gaussian process is a generalisation of the Gaussian probability distributions, which are defined over scalars or vectors. Gaussian processes are defined over functions. Since functions have an infinite domain, a Gaussian process is a Gaussian random variable with infinite dimensions. Any subset of its random variables has a multivariate normal distribution. A Gaussian process is specified by its mean function and covariance function, also known as the kernel. The kernel inputs 2 points $z, z^{'} \in \mathbb{R}^n$ and outputs the similarity measure between them as a scalar, $k : \mathbb{R}^n \times \mathbb{R}^n, \Sigma = Cov(X, X^{'}) = k(z, z^{'})$. By evaluating all the points pairwise, the kernel function calculates the covariance matrix. The choice of the kernel determines the shape that the fitted functions can take. The kernel used here is the Radial Basis Function

(RBF) kernel.

$$k_\lambda(z, z^{'}) = exp(-||z - z^{'}||^2/2\lambda^2) \tag{6.8}$$

where λ is the lengthscale parameter. As $k_\lambda(z, z^{'}) \in (0, 1)$ the closer 2 points are the closer the similarity is to 1 (highly correlated), and the further away 2 points are the closer the similarity is 0 (independent). The lengthscale is the kernel's influence between points (so how correlated those two points are). The hyperparameters (parameters of the prior distribution) are $\theta = (\sigma^2_{fixed} I, \sigma^2_{random} k_\lambda, \lambda)$. By assigning priors onto θ, we will learn them in a fully Bayesian way. An important consideration is how we deal with the lengthscale as its size determines the smoothness of the function. A lengthscale too small would risk overfitting. In some situations, it would be better to set the lengthscale if we have apriori knowledge of lengthscale that best fits the random variability. However, we elect to set a prior on the lengthscale as this will give an in-site into how well our data predict fractures.

6.4.1 Variational Bayes

To perform inference in a Bayesian way we need to sample the posterior distribution which is the conditional distribution of the parameters β, g, θ given the data $\{Y_i, x_i, z_i\}_{i=1,\dots,n}$. The posterior is proportional to the likelihood times the prior:

$$p(\beta, g, \theta | \{Y_i, x_i, z_i\}_{i=1,\dots,n}) \propto \prod_{i=1}^{n} p(Y_i | x_i, z_i, \beta, g, \theta) p(\beta, g | \theta) p(\theta). \tag{6.9}$$

by finding the marginal distribution, we can isolate the fixed effects β. The inference scheme developed by Hensman et al. (2015) combines variational methods with MCMC by

making an inducing point approximation. Inducing points methods (also known as sparse GPs) reduce effective data by selecting a small subset of a total number of samples, thus reducing the size of the covariance matrix. As discussed in chapter 5, to define the locations of the inducing points, we use a K-mean clustering algorithm. The target number K is the number of centroids that every fracture index point is allocated. The inducing points are defined by these centroid locations (Figure 6.1).

We can rewrite the model as follows:

$$\Phi(p(Y_i = 1)) = x_i^T \beta + g(z_i) := f(x_i, z_i). \tag{6.10}$$

Since $x_i^T \beta + g(z_i)$ and $g(z_i)$ is Gaussian then $f(x_i, z_i)$ is a Gaussian process, $f \sim N(0, \widetilde{k})$ where the kernel is defined by

$$\widetilde{k}((x, z), (x', z')) = \sigma^2_{\text{fixed}} x^T x' + \sigma^2_{\text{random}} k_\lambda(z, z') \tag{6.11}$$

We will write $\mathbf{f} = ((f(x_1, z_1), ..., f(x_n, z_n))$, and the target of out algorithm will be to sample the posterior, which can be written as $p(\mathbf{f}, \theta | Y)$.

Variational methods introduce additional variables, known as variational parameters, to transform the problem into an equivalent minimisation problem. Define q^* as an approximation of the posterior that minimises the KL divergence to the true posterior in some family $\mathcal{Q}$:

$$q^*(\mathbf{f}, \theta) = \underset{q \in \mathcal{Q}}{\operatorname{argmin}} KL(q(\mathbf{f}|\theta)||p(\mathbf{f}, \theta|Y)), \tag{6.12}$$

where the KL divergence is a similarity measure between distributions. To do this $\mathcal{Q}$ needs to be defined. This is done by making the inducing point approximation (Sparse

GP approximation) (Titsias, 2009). Let $\mathbf{u} = L\mathbf{f}$ for some linear operator $L \in \mathbb{R}^{m \times n}$ with $m \ll n$, where m is the number of inducing points. We aim to approximate the joint posterior $p(\mathbf{f}, \mathbf{u}, \theta | Y)$. Since $\mathbf{u}$ is a function of $\mathbf{f}$ the joint posterior is the same as our target posterior. We also know a priori that $p(\mathbf{f}|\mathbf{u}, \theta)$ is normal. We define $\mathcal{Q}$ to be the family of distributions of the form $q(\mathbf{f}, \mathbf{u}, \theta) = q(\mathbf{u}, \theta)p(\mathbf{f}|\mathbf{u}, \theta)$. In the variational approximation, the marginal $q(\mathbf{u}, \theta)$ is unconstrained, but we restrict $\mathbf{f}|\mathbf{u}, \theta$ to have the prior conditional distribution.

It can be shown that the solution to the Variational Bayes problem is:

$$\log q^*(\mathbf{u}, \theta) = \mathbb{E}_{p(\mathbf{f}|\mathbf{u},\theta)}(\log p(\mathbf{Y}|\mathbf{f})) + \log p(\mathbf{u}|\theta) + \log p(\theta) - \log C \tag{6.13}$$

where C is an intractable constant that normalises the distribution and is independent of q. This variational approximation is then sampled with MCMC. MCMC can be applied if we can calculate the log of the target distribution up to a constant. Therefore, if the right-hand side of equation 6.13 can be calculated, MCMC can be applied. The authors make a few observations to sample effectively. The first term in equation 6.13 is not known in closed form; however, it can be approximated effectively by quadrature. The distribution can be whitened by the reparameterisation $\mathbf{u} = \mathbf{R}\mathbf{v}$ such that $\mathbf{R}\mathbf{R}^T = \mathbf{K}_{uu}$,$v$ $N(0, \mathbf{I})$. Resulting in the optimal variational solution:

$$\log q^*(\mathbf{V}, \theta) = \mathbb{E}_{p(\mathbf{f}|\mathbf{u}=\mathbf{R}\mathbf{v})}(\log p(\mathbf{Y}|\mathbf{f})) + \log p(\mathbf{V}) + \log p(\theta) - \log C \tag{6.14}$$

This transformation changes the shape of the distribution to be more spherical. In chapter 5, we discuss the benefits of using the Hamiltonian Monte Carlo (HMC) over more common MCMC schemes. In short, Hamiltonian Monte Carlo (HMC) is more efficient than a standard random walk-metropolis as the only dependence on the number of samples n

is a one time $O(n)$ computation. The reduction in computational cost allows models with significant data to be solved in a fully Bayesian way. A Maximum A Posteriori (MAP) estimation is made to generate initial values for the hyperparameters, and these values are then used for an estimate of the accuracy predicting the training data (referred to as a MAP model) Matthews et al. (2017) developed the GPFlow python package that implements the hybrid MCMC inference method used. GPFlow utilises the Tensorflow Architecture.

6.4.2 Convergence criteria

As with chapter 5, we need to ensure that we run a sufficient number of samples to be confident in the results of the HMC. Convergence of HMC chain is tested by a potential scale reduction $\hat{R}$ test; this is a ratio between the average variance of each chain to the average variance of the chains together. If the chain converges to a common distribution, then the ratio will be close to 1. We follow standard practice by concluding an approximate convergence if $\hat{R} \leq 1.2$. Comparing each of the inducing point coefficients would be too strict of a test. We limited it to the coefficients of the predictors and 10 randomly selected inducing point coefficients, resulting in the number of burn-in steps and total samples being 5000, and 10,000 respectively.

6.4.3 Model training

To make predictions of the fracture probabilities of each climate scenario, we first train the model using the fracture index data and the flow parameters calculated from the non-transient ISSM simulation. As outlined above, we initialise the locations of the inducing points via K-means. We set the number of inducing points to 200 for this simulation as the model becomes unstable past this. The hyperparameters θ are given priors such that

$\sigma^2_{fixed}I = Gamma(1,1)$, $\sigma^2_{random}k_\lambda = Gamma(1,1)$, and $\lambda = \mathcal{N}(0,1)$. A MAP model estimates the initial values for the coefficients, which had a classification accuracy of 0.988. We drew 10,000 samples from the HMC discarding the first 5000; this met the convergence criteria outlined in section 3. The hyperparameter values are $\sigma^2_{fixed}I = 17.55$, $\sigma^2_{random}k_\lambda = 9.62$, and $\lambda = 0.1$ (Figure 6.7).

By investigating the posterior distributions of each of the predictors, we can determine which of the proposed predictors are statistically significant. We can conclude statistical significance if the distribution is set away from 0. From Figure 6.6, out of the 9 predictors present in the model, 7 are statistically significant.. The principal stress 1 and principal strain 2 are not significant. It can also be determined that the strongest predictors are damage and effective strain as they set furthest away from 0, with damage being significantly further than any other variable. Damage and fractures are closely linked, as discussed in the previous section. Velocity is significant; however, the confidence interval is not set that far away. While velocity varies over each ice shelf, it is crucial to keep in mind the fracture index locations. Most are around the grounding line and clustered together. Hence not capturing the full range of velocities across ice shelves. For example, the ice of LCIS speeds up towards the centre/front; however, as mentioned, this area has no fracture index points, so not all behaviour is captured.

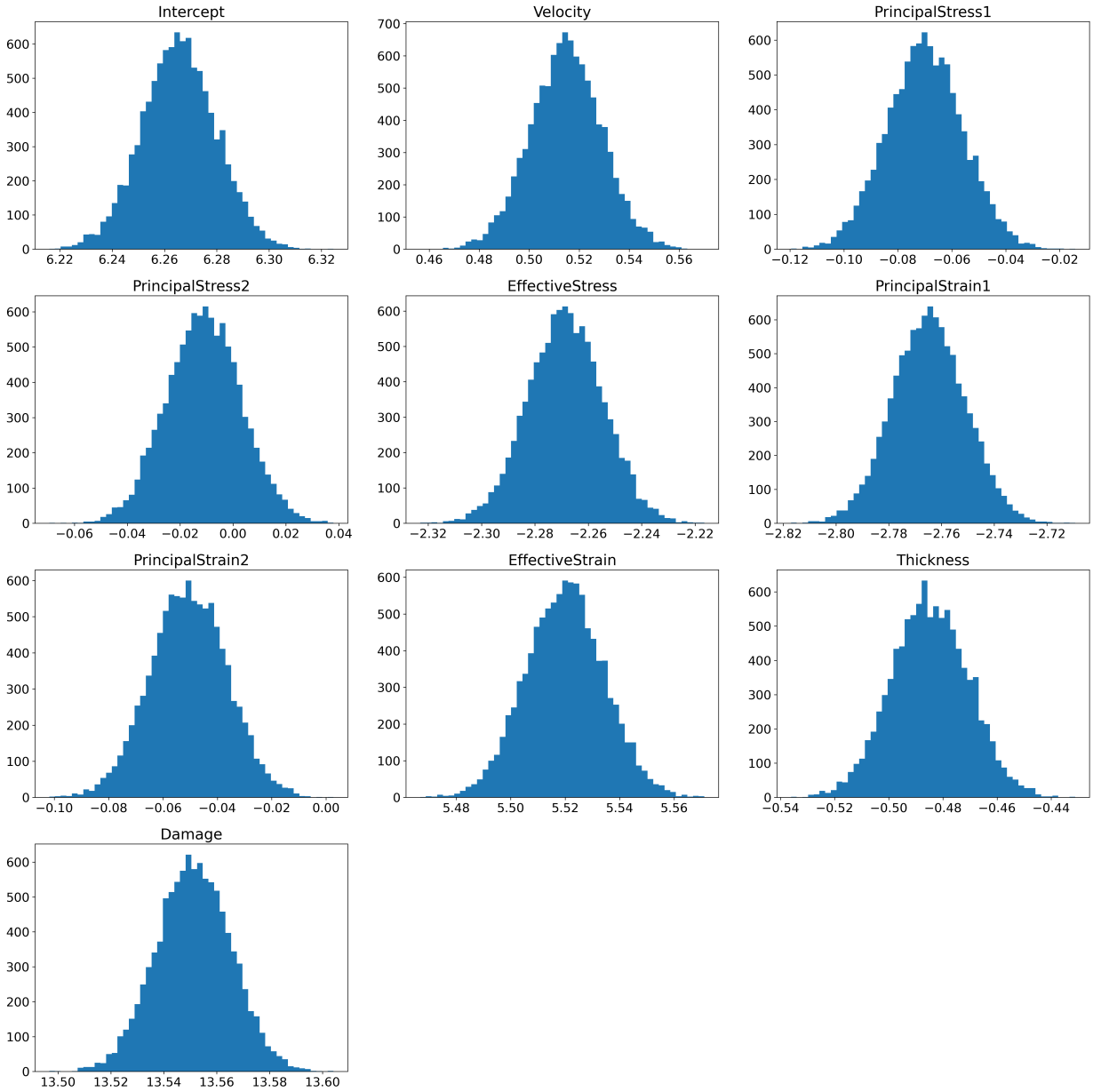


Figure 6.6: Posterior distributions of the predictor coefficients after 10000 samples - y-axis is the number of samples, x-axis is the coefficient. All but one of the distributions are set away from 0 suggesting that the correlation to fractures are statistically significant.

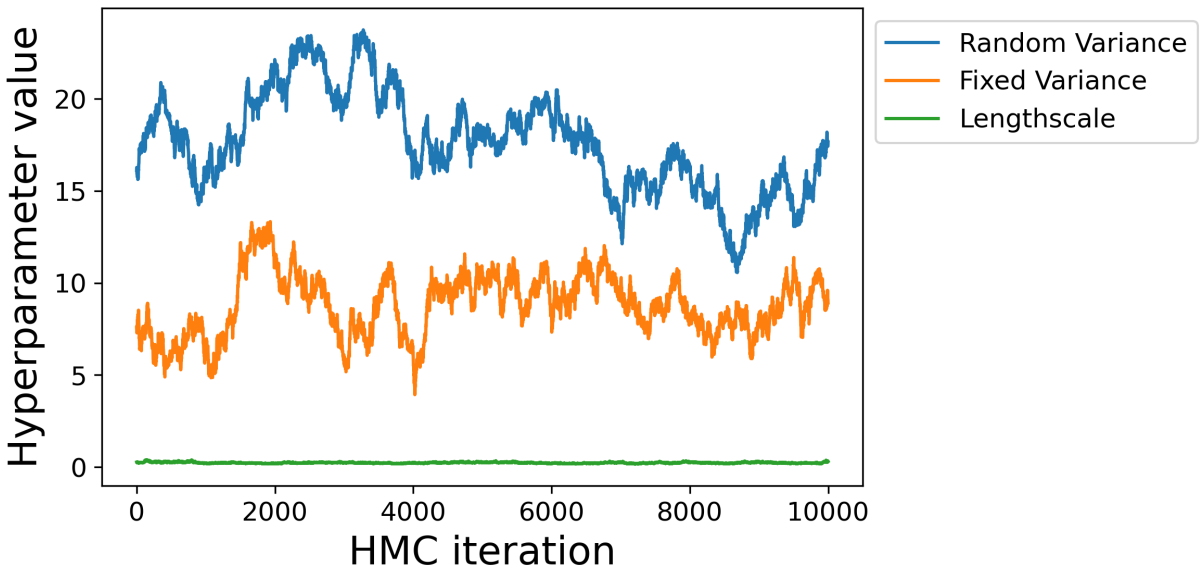


Figure 6.7: Evolution on the hyperparameter $(\theta = (\sigma^2_{fixed} I, \sigma^2_{random} k_\lambda), \lambda)$ values as a function of the Hamiltonian Monte Carlo (HMC) iterations.

We can now make predictions using our model across all three ice shelf regions. Given how few fracture index points are available, the model can pick up some interesting details with the fracture probability (Figure 6.8). Starting with LCIS, the model over predicts the centre of the ice shelf, as expected given the fracture indexing. Fracture probability is much lower of grounded ice with the start of the high fracture probability at the grounding line, an area that we know to be particularly fractured from the fracture index data and satellite images. The southeast region is reasonably well observed and is known to feature large rifts. From Figure 6.8 we can see this is modelled in good detail. A rift can is visible by the blue line where the ice shelf has separated. This rifting can also be visible in the Northwest of the ice shelf near the Bawden ice rise. The prediction for the GVIIS shows high probabilities at the northern front, which is well documented to be highly fractured through satellite observations. At the southern front, we also see high fracture probabilities, as documented in observations. Away from the front, we see areas of high fracture probability

at the grounding line where the ice shelf meets Palmer Land. These fractures are visible in Google Earth at a low resolution from the large tributary glacier of the ice shelf. We also see high probabilities at some points of the grounding line with Alexander island. As the ice flows laterally across from Palmer Land, sections of that grounding line become heavily fractured. For the WIS, we see high fracture probability at both fronts. However, both contain a small strip with a reduced probability. We believe this to be an error in the ice shelf boundary rather than a predictive flaw. The ice bridge that connects the ice shelf to Charcot Island collapsed in 2009. There are two interesting observations to be made about the model results here. Firstly fracture probability on either side of the bridge is greater than that of the centre, coinciding with the pattern of treat where long thin icebergs calved from either side of the ice bridge. This collapse occurred in the Austral winter and was driven by bending stresses rather than summer melt Braun and Humbert (2009) and is seen in the model output. Secondly, there is a clear change back to high fracture probability toward the rest of the ice shelf, matching up to the new front post-collapse.

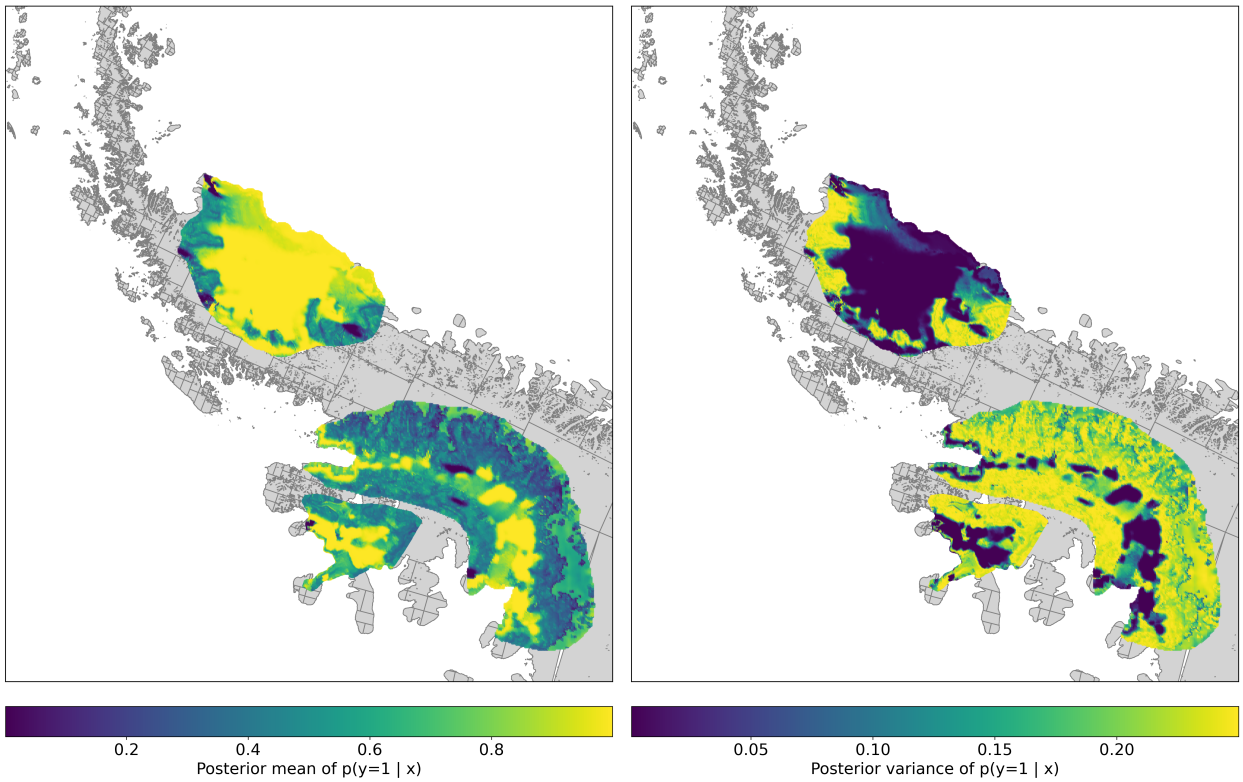


Figure 6.8: Model prediction of training data as a function of the predictors x for the grid locations in the ISSM datasets. The plot contains the estimated fracture probability (posterior mean) (left) and posterior variance (right) of the function $p(y = 1|x)$.

The variance of the posterior acts as we expect, such that it is high in areas in regions that change between high and low fracture probability. While we are not particularly interested in random effects on their own, plotting them gives insights into how they act on the model. Figure 6.9 shows the magnitude the random effects have at the fracture index locations. Since $\lambda = 0.1$, this means that points within 0.1 degrees of each other are highly correlated, and the further they get, the less correlated they are. A small variance could suggest that the set of predictors does not entirely describe the data. Considering that we use a small number of predictors, this is likely a factor. However, the scale of an ice shelf translates to the scale of the width of a tributary glacier. The random-effects variance shows a sharp transition between the fracture index locations and areas where the random effects

are 0. These transitional areas have the greatest uncertainty.

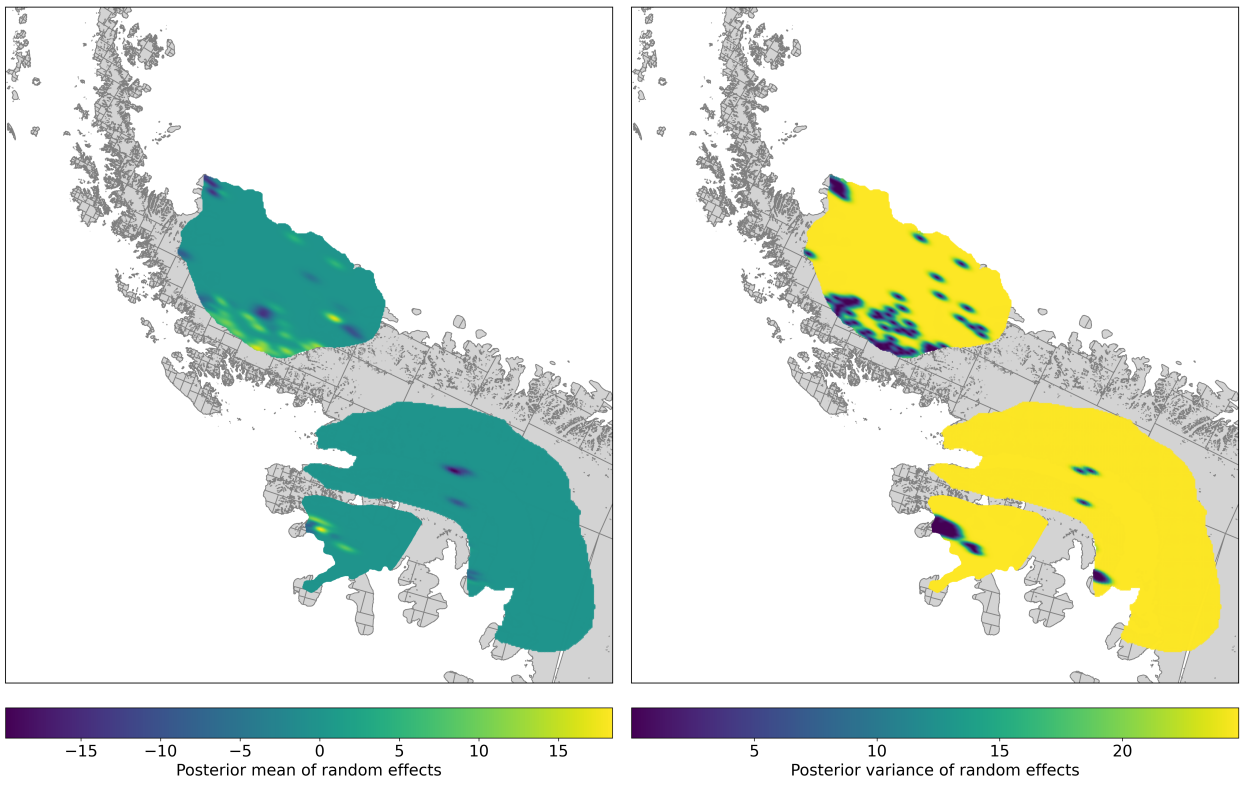


Figure 6.9: Prediction of the model $p(y = 1|x)$ s a function of the predictors x for the grid locations in the ISSM datasets. Posterior mean of the random effects (Left) and posterior variance of the random effects (Right) of the function.

6.5 Results

We applied the trained mixed effect model to each transient simulation to predict fracture probability changes under our forced climate scenarios. Before we make these predictions, we must consider how to interpret the random effects going forward. Random effects are calculated around the inducing points, which are positioned around observed fractures. The positioning of the inducing points raises a question of the validity of including random effects when predicting fracture probability for 100-year simulations.

In the following subsections, we compare each scenario prediction to the non-transient prediction and each other. We can consider how the fracture predictions change over time and between scenarios. We will not discuss the uncertainty for each scenario separately since all uncertainties occur as expected with higher variance in transitional regions.

6.5.1 Scenario 1 (No Forcing)

As discussed, the no forcing scenario simulations for LCIS and WIS projects increased thickness and decreased damage. This is reflected in the fracture probability predictions (Figure 6.10). For the LCIS, we see a clear reduction in fracture probability around the grounding line and around the Bawden Ice rise. Toward the southeast, we see the forward migration of high probability fractures. GVIIS has an even larger decrease in fracture probability, which gives then outputs from the transient simulation is expected. We see a migration of fracture probability from Palmer Land towards Alexander Island; however, few new fractures are formed from the tributary glaciers. Both fronts also see lower fracture probability. WIS is the only ice shelf to have greater mean damage under no forcing, and it has a higher overall fracture probability. To compare the fracture probability for each scenario, we calculate the average fracture probability of the floating ice. For scenario 1, the average fracture probability on the ice shelves is 51.7%

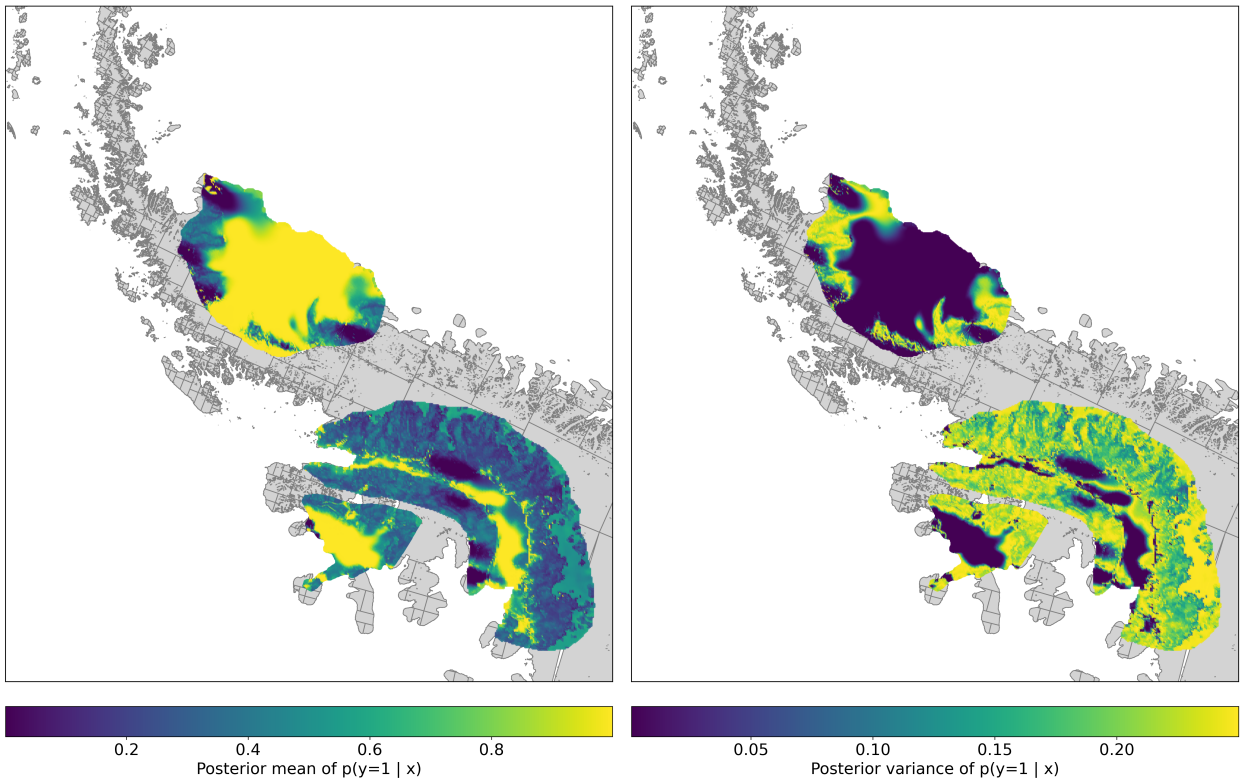


Figure 6.10: Model prediction of scenario 1 (no forcing) as a function of the predictors x for the grid locations in the ISSM datasets. The plot contains the posterior mean (Left) and posterior variance (Right) of the function $p(y = 1|x)$.

6.5.2 Scenario 2 (RCP2.6) and 3 (RCP4.5)

Under forcing representing SMB and BMR change in the RCP2.6, there is a minimal change compared to no forcing in the ISSM simulations, reflected in the fracture probability. Similarly, changes under RCP4.5 forcing are only incremental. Figures 6.11 and 6.12 see little overall change in fracture probability prediction compared to 6.10, especially on floating ice. There are some minor advancements under RCP4.5. Grounded ice, however, sees a reduction in fracture probability. For scenarios 2 and 3, the average fracture probability on the ice shelves is 52% and 53.3%, respectively.

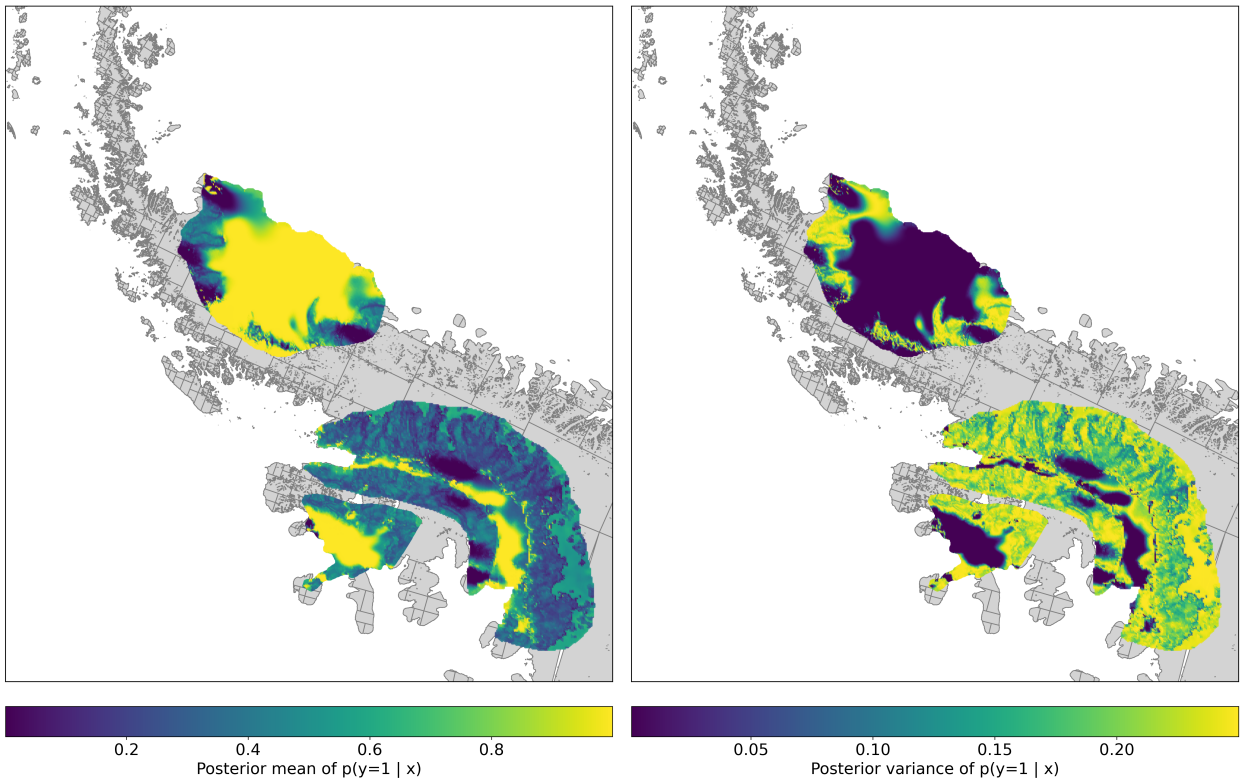


Figure 6.11: Model prediction of scenario 2 (RCP2.6) as a function of the predictors x for the grid locations in the ISSM datasets. The plot contains the estimated fracture probability (posterior mean) (left) and posterior variance (right) of the function $p(y = 1|x)$..

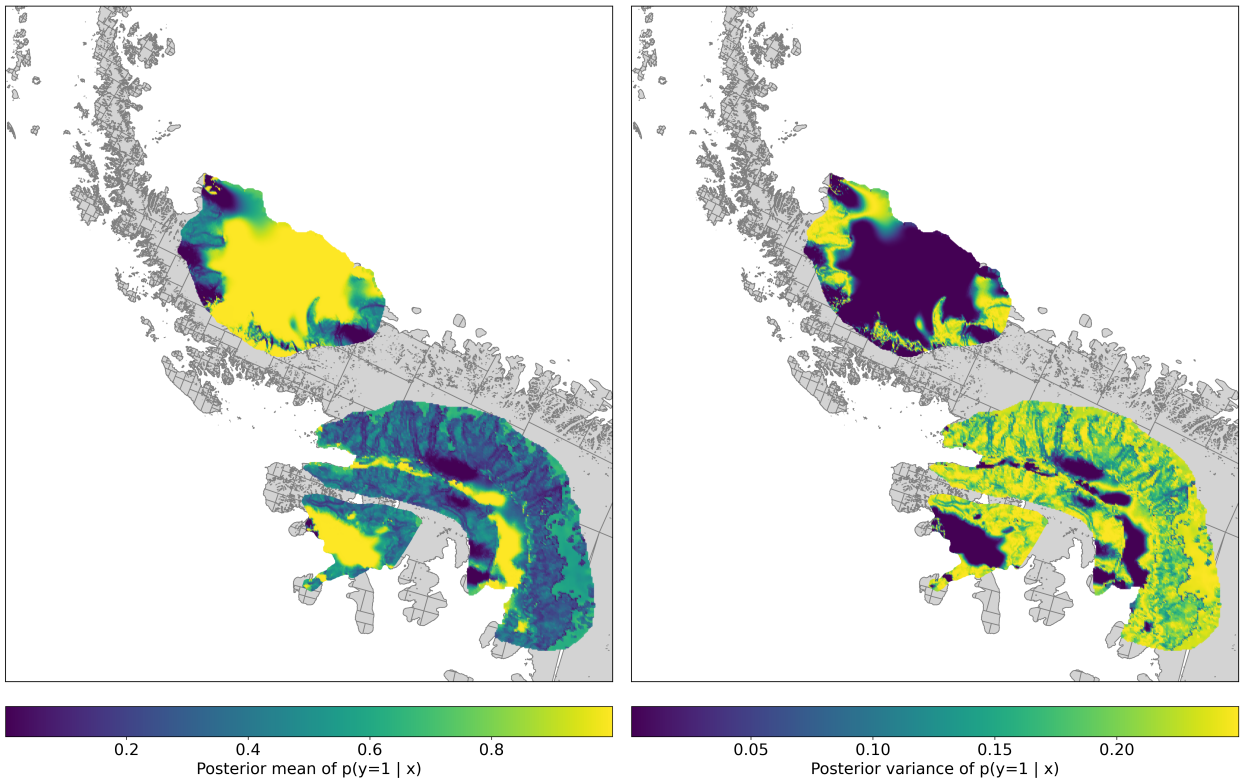


Figure 6.12: Model prediction of scenario 3 (RCP4.5) as a function of the predictors x for the grid locations in the ISSM datasets. The plot contains the estimated fracture probability (posterior mean) (left) and posterior variance (right) of the function $p(y = 1|x)$.

6.5.3 Scenario 4 (RCP8.5)

Under the RCP8.5 scenario representing SMB and BMR levels during high emissions, we can see that when compared to no forcing, there is a definite reduction in fracture probability on grounded ice for all ice shelf regions. However, in scenario 4, there is an increase in fracture probability on floating ice, particularly LCIS and WIS. In our simulations GVIIS, high fracture probability migrate laterally, consistent with the ice shelf flow regime. For scenario 4, the average fracture probability on the ice shelves is 58%.

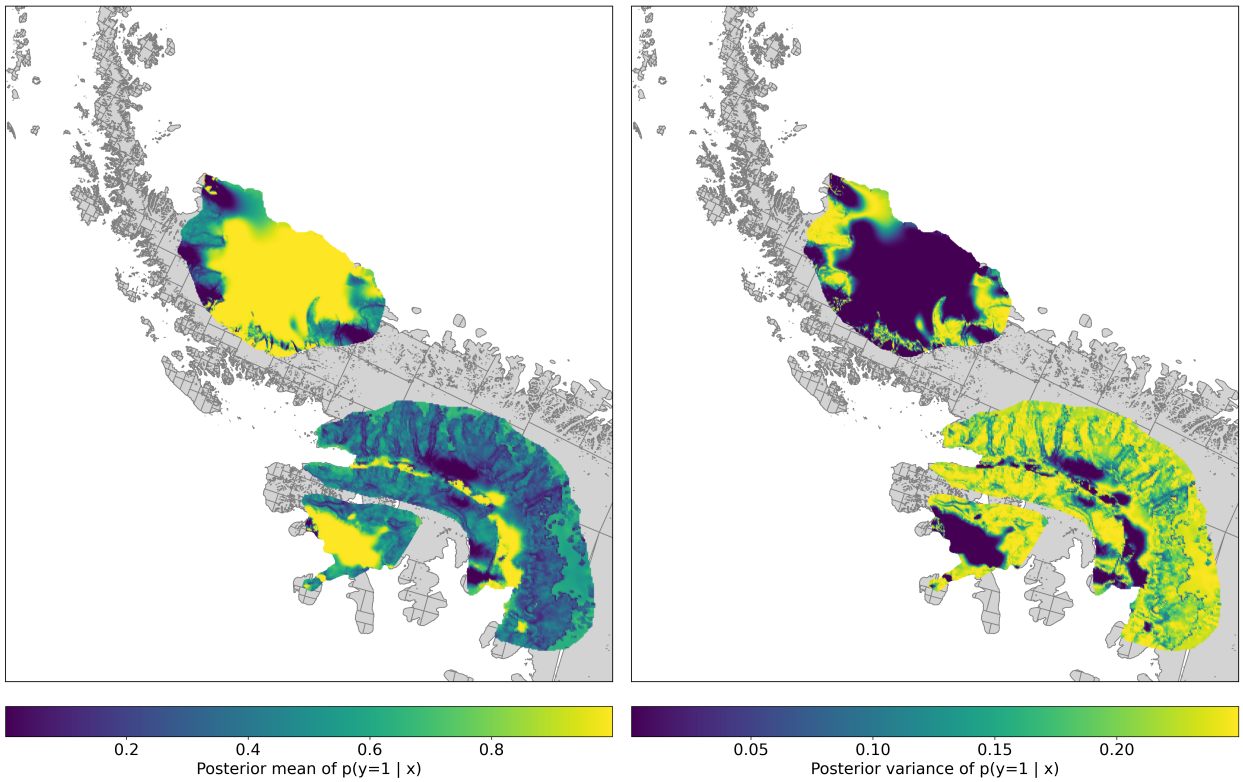


Figure 6.13: Model prediction of scenario 4 (RCP8.5) as a function of the predictors x for the grid locations in the ISSM datasets. The plot contains the estimated fracture probability (posterior mean) (left) and posterior variance (right) of the function $p(y = 1|x)$.

6.6 Discussion

Our transient simulations and fracture prediction find that the flow parameters between RCPs vary slowly, particularly for the RCP2.6 and RCP4.5 scenarios. While changes in SMB and BMR are significant in themselves, the direct impact on flow parameters is small over the next century. However, this does not necessarily imply that the ice shelves will remain stable over the next 100 years no matter the RCP pathway. Comparing the average estimated fracture probability of each scenario, we find no difference between the no forcing and the low emissions. There is a small difference between the low and medium emission

scenarios of around 1.3% and a considerable difference between the medium and high emission scenarios (4.7%). We do not consider the effect of melt ponding and hydrofracture within our simulations; this is driven by excess surface melting and is a crucial aspect of fracture formation, propagation, and retreat. As observed in 2002 with the collapse of the Larsen B ice shelf, collapse can occur swiftly and unexpectedly (Scambos et al., 2004). Also, we have not simulated calving, which would undoubtedly affect both ice shelf thickness and the velocity over the simulation period.

Predictions for LCIS suffer the most from overestimation over much of the ice shelf (Figure 6.8). While there is evidence of high fractures in the centre of the ice shelf, predicting high probability all over is not realistic. We do not attempt to distinguish between the type of fracture; however, the presence of suture zones on the LCIS which, are likely fractured themselves, inhibit fracture propagation from other regions. We would expect to see some heterogeneity in the fracture probability due to a lack of fracture index locations away from the grounding line, particularly non-fracture locations, and a set of predictors that do not describe the flow in the centre of the shelf that well. Transient simulations limit the available flow predictors that we can include. Overestimation remains a significant challenge to overcome on a model such as this. In regions such as the southeast and the grounding line, the results improve significantly. In these regions, we see that there is advancement in high probability into previous low probability areas.

Fracture probability is surprisingly good for GVIIS considering the lack of reliable fracture index locations (Figure 6.1). We believe this is because the predictors describe the flow of GVIIS well. Given the stability of fracture prediction between the scenarios, we find GVIIS robust against fracture formation from changes in flow parameters due to surface and basal conditions. Its confinement in the George VI Sound acts as a defence against fracture mechanisms such as ocean swell. High fracture probability is predicted at both fronts under all RCPs. GVIIS has retreated from both ends over the last 30 years, and these high fracture

probabilities are of particular concern as fractures near the calving front carry the greatest immediate risk for retreat. Compared to our present-day fracture prediction, we observe a migration of fractures laterally across the shelf into Alexander Island, becoming stronger as the RCP increases. This behaviour is observed by Holt et al. (2013a) as glaciers from Palmer Land dominate inflow. Due to a lack of fracture index points and the overall decrease of projected damage on these glaciers, we see fracture probability decreases from 1 to 0.5 on new inflowing ice at the end of the simulation period in the RCP8.5 scenario.

The WIS fracture predictions have some interesting behaviour. In all simulations, we see the high probabilities from the grounding line up to what became the new grounding line after the collapse of the ice bridge, again an overestimation as we would not expect homogeneous high fractures; however, large surface fractures are present (Braun and Humbert, 2009). Past that point, the fracture probabilities are reduced. Given the set of predictors used, this does fit what we understand about the collapse of WIS. Since the collapse was driven by buoyancy forces rather than flow parameters, we would not expect high fracture probability from this relatively thick, slow-moving region; highlighting a limitation of our predictors and the data-driven approach. Ice shelves, such as WIS that do not follow the expected pattern of retreat may not be well described by the data.

Without improved fracture indexing methods, the accuracy of statistical methods in certain regions will remain limited, as will the usefulness of such methods. Improvements in high-quality satellite images would significantly improve the fracture indexing process. However, snow cover would still become an issue. The addition of other remote sensing techniques to supplement is needed. Radar-based remote sensing techniques can penetrate the surface snow and accurately observe ice shelf fractures at specific wavelengths; this could significantly improve the amount of data available to train the model (Arcone et al., 2016; Dunmire et al., 2020). Another limitation is the manual selection of fracture and non-fractures points as it is time-consuming, subjective, and inconsistent. The datset was

time-consuming for this study, where we only manually selected fracture index data for three ice shelves (with supplementation from the Emetc et al. (2018) data). If this method wanted to be expanded to all AIS ice shelves or even an entire ice sheet, this indexing method would not be feasible. Even point distance is difficult to maintain due to the difference in scale for each image/ice shelf.

This study intends to investigate how potential forcing scenarios guided by RCP2.6, 4.5, and 8.5 would change simulated AP ice shelf flow parameters over the next 100 years and apply modern statistical methods that we first presented in chapter 5 to see how fracture predictions are influenced. Both to better understand potential fracture probability and to test how the model performs in a predictive situation. The use of sparse variational Bayes address two primary issues; firstly, it offers a framework to include multiple ice shelves within the same model. It is crucial to quantify dependence between adjacent points to incorporate statistical methods within the large scale flow and calving models. The second issue they address is the ability to sample the posterior when the data is large. Without implementing the inducing points approximation and transformation to a minimisation problem, it would be too computationally expensive to sample the posterior. To improve the model performance and usefulness, improvements in fracture indexing is crucial; this would take new remote-sensing data and advancements in automated fracture detection. As random effects are centred around the inducing points, the value of random effects is lost in some regions. Expanding the predictors available in the statistical model would further improve the models' predictive capabilities and usefulness as a diagnostic tool to determine key variables for fracture formation.

6.7 Conclusions

In this chapter, we applied a mixed effect Gaussian process model, using modern sampling techniques that allow MCMC to be applied to large data to unseen 100-year simulations to predict fracture probability under various scenarios. The novelty of this method is that it offers a mathematically rigorous way to model multiple ice shelf regions together, a key consideration for the implementation of statistical methods into large scale ice models. Random effects allow the inclusion of different flow parameters and geometries into the model by accounting for the correlation between adjacent fractures. We forced transient simulations with SMB and BMR as proxies for air and ocean warming, respectively. Our simulations show that the flow parameters are negatively affected under increasing emission scenarios. Ice volume decreased of the 100-years for all scenarios, but under RCP8.5, the decrease in modelled ice volume was between 13% and 29%. However, damage varies slowly as emissions increase. Under all RCPs, GVIIS damage at the end of the simulation remains lower than at the beginning. This is reflected in our fracture model predictions. Average floating ice fracture probability remains almost constant between the no forcing, RCP2.6 and RCP4.5 scenarios. Under the RCP8.5 scenario, the floating ice average fracture probability increases by around 5%.

We have not directly compared the model to damage as we do not see this as a replacement or potential alternative to a damage calculation but to be used in combination. Damage, if used to calculate fractures, is not intended for underestimated the number of fractures present. Our approach suffers areas of overestimation with homogeneous high probability due to lack of data; however, we have shown it to be effective in certain key areas.

We have outlined the current limitation of this statistical method. Improvements in remote sensing data and physicals models will lead to statistical methods being a viable

contributor to the fracture stimulation. Radar-based satellites sensing would be useful in the application of fracture indexing as it can penetrate the surface and find hidden crevasses. For future work, we recommend developing a new fracture indexing method and expanding the set of predictors.

Chapter Seven

Conclusions

7.1 Summary of Main Findings

The overarching aim of the research presented in this thesis was to introduce a framework that estimates AP ice shelf fracture probability that could model multiple ice shelves within the same simulation and be applied to forward projections. To achieve this aim, physical ice shelf flow models are combined with modern statistical methods. In chapter 1, we outlined the three research objectives that we set out to complete:

- Investigate the correlation between AP ice shelf area change and potential contributing environmental and glaciological predictors by applying a Quantile Regression analysis.
- Quantify fracture probability on major AP ice shelves by introducing a Gaussian process (GP) mixed-effects model framework.
- Apply the model framework to a forced transient simulation to project fracture changes under the RCP2.6, 4.5 and 8.5 emissions scenarios over the 21st century.

7.1.1 Twenty-first century AP ice shelf extent and contributors to retreat

Previous studies that delineated AP ice shelf extent focused either on individual ice shelves or long term trends (Cooper, 1997; Cook and Vaughan, 2010; Braun and Humbert, 2009; Ward, 1995; Rott et al., 1996; Fox and Vaughan, 2005; Doake and Vaughan, 1991; Holt et al., 2014; Holt et al., 2013a). We used MODIS and AVHRR images made available from the National Snow and Ice Data Centre (NSIDC) and data from previous studies to determine ice shelf fronts in ArcGIS, producing an annual ice shelf extent data set for the LBIS (1992-2009), LCIS (1992-2019), WIS (1990-2019) and GVIIS (2002-2019). Over these periods, the four ice shelves lost a combined area of 21.5% $\pm$ 0.2% to calving. The motivation for producing the annual extent data set was to analyse the relationship between a set of glaciological and environmental predictors and retreat. The available research and data motivated the choice of predictors: T2M, SMB, height change and sea ice concentration. QR was the chosen method over a more common least-squares regression. QR does not make any assumptions on the conditional distribution and can highlight relationships between predictors and the most significant retreat.

Mean annual 2 m air temperature was identified to have a statistically significant association with ice shelf retreat at the 50th and 20th quantiles. Our results suggest an increase of 1° C to the annual mean 2 m air temperature corresponds with a 2% loss from calving at the 50th quantile and a 6% loss from calving a the 20th quantile. We also identified that summer and autumn SIC has a statistically significant relationship with ice shelf retreat. Our results suggest that a 10% lower SIC in the austral summer and autumn will increase calving by 1.6%. These results supported the idea that rising air temperatures and reduced SIC can trigger calving (Massom et al., 2018; Vaughan et al., 2003). Correlation at the 50th and 20th quantiles suggests an association between the predictor and medium

or large retreats, respectively. Warming induced melt and ocean swell induced flexure are linked to fracture propagation and hydrofracture, suggesting fractures play a crucial role in calving. The lack of statistically significant SMB and height-change results suggests that these processes do not play a primary role in triggering ice shelf retreat. A limitation of the model does not consider that different ice shelves may influence the predictor in different ways. For example, both GVIIS and LCIS lowered over the study period; however, GVIIS lowering is driven by basal melt and LCIS is mainly caused by compaction of the firn layer.

The primary aim of Chapter 4 is to apply regression analysis to determine whether there is a correlation between annual AP ice shelf area change and hypothesised contributing factors. To achieve this, annual ice shelf extent data need to be improved and updated. The ice extent location presented in this chapter is the most comprehensive annual dataset for the Larsen B, Larsen C, Wilkins and George VI Ice Shelves. The quantile regression results provide further evidence that air temperature and sea ice concentration are essential measures for ice stability. An aim throughout this thesis it introduces new methods for the study of ice shelf stability. Chapter 4 has shown the potential for using quantile regression analysis and, more broadly, regression analysis to support hypothesis contributors to retreat. As data becomes easy and cheaper to collect, statistical methods such as QR will be invaluable tools for utilising it.

7.1.2 A statistical framework to estimate fracture probability of multiple AP ice shelves that is computationally inexpensive and scalable

Many physical ice shelf flow models have incorporated calving criteria; however, none contain ice shelf surface fractures. The presence of surface fractures plays a critical in ice shelf calving

(Albrecht and Levermann, 2014). We introduce a statistical framework that enables multiple ice shelves to be modelled simultaneously to estimate surface fracture probability. Mixed-effects models are a category of models containing fixed and random effects, taking into account the correlation between adjacent fractures. We applied a Bayesian Gaussian process spatial mixed effects model. While this type of model is powerful, they are computationally expensive to implement for large data sets. To solve this issue, we employ the MCMC for sparse Gaussian processes sampling scheme developed by Matthews et al. (2017). This sampling scheme drastically reduces the computation time, allowing for the introduction of larger data. We use the ISSM flow model to model the physical flow variables of the LCIS, WIS and GVIIS. The outputs from these simulations and observational data are the predictor variables in the statistical model. This includes an inverse process to obtain an estimate for continuum damage. The inverse process involved the tuning of cost functions which, is achieved by manually tuning the parameters until the modelled velocity is a good fit to input velocity.

We were interested in determining the best method for manually indexing fracture/non-fractures locations. Two fracture indexing methods were used; the first fracture indexing method was similar the that of Emetc et al., 2018 and their data was incorporated. Using only high-resolution images from Google Maps Pro we indexed the visible fractured and non-fractured locations, resulting in a reliable but sparse data set. The second method used the highest resolution available in Google Maps Pro to find all visible fractures. All other locations are designated as non-fractured, resulting in a comprehensive but inaccurate data set. Proceeding with these data sets, we begin constructing our statistical model. The sampling method that we utilised makes an inducing point approximation, the inducing points are selected via the K-means cluster algorithm. We assign priors to the hyperparameters, including the length scale (for the initial simulation). MAP estimation was used to obtain initial estimates for the hyperparameters, and this model had an accuracy of 95.9% for the

HRM and 82.3% for the LRM. We ran the HMC for a sufficient number of samples to meet our convergence criteria. For the HRM, the posterior distribution of coefficients tells us that all the predictors are statistically significant, with velocity, damage, strain rates and stresses being the most influential. For the LRM model, all predictors are statistically significant excluding ice thickness, with strain rates and stresses being the most influential.

Fracture probability predictions for both the HRM and LRM matched observed surface fractures; however, certain regions are overestimated, particularly for the HRM, likely due to a lack of fracture index data. Between the two models, the HRM model performs slightly better on unseen data with a misclassification rate of 20% $\pm$ 5% and better matches observed fractures. From this, we concluded that using the high-resolution fracture index data set is more appropriate for future predictions.

The primary aim of Chapter 5 was to improve the predictions of ice shelf fracture probability. The statistical framework introduced in Chapter 5 improves on previous work by enabling the modelling of fracture probability for multiple ice shelves that vary greatly in environmental conditions and dynamic properties. A benefit is that it allows new data to be included or flow conditions to be altered without the need to perform new simulations for each ice shelf, making the method easily scalable. The number of powerful ice flow models and available observational data supports the further use and development of data-driven statistical models, such as in Chapter 5. The model's performance was promising, given the limited number of predictors and poor coverage of fracture index locations. Predictions were highly accurate in vital locations and those with better coverage of high resolution. Improving fracture prediction is vital in predicting the potential magnitude and location of calving, which will help better determine the region's SLR.

7.1.3 Evolution of ice shelf fracture over the next 100 years

ice shelf stability is critical to the SLR contribution of the AP over the next 100 years. The tributary glaciers that previously fed the LAIS and LBIS accelerated and thinned for a decade following their collapse. As the region continues to warm, future ice shelf viability is of great concern. To investigate how potential climate forcing will affect fracture probability, we run multiple 100-year simulations with ISSM that we forced with project SMB and BMR under the no forcing, RCP2.6, RCP4.5 and RCP8.5 climate scenarios. All forcing was applied linearly to the end of the simulation. Our projections suggest that the ice shelves are resilient to the RCP2.6 and RCP4.5 forcing. There was a smaller set of predictors for the transient simulations as not all predictors are available for the transient simulation. Damage is available; however, the analytical law was not available, the damage calculation used is from Pralong and Funk (2005). The model was trained using the high-resolution fracture index data. Following this, we could predict fracture probability for the transient simulations.

As the forcing increased, fracture probability became higher on floating ice in some key regions, the average estimated fracture probability for the RCP4.5 scenario was 53.3% and the average fracture probability for RCP8.5 scenario was 58%. However, there was a surprising reduction in estimated fracture probability in some inflowing grounded ice regions. Since damage is an important predictor for the statistical model, this may indicate that the damage law applied is not appropriate for some regions. The regions that reduced fracture probability the most are the fast flowing glaciers of the GVIIS. Likely, the velocity of these regions contributed to poor damage calculation using the (Pralong and Funk, 2005) solution.

The primary aim of Chapter 6 was to determine how fracture probability would evolve over the next 100 years under potential climate scenarios. The key findings of the analysis in Chapter 6 suggest that the future stability of the AP ice shelves is at significant

risk if climate change is not limited over the next 100 years. As discussed throughout this thesis, the formation and propagation of fractures occur before large calving events. The significant increase in average fracture probability between RCP4.5 and RCP8.5 is a worrying result as our simplified transient simulation only forced basal melt rate and surface mass balance. Including changing ice front position and sea ice concentration would likely paint an even more dire picture. Chapter 6 was to show the potential for combining physical model projections within a statistical framework to project fracture probability under increasingly worsening climate scenarios.

7.2 Limitations and Future Work

This research has demonstrated the advantages of using statistical methods within the field of ice shelf extent and fracture modelling. We recommend that these approaches are used in future ice shelf fracture modelling studies and adapted for other applications. As the availability of glaciological and climate data expands, statistical methods offer diagnostic and prognostic capabilities. It is important to note that this research is only the first step in the application of GP models in glaciologic studies. The limitations of each study have already been highlighted in each chapter. In this section, the limitations of the research will be reviewed, and suggestions for future work are made.

A key limitation common throughout this research is the limited data. Annual satellite images are not available for all ice shelves and do not go back that far. This must be kept in mind when considering results from regression analysis as in chapter 4, with a maximum of only a 19-year time series, the sample size is relatively small. Unfortunately, getting a more complete data set will take a couple of decades. Two predictors were found to have a statistically significant relationship with ice shelf retreat; however, oceanographic forcing is

an important aspect of ice shelf stability and is the primary ablation source for the GVIIS. We could not add this into our investigation due to the lack of annual ocean temperature or basal melt data. However, further investigation into the link between basal melt and retreat is vital in understanding ice shelf retreat.

The most significant limitation of chapters 5 and 6 is poor fracture indexing of the ice shelf surface, particularly the non-fracture points. High-resolution images are not available for large sections of most ice shelves using Google Earth; the fracture index points are sparse and poorly distributed across the ice shelf surface. Google Earth was chosen as the source of satellite images as it allowed for a convenient method of indexing fractured and non-fractured locations; however, there are other satellite image repositories such as Landsat with better coverage at high resolutions. Since random effects are positioned around inducing points, this limits their level of influence. Heavy snow cover on the ice shelf surface limits fracture indexing from satellite images. Radar-based satellite sensing would help improve fracture indexing as it can penetrate the surface and find hidden fractures/crevasses. A study by King et al. (2018) conducted a ground penetrating radar survey of the Brunt Ice Shelf, allowing for a view of the ice shelf surface. Future work should incorporate multiple image sources to produce a more consistent fracture index map for each ice shelf. Doing this would greatly improve the quality of the model prediction across the entire ice shelf surface. This would greatly benefit future projections of fracture probability as the initial fracture probability would be based on observations rather than predictions.

A further limitation is the small choice of predictors. This was unavoidable for the transient simulations in Chapter 6, there is a limited set of predictors that can be calculated. However, there is scope to include more predictors in the non transient model. There are a number of key predictors that could be added; however, the priority of further work should be to include sea-ice concentrations at the ice front and meltwater on the surface. Studies by Massom et al. (2018) and Holt and Glasser (2022), and the results from Chapter 4 all

highlight the key role that sea ice concentration plays in reducing calving and hydrofracture triggered by excess meltwater was the primary driver of the Larsen B collapse (Leeson et al., 2020; Broeke, 2005). Expanding the set of predictors would better describe the data, particularly at the ice front. This would allow for more predictions to be made about the potential for calving.

The MCMC scheme employed in chapters 5 and 6 is a powerful tool that opens the door for using more complex and versatile GP models in ice shelf studies. The inducing point approximation requires far fewer inducing points than available data; however, the GPflow package did not allow for more than around 200 inducing points; whether this has a detrimental effect on the results is unknown. A further improvement that could be made is to incorporate variable selection such that the coefficients of the predictors can change for each ice shelf. In terms of the physical modelling, as mentioned, the transient damage module in the ISSM model is still under construction. The analytical damage solution was not available. We used the Pralong and Funk (2005) damage calculation. This method was developed for Alpine glaciers, its validity for the use of ice shelves is unclear. Further work could compare the two damage calculation methods to help understand how damage differs between Alpine glaciers, ice shelves and ice shelf tributary glaciers.

Appendix One

Appendix 1

This appendix contains the code or links to code used throughout this thesis.

In chapter 3, Climate Data Operators (CDO) are used to manipulate RACMO2.3 data. Below is the R script used to extract the annual data within the ice-shelf extent. All quantile regressions are calculated using the quantreg package. Link: https://cran.r-project.org/web/packages/quantreg/quantreg.pdf

```
source("http://bioconductor.org/biocLite.R")
biocLite("rhdf5")
library(rhdf5)
library(rgdal)
library(raster)
library(ncdf4)
pr <- "+proj=laea +lat_0=-90 +ellps=WGS84 +datum=WGS84 +no_defs +
    towgs84=0,0,0"
dump<- h5dump("C:/Users/Marko/Downloads/AntPen_mass_balance_
    1994-2016.h5",recursive = TRUE)
test_brick <- raster(dump$net_mass_balance)
flpbrick <-flip(test_brick,direction = "y")
```

```
flpbrick <- setExtent(flpbrick, new_extent2)
crs(flpbrick) <- "+init=epsg:4326"
proj_brick <-  projectRaster(flpbrick, crs=pr)
new_extent2 <- extent(-78.375, -59.625, -73.625, -65.625)
pr <- "+proj=laea +lat_0=-90 +ellps=WGS84 +datum=WGS84 +no_defs +
    towgs84=0,0,0"
dump<- h5dump("Z:/AntPen_height_changes_1994-2017.h5",recursive =
    TRUE)
test_brick <- brick(dump$h_altimetry)
flpbrick <-flip(test_brick,direction = "y")
flpbrick <- setExtent(flpbrick, new_extent2)
crs(flpbrick) <- "+init=epsg:4326"
proj_brick <-  projectRaster(flpbrick, crs=pr)
larsen_b <- readOGR("LarsenB_all_EA_areas.shp")
larsen_b <- spTransform(larsen_b,crs(pr))
#Larsen C ice-shelf
larsen_c <- readOGR("LarsenC_all_EA_areas.shp")
larsen_c <- spTransform(larsen_c,crs(pr))
# GVIIS CENTER
GVI_CENTER <- readOGR("George_centre_EA_area.shp") # Load in
    Center shapefile
GVI_C<-spTransform(GVI_CENTER,crs(pr)) # change projection
GNC <- GVI_C[GVI_C$year==6,] # Isolate the Northern section of the
     centre
GSC <- GVI_C[GVI_C$year==7,] # Isolate the southern section of the
     centre
```

```
#George VI North
GVI_North <- readOGR("NGeorgeVI_all_EA_areas.shp")
GVI_North <- spTransform(GVI_North,crs(pr))
#George VI South
GVI_South <- readOGR("SGeorgeVI_all_EA_areas.shp")
GVI_South <- spTransform(GVI_South,crs(pr))
#Wilkins
Wilkins <- readOGR("Wilkins_all_EA_areas_09.shp")
Wilkins <- spTransform(Wilkins,crs(pr))
day = c(1:31)
nc_time <- 1:94
nc1994 <- nc_time[1:4]
nc1995 <- nc_time[5:8]
nc1996 <- nc_time[9:12]
nc1997 <- nc_time[13:16]
nc1998 <- nc_time[17:20]
nc1999 <- nc_time[21:24]
nc2000 <- nc_time[25:28]
nc2001 <- nc_time[29:32]
nc2002 <- nc_time[33:36]
nc2003 <- nc_time[37:40]
nc2004 <- nc_time[41:44]
nc2005 <- nc_time[45:48]
nc2006 <- nc_time[49:52]
nc2007 <- nc_time[53:56]
nc2008 <- nc_time[57:60]
```

```
nc2009 <- nc_time[61:64]
nc2010<- nc_time[65:68]
nc2011<- nc_time[69:72]
nc2012<- nc_time[73:76]
nc2013<- nc_time[77:80]
nc2014<- nc_time[81:84]
nc2015<- nc_time[85:88]
nc2016<- nc_time[89:92]
##############
###############
#############
months <- c("jan","feb","mar","apr","may","jun","jul","aug","sep",
    "oct","nov","dec")
#### Larsen B
years_lb <- 1994:2012
for(j in years_lb){
  valtest <-list()
  for (i in get(paste("nc",j,sep=""))){
    output <- extract(proj_brick[[paste("layer.",i,sep="")]],
        larsen_b[larsen_b$year==j,], df=TRUE)
    valtest[i] <- mean(output[[2]], na.rm=TRUE)
  }
  #valtest[[1]] <- NULL
  assign(paste("lbmean",j,sep=""),unlist(valtest))
}
#### Larsen C
```

```
years_lc <- 1994:2016
for(j in years_lc){
  valtest <-list()
  for (i in get(paste("nc",j,sep=""))){
    output <- extract(proj_brick[[paste("layer.",i,sep="")]],
        larsen_c[larsen_c$year==j,],df=TRUE)
    valtest[i] <- mean(output[[2]],na.rm=TRUE)
  }
  #valtest[[1]] <- NULL
  assign(paste("lcmean",j,sep=""),unlist(valtest))
}
#### George VI South
years_gvis <- 2002:2016
for(j in years_gvis){
  valtest <-list()
  for (i in get(paste("nc",j,sep=""))){
    output <- extract(proj_brick[[paste("layer.",i,sep="")]], bind
        (GVI_South[GVI_South$year==j,],GSC),df=TRUE)
    valtest[i] <- mean(output[[2]],na.rm=TRUE)
  }
  #valtest[[1]] <- NULL
  assign(paste("gvismean",j,sep=""),unlist(valtest))
}
##### George VI North
years_gvin <- 2000:2016
for(j in years_gvin){
```

```
  valtest <-list()
  for (i in get(paste("nc",j,sep=""))){
    output <- extract(proj_brick[[paste("layer.",i,sep="")]], bind
        (GVI_North[GVI_North$year==j,],GNC),df=TRUE)
    valtest[i] <- mean(output[[2]],na.rm=TRUE)
  }
  #valtest[[1]] <- NULL
  assign(paste("gvinmean",j,sep=""),unlist(valtest))
}
###Wilkins
years_w <- 1994:2016
for(j in years_w){
  valtest <-list()
  for (i in get(paste("nc",j,sep=""))){
    output <- extract(proj_brick[[paste("layer.",i,sep="")]],
        Wilkins[Wilkins$year==j,],df=TRUE)
    valtest[i] <- mean(output[[2]],na.rm=TRUE)
  }
  #valtest[[1]] <- NULL
  assign(paste("Wmean",j,sep=""),unlist(valtest))
}
GVISmean_matrix <- cbind(gvismean2002,gvismean2003,gvismean2004,
    gvismean2005,gvismean2006,
                                gvismean2007,gvismean2008,gvismean2009,
                                    gvismean2010,gvismean2011,gvismean2012
                                    ,gvismean2013,
```

```
                                gvismean2014 , gvismean2015 , gvismean2016 )

GVINmean_matrix <- cbind( gvinmean2000 , gvinmean2001 , gvinmean2002 ,
    gvinmean2003 , gvinmean2004 , gvinmean2005 , gvinmean2006 ,
                                gvinmean2007 , gvinmean2008 , gvinmean2009 ,
                                    gvinmean2010 , gvinmean2011 , gvinmean2012
                                    , gvinmean2013 ,
                                gvinmean2014 , gvinmean2015 , gvinmean2016 )

LBmean_matrix <- cbind( lbmean1994 , lbmean1995 , lbmean1996 , lbmean1997
    , lbmean1998 , lbmean1999 ,
                                lbmean2000 , lbmean2001 , lbmean2002 , lbmean2003
                                    , lbmean2004 , lbmean2005 , lbmean2006 ,
                                    lbmean2007 , lbmean2008 , lbmean2009 ,
                                lbmean2010 , lbmean2011 , lbmean2012 )

LCmean_matrix <- cbind( lcmean1994 , lcmean1995 , lcmean1996 , lcmean1997
    , lcmean1998 , lcmean1999 , lcmean2000 ,
                                lcmean2001 , lcmean2002 , lcmean2003 , lcmean2004
                                    , lcmean2005 , lcmean2006 , lcmean2007 ,
                                    lcmean2008 , lcmean2009 ,
                                lcmean2010 , lcmean2011 , lcmean2012 , lcmean2013
                                    , lcmean2014 , lcmean2015 , lcmean2016 )

WILKmean_matrix <- cbind( Wmean1994 , Wmean1995 , Wmean1996 , Wmean1997 ,
    Wmean1998 , Wmean1999 , Wmean2000 , Wmean2001 , Wmean2002 , Wmean2003 ,
```

```
    Wmean2004,
                                    Wmean2005,Wmean2006,Wmean2007,Wmean2008,
                                        Wmean2009,Wmean2010,Wmean2011,
                                        Wmean2012,Wmean2013,Wmean2014,
                                        Wmean2015,Wmean2016)


spatialmeanLB <- t(LBmean_matrix)
spatialmeanLC <- t(LCmean_matrix)
spatialmeanGVIN <- t(GVINmean_matrix)
spatialmeanGVIS <- t(GVISmean_matrix)
spatialmeanW <- t(WILKmean_matrix)
SMB_area_avg_outputs=rbind(spatialmeanLB,spatialmeanLC,
    spatialmeanGVIN,spatialmeanGVIS,spatialmeanW)
write.csv(SMB_area_avg_outputs,"Height_area_meanFINAL2020.csv")

# cdo test script
# Extract method test
library(rgdal)
library(raster)
library(ncdf4)
smb_brick <- brick("smb_902.nc",varname= 'smb')
smb_layer <- smb_brick$X2010.01.16
pr <- "+proj=laea +lat_0=-90 +ellps=WGS84 +datum=WGS84 +no_defs +
    towgs84=0,0,0"
test_proj <- projectRaster(smb_layer, crs=pr )
proj_brick <- projectRaster(smb_brick, crs=pr)
plot(smb_layer,
```

```
      #xlim=c(-2e+06,2e+06),
      #ylim=c(-2e+06,2e+06),
      add=FALSE)
LarsenB_areas <- readOGR("Ice_shelf_shapefiles/LarsenBareas.shp")
LB_2010 <- LarsenB_areas[LarsenB_areas$year==2010,]
RP_LB2010 <- spTransform(LB_2010,crs(pr))
#Larsen C ice-shelf
larsen_c <- readOGR("Ice_shelf_shapefiles/LarsenC_all_EA_areas.shp
    ")
#Split each layer in shp file
LC_2001 <- larsen_c[larsen_c$year==2001,]
LC_2002 <- larsen_c[larsen_c$year==2002,]
LC_2003 <- larsen_c[larsen_c$year==2003,]
LC_2004 <- larsen_c[larsen_c$year==2004,]
LC_2005 <- larsen_c[larsen_c$year==2005,]
LC_2006 <- larsen_c[larsen_c$year==2006,]
LC_2007 <- larsen_c[larsen_c$year==2007,]
LC_2008 <- larsen_c[larsen_c$year==2008,]
LC_2009 <- larsen_c[larsen_c$year==2009,]
LC_2010 <- larsen_c[larsen_c$year==2010,]
LC_2011 <- larsen_c[larsen_c$year==2011,]
LC_2012 <- larsen_c[larsen_c$year==2012,]
#Transform each layers
RP_LC2001 <-spTransform(LC_2001,crs(pr))
RP_LC2002 <-spTransform(LC_2002,crs(pr))
RP_LC2003 <-spTransform(LC_2003,crs(pr))
```

```
RP_LC2004 <-spTransform(LC_2004,crs(pr))
RP_LC2005 <-spTransform(LC_2005,crs(pr))
RP_LC2006 <-spTransform(LC_2006,crs(pr))
RP_LC2007 <-spTransform(LC_2007,crs(pr))
RP_LC2008 <-spTransform(LC_2008,crs(pr))
RP_LC2009 <-spTransform(LC_2009,crs(pr))
RP_LC2010 <-spTransform(LC_2010,crs(pr))
RP_LC2011 <-spTransform(LC_2011,crs(pr))
RP_LC2012 <-spTransform(LC_2012,crs(pr))
#George VI North
GVI_North <- readOGR("Ice_shelf_shapefiles/NGeorgeVI_all_EA_areas.
    shp")
GVIN_2002 <- GVI_North[GVI_North$year==2002,]
GVIN_2003 <- GVI_North[GVI_North$year==2003,]
GVIN_2004 <- GVI_North[GVI_North$year==2004,]
GVIN_2005 <- GVI_North[GVI_North$year==2005,]
GVIN_2006 <- GVI_North[GVI_North$year==2006,]
GVIN_2007 <- GVI_North[GVI_North$year==2007,]
GVIN_2008 <- GVI_North[GVI_North$year==2008,]
GVIN_2009 <- GVI_North[GVI_North$year==2001,]
RP_GVIN2002 <-spTransform(GVIN_2002,crs(pr))
RP_GVIN2003 <-spTransform(GVIN_2003,crs(pr))
RP_GVIN2004 <-spTransform(GVIN_2004,crs(pr))
RP_GVIN2005 <-spTransform(GVIN_2005,crs(pr))
RP_GVIN2006 <-spTransform(GVIN_2006,crs(pr))
RP_GVIN2007 <-spTransform(GVIN_2007,crs(pr))
```

```
RP_GVIN2008 <-spTransform(GVIN_2008,crs(pr))
RP_GVIN2009 <-spTransform(GVIN_2009,crs(pr))
#George VI South
GVI_South <- readOGR("Ice_shelf_shapefiles/SGeorgeVI_all_EA_areas.
    shp")
GVIS_2003 <- GVI_South[GVI_South$year==2003,]
GVIS_2004 <- GVI_South[GVI_South$year==2004,]
GVIS_2005 <- GVI_South[GVI_South$year==2005,]
GVIS_2006 <- GVI_South[GVI_South$year==2006,]
GVIS_2007 <- GVI_South[GVI_South$year==2007,]
GVIS_2008 <- GVI_South[GVI_South$year==2008,]
GVIS_2009 <- GVI_South[GVI_South$year==2009,]
RP_GVIS2003 <-spTransform(GVIS_2003,crs(pr))
RP_GVIS2004 <-spTransform(GVIS_2004,crs(pr))
RP_GVIS2005 <-spTransform(GVIS_2005,crs(pr))
RP_GVIS2006 <-spTransform(GVIS_2006,crs(pr))
RP_GVIS2007 <-spTransform(GVIS_2007,crs(pr))
RP_GVIS2008 <-spTransform(GVIS_2008,crs(pr))
RP_GVIS2009 <-spTransform(GVIS_2009,crs(pr))


#Wilkins
Wilkins <- readOGR("Ice_shelf_shapefiles/Wilkins_all_EA_areas_09.
    shp")
W_1996 <- Wilkins[Wilkins$year==1996,]
W_1997 <- Wilkins[Wilkins$year==1997,]
W_1998 <- Wilkins[Wilkins$year==1998,]
```

```
W_1999 <- Wilkins[Wilkins$year==1999,]
W_2000 <- Wilkins[Wilkins$year==2000,]
W_2001 <- Wilkins[Wilkins$year==2001,]
W_2002 <- Wilkins[Wilkins$year==2002,]
W_2003 <- Wilkins[Wilkins$year==2003,]
W_2004 <- Wilkins[Wilkins$year==2004,]
W_2005 <- Wilkins[Wilkins$year==2005,]
W_2006 <- Wilkins[Wilkins$year==2006,]
W_2007 <- Wilkins[Wilkins$year==2007,]
W_2008 <- Wilkins[Wilkins$year==2008,]
W_2009 <- Wilkins[Wilkins$year==2009,]
W_2010 <- Wilkins[Wilkins$year==2010,]
W_2011 <- Wilkins[Wilkins$year==2011,]
W_2012 <- Wilkins[Wilkins$year==2012,]
#Transform each layers
RP_W1996 <-spTransform(W_1996,crs(pr))
RP_W1997 <-spTransform(W_1997,crs(pr))
RP_W1998 <-spTransform(W_1998,crs(pr))
RP_W1999 <-spTransform(W_1999,crs(pr))
RP_W2000 <-spTransform(W_2000,crs(pr))
RP_W2001 <-spTransform(W_2001,crs(pr))
RP_W2002 <-spTransform(W_2002,crs(pr))
RP_W2003 <-spTransform(W_2003,crs(pr))
RP_W2004 <-spTransform(W_2004,crs(pr))
RP_W2005 <-spTransform(W_2005,crs(pr))
RP_W2006 <-spTransform(W_2006,crs(pr))
```

```
RP_W2007 <-spTransform(W_2007,crs(pr))
RP_W2008 <-spTransform(W_2008,crs(pr))
RP_W2009 <-spTransform(W_2009,crs(pr))
RP_W2010 <-spTransform(W_2010,crs(pr))
RP_W2011 <-spTransform(W_2011,crs(pr))
RP_W2012 <-spTransform(W_2012,crs(pr))
day = c(1:31)
nc_time<-convertDateNcdf2R("smb_902.nc",units="days",
                    origin =as.POSIXct("1800-01-01",tz="UTC"),
                    time.format=c("%Y-%m-%d"))
nc_time <- gsub("00:00:00","",nc_time)
nc_time <- gsub("12:00:00","",nc_time)
nc_time <- gsub(" ","",nc_time)
nc_time <- gsub("-",".",nc_time)
nc1996 <- nc_time[205:216]
nc1997 <- nc_time[217:228]
nc1998 <- nc_time[229:240]
nc1999 <- nc_time[241:252]
nc2000 <- nc_time[253:264]
nc2001 <- nc_time[265:276]
nc2002 <- nc_time[277:288]
nc2003 <- nc_time[289:300]
nc2004 <- nc_time[301:312]
nc2005 <- nc_time[313:324]
nc2006 <- nc_time[325:336]
nc2007 <- nc_time[337:348]
```

```
nc2008 <- nc_time[349:360]
nc2009 <- nc_time[361:372]
nc2010 <- nc_time[373:384]
nc2011 <- nc_time[385:396]
nc2012 <- nc_time[397:408]
mean(val2[[1]])
val2 <- extract(proj_brick[["X2010.03.16"]], RP_LC2010,df=TRUE)
val2[[2]]
mean(val2[[2]])
paste("RP_LC",j,sep="")
months <- c("jan","feb","mar","apr","may","jun","jul","aug","sep",
   "oct","nov","dec")
#### Larsen C
years_lc <- 2001:2012
for(j in years_lc){
  valtest <-list()
  for (i in get(paste("nc",j,sep=""))){
    output <- extract(proj_brick[[paste("X",i,sep="")]], get(paste
       ("RP_LC",j,sep="")),df=TRUE)
    valtest[i] <- mean(output[[2]])
  }
  #valtest[[1]] <- NULL
  assign(paste("lcmean",j,sep=""),unlist(valtest))
}
LCmean_matrix <- cbind(lcmean2001,lcmean2002,lcmean2003,lcmean2004
   ,lcmean2005,lcmean2006,
```

```
                                lcmean2007,lcmean2008,lcmean2009,lcmean2010
                                    ,lcmean2011,lcmean2012)
rownames(LCmean_matrix) <- months
#### George VI South
years_gvis <- 2003:2009
for(j in years_gvis){
  valtest <-list()
  for (i in get(paste("nc",j,sep=""))){
    output <- extract(proj_brick[[paste("X",i,sep="")]], get(paste
      ("RP_GVIS",j,sep="")),df=TRUE)
    valtest[i] <- mean(output[[2]])
  }
  #valtest[[1]] <- NULL
  assign(paste("gvismean",j,sep=""),unlist(valtest))
}
GVISmean_matrix <- cbind(gvismean2003,gvismean2004,gvismean2005,
   gvismean2006,
                              gvismean2007,gvismean2008,gvismean2009,
                                  gvismean2010,gvismean2011,gvismean2012
                                  )
rownames(GVISmean_matrix) <- months
##### George VI North
years_gvin <- 2002:2009
for(j in years_gvin){
  valtest <-list()
  for (i in get(paste("nc",j,sep=""))){
```

```
    output <- extract(proj_brick[[paste("X",i,sep="")]], get(paste
        ("RP_GVIN",j,sep="")),df=TRUE)
    valtest[i] <- mean(output[[2]])
  }
  #valtest[[1]] <- NULL
  assign(paste("gvinmean",j,sep=""),unlist(valtest))
}
GVINmean_matrix <- cbind(gvinmean2002,gvinmean2003,gvinmean2004,
   gvinmean2005,gvinmean2006,
                            gvinmean2007,gvinmean2008,gvinmean2009,
                               gvinmean2010,gvinmean2011,gvinmean2012
                               )
rownames(GVINmean_matrix) <- months
###Wilkins
years_w <- 1996:2012
for(j in years_w){
  valtest <-list()
  for (i in get(paste("nc",j,sep=""))){
    output <- extract(proj_brick[[paste("X",i,sep="")]], get(paste
        ("RP_W",j,sep="")),df=TRUE)
    valtest[i] <- mean(output[[2]])
  }
  #valtest[[1]] <- NULL
  assign(paste("Wmean",j,sep=""),unlist(valtest))
}
WILKmean_matrix <- cbind(Wmean1996,Wmean1997,Wmean1998,Wmean1999,
```

```
    Wmean2000,Wmean2001,Wmean2002,Wmean2003,Wmean2004,Wmean2005,
    Wmean2006,
                                    Wmean2007,Wmean2008,Wmean2009,Wmean2010,
                                        Wmean2011,Wmean2012)
rownames(WILKmean_matrix) <- months
spatialmeanLC <- t(LCmean_matrix)
spatialmeanGVIN <- t(GVINmean_matrix)
spatialmeanGVIS <- t(GVISmean_matrix)
spatialmeanW <- t(WILKmean_matrix)
SMB_area_avg_outputs=rbind(spatialmeanLC,spatialmeanGVIN,
    spatialmeanGVIS,spatialmeanW)
write.csv(SMB_area_avg_outputs,"SMB_area_avg_outputs.csv")
valtest <-list()
for (i in nc2012){
  output <- extract(proj_brick[[paste("X",i,sep="")]], RP_LC2012,
      df=TRUE)
  valtest[i] <- mean(output[[2]])
}
#valtest[[1]] <- NULL
lcmean2012 <- unlist(valtest)
LC_matrix <-cbind(lcmean2001,lcmean2002,lcmean2003,lcmean2004,
    lcmean2005,lcmean2006,
                    lcmean2007,lcmean2008,lcmean2009,lcmean2010,
                        lcmean2011,lcmean2012)
val2 <- extract(proj_brick[["X2010.01.16"]], RP_LC2010)
mydf <- data.frame(matrix())
```

```
for (i in nc_time){
  vals <- extract(proj_brick[[paste("X",i,sep="")]], RP_LC2010, df
    =TRUE)
  mydf[,i] <- vals
}
mydf <- data.frame(matrix())
for (i in nc2010){
  vals <- extract(proj_brick[[paste("X",i,sep="")]], RP_LC2010, df
    =TRUE)
  vals[1] <- NULL
  mydf[,i]
}
```

The ISSM simulations in chapters 4 and 5 are developed from tutorial code available on the ISSM documentation with help from Dr. Mathieu Morlighem. Link to documentation: https://issm.jpl.nasa.gov/documentation/tutorials/

The python code for the fracture probability model which, was developed with the help of Dr Sergio Bacallado, is below. The GPflow package was critical for this model. Parts of code from the example on the GPflow site was used. Link to example: https://bit.ly/2Yr52On

```
import pandas as pd
from scipy import interpolate
import numpy as np
from matplotlib import pyplot as plt
import geopandas as gpd
fracDFs = []
shelves = ["GVIIS", "Wilkins", "LarsenC"]
```

```
for shelf in shelves:
    ISSM_predictors = pd.read_csv("data/Transient/TrainingData/NEW
        _SETUP_"+shelf+"_ISSMoutputs_200x200.csv")
    ISSM_predictors.dropna(inplace=True)    # Drop all grid points
        with NA values
    fracs = pd.read_csv("data/Project2_3ice-shelves/High␣
        resolution␣-␣Frac_NonFrac/"+shelf+"_Frac_non_frac.csv")
    points = ISSM_predictors.loc[:,["Lat","Lon"]].to_numpy()
    fracPoints = fracs.loc[:,["Latitude","Longitude"]].to_numpy()
    linInt = interpolate.LinearNDInterpolator(points,ISSM_
        predictors.Velocity)
    for col in ISSM_predictors.columns:
        if col not in ["Lat","Lon"]:
            linInt = interpolate.LinearNDInterpolator(linInt.tri,
                ISSM_predictors[col])
            fracs[col] = linInt(fracPoints)
    fracs["shelf"] = shelf
    fracDFs.append(fracs)
fracs = pd.concat(fracDFs)
fracs.drop("Unnamed:␣0", axis=1, inplace=True)
fracs.Fractured = fracs.Fractured.astype("category")
fracs.dropna(inplace=True)
from scipy import cluster
k = 200  # Number of clusters
clust = cluster.vq.kmeans(fracs.loc[:,["Longitude","Latitude"]], k
    , iter=100, thresh=1e-05, check_finite=True)
```

```
centroids = gpd.GeoDataFrame(geometry=gpd.points_from_xy(clust
    [0][:,0],clust[0][:,1]))
centroids.crs = "EPSG:4326"

predictors = ['Velocity', 'PrincipalStress1', 'PrincipalStress2',
    'EffectiveStress', 'PrincipalStrain1', 'PrincipalStrain2',
                'EffectiveStrain', 'Thickness','Damage']

import matplotlib
import tensorflow as tf
import tensorflow_probability as tfp
from tensorflow_probability import distributions as tfd
import gpflow
from gpflow.ci_utils import ci_niter
from gpflow import set_trainable
from gpflow.utilities import print_summary, positive
gpflow.config.set_default_float(np.float64)
gpflow.config.set_default_jitter(1e-4)
gpflow.config.set_default_summary_fmt("notebook")
# convert to float64 for tfp to play nicely with gpflow in 64
f64 = gpflow.utilities.to_default_float
tf.random.set_seed(123)
%matplotlib inline

class MixedModelKernel(gpflow.kernels.Kernel):
    def __init__(self,p):
```

```
        super().__init__(active_dims=np.arange(p+3))
        self.kernelRandom = gpflow.kernels.SquaredExponential(
            active_dims=[1,2])
        self.kernelFixed = gpflow.kernels.Linear(active_dims=range
            (3,p+3))

    def K(self, X, X2=None):
        if X2 is None:
            X2 = X
        return self.kernelFixed(X,X2) + \
                tf.tensordot(tf.cast(X[:,0]==1,dtype=tf.float64),
                             tf.cast(X2[:,0]==1,dtype=tf.float64),
                                 axes=0) * self.kernelRandom(X,X2)

    def K_diag(self, X):
        return self.kernelFixed(X,X2=None,full_cov=False) + \
                tf.where(X[:,0]==1,self.kernelRandom(X,X2=None,full
                    _cov=False),0)
p = len(predictors)+1    # Number of predictors including intercept
n = fracs.shape[0]       # Number of samples
Y = fracs.Fractured.to_numpy(dtype="float64").reshape(n,1)
X = fracs.loc[:,predictors]
X = ((X-X.mean(0))/X.std(0)).to_numpy()       # Standardize
    predictors
coords = fracs.loc[:,["Longitude","Latitude"]].to_numpy()
X = np.concatenate([np.ones([X.shape[0],1]),coords,np.ones([X.
```

```
    shape[0],1]),X],axis=1)
data = (X,Y)
# Inducing variables for coefficients beta
inducing = []
for i in range(p):
    inducing.append([0]*(3+i)+[1]+[0]*(p-i-1))
# Inducing variables for random effects at k-means clustering
    locations
for i,j in clust[0]:
    inducing.append([1,i,j]+[0]*p)
inducing = np.array(inducing,dtype="float64")
kernel = MixedModelKernel(p)
model = gpflow.models.SGPMC(
    data,
    kernel=kernel,
    likelihood=gpflow.likelihoods.Bernoulli(),
    inducing_variable=inducing,
    num_latent_gps=1,
)
## These settings reproduce something quite similar to the model
    without random effects,
## i.e. sigma^2_random ~ 0
#set_trainable(model.kernel.kernelRandom.variance,False)
#model.kernel.kernelRandom.variance.assign(0.0001)
#model.kernel.kernelFixed.variance.prior = tfd.Gamma(f64(1.0), f64
    (1.0))
```

```
# Put exponential priors on the variance of fixed and random
    effects
model.kernel.kernelRandom.variance.prior = tfd.Gamma(f64(1.0), f64
    (1.0))
model.kernel.kernelFixed.variance.prior = tfd.Gamma(f64(1.0), f64
    (1.0))
#ADD PRIOR TO LENGTHSCALE
model.kernel.kernelRandom.lengthscales.prior = tfd.Normal(f64(0.0)
    , f64(1.0))
# Fix the lengthscale of the random effects RBF kernel, and fix
    the inducing points
#set_trainable(model.kernel.kernelRandom.lengthscales, False)
#model.kernel.kernelRandom.lengthscales.assign(0.25)
set_trainable(model.inducing_variable,False)
gpflow.utilities.print_summary(model)
model.kernel.kernelRandom.lengthscales.prior
optimizer = gpflow.optimizers.Scipy()
optimizer.minimize(model.training_loss, model.trainable_variables,
     options={"maxiter": 1000})
print(f"log␣posterior␣density␣at␣optimum:␣{model.log_posterior_
    density()}")
gpflow.utilities.print_summary(model)
preds = (model.predict_f(X)[0].numpy().flatten()>0.5)
(fracs.Fractured==preds).sum()/len(preds)
coefs = model.predict_f(inducing)[0].numpy()
print("%20.20s:␣%.3f"%("Intercept",coefs[0]))
```

```
for i in range(len(predictors)):
    print("%20.20s: %.3f"%(predictors[i],coefs[i+1]))
num_burnin_steps = ci_niter(5000)
num_samples = ci_niter(10000)
# Note that here we need model.trainable_parameters, not trainable
   _variables - only parameters can have priors!
hmc_helper = gpflow.optimizers.SamplingHelper(
    model.log_posterior_density, model.trainable_parameters
)
hmc = tfp.mcmc.HamiltonianMonteCarlo(
    target_log_prob_fn=hmc_helper.target_log_prob_fn, num_leapfrog
       _steps=10, step_size=0.01
)
adaptive_hmc = tfp.mcmc.SimpleStepSizeAdaptation(
    hmc, num_adaptation_steps=10, target_accept_prob=f64(0.75),
       adaptation_rate=0.1
)
@tf.function
def run_chain_fn():
    return tfp.mcmc.sample_chain(
        num_results=num_samples,
        num_burnin_steps=num_burnin_steps,
        current_state=hmc_helper.current_state,
        kernel=adaptive_hmc,
        trace_fn=lambda _, pkr: pkr.inner_results.is_accepted,
    )
```

```
from time import time
s1=time()


samples1, _ = run_chain_fn()
#samples2, _ = run_chain_fn()
#samples3, _ = run_chain_fn()
constrained_samples1 = hmc_helper.convert_to_constrained_values(
    samples1)
#constrained_samples2 = hmc_helper.convert_to_constrained_values(
    samples2)
#constrained_samples3 = hmc_helper.convert_to_constrained_values(
    samples3)


e1 = time()
print((e1-s1)/3600)
cstensor1 = tf.convert_to_tensor(constrained_samples1[0])
cstensor1 = tf.reshape(cstensor1,[10000,1,210])
cstensor2 = tf.convert_to_tensor(constrained_samples2[0])
cstensor2 = tf.reshape(cstensor2,[10000,1,210])
cstensor3 = tf.convert_to_tensor(constrained_samples3[0])
cstensor3 = tf.reshape(cstensor3,[5000,1,133])
multi_chains = tf.concat([cstensor1,cstensor2],1)
multi_chains
from numpy import random
randy=random.randint(low=14, high=k, size=(10))
ConVergTestPoints = list(range(0, 12))
```

```
ConVergTestPoints.extend(randy)
ConVergTestPoints
MultiCHAIN = multi_chains.numpy()
MultiCHAINsub = MultiCHAIN[:,:,ConVergTestPoints]
CT = tfp.mcmc.potential_scale_reduction(MultiCHAINsub)
CT.numpy()

matplotlib.rcParams['font.size'] = 12
param_to_name = {param: name for name, param in gpflow.utilities.
    parameter_dict(model).items()}
name_to_index = {param_to_name[param]: i for i, param in enumerate
    (model.trainable_parameters)}
hyperparameters = [".kernel.kernelRandom.variance", ".kernel.
    kernelFixed.variance",".kernel.kernelRandom.lengthscales"]

plt.figure(figsize=(8, 4))
for param_name in hyperparameters:
     plt.plot(constrained_samples1[name_to_index[param_name]],
         label=param_name)
plt.legend(('Random Variance', 'Fixed Variance', 'Lengthscale'),
    bbox_to_anchor=(1, 1))
plt.xlabel("HMC iteration",fontsize=18)
_ = plt.ylabel("Hyperparameter value",fontsize=18)
plt.tight_layout()
#plt.savefig('HS_Transient_HyperValues2.png',dpi=300)
coef_samples = model.predict_f_samples(inducing[0:p,:],10000).
```

```
    numpy()
coef_samples.shape
coef_samples = pd.DataFrame(coef_samples[:,:,0])
matplotlib.rcParams['font.size'] = 16
from matplotlib.ticker import FormatStrFormatter
coef_samples.columns = ["Intercept"]+predictors
coef_samples.hist(figsize=[20,20],bins=50,grid=False)
plt.tight_layout()
plt.xticks(range(3))
#plt.savefig('HS_Transient_Distributions.png',dpi=300)
plt.show()
pd.plotting.scatter_matrix(coef_samples,figsize=(20,20))
plt.xticks(range(1))
plt.show()
ISSM_DFs = []
shelves = ["GVIIS", "Wilkins", "LarsenC"]
for shelf in shelves:
    ISSM_predictors = pd.read_csv("data/Transient/TrainingData/NEW
        _SETUP_"+shelf+"_ISSMoutputs_200x200.csv")
    #ISSM_predictors = pd.read_csv("data/Transient/Scenario4/"+
        shelf+"_Damage_scenario4(updated).csv")
    ISSM_predictors.dropna(inplace=True)    # Drop all grid points
        with NA values
    ISSM_DFs.append(ISSM_predictors)
ISSM_predictors = pd.concat(ISSM_DFs)
Xnew = ISSM_predictors.loc[:,predictors]
```

```
Xnew = ((Xnew-Xnew.mean(0))/Xnew.std(0)).to_numpy()        #
    Standardize predictors
coords = ISSM_predictors.loc[:,["Lon","Lat"]].to_numpy()
Xnew = np.concatenate([np.ones([Xnew.shape[0],1]),coords,np.ones([
    Xnew.shape[0],1]),Xnew], axis=1)
preds = model.predict_y(Xnew)
latentfun = model.predict_f(Xnew)
ISSM_predictors["Predicted_y"] = preds[0].numpy()
ISSM_predictors["Predicted_y_var"] = preds[1].numpy()
floating=ISSM_predictors.loc[ISSM_predictors["Float"]==1]
np.mean(floating["Predicted_y"])
np.mean(ISSM_predictors["Predicted_y"])
from pyproj import Proj, transform
wgs84=Proj("+init=EPSG:4326")
AntPol=Proj("+init=EPSG:3031")
#TESTfracs.Longitude
#TESTfracs.Latitude
wgs84lon=list(ISSM_predictors.Lon)
wgs84lat=list(ISSM_predictors.Lat)
xx, yy = transform(wgs84, AntPol, wgs84lon, wgs84lat)
ISSM_predictors.insert(2, "antpolLON", xx, True)
ISSM_predictors.insert(2, "antpolLAT", yy, True)

#TESTgeoFracs = gpd.GeoDataFrame(TESTfracs,geometry=gpd.points_
    from_xy(TESTfracs.antpolLON,TESTfracs.antpolLAT))
iceshelves = gpd.read_file("data/antarctica-icesheet-polygons-3857
```

```
    ")
#TESTgeoFracs.crs = "EPSG:3031"
iceshelves.to_crs("EPSG:3031",inplace=True)
ISSM_predictors = gpd.GeoDataFrame(ISSM_predictors,
                                   geometry=gpd.points_from_xy(
                                       ISSM_predictors.antpolLON,
                                       ISSM_predictors.antpolLAT))
ISSM_predictors.crs = "EPSG:3031"

matplotlib.rcParams['font.size'] = 18
fig, (ax1, ax2) = plt.subplots(ncols=2, sharex=True, sharey=True,
    figsize=(20,20))
base=iceshelves.plot(ax=ax1,color="lightgrey",edgecolor="grey")
for axis in ['top','bottom','left','right']:
  ax1.spines[axis].set_linewidth(1)
plt.xlim([-2662213,-1582943])
plt.ylim([400000,1600000])
plt.xticks([])
plt.yticks([])
ISSM_predictors.plot(ax=ax1,column="Predicted_y",markersize=6,
    alpha=0.7,cmap='viridis',
                         legend=True,
                         legend_kwds=dict(orientation='horizontal',
                             label='Posterior mean of p(y=1 | x)', pad
                             =0.02))
```

```
base1=iceshelves.plot(ax=ax2,color="lightgrey",edgecolor="grey")
for axis in ['top','bottom','left','right']:
  ax2.spines[axis].set_linewidth(1)
plt.xlim([-2662213,-1582943])
plt.ylim([400000,1600000])
plt.xticks([])
plt.yticks([])
ISSM_predictors.plot(ax=base1,column="Predicted_y_var",markersize
    =6,alpha=0.7,cmap='viridis',
                         legend=True,
                         legend_kwds=dict(orientation='horizontal',
                            label='Posterior␣variance␣of␣p(y=1␣|␣x)',
                            pad=0.02, ticks= [0.05,0.10,0.15,0.20]))

plt.tight_layout(pad=1.0, h_pad=0.0)

coords = ISSM_predictors.loc[:,["Lon","Lat"]].to_numpy()
Xnew = np.concatenate([np.ones([coords.shape[0],1]),coords,np.
    zeros((coords.shape[0],p+3))],axis=1)

preds = model.predict_f(Xnew)
ISSM_predictors["Predicted_g"] = preds[0].numpy()
ISSM_predictors["Predicted_g_var"] = preds[1].numpy()

matplotlib.rcParams['font.size'] = 18
fig, (ax1, ax2) = plt.subplots(ncols=2, sharex=True, sharey=True,
```

```
    figsize=(20,20))
base=iceshelves.plot(ax=ax1,color="lightgrey",edgecolor="grey")
for axis in ['top','bottom','left','right']:
  ax1.spines[axis].set_linewidth(1)
plt.xlim([-2662213,-1582943])
plt.ylim([400000,1600000])
plt.xticks([])
plt.yticks([])
ISSM_predictors.plot(ax=ax1,column="Predicted_g",markersize=6,
    alpha=0.7,cmap='viridis',
                         legend=True,
                         legend_kwds=dict(orientation='horizontal',
                             label='Posterior mean of random effects',
                             pad=0.02))


base1=iceshelves.plot(ax=ax2,color="lightgrey",edgecolor="grey")
for axis in ['top','bottom','left','right']:
  ax2.spines[axis].set_linewidth(1)
plt.xlim([-2662213,-1582943])
plt.ylim([400000,1600000])
plt.xticks([])
plt.yticks([])
ISSM_predictors.plot(ax=base1,column="Predicted_g_var",markersize
    =6,alpha=0.7,cmap='viridis',
                         legend=True,
                         legend_kwds=dict(orientation='horizontal',
```

```
                    label='Posterior variance of random
                    effects', pad=0.02))

plt.tight_layout(pad=1.0, h_pad=0.0)
```

References

Adusumilli, S., H. A. Fricker, M. R. Siegfried, L. Padman, F. S. Paolo, and S. R. Ligtenberg (2018). "Variable Basal Melt Rates of Antarctic Peninsula Ice Shelves, 1994–2016". *Geophysical Research Letters* 45.9, pp. 4086–4095. DOI: 10.1002/2017GL076652.

Albrecht, T. and A. Levermann (2014). "Fracture-induced softening for large-scale ice dynamics". *The Cryosphere* 8.2, pp. 587–605. DOI: 10.5194/tc-8-587-2014.

Ali, A. (1996). "Vulnerability of Bangladesh to climate change and sea level rise through tropical cyclones and storm surges". *Water, Air, and Soil Pollution*. Vol. 92. 1-2. Springer, Dordrecht, pp. 171–179. DOI: 10.1007/978-94-017-1053-4{_}16.

Alley, K. E., T. A. Scambos, J. Z. Miller, D. G. Long, and M. MacFerrin (2018). "Quantifying vulnerability of Antarctic ice shelves to hydrofracture using microwave scattering properties". *Remote Sensing of Environment* 210, pp. 297–306. DOI: 10.1016/J.RSE.2018.03.025.

Alley, K. E., T. A. Scambos, M. R. Siegfried, and H. A. Fricker (2016). "Impacts of warm water on Antarctic ice shelf stability through basal channel formation". *Nature Geoscience* 9.4, pp. 290–293. DOI: 10.1038/ngeo2675.

Alley, R. B., H. J. Horgan, I. Joughin, K. M. Cuffey, T. K. Dupont, B. R. Parizek, S. Anandakrishnan, and J. Bassis (2008). "A simple law for ice-shelf calving". *Science* 322.5906, p. 1344. DOI: 10.1126/science.1162543.

Arcone, S. A., J. H. Lever, L. E. Ray, B. S. Walker, G. Hamilton, and L. Kaluzienski (2016). "Ground-penetrating radar profiles of the McMurdo Shear Zone, Antarctica, acquired with an unmanned rover: Interpretationof crevasses, fractures, and folds within firn and marine ice". *Geophysics* 81.1, WA21–WA34. DOI: 10.1190/GEO2015-0132.1.

Arendt, A. A., S. B. Luthcke, C. F. Larsen, W. Abdalati, W. B. Krabill, and M. J. Beedle (2008). "Validation of high-resolution GRACE mascon estimates of glacier mass changes in the St. Elias Mountains, Alaska, USA, using aircraft laser altimetry". *Journal of Glaciology* 54.188, pp. 778–787. DOI: 10.3189/002214308787780067.

Aschwanden, A., E. Bueler, C. Khroulev, and H. Blatter (2012). "An enthalpy formulation for glaciers and ice sheets". *Journal of Glaciology* 58.209, pp. 441–457. DOI: 10.3189/2012JoG11J088.

Aschwanden, A., M. A. Fahnestock, M. Truffer, D. J. Brinkerhoff, R. Hock, C. Khroulev, R. Mottram, and S. Abbas Khan (2019). "Contribution of the Greenland Ice Sheet to sea level over the next millennium". *Science Advances* 5.6, eaav9396. DOI: 10.1126/sciadv.aav9396.

Ashmore, D. W., B. Hubbard, A. Luckman, B. Kulessa, S. Bevan, A. Booth, P. K. Munneke, M. O'Leary, H. Sevestre, and P. R. Holland (2017). "Ice and firn heterogeneity within Larsen C Ice Shelf from borehole optical televiewing". *Journal of Geophysical Research: Earth Surface* 122.5, pp. 1139–1153. DOI: 10.1002/2016JF004047.

Balica, S. F., N. G. Wright, and F. van der Meulen (2012). "A flood vulnerability index for coastal cities and its use in assessing climate change impacts". *Natural Hazards* 64.1, pp. 73–105. DOI: 10.1007/s11069-012-0234-1.

Banwell, A. F., M. Caballero, N. S. Arnold, N. F. Glasser, L. M. Cathles, and D. R. MacAyeal (2014). "Supraglacial lakes on the Larsen B ice shelf, Antarctica, and at Paakitsoq, West Greenland: A comparative study". *Annals of Glaciology* 55.66, pp. 1–8. DOI: 10.3189/2014AoG66A049.

Banwell, A. F., D. R. MacAyeal, and O. V. Sergienko (2013). "Breakup of the Larsen B Ice Shelf triggered by chain reaction drainage of supraglacial lakes". *Geophysical Research Letters* 40.22, pp. 5872–5876. DOI: 10.1002/2013GL057694.

Banwell, A. F., I. C. Willis, G. J. Macdonald, B. Goodsell, and D. R. MacAyeal (2019). "Direct measurements of ice-shelf flexure caused by surface meltwater ponding and drainage". *Nature Communications* 10.1, pp. 1–10. DOI: 10.1038/s41467-019-08522-5.

Barrand, N. E., D. G. Vaughan, N. Steiner, M. Tedesco, P. Kuipers Munneke, M. R. Van Den Broeke, and J. S. Hosking (2013). "Trends in Antarctic Peninsula surface melting conditions from observations and regional climate modeling". *Journal of Geophysical Research: Earth Surface* 118.1, pp. 315–330. DOI: 10.1029/2012JF002559.

Baur, D., M. Saisana, and N. Schulze (2004). "Modelling the effects of meteorological variables on ozone concentration - A quantile regression approach". *Atmospheric Environment* 38.28, pp. 4689–4699. DOI: 10.1016/j.atmosenv.2004.05.028.

Benn, D. I., C. R. Warren, and R. H. Mottram (2007). "Calving processes and the dynamics of calving glaciers". *Earth-Science Reviews* 82.3-4, pp. 143–179. DOI: 10.1016/J.EARSCIREV.2007.02.002.

Bentley, C. R. (1993). "Antarctic mass balance and sea level change". *Eos, Transactions American Geophysical Union* 74.50, pp. 585–586. DOI: 10.1029/93EO00653.

Bentley, M. J., D. A. Hodgson, D. E. Sugden, S. J. Roberts, J. A. Smith, M. J. Leng, and C. Bryant (2005). "Early Holocene retreat of the George VI Ice Shelf, Antarctic Peninsula". *Geology* 33.3, pp. 173–176. DOI: 10.1130/G21203.1.

Berthier, E., T. A. Scambos, and C. A. Shuman (2012). "Mass loss of Larsen B tributary glaciers (Antarctic Peninsula) unabated since 2002". *Geophysical Research Letters* 39.13, n/a–n/a. DOI: 10.1029/2012GL051755.

Betancourt, M. (2017). *A Conceptual Introduction to Hamiltonian Monte Carlo*.

Bevan, S., A. Luckman, H. Hendon, and G. Wang (2020). "The 2020 Larsen C Ice Shelf surface melt is a 40-year record high". *The Cryosphere* 14.10, pp. 3551–3564. DOI: 10.5194/tc-14-3551-2020.

Bhattachan, A., M. D. Jurjonas, A. C. Moody, P. R. Morris, G. M. Sanchez, L. S. Smart, P. J. Taillie, R. E. Emanuel, and E. L. Seekamp (2018). *Sea level rise impacts on rural coastal social-ecological systems and the implications for decision making*. DOI: 10.1016/j.envsci.2018.10.006.

Bindschadler, R., T. A. Scambos, H. Rott, P. Skvarca, and P. Vornberger (2002). "Ice dolines on Larsen Ice Shelf, Antarctica". *Annals of Glaciology* 34, pp. 283–290. DOI: 10.3189/172756402781817996.

Bindschadler, R. A., S. Nowicki, A. Abe-OUCHI, A. Aschwanden, H. Choi, J. Fastook, G. Granzow, R. Greve, G. Gutowski, U. Herzfeld, C. Jackson, J. Johnson, C. Khroulev, A. Levermann, W. H. Lipscomb, M. A. Martin, M. Morlighem, B. R. Parizek, D. Pollard, S. F. Price, D. Ren, F. Saito, T. Sato, H. Seddik, H. Seroussi, K. Takahashi, R. Walker, and W. L. Wang (2013). "Ice-sheet model sensitivities to environmental forcing and their use in projecting future sea level (the SeaRISE project)". *Journal of Glaciology* 59.214, pp. 195–224. DOI: 10.3189/2013JoG12J125.

Blatter, H., R. Greve, and A. Abe-Ouchi (2011). *A short history of the thermomechanical theory and modeling of glaciers and ice sheets*. DOI: 10.3189/002214311796406059.

Borstad, C. P., A. Khazendar, E. Larour, M. Morlighem, E. Rignot, M. P. Schodlok, and H. Seroussi (2012). "A damage mechanics assessment of the Larsen B ice shelf prior to collapse: Toward a physically-based calving law". *Geophysical Research Letters* 39.17. DOI: 10.1029/2012GL053317.

Borstad, C. P., E. Rignot, J. Mouginot, and M. P. Schodlok (2013). "Creep deformation and buttressing capacity of damaged ice shelves: Theory and application to Larsen C ice shelf". *The Cryosphere* 7.6, pp. 1931–1947. DOI: 10.5194/tc-7-1931-2013.

Borstad, C., D. McGrath, and A. Pope (2017). "Fracture propagation and stability of ice shelves governed by ice shelf heterogeneity". *Geophysical Research Letters* 44.9, pp. 4186–4194. DOI: 10.1002/2017GL072648.

Braun, M., A. Humbert, and A. Moll (2009). "Changes of Wilkins Ice Shelf over the past 15 years and inferences on its stability". *The Cryosphere* 3.1, pp. 41–56. DOI: 10.5194/tc-3-41-2009.

Braun, M. and A. Humbert (2009). "Recent retreat of wilkins ice shelf reveals new insights in ice shelf breakup mechanisms". *IEEE Geoscience and Remote Sensing Letters* 6.2, pp. 263–267. DOI: 10.1109/LGRS.2008.2011925.

Broeke, M. van den (2005). "Strong surface melting preceded collapse of Antarctic Peninsula ice shelf". *Geophysical Research Letters* 32.12, pp. 1–4. DOI: 10.1029/2005GL023247.

Broeke, M. R. van den, E. M. Enderlin, I. M. Howat, P. Kuipers Munneke, B. P. Noël, W. Jan Van De Berg, E. Van Meijgaard, and B. Wouters (2016). "On the recent contribution of the Greenland ice sheet to sea level change". *The Cryosphere* 10.5, pp. 1933–1946. DOI: 10.5194/tc-10-1933-2016.

Brunkard, J., G. Namulanda, and R. Ratard (2008). "Hurricane katrina deaths, Louisiana, 2005". *Disaster Medicine and Public Health Preparedness* 2.4, pp. 215–223. DOI: 10.1097/DMP.0b013e31818aaf55.

Burton, M. L. and M. J. Hicks (2005). "Hurricane Katrina : Preliminary Estimates of Commercial and Public Sector Damages". *Defense* September.

Campbell, S., S. Roy, K. Kreutz, S. A. Arcone, E. C. Osterberg, and P. Koons (2013). "Strain-rate estimates for crevasse formation at an alpine ice divide: Mount Hunter, Alaska". *Annals of Glaciology* 54.63, pp. 200–208. DOI: 10.3189/2013AoG63A266.

Cape, M. R., M. Vernet, P. Skvarca, S. Marinsek, T. Scambos, and E. Domack (2015). "Foehn winds link climate-driven warming to ice shelf evolution in Antarctica". *Journal of Geophysical Research* 120.21, pp. 037–11. DOI: 10.1002/2015JD023465.

Castro Ortiz, C. A. (1994). "Sea-level rise and its impact on Bangladesh". *Ocean and Coastal Management* 23.3, pp. 249–270. DOI: 10.1016/0964-5691(94)90022-1.

Cook, A. J., A. J. Fox, D. G. Vaughan, and J. G. Ferrigno (2005). "Retreating glacier fronts on the Antarctic Peninsula over the past half-century". *Science* 308.5721, pp. 541–544. DOI: 10.1126/science.1104235.

Cook, A. J. and D. G. Vaughan (2010). "Overview of areal changes of the ice shelves on the Antarctic Peninsula over the past 50 years". *The Cryosphere* 4.1, pp. 77–98. DOI: 10.5194/tc-4-77-2010.

Cook, B. L. and W. G. Manning (2013). "Thinking beyond the mean: a practical guide for using quantile regression methods for health services research". *Shanghai Archives of Psychiatry* 25.1, p. 55. DOI: 10.3969/J.ISSN.1002-0829.2013.01.011.

Cooper, A. P. (1997). "Historical observations of Prince Gustav ice shelf". *Polar Record* 33.187, pp. 285–294. DOI: 10.1017/S0032247400025389.

Crooks, S. (2004). "The effect of sea-level rise on coastal geomorphology". *Ibis* 146.SUPPL.1, pp. 18–20. DOI: 10.1111/j.1474-919X.2004.00323.x.

Davies, B. J., N. R. Golledge, N. F. Glasser, J. L. Carrivick, S. R. M. Ligtenberg, N. E. Barrand, M. R. van den Broeke, M. J. Hambrey, and J. L. Smellie (2014). "Modelled glacier response to centennial temperature and precipitation trends on the Antarctic Peninsula". *Nature Climate Change* 4.11, pp. 993–998. DOI: 10.1038/nclimate2369.

De Angelis, H. and P. Skvarca (2003). "Glacier surge after ice shelf collapse". *Science* 299.5612, pp. 1560–1562. DOI: 10.1126/science.1077987.

De Rydt, J., G. H. Gudmundsson, H. Rott, and J. L. Bamber (2015). "Modeling the instantaneous response of glaciers after the collapse of the Larsen B Ice Shelf". *Geophysical Research Letters* 42.13, pp. 5355–5363. DOI: 10.1002/2015GL064355.

DeConto, R. M. and D. Pollard (2016). "Contribution of Antarctica to past and future sea-level rise". *Nature* 531.7596, pp. 591–597. DOI: 10.1038/nature17145.

Depoorter, M. A., J. L. Bamber, J. A. Griggs, J. T. Lenaerts, S. R. Ligtenberg, M. R. Van Den Broeke, and G. Moholdt (2013). "Calving fluxes and basal melt rates of Antarctic ice shelves". *Nature* 502.7469, pp. 89–92. DOI: 10.1038/nature12567.

Dinniman, M. S., J. M. Klinck, and E. E. Hofmann (2012). "Sensitivity of Circumpolar Deep Water Transport and Ice Shelf Basal Melt along the West Antarctic Peninsula to Changes in the Winds". *Journal of Climate* 25.14, pp. 4799–4816. DOI: 10.1175/JCLI-D-11-00307.1.

Doake, C. S. M., H.F.J.Corr, H. Rott, P. Skvarca, and N. W. Youngs (1998). "Breakup conditions for stability of the nothern Larsen Ice Shelf, Antarctica". *Nature* 391.February, pp. 778–780.

Doake, C. S. and D. G. Vaughan (1991). "Rapid disintegration of the Wordie Ice Shelf in response to atmospheric warming". *Nature* 350.6316, pp. 328–330. DOI: 10.1038/350328a0.

Doake, C. (2001). "Ice-shelf Stability". *Encyclopedia of Ocean Sciences*, pp. 1282–1290. DOI: 10.1006/rwos.2001.0005.

Domack, E., D. Duran, A. Leventer, S. Ishman, S. Doane, S. McCallum, D. Amblas, J. Ring, R. Gilbert, and M. Prentice (2005). "Stability of the Larsen B ice shelf on the Antarctic Peninsula during the Holocene epoch". *Nature* 436.7051, pp. 681–685. DOI: 10.1038/nature03908.

Dow, C. F., W. S. Lee, J. S. Greenbaum, C. A. Greene, D. D. Blankenship, K. Poinar, A. L. Forrest, D. A. Young, and C. J. Zappa (2018). "Basal channels drive active surface hydrology and transverse ice shelf fracture". *Science Advances* 4.6. DOI: 10.1126/SCIADV.AAO7212.

Drewry, D. J. (1991). "The response of the Antarctic ice sheet to climatic change". *Polar Research Series* 338.1285, p. 90. DOI: 10.1098/rstb.1992.0143.

Dunmire, D., J. T. Lenaerts, A. F. Banwell, N. Wever, J. Shragge, S. Lhermitte, R. Drews, F. Pattyn, J. S. Hansen, I. C. Willis, J. Miller, and E. Keenan (2020). "Observations

of Buried Lake Drainage on the Antarctic Ice Sheet". *Geophysical Research Letters* 47.15, e2020GL087970. DOI: 10.1029/2020GL087970.

Dupont, T. K. and R. B. Alley (2005). "Assessment of the importance of ice-shelf buttressing to ice-sheet flow". *Geophysical Research Letters* 32.4, pp. 1–4. DOI: 10.1029/2004GL022024.

Dutta, D. (2011). "Un outil intégré pour l'évaluation de la vulnérabilité des villes côtiéres aux inondations dues á l'élévation du niveau des mers et des impacts socio-économiques potentiels: Une étude de cas áBangkok, Thaïlande". *Hydrological Sciences Journal* 56.5, pp. 805–823. DOI: 10.1080/02626667.2011.585611.

Elvidge, A. D., I. A. Renfrew, J. C. King, A. Orr, T. A. Lachlan-Cope, M. Weeks, and S. L. Gray (2015). "Foehn jets over the Larsen C Ice Shelf, Antarctica". *Quarterly Journal of the Royal Meteorological Society* 141.688, pp. 698–713. DOI: 10.1002/qj.2382.

Emetc, V., P. Tregoning, M. Morlighem, C. Borstad, and M. Sambridge (2018). "A statistical fracture model for Antarctic ice shelves and glaciers". *The Cryosphere* 12.10, pp. 3187–3213. DOI: 10.5194/tc-12-3187-2018.

Etourneau, J., G. Sgubin, X. Crosta, D. Swingedouw, V. Willmott, L. Barbara, M. N. Houssais, S. Schouten, J. S. Damsté, H. Goosse, C. Escutia, J. Crespin, G. Massé, and J. H. Kim (2019). "Ocean temperature impact on ice shelf extent in the eastern Antarctic Peninsula". *Nature Communications* 10.1, pp. 1–8. DOI: 10.1038/s41467-018-08195-6.

Farinotti, D., M. Huss, J. J. Fürst, J. Landmann, H. Machguth, F. Maussion, and A. Pandit (2019). "A consensus estimate for the ice thickness distribution of all glaciers on Earth". *Nature Geoscience* 12.3, pp. 168–173. DOI: 10.1038/s41561-019-0300-3.

Favier, L. and F. Pattyn (2015). "Antarctic ice rise formation, evolution, and stability". *Geophysical Research Letters* 42.11, pp. 4456–4463. DOI: 10.1002/2015GL064195.

Ferrigno, J. G., R. S. Williams, and K. M. Foley (2004). "Coastal-change and glaciological map of the Saunders Coast area, Antarctica: 1972-97". *Annals of Glaciology* 39, pp. 245–250. DOI: 10.3189/172756404781814285.

Fox, A. J. and D. G. Vaughan (2005). "The retreat of Jones Ice Shelf, Antarctic Peninsula". *Journal of Glaciology* 51.175, pp. 555–560. DOI: 10.3189/172756505781829043.

Fretwell, P., H. D. Pritchard, D. G. Vaughan, J. L. Bamber, N. E. Barrand, R. Bell, C. Bianchi, R. G. Bingham, D. D. Blankenship, G. Casassa, G. Catania, D. Callens, H. Conway, A. J. Cook, H. F. Corr, D. Damaske, V. Damm, F. Ferraccioli, R. Forsberg, S. Fujita, Y. Gim, P. Gogineni, J. A. Griggs, R. C. Hindmarsh, P. Holmlund, J. W. Holt, R. W. Jacobel, A. Jenkins, W. Jokat, T. Jordan, E. C. King, J. Kohler, W. Krabill, M. Riger-Kusk, K. A. Langley, G. Leitchenkov, C. Leuschen, B. P. Luyendyk, K. Matsuoka, J. Mouginot, F. O. Nitsche, Y. Nogi, O. A. Nost, S. V. Popov, E. Rignot, D. M. Rippin, A. Rivera, J. Roberts, N. Ross, M. J. Siegert, A. M. Smith, D. Steinhage, M. Studinger, B. Sun, B. K. Tinto, B. C. Welch, D. Wilson, D. A. Young, C. Xiangbin, and A. Zirizzotti (2013). "Bedmap2: Improved ice bed, surface and thickness datasets for Antarctica". *The Cryosphere* 7.1, pp. 375–393. DOI: 10.5194/tc-7-375-2013.

Fürst, J. J., G. Durand, F. Gillet-Chaulet, L. Tavard, M. Rankl, M. Braun, and O. Gagliardini (2016). "The safety band of Antarctic ice shelves". *Nature Climate Change* 6.5, pp. 479–482. DOI: 10.1038/nclimate2912.

Geiges, A., A. Nauels, P. Yanguas Parra, M. Andrijevic, W. Hare, P. Pfleiderer, M. Schaeffer, and C. F. Schleussner (2020). "Incremental improvements of 2030 targets insufficient to achieve the Paris Agreement goals". *Earth System Dynamics* 11.3, pp. 697–708. DOI: 10.5194/esd-11-697-2020.

Gilbert, E. and C. Kittel (2021). "Surface Melt and Runoff on Antarctic Ice Shelves at 1.5°C, 2°C, and 4°C of Future Warming". *Geophysical Research Letters* 48.8, e2020GL091733. DOI: 10.1029/2020GL091733.

Glasser, N. F. and G. H. Gudmundsson (2012). "Longitudinal surface structures (flowstripes) on Antarctic glaciers". *Cryosphere* 6.2, pp. 383–391. DOI: 10.5194/TC-6-383-2012.

Glasser, N. F. and T. A. Scambos (2008). "A structural glaciological analysis of the 2002 Larsen B ice-shelf collapse". *Journal of Glaciology* 54.184, pp. 3–16. DOI: 10.3189/002214308784409017.

Glasser, N. F., T. A. Scambos, J. Bohlander, M. Truffer, E. Pettit, and B. J. Davies (2011). *From ice-shelf tributary to tidewater glacier: Continued rapid recession, acceleration and thinning of Röhss Glacier following the 1995 collapse of the Prince Gustav Ice Shelf, Antarctic Peninsula*. Tech. rep. 203, pp. 397–406. DOI: 10.3189/002214311796905578.

Glasser, N., B. Kulessa, A. Luckman, D. Jansen, E. King, P. Sammonds, T. Scambos, and K. Jezek (2009). "Surface structure and stability of the Larsen C ice shelf, Antarctic Peninsula". *Journal of Glaciology* 55.191, pp. 400–410. DOI: 10.3189/002214309788816597.

Goelzer, H., S. Nowicki, A. Payne, E. Larour, H. Seroussi, W. H. Lipscomb, J. Gregory, A. Abe-Ouchi, A. Shepherd, E. Simon, C. Agosta, P. Alexander, A. Aschwanden, A. Barthel, R. Calov, C. Chambers, Y. Choi, J. Cuzzone, C. Dumas, T. Edwards, D. Felikson, X. Fettweis, N. R. Golledge, R. Greve, A. Humbert, P. Huybrechts, S. Le Clec'H, V. Lee, G. Leguy, C. Little, D. Lowry, M. Morlighem, I. Nias, A. Quiquet, M. Rückamp, N. J. Schlegel, D. A. Slater, R. Smith, F. Straneo, L. Tarasov, R. Van De Wal, and M. Van Den Broeke (2020). "The future sea-level contribution of the Greenland ice sheet: A multi-model ensemble study of ISMIP6". *Cryosphere* 14.9, pp. 3071–3096. DOI: 10.5194/tc-14-3071-2020.

Goldberg, D. N. (2017). "Ice Shelf Buttressing". *International Encyclopedia of Geography: People, the Earth, Environment and Technology*, pp. 1–9. DOI: 10.1002/9781118786352.wbieg0567.

Greene, C. A., D. A. Young, D. E. Gwyther, B. K. Galton-Fenzi, and D. D. Blankenship (2018). "Seasonal dynamics of Totten Ice Shelf controlled by sea ice buttressing". *The Cryosphere* 12.9, pp. 2869–2882. DOI: 10.5194/tc-12-2869-2018.

Gudmundsson, G. H. (2013). "Ice-shelf buttressing and the stability of marine ice sheets". *The Cryosphere* 7.2, pp. 647–655. DOI: 10.5194/tc-7-647-2013.

Gudmundsson, G. H., J. Krug, G. Durand, L. Favier, and O. Gagliardini (2012). "The stability of grounding lines on retrograde slopes". *The Cryosphere* 6.6, pp. 1497–1505. DOI: 10.5194/tc-6-1497-2012.

Gudmundsson, G. H., C. F. Raymond, and R. Bindschadler (1998). "The origin and longevity of flow stripes on Antarctic ice streams". *Annals of Glaciology* 27, pp. 145–152. DOI: 10.3189/1998AOG27-1-145-152.

Hambrey, M. J. (1977). "Foliation, minor folds and strain in glacier ice". *Tectonophysics* 39.1-3, pp. 397–416. DOI: 10.1016/0040-1951(77)90106-8.

Han, H., S. Lee, J. I. Kim, S. H. Kim, and H. C. Kim (2019). "Changes in a giant iceberg created from the collapse of the Larsen C Ice Shelf, Antarctic Peninsula, derived from Sentinel-1 and CryoSat-2 data". *Remote Sensing* 11.4, p. 404. DOI: 10.3390/rs11040404.

Hao, L. and D. Q. Naiman (2007). *Quantitative Applications in the Social Sciences: Quantile regression.* Thousand Oaks, CA: SAGE Publications.

Hausfather, Z. and G. P. Peters (2020). *Emissions – the 'business as usual' story is misleading.* DOI: 10.1038/d41586-020-00177-3.

Helsen, M. M., M. R. van den Broeke, R. S. van de Wal, W. J. van de Berg, E. van Meijgaard, C. H. Davis, Y. Li, and I. Goodwin (2008). "Elevation changes in antarctica mainly determined by accumulation variability". *Science* 320.5883, pp. 1626–1629. DOI: 10.1126/science.1153894.

Hensman, J., A. G. De Matthews, M. Filippone, and Z. Ghahramani (2015). "MCMC for variationally sparse Gaussian processes". *Advances in Neural Information Processing Systems*. Vol. 2015-Janua, pp. 1648–1656.

Heuzé, C., K. J. Heywood, D. P. Stevens, and J. K. Ridley (2015). "Changes in global ocean bottom properties and volume transports in CMIP5 models under climate change scenarios". *Journal of Climate* 28.8, pp. 2917–2944. DOI: 10.1175/JCLI-D-14-00381.1.

Hogg, A. E. and G. H. Gudmundsson (2017). *Commentary: Impacts of the Larsen-C Ice Shelf calving event*. DOI: 10.1038/nclimate3359.

Hogg, A. E., A. Shepherd, S. L. Cornford, K. H. Briggs, N. Gourmelen, J. A. Graham, I. Joughin, J. Mouginot, T. Nagler, A. J. Payne, E. Rignot, and J. Wuite (2017). "Increased ice flow in Western Palmer Land linked to ocean melting". *Geophysical Research Letters* 44.9, pp. 4159–4167. DOI: 10.1002/2016GL072110.

Holland, P. R., A. Brisbourne, H. F. Corr, D. McGrath, K. Purdon, J. Paden, H. A. Fricker, F. S. Paolo, and A. H. Fleming (2015). "Oceanic and atmospheric forcing of Larsen C Ice-Shelf thinning". *The Cryosphere* 9.3, pp. 1005–1024. DOI: 10.5194/tc-9-1005-2015.

Holt, T. O., N. F. Glasser, H. A. Fricker, L. Padman, A. Luckman, O. King, D. J. Quincey, and M. R. Siegfried (2014). "The structural and dynamic responses of Stange Ice Shelf to recent environmental change". *Antarctic Science* 26.6, pp. 646–660. DOI: 10.1017/S095410201400039X.

Holt, T. O., N. F. Glasser, D. J. Quincey, and M. R. Siegfried (2013a). "Speedup and fracturing of George VI Ice Shelf, Antarctic Peninsula". *The Cryosphere* 7.3, pp. 797–816. DOI: 10.5194/tc-7-797-2013.

Holt, T. (2013). "An assessment of the stability of southwest Antarctic Peninsula Ice Shelves". PhD thesis. Aberystwyth: Aberystwyth University.

Holt, T., N. Glasser, and D. Quincey (2013b). "The structural glaciology of southwest Antarctic Peninsula Ice Shelves (ca. 2010)". *Journal of Maps* 9.4, pp. 523–531. DOI: 10.1080/17445647.2013.822836/SUPPL{_}FILE/TJOM{_}A{_}822836{_}SM8611.PDF.

Holt, T. and N. F. Glasser (2022). "Changes in area, flow speed and structure of southwest Antarctic Peninsula ice shelves in the 21st century". *Journal of Glaciology*, pp. 1–19. DOI: 10.1017/jog.2022.7.

Hooke, R. L. and P. J. Hudleston (1978). "Origin of Foliation in Glaciers". *Journal of Glaciology* 20.83, pp. 285–299. DOI: 10.3189/S0022143000013848.

Horton, B. P., N. S. Khan, N. Cahill, J. S. Lee, T. A. Shaw, A. J. Garner, A. C. Kemp, S. E. Engelhart, and S. Rahmstorf (2020). "Estimating global mean sea-level rise and its uncertainties by 2100 and 2300 from an expert survey". *npj Climate and Atmospheric Science* 3.1, pp. 1–8. DOI: 10.1038/s41612-020-0121-5.

Hughes, T. (1983). *On the disintegration of ice shelves: the role of fracture.* Tech. rep. 101, pp. 98–117. DOI: 10.1017/S0022143000005177.

Humbert, A., D. Gross, R. Müller, M. Braun, R. S. Van De Wal, M. R. Van Den Broeke, D. G. Vaughan, and W. J. Van De Berg (2010). "Deformation and failure of the ice bridge on the Wilkins Ice Shelf, Antarctica". *Annals of Glaciology* 51.55, pp. 49–55. DOI: 10.3189/172756410791392709.

Humbert, A. (2007). "Numerical simulations of the ice flow dynamics of George VI Ice Shelf, Antarctica". *Journal of Glaciology* 53.183, pp. 659–664. DOI: 10.3189/002214307784409180.

Humbert, A. and M. Braun (2008). "The Wilkins Ice Shelf, Antarctica: Break-up along failure zones". *Journal of Glaciology* 54.188, pp. 943–944. DOI: 10.3189/002214308787780012.

IACS (2011). "Glossary of Glacier Mass". *Internation Hydrological Programme of the United Nations Educational, Scientific and Cultural Organization (UNESCO)* 86, p. 114.

IPCC (2021). *Sixth Assessment Report.* Tech. rep. August, pp. 1–2.

Jacob, K. H. (2015). "Sea level rise, storm risk, denial, and the future of coastal cities". *Bulletin of the Atomic Scientists* 71.5, pp. 40–50. DOI: 10.1177/0096340215599777.

Jaeger, J. C. (2009). "Fundamentals of Rock Mechanics". *Geofluids* 9.3, pp. 251–252. DOI: 10.1111/j.1468-8123.2009.00251.x.

Jansen, D., B. Kulessa, P. R. Sammonds, A. Luckman, E. C. King, and N. F. Glasser (2010). *Present stability of the Larsen C ice shelf, Antarctic Peninsula*. Tech. rep. 198, pp. 593–600. DOI: 10.3189/002214310793146223.

Jansen, D., A. Luckman, B. Kulessa, P. R. Holland, and E. C. King (2013). "Marine ice formation in a suture zone on the Larsen C Ice Shelf and its influence on ice shelf dynamics". *Journal of Geophysical Research: Earth Surface* 118.3, pp. 1628–1640. DOI: 10.1002/jgrf.20120.

Jenkins, A. and S. Jacobs (2008). "Circulation and melting beneath George VI ice shelf, Antartica". *Journal of Geophysical Research: Oceans* 113.4, p. C04013. DOI: 10.1029/2007JC004449.

Johnson, J. S., M. J. Bentley, S. J. Roberts, S. A. Binnie, and S. P. Freeman (2011). "Holocene deglacial history of the northeast Antarctic Peninsula – A review and new chronological constraints". *Quaternary Science Reviews* 30.27-28, pp. 3791–3802. DOI: 10.1016/J.QUASCIREV.2011.10.011.

Jordan, M. I., Z. Ghahramani, T. S. Jaakkola, and L. K. Saul (1999). "Introduction to variational methods for graphical models". *Machine Learning* 37.2, pp. 183–233. DOI: 10.1023/A:1007665907178.

Joughin, I. and R. B. Alley (2011). "Stability of the West Antarctic ice sheet in a warming world". *Nature Geoscience* 4.8, pp. 506–513. DOI: 10.1038/ngeo1194.

Joughin, I. and D. R. MacAyeal (2005). "Calving of large tabular icebergs from ice shelf rift systems". *Geophysical Research Letters* 32.2, pp. 1–4. DOI: 10.1029/2004GL020978.

Kachanov, L. M. (1999). "Rupture time under creep conditions". *International Journal of Fracture*. Vol. 97. 1-4. Springer, pp. 11–18. DOI: 10.1023/a:1018671022008.

Kellerer-Pirklbauer, A. and B. Kulmer (2019). "The evolution of brittle and ductile structures at the surface of a partly debris-covered, rapidly thinning and slowly moving glacier in 1998–2012 (Pasterze Glacier, Austria)". *Earth Surface Processes and Landforms* 44.5, pp. 1034–1049. DOI: 10.1002/ESP.4552.

Khazendar, A., E. Rignot, and E. Larour (2007). "Larsen B Ice Shelf rheology preceding its disintegration inferred by a control method". *Geophysical Research Letters* 34.19, p. L19503. DOI: 10.1029/2007GL030980.

— (2011). "Acceleration and spatial rheology of Larsen C Ice Shelf, Antarctic Peninsula". *Geophysical Research Letters* 38.9, n/a–n/a. DOI: 10.1029/2011GL046775.

Khazendar, A., C. P. Borstad, B. Scheuchl, E. Rignot, and H. Seroussi (2015). "The evolving instability of the remnant Larsen B Ice Shelf and its tributary glaciers". *Earth and Planetary Science Letters* 419, pp. 199–210. DOI: 10.1016/j.epsl.2015.03.014.

King, E. C., J. De Rydt, and G. H. Gudmundsson (2018). "The internal structure of the Brunt Ice Shelf from ice-penetrating radar analysis and implications for ice shelf fracture". *The Cryosphere* 12.10, pp. 3361–3372. DOI: 10.5194/tc-12-3361-2018.

King, J. C. (1994). "Recent climate variability in the vicinity of the antarctic peninsula". *International Journal of Climatology* 14.4, pp. 357–369. DOI: 10.1002/joc.3370140402.

Kittel, C., C. Amory, C. Agosta, N. C. Jourdain, S. Hofer, A. Delhasse, S. Doutreloup, P. V. Huot, C. Lang, T. Fichefet, and X. Fettweis (2021). "Diverging future surface mass balance between the Antarctic ice shelves and grounded ice sheet". *The Cryosphere* 15.3, pp. 1215–1236. DOI: 10.5194/tc-15-1215-2021.

Koenker, R. (2010). "Quantile Regression in R: A Vignette". *Quantile Regression*, pp. 295–316. DOI: 10.1017/cbo9780511754098.011.

Koenker, R. and G. Bassett (1978). "Regression Quantiles". *Econometrica* 46.1, p. 33. DOI: 10.2307/1913643.

Koenker, R. and K. Hallock (2000). "Quantile Regression: An Introduction".

Koenker, R. and K. F. Hallock (2001). "Quantile regression". *Journal of Economic Perspectives* 15.4, pp. 143–156. DOI: 10.1257/jep.15.4.143.

Krug, J., J. Weiss, O. Gagliardini, and G. Durand (2014). "Combining damage and fracture mechanics to model calving". *The Cryosphere* 8.6, pp. 2101–2117. DOI: 10.5194/tc-8-2101-2014.

Kuipers Munneke, P., A. J. Luckman, S. L. Bevan, C. J. Smeets, E. Gilbert, M. R. van den Broeke, W. Wang, C. Zender, B. Hubbard, D. Ashmore, A. Orr, J. C. King, and B. Kulessa (2018). "Intense Winter Surface Melt on an Antarctic Ice Shelf". *Geophysical Research Letters* 45.15, pp. 7615–7623. DOI: 10.1029/2018GL077899.

Kulessa, B., D. Jansen, A. J. Luckman, E. C. King, and P. R. Sammonds (2014). "Marine ice regulates the future stability of a large Antarctic ice shelf". *Nature Communications* 5.1, pp. 1–7. DOI: 10.1038/ncomms4707.

Lai, C. Y., J. Kingslake, M. G. Wearing, P. H. C. Chen, P. Gentine, H. Li, J. J. Spergel, and J. M. van Wessem (2020). "Vulnerability of Antarctica's ice shelves to meltwater-driven fracture". *Nature* 584.7822, pp. 574–578. DOI: 10.1038/s41586-020-2627-8.

Larour, E., E. Rignot, and D. Aubry (2004). "Modelling of rift propagation on Ronne Ice Shelf, Antarctica, and sensitivity to climate change". *Geophysical Research Letters* 31.16. DOI: 10.1029/2004GL020077.

Larour, E., H. Seroussi, M. Morlighem, and E. Rignot (2012). "Continental scale, high order, high spatial resolution, ice sheet modeling using the Ice Sheet System Model (ISSM)". *Journal of Geophysical Research: Earth Surface* 117.1, p. 1022. DOI: 10.1029/2011JF002140.

Larour, E., E. Rignot, I. Joughin, and D. Aubry (2005). "Rheology of the Ronne Ice Shelf, Antarctica, inferred from satellite radar interferometry data using an inverse control method". *Geophysical Research Letters* 32.5, pp. 1–4. DOI: 10.1029/2004GL021693.

Leeson, A. A., E. Forster, A. Rice, N. Gourmelen, and J. M. van Wessem (2020). "Evolution of Supraglacial Lakes on the Larsen B Ice Shelf in the Decades Before it Collapsed". *Geophysical Research Letters* 47.4, e2019GL085591. DOI: 10.1029/2019GL085591.

Levermann, A., T. Albrecht, R. Winkelmann, M. A. Martin, M. Haseloff, and I. Joughin (2012). "Kinematic first-order calving law implies potential for abrupt ice-shelf retreat". *The Cryosphere* 6.2, pp. 273–286. DOI: 10.5194/tc-6-273-2012.

Lipscomb, W. H., S. F. Price, M. J. Hoffman, G. R. Leguy, A. R. Bennett, S. L. Bradley, K. J. Evans, J. G. Fyke, J. H. Kennedy, M. Perego, D. M. Ranken, W. J. Sacks, A. G. Salinger, L. J. Vargo, and P. H. Worley (2019). "Description and evaluation of the Community Ice Sheet Model (CISM) v2.1". *Geoscientific Model Development* 12.1, pp. 387–424. DOI: 10.5194/gmd-12-387-2019.

Lucchitta, B. K. and C. E. Rosanova (1998). "Retreat of northern margins of George VI and Wilkins Ice Shelves, Antarctic Peninsula". *Annals of Glaciology* 27, pp. 41–46. DOI: 10.3189/1998AoG27-1-41-46.

Luckman, A., D. Jansen, B. Kulessa, E. C. King, P. Sammonds, and D. I. Benn (2012). "Basal crevasses in Larsen C Ice Shelf and implications for their global abundance". *The Cryosphere* 6, pp. 113–123. DOI: 10.5194/tc-6-113-2012.

Luckman, A., A. Elvidge, D. Jansen, B. Kulessa, P. Kuipers Munneke, J. King, and N. E. Barrand (2014). "Surface melt and ponding on Larsen C Ice Shelf and the impact of föhn winds". *Antarctic Science* 26.6, pp. 625–635. DOI: 10.1017/S0954102014000339.

Luthcke, S. B., A. A. Arendt, D. D. Rowlands, J. J. McCarthy, and C. F. Larsen (2008). "Recent glacier mass changes in the Gulf of Alaska region from GRACE mascon solutions". *Journal of Glaciology* 54.188, pp. 767–777. DOI: 10.3189/002214308787779933.

Macayeal, D. R. and O. V. Sergienko (2013). "The flexural dynamics of melting ice shelves". *Annals of Glaciology* 54.63, pp. 1–10. DOI: 10.3189/2013AoG63A256.

MacAyeal, D. R., T. A. Scambos, C. L. Hulbe, and M. A. Fahnestock (2003). "Catastrophic ice-shelf break-up by an ice-shelf-fragment-capsize mechanism". *Journal of Glaciology* 49.164, pp. 22–36. DOI: 10.3189/172756503781830863.

Mackay, D. J. C. (2004). "Information theory, inference, and learning algorithms". *Choice Reviews Online* 41.10, pp. 41–5949. DOI: 10.5860/choice.41-5949.

Martin, M. A., R. Winkelmann, M. Haseloff, T. Albrecht, E. Bueler, C. Khroulev, and A. Levermann (2011). "The Potsdam Parallel Ice Sheet Model (PISM-PIK) - Part

2: Dynamic equilibrium simulation of the Antarctic ice sheet". *The Cryosphere* 5.3, pp. 727–740. DOI: 10.5194/tc-5-727-2011.

Massom, R. A., T. A. Scambos, L. G. Bennetts, P. Reid, V. A. Squire, and S. E. Stammerjohn (2018). "Antarctic ice shelf disintegration triggered by sea ice loss and ocean swell". *Nature* 558.7710, pp. 383–389. DOI: 10.1038/s41586-018-0212-1.

Matthews, A. G. G., M. Van Der Wilk, T. Nickson, K. Fujii, A. Boukouvalas, P. León-Villagrá, Z. Ghahramani, and J. Hensman (2017). *GPflow: A Gaussian Process Library using TensorFlow*. Tech. rep.

McAlpine, S. A. and J. R. Porter (2018). "Estimating Recent Local Impacts of Sea-Level Rise on Current Real-Estate Losses: A Housing Market Case Study in Miami-Dade, Florida". *Population Research and Policy Review* 37.6, pp. 871–895. DOI: 10.1007/s11113-018-9473-5.

McGrath, D., K. Steffen, P. R. Holland, T. Scambos, H. Rajaram, W. Abdalati, and E. Rignot (2014). "The structure and effect of suture zones in the Larsen C Ice Shelf, Antarctica". *Journal of Geophysical Research: Earth Surface* 119.3, pp. 588–602. DOI: 10.1002/2013JF002935.

McGrath, D., K. Steffen, H. Rajaram, T. Scambos, W. Abdalati, and E. Rignot (2012a). "Basal crevasses on the Larsen C Ice Shelf, Antarctica: Implications for meltwater ponding and hydrofracture". *Geophysical Research Letters* 39.16, p. 16504. DOI: 10.1029/2012GL052413.

McGrath, D., K. Steffen, T. Scambos, H. Rajaram, G. Casassa, and J. L. Rodriguez Lagos (2012b). "Basal crevasses and associated surface crevassing on the larsen c ice shelf, antarctica, and their role in ice-shelf instability". *Annals of Glaciology* 53.60, pp. 10–18. DOI: 10.3189/2012AoG60A005.

Meier, M. F., M. B. Dyurgerov, U. K. Rick, S. O'Neel, W. T. Pfeffer, R. S. Anderson, S. P. Anderson, and A. F. Glazovsky (2007). "Glaciers dominate eustatic sea-level rise in the 21st century". *Science* 317.5841, pp. 1064–1067. DOI: 10.1126/science.1143906.

Mercer, J. H. (1978). "West Antarctic ice sheet and CO2 greenhouse effect: a threat of disaster". *Nature* 271.5643, pp. 321–325. DOI: 10.1038/271321a0.

Meredith, M. P. and J. C. King (2005). "Rapid climate change in the ocean west of the Antarctic Peninsula during the second half of the 20th century". *Geophysical Research Letters* 32.19, pp. 1–5. DOI: 10.1029/2005GL024042.

Merry, C. J. and I. M. Whillans (1993). "Ice-flow features on Ice Stream B, Antarctica, revealed by SPOT HRV imagery". *Journal of Glaciology* 39.133, pp. 515–527. DOI: 10.3189/S0022143000016415.

Morlighem, M., C. N. Williams, E. Rignot, L. An, J. E. Arndt, J. L. Bamber, G. Catania, N. Chauché, J. A. Dowdeswell, B. Dorschel, I. Fenty, K. Hogan, I. Howat, A. Hubbard, M. Jakobsson, T. M. Jordan, K. K. Kjeldsen, R. Millan, L. Mayer, J. Mouginot, B. P. Noël, C. O'Cofaigh, S. Palmer, S. Rysgaard, H. Seroussi, M. J. Siegert, P. Slabon, F. Straneo, M. R. van den Broeke, W. Weinrebe, M. Wood, and K. B. Zinglersen (2017). "BedMachine v3: Complete Bed Topography and Ocean Bathymetry Mapping of Greenland From Multibeam Echo Sounding Combined With Mass Conservation". *Geophysical Research Letters* 44.21, pp. 051–11. DOI: 10.1002/2017GL074954.

Morlighem, M., E. Rignot, T. Binder, D. Blankenship, R. Drews, G. Eagles, O. Eisen, F. Ferraccioli, R. Forsberg, P. Fretwell, V. Goel, J. S. Greenbaum, H. Gudmundsson, J. Guo, V. Helm, C. Hofstede, I. Howat, A. Humbert, W. Jokat, N. B. Karlsson, W. S. Lee, K. Matsuoka, R. Millan, J. Mouginot, J. Paden, F. Pattyn, J. Roberts, S. Rosier, A. Ruppel, H. Seroussi, E. C. Smith, D. Steinhage, B. Sun, M. R. d. Broeke, T. D. Ommen, M. v. Wessem, and D. A. Young (2020). "Deep glacial troughs and stabilizing ridges unveiled beneath the margins of the Antarctic ice sheet". *Nature Geoscience* 13.2, pp. 132–137. DOI: 10.1038/s41561-019-0510-8.

Morris, E. M. and D. G. Vaughan (2013). "Spatial and Temporal Variation of Surface Temperature on the Antarctic Peninsula And The Limit of Viability of Ice Shelves". *Antarctic Research Series* 79, pp. 61–68. DOI: 10.1029/ar079p0061.

Moss, R. H., J. A. Edmonds, K. A. Hibbard, M. R. Manning, S. K. Rose, D. P. Van Vuuren, T. R. Carter, S. Emori, M. Kainuma, T. Kram, G. A. Meehl, J. F. Mitchell, N. Nakicenovic, K. Riahi, S. J. Smith, R. J. Stouffer, A. M. Thomson, J. P. Weyant, and T. J. Wilbanks (2010). *The next generation of scenarios for climate change research and assessment*. DOI: 10.1038/nature08823.

Mulvaney, R., N. J. Abram, R. C. Hindmarsh, C. Arrowsmith, L. Fleet, J. Triest, L. C. Sime, O. Alemany, and S. Foord (2012). "Recent Antarctic Peninsula warming relative to Holocene climate and ice-shelf history". *Nature* 489.7414, pp. 141–144. DOI: 10.1038/nature11391.

Munneke, P. K., S. R. Ligtenberg, M. R. Van Den Broeke, and D. G. Vaughan (2014). "Firn air depletion as a precursor of Antarctic ice-shelf collapse". *Journal of Glaciology* 60.220, pp. 205–214. DOI: 10.3189/2014JOG13J183.

Naughtena, K. A., K. J. Meissner, B. K. Galton-Fenzi, M. H. England, R. Timmermann, and H. H. Hellmer (2018). "Future Projections of Antarctic Ice Shelf Melting Based on CMIP5 Scenarios". *Journal of Climate* 31.13, pp. 5243–5261. DOI: 10.1175/JCLI-D-17-0854.1.

Nicholls, K. W., C. J. Pudsey, and P. Morris (2004). "Summertime water masses off the northern Larsen C Ice Shelf, Antarctica". *Geophysical Research Letters* 31.9, n/a–n/a. DOI: 10.1029/2004GL019924.

Nicholls, R., S. Hanson, C. Herweijer, N. Patmore, S. Hallegatte, J. Corfee-Morlot, J. Chateau, and R. Muir-Wood (2007). "Ranking of The World's Cities Most Exposed to Coastal Flooding Today Executive Summary". *Organisation for Economic Cooperation and Development*.

Nick, F. M., C. J. van der Veen, A. Vieli, and D. I. Benn (2010). "A physically based calving model applied to marine outlet glaciers and implications for the glacier dynamics". *Journal of Glaciology* 56.199, pp. 781–794. DOI: 10.3189/002214310794457344.

Nývlt, D., R. Braucher, Z. Engel, B. Mlčoch, and A. Team (2014). "Timing of the Northern Prince Gustav Ice Stream retreat and the deglaciation of northern James Ross Island, Antarctic Peninsula during the last glacial–interglacial transition". *Quaternary Research* 82.2, pp. 441–449. DOI: 10.1016/J.YQRES.2014.05.003.

Orbanz, P. (2010). "Bayesian Nonparametric Models Definition Motivation and Background". *Encyclopedia of Machine Learning* 1, pp. 1–14.

Padman, L., D. P. Costa, M. S. Dinniman, H. A. Fricker, M. E. Goebel, L. A. Huckstadt, A. Humbert, I. Joughin, J. T. Lenaerts, S. R. Ligtenberg, T. Scambos, and M. R. Van Den Broeke (2012). "Oceanic controls on the mass balance of Wilkins Ice Shelf, Antarctica". *Journal of Geophysical Research: Oceans* 117.1. DOI: 10.1029/2011JC007301.

Padman, L., M. R. Siegfried, and H. A. Fricker (2018). "Ocean Tide Influences on the Antarctic and Greenland Ice Sheets". *Reviews of Geophysics* 56.1, pp. 142–184. DOI: 10.1002/2016RG000546.

Palerme, C., C. Genthon, C. Claud, J. E. Kay, N. B. Wood, and T. L'Ecuyer (2016). "Evaluation of current and projected Antarctic precipitation in CMIP5 models". *Climate Dynamics 2016 48:1* 48.1, pp. 225–239. DOI: 10.1007/S00382-016-3071-1.

Paolo, F. S., H. A. Fricker, and L. Padman (2015). "Volume loss from Antarctic ice shelves is accelerating". *Science* 348.6232, pp. 327–331. DOI: 10.1126/science.aaa0940.

Paterson (1994). "The Physics of Glaciers, third edition." *Earth Surface Processes and Landforms* 21.10, pp. 980–981. DOI: 10.1002/(SICI)1096-9837(199610)21:10<980::AID-ESP586>3.0.CO;2-G.

Pattyn, F. (2003). "A new three-dimensional higher-order thermomechanical ice sheet model: Basic sensitivity, ice stream development, and ice flow across subglacial lakes". *Journal of Geophysical Research* 108.B8, p. 2382. DOI: 10.1029/2002jb002329.

Pavri, F. (2009). "Urban Expansion and Sea-Level Rise Related Flood Vulnerability for Mumbai (Bombay), India Using Remotely Sensed Data". *Geospatial Techniques in*

Urban Hazard and Disaster Analysis. Springer, Dordrecht, pp. 31–49. DOI: 10.1007/978-90-481-2238-7{_}3.

Pegler, S. S. (2016). "The dynamics of confined extensional flows". *Journal of Fluid Mechanics* 804, pp. 24–57. DOI: 10.1017/jfm.2016.516.

— (2018). "Marine ice sheet dynamics: The impacts of ice-shelf buttressing". *Journal of Fluid Mechanics* 857, pp. 605–647. DOI: 10.1017/jfm.2018.741.

Pingree, K., M. Lurie, and T. Hughes (2011). "Is the East Antarctic ice sheet stable?" *Quaternary Research* 75.3, pp. 417–429. DOI: 10.1016/J.YQRES.2010.12.001.

Potter, J. R., J. G. Paren, and J. Loynes (1984). "Glaciological and oceanographic calculations of the mass balance and oxygen isotope ratio of a melting ice shelf." *Journal of Glaciology* 30.105, pp. 161–170. DOI: 10.1017/S002214300000589X.

Pralong, A. and M. Funk (2005). "Dynamic damage model of crevasse opening and application to glacier calving". *Journal of Geophysical Research* 110.B1, B01309. DOI: 10.1029/2004JB003104.

Pramanik, M. K. (2017). "Impacts of predicted sea level rise on land use/land cover categories of the adjacent coastal areas of Mumbai megacity, India". *Environment, Development and Sustainability* 19.4, pp. 1343–1366. DOI: 10.1007/s10668-016-9804-9.

Pritchard, H. D., S. R. Ligtenberg, H. A. Fricker, D. G. Vaughan, M. R. Van Den Broeke, and L. Padman (2012). "Antarctic ice-sheet loss driven by basal melting of ice shelves". *Nature* 484.7395, pp. 502–505. DOI: 10.1038/nature10968.

Pudsey, C. J. and J. Evans (2002). "First survey of Antarctic sub-ice shelf sediments reveals mid-Holocene ice shelf retreat". *Geology* 29.9, pp. 787–790. DOI: 10.1130/0091-7613(2001)029<0787:FSOASI>2.0.CO;2.

Qiao, G., Y. Li, S. Guo, and W. Ye (2019). "Evolving Instability of the Scar Inlet Ice Shelf based on Sequential Landsat Images Spanning 2005–2018". *Remote Sensing 2020, Vol. 12, Page 36* 12.1, p. 36. DOI: 10.3390/RS12010036.

Rack, W. and H. Rott (2004). *Pattern of retreat and disintegretaion of the Larsen B Ice Shelf*. Tech. rep., pp. 505–510. DOI: 10.3189/172756404781814005.

Rankl, M., J. Jakob Fürst, A. Humbert, and M. Holger Braun (2017). "Dynamic changes on the Wilkins Ice Shelf during the 2006-2009 retreat derived from satellite observations". *Cryosphere* 11.3, pp. 1199–1211. DOI: 10.5194/TC-11-1199-2017.

Ravenzwaaij, D. van, P. Cassey, and S. D. Brown (2018). "A simple introduction to Markov Chain Monte–Carlo sampling". *Psychonomic Bulletin and Review* 25.1, pp. 143–154. DOI: 10.3758/s13423-016-1015-8.

Rebesco, M., E. Domack, F. Zgur, C. Lavoie, A. Leventer, S. Brachfeld, V. Willmott, G. Halverson, M. Truffer, T. Scambos, J. Smith, and E. Pettit (2014). "Boundary condition of grounding lines prior to collapse, Larsen-B Ice Shelf, Antarctica". *Science* 345.6202, pp. 1354–1358. DOI: 10.1126/SCIENCE.1256697.

Reese, R., G. H. Gudmundsson, A. Levermann, and R. Winkelmann (2018). "The far reach of ice-shelf thinning in Antarctica". *Nature Climate Change* 8.1, pp. 53–57. DOI: 10.1038/s41558-017-0020-x.

Rémy, F. and S. Parouty (2009). *Antarctic ice sheet and radar altimetry: A Review*. DOI: 10.3390/rs1041212.

Reynolds, J. M. and M. J. Hambrey (1988). "The structural glaciology of George VI Ice Shelf, Antarctic Peninsula". *British Antarctic Survey Bulletin* 79, pp. 79–95.

Riahi, K., S. Rao, V. Krey, C. Cho, V. Chirkov, G. Fischer, G. Kindermann, N. Nakicenovic, and P. Rafaj (2011). "RCP 8.5-A scenario of comparatively high greenhouse gas emissions". *Climatic Change* 109.1, pp. 33–57. DOI: 10.1007/s10584-011-0149-y.

Riedl, C., H. Rott, and W. Rack (2005). "Recent variations of Larsen Ice Shelf, Antarctic Peninsula, Observed by Envisat".

Rignot, E., J. Mouginot, and B. Scheuchl (2011a). "Ice flow of the antarctic ice sheet". *Science* 333.6048, pp. 1427–1430. DOI: 10.1126/science.1208336.

Rignot, E., J. Mouginot, and B. Scheuchl (2011b). "MEaSUREs InSAR-Based Antarctica Ice Velocity Map, Boulder, Colorado USA: National Snow and Ice Data Center". *Digital media*.

Rignot, E., G. Casassa, P. Gogineni, W. Krabill, A. Rivera, and R. Thomas (2004). "Accelerated ice discharge from the Antarctic Peninsula following the collapse of Larsen B ice shelf". *Geophysical Research Letters* 31.18, p. L18401. DOI: 10.1029/2004GL020697.

Rignot, E., S. Jacobs, J. Mouginot, and B. Scheuchl (2013). "Ice-shelf melting around antarctica". *Science* 341.6143, pp. 266–270. DOI: 10.1126/science.1235798.

Rignot, E., J. Mouginot, B. Scheuchl, M. Van Den Broeke, M. J. Van Wessem, and M. Morlighem (2019). "Four decades of Antarctic ice sheet mass balance from 1979–2017". *Proceedings of the National Academy of Sciences of the United States of America* 116.4, pp. 1095–1103. DOI: 10.1073/pnas.1812883116.

Rintoul, S. R., S. L. Chown, R. M. DeConto, M. H. England, H. A. Fricker, V. Masson-Delmotte, T. R. Naish, M. J. Siegert, and J. C. Xavier (2018). "Choosing the future of Antarctica". *Nature* 558.7709, pp. 233–241. DOI: 10.1038/s41586-018-0173-4.

Rist, M. A., P. R. Sammonds, H. Oerter, and C. S. M. Doake (2002). "Fracture of Antarctic shelf ice". *Journal of Geophysical Research: Solid Earth* 107.B1, pp. 2–1. DOI: 10.1029/2000jb000058.

Robel, A. A. and A. F. Banwell (2019). "A Speed Limit on Ice Shelf Collapse Through Hydrofracture". *Geophysical Research Letters* 46.21, pp. 12092–12100. DOI: 10.1029/2019GL084397.

Robertson, R., M. Visbeck, A. L. Gordon, and E. Fahrbach (2002). "Long-term temperature trends in the deep waters of the Weddell Sea". *Deep-Sea Research Part II: Topical Studies in Oceanography* 49.21, pp. 4791–4806. DOI: 10.1016/S0967-0645(02)00159-5.

Robin, G. D. Q. (1979). "Formation, Flow, and Disintegration Of Ice Shelves". *Journal of Glaciology* 24.90, pp. 259–271. DOI: 10.3189/S0022143000014787.

Rott, H., F. Müller, T. Nagler, and D. Floricioiu (2011). "The imbalance of glaciers after disintegration of Larsen-B ice shelf, Antarctic Peninsula". *The Cryosphere* 5.1, pp. 125–134. DOI: 10.5194/tc-5-125-2011.

Rott, H., W. Rack, P. Skvarca, and H. D. Angelis (2002). "Northern Larsen Ice Shelf, Antarctica: further retreat after collapse". *Annals of Glaciology* 34, pp. 277–282. DOI: 10.3189/172756402781817716.

Rott, H., P. Skvarca, and T. Nagler (1996). "Rapid collapse of northern Larsen Ice Shelf, Antarctica". *Science* 271.5250, pp. 788–792. DOI: 10.1126/science.271.5250.788.

Royston, S. and G. H. Gudmundsson (2016). "Changes in ice-shelf buttressing following the collapse of Larsen A Ice Shelf, Antarctica, and the resulting impact on tributaries". *Journal of Glaciology* 62.235, pp. 905–911. DOI: 10.1017/jog.2016.77.

Scambos, T. A., J. A. Bohlander, C. A. Shuman, and P. Skvarca (2004). *Glacier acceleration and thining after ice shelf collapse in the B Larsen embayment, Antarctica*. Tech. rep. 18, L18402. (10.1029/2004GL020670.)

Scambos, T. A., C. Hulbe, M. Fahnestock, and J. Bohlander (2000). "The link between climate warming and break-up of ice shelves in the Antarctic Peninsula". *Journal of Glaciology* 46.154, pp. 516–530. DOI: 10.3189/172756500781833043.

Scambos, T., H. A. Fricker, C. C. Liu, J. Bohlander, J. Fastook, A. Sargent, R. Massom, and A. M. Wu (2009). "Ice shelf disintegration by plate bending and hydro-fracture: Satellite observations and model results of the 2008 Wilkins ice shelf break-ups". *Earth and Planetary Science Letters* 280.1-4, pp. 51–60. DOI: 10.1016/j.epsl.2008.12.027.

Schannwell, C., N. E. Barrand, and V. Radić (2016). "Future sea-level rise from tidewater and ice-shelf tributary glaciers of the Antarctic Peninsula". *Earth and Planetary Science Letters* 453, pp. 161–170. DOI: 10.1016/j.epsl.2016.07.054.

Schannwell, C., S. Cornford, D. Pollard, and N. E. Barrand (2018). "Dynamic response of Antarctic Peninsula Ice Sheet to potential collapse of Larsen C and George VI ice shelves". *The Cryosphere* 12.7, pp. 2307–2326. DOI: 10.5194/tc-12-2307-2018.

Schmidtko, S., K. J. Heywood, A. F. Thompson, and S. Aoki (2014). "Multidecadal warming of Antarctic waters". *Science* 346.6214, pp. 1227–1231. DOI: 10.1126/science.1256117.

Sergienko, O. V. (2010). "Elastic response of floating glacier ice to impact of long-period ocean waves". *Journal of Geophysical Research: Earth Surface* 115.4, F04028. DOI: 10.1029/2010JF001721.

Shaw, J. (1977). "Till body morphology and structure related to glacier flow". *Boreas* 6.2, pp. 189–201. DOI: 10.1111/J.1502-3885.1977.TB00348.X.

Shepherd, A., E. Ivins, E. Rignot, B. Smith, M. van den Broeke, I. Velicogna, P. Whitehouse, K. Briggs, I. Joughin, G. Krinner, S. Nowicki, T. Payne, T. Scambos, N. Schlegel, G. A, C. Agosta, A. Ahlstrøm, G. Babonis, V. R. Barletta, A. A. Bjørk, A. Blazquez, J. Bonin, W. Colgan, B. Csatho, R. Cullather, M. E. Engdahl, D. Felikson, X. Fettweis, R. Forsberg, A. E. Hogg, H. Gallee, A. Gardner, L. Gilbert, N. Gourmelen, A. Groh, B. Gunter, E. Hanna, C. Harig, V. Helm, A. Horvath, M. Horwath, S. Khan, K. K. Kjeldsen, H. Konrad, P. L. Langen, B. Lecavalier, B. Loomis, S. Luthcke, M. McMillan, D. Melini, S. Mernild, Y. Mohajerani, P. Moore, R. Mottram, J. Mouginot, G. Moyano, A. Muir, T. Nagler, G. Nield, J. Nilsson, B. Noël, I. Otosaka, M. E. Pattle, W. R. Peltier, N. Pie, R. Rietbroek, H. Rott, L. Sandberg Sørensen, I. Sasgen, H. Save, B. Scheuchl, E. Schrama, L. Schröder, K. W. Seo, S. B. Simonsen, T. Slater, G. Spada, T. Sutterley, M. Talpe, L. Tarasov, W. J. van de Berg, W. van der Wal, M. van Wessem, B. D. Vishwakarma, D. Wiese, D. Wilton, T. Wagner, B. Wouters, and J. Wuite (2020). "Mass balance of the Greenland Ice Sheet from 1992 to 2018". *Nature* 579.7798, pp. 233–239. DOI: 10.1038/s41586-019-1855-2.

Shepherd, A., E. Ivins, E. Rignot, B. Smith, M. Van Den Broeke, I. Velicogna, P. Whitehouse, K. Briggs, I. Joughin, G. Krinner, S. Nowicki, T. Payne, T. Scambos, N. Schlegel, A. Geruo, C. Agosta, A. Ahlstrøm, G. Babonis, V. Barletta, A. Blazquez, J. Bonin, B. Csatho, R. Cullather, D. Felikson, X. Fettweis, R. Forsberg, H. Gallee, A. Gardner, L. Gilbert, A. Groh, B. Gunter, E. Hanna, C. Harig, V. Helm, A. Horvath, M. Hor-

wath, S. Khan, K. K. Kjeldsen, H. Konrad, P. Langen, B. Lecavalier, B. Loomis, S. Luthcke, M. McMillan, D. Melini, S. Mernild, Y. Mohajerani, P. Moore, J. Mouginot, G. Moyano, A. Muir, T. Nagler, G. Nield, J. Nilsson, B. Noel, I. Otosaka, M. E. Pattle, W. R. Peltier, N. Pie, R. Rietbroek, H. Rott, L. Sandberg-Sørensen, I. Sasgen, H. Save, B. Scheuchl, E. Schrama, L. Schröder, K. W. Seo, S. Simonsen, T. Slater, G. Spada, T. Sutterley, M. Talpe, L. Tarasov, W. J. Van De Berg, W. Van Der Wal, M. Van Wessem, B. D. Vishwakarma, D. Wiese, and B. Wouters (2018). *Mass balance of the Antarctic Ice Sheet from 1992 to 2017*. DOI: 10.1038/s41586-018-0179-y.

Shepherd, A., D. Wingham, T. Payne, and P. Skvarca (2003). "Larsen Ice Shelf Has Progressively Thinned". *Science* 302.5646, pp. 856–859. DOI: 10.1126/science.1089768.

Shepherd, A., D. J. Wingham, and J. A. Mansley (2002). "Inland thinning of the Amundsen Sea sector, West Antarctica". *Geophysical Research Letters* 29.10, pp. 2–1. DOI: 10.1029/2001gl014183.

Singh, P. and U. K. Haritashya (2011). "Encyclopedia of Snow, Ice and Glaciers". *Encyclopedia of Earth Sciences Series*. Encyclopedia of Earth Sciences Series. Ed. by V. P. Singh, P. Singh, and U. K. Haritashya, p. 1300. DOI: 10.1007/978-90-481-2642-2.

Skvarca, P. (1994). "Changes and surface features of the Larsen Ice Shelf, Antarctica, derived from Landsat and Kosmos mosaics". *Annals of Glaciology* 20, pp. 6–12. DOI: 10.3189/1994AoG20-1-6-12.

Skvarca, P., W. Rack, and H. Rott (1999). "34 year satellite time series to monitor characteristics, extent and dynamics of Larsen B Ice Shelf, Antarctic Peninsula". *Annals of Glaciology* 29.January 1990, pp. 255–260. DOI: 10.3189/172756499781821283.

Smith, J. A., M. J. Bentley, D. A. Hodgson, and A. J. Cook (2007). "George VI Ice Shelf: Past history, present behaviour and potential mechanisms for future collapse". *Antarctic Science* 19.1, pp. 131–142. DOI: 10.1017/S0954102007000193.

Sugden, D. E. (1996). "The East Antarctic Ice Sheet: Unstable Ice or Unstable Ideas?" *Transactions of the Institute of British Geographers* 21.3, p. 443. DOI: 10.2307/622590.

Talbot, M. H. (1988). "Oceanic Environment of George VI Ice Shelf, Antarctic Peninsula". *Annals of Glaciology* 11, pp. 161–164. DOI: 10.1017/S0260305500006480.

Tapley, B. D., S. Bettadpur, M. Watkins, and C. Reigber (2004). "The gravity recovery and climate experiment: Mission overview and early results". *Geophysical Research Letters* 31.9. DOI: 10.1029/2004GL019920.

Tareghian, R. and P. Rasmussen (2013). "Analysis of Arctic and Antarctic sea ice extent using quantile regression". *International Journal of Climatology* 33.5, pp. 1079–1086. DOI: 10.1002/joc.3491.

Titsias, M. K. (2009). *Variational learning of inducing variables in sparse Gaussian processes*. Tech. rep., pp. 567–574.

Turner, J., H. Lu, I. White, J. C. King, T. Phillips, J. S. Hosking, T. J. Bracegirdle, G. J. Marshall, R. Mulvaney, and P. Deb (2016). "Absence of 21st century warming on Antarctic Peninsula consistent with natural variability". *Nature* 535.7612, pp. 411–415. DOI: 10.1038/nature18645.

United Nations (2007). "PERCENTAGE OF TOTAL POPULATION LIVING IN COASTAL AREAS Oceans, Seas and Coasts Coastal Zone Core indicator".

Van Der Veen, C. J. and A. J. Payne (2009). "Modelling land-ice dynamics". *Mass Balance of the Cryosphere*. Cambridge University Press, pp. 169–226. DOI: 10.1017/cbo9780511535659.008.

Vaughan, D. G., D. R. Mantripp, J. Sievers, and C. S. M. Doak (1993). "A synthesis of remote sensing data on Wilkins Ice Shelf, Antarctica". *Annals of Glaciology* 17, pp. 211–218. DOI: 10.3189/s0260305500012866.

Vaughan, D. G. (1993). "Relating the occurrence of crevasses to surface strain rates". *Journal of Glaciology* 39.132, pp. 255–266. DOI: 10.3189/s0022143000015926.

Vaughan, D. G., G. J. Marshall, W. M. Connolley, C. Parkinson, R. Mulvaney, D. A. Hodgson, J. C. King, C. J. Pudsey, and J. Turner (2003). *Recent rapid regional climate*

warming on the Antarctic Peninsula. Tech. rep. 3, pp. 243–274. DOI: 10.1023/A:1026021217991.

Vaughen, D. G. and S. M. Doake (1996). *Recent atmosheric warming and retreat of ice shelves on the Antarctic Peninsula*.

Veen, C. J. van der (1998). "Fracture mechanics approach to penetration of bottom crevasses on glaciers". *Cold Regions Science and Technology* 27.3, pp. 213–223. DOI: 10.1016/S0165-232X(98)00006-8.

Velicogna, I. (2009). "Increasing rates of ice mass loss from the Greenland and Antarctic ice sheets revealed by GRACE". *Geophysical Research Letters* 36.19. DOI: 10.1029/2009GL040222.

Velicogna, I. and J. Wahr (2005). "Greenland mass balance from GRACE". *Geophysical Research Letters* 32.18, pp. 1–4. DOI: 10.1029/2005GL023955.

Vieli, A., A. J. Payne, A. Shepherd, and Z. Du (2007). "Causes of pre-collapse changes of the Larsen B ice shelf: Numerical modelling and assimilation of satellite observations". *Earth and Planetary Science Letters* 259.3-4, pp. 297–306. DOI: 10.1016/j.epsl.2007.04.050.

Vieli, A., A. J. Payne, Z. Du, and A. Shepherd (2006). "Numerical modelling and data assimilation of the Larsen B ice shelf, Antarctic Peninsula". *Philosophical Transactions of the Royal Society A: Mathematical, Physical and Engineering Sciences* 364.1844, pp. 1815–1839. DOI: 10.1098/rsta.2006.1800.

Vuuren, D. P. van, J. Edmonds, M. Kainuma, K. Riahi, A. Thomson, K. Hibbard, G. C. Hurtt, T. Kram, V. Krey, J. F. Lamarque, T. Masui, M. Meinshausen, N. Nakicenovic, S. J. Smith, and S. K. Rose (2011). "The representative concentration pathways: An overview". *Climatic Change* 109.1, pp. 5–31. DOI: 10.1007/s10584-011-0148-z.

Wang, J., W. Gao, S. Xu, and L. Yu (2012). "Evaluation of the combined risk of sea level rise, land subsidence, and storm surges on the coastal areas of Shanghai, China". *Climatic Change* 115.3-4, pp. 537–558. DOI: 10.1007/s10584-012-0468-7.

Ward, C. G. (1995). "Short Note Mapping Ice front Changes of Wilier Ice Shelf, Antarctic Peninsula". *Antarctic Science* 7.2, pp. 197–198. DOI: 10.1017/S0954102095000265.

Warner, R. C., H. A. Fricker, S. Adusumilli, P. Arndt, J. Kingslake, and J. J. Spergel (2021). "Rapid Formation of an Ice Doline on Amery Ice Shelf, East Antarctica". *Geophysical Research Letters* 48.14, e2020GL091095. DOI: 10.1029/2020GL091095.

Watanabe, O., J. Jouzel, S. Johnsen, F. Parrenin, H. Shoji, and N. Yoshida (2003). "Homogeneous climate variability across East Antarctica over the past three glacial cycles". *Nature* 422.6931, pp. 509–512. DOI: 10.1038/nature01525.

Wdowinski, S., R. Bray, B. P. Kirtman, and Z. Wu (2016). "Increasing flooding hazard in coastal communities due to rising sea level: Case study of Miami Beach, Florida". *Ocean and Coastal Management* 126, pp. 1–8. DOI: 10.1016/j.ocecoaman.2016.03.002.

Weertman, J. (1983). "Creep deformation of ice." *Annual review of earth and planetary sciences.* 11, pp. 215–240. DOI: 10.1146/annurev.ea.11.050183.001243.

Weis, M., R. Greve, and K. Hutter (1999). "Theory of shallow ice shelves". *Continuum Mechanics and Thermodynamics* 11.1, pp. 15–50. DOI: 10.1007/s001610050102.

Wendt, J., A. Rivera, A. Wendt, F. Bown, R. Zamora, G. Casassa, and C. Bravo (2010). *Recent ice-surface-elevation changes of Fleming Glacier in response to the removal of the Wordie Ice Shelf, Antarctic Peninsula.* Tech. rep. 55, pp. 97–102. DOI: 10.3189/172756410791392727.

Wessem, J. M. van, S. R. Ligtenberg, C. H. Reijmer, W. J. Van De Berg, M. R. Van Den Broeke, N. E. Barrand, E. R. Thomas, J. Turner, J. Wuite, T. A. Scambos, and E. Van Meijgaard (2016). "The modelled surface mass balance of the Antarctic Peninsula at 5.5¯km horizontal resolution". *The Cryosphere* 10.1, pp. 271–285. DOI: 10.5194/tc-10-271-2016.

Wingham, D. J., D. W. Wallis, and A. Shepherd (2009). "Spatial and temporal evolution of Pine Island Glacier thinning, 1995–2006". *Geophysical Research Letters* 36.17. DOI: 10.1029/2009GL039126.

Wingham, D., A. Shepherd, A. Muir, and G. Marshall (2006). "Mass balance of the Antarctic ice sheet". *Philosophical Transactions of the Royal Society A: Mathematical, Physical and Engineering Sciences* 364.1844, pp. 1627–1635. DOI: 10.1098/RSTA.2006.1792.

Wu, S. Y., B. Yarnal, and A. Fisher (2002). "Vulnerability of coastal communities to sea-level rise: A case study of Cape May County, New Jersey, USA". *Climate Research* 22.3, pp. 255–270. DOI: 10.3354/cr022255.

Zhang, X., A. F. Thompson, M. M. Flexas, F. Roquet, and H. Bornemann (2016). "Circulation and meltwater distribution in the Bellingshausen Sea: From shelf break to coast". *Geophysical Research Letters* 43.12, pp. 6402–6409. DOI: 10.1002/2016GL068998.